Plasma-Catalytic DRM: Study of LDH-Derived Catalyst for DRM in a GAP Plasma System

Wencong Xu

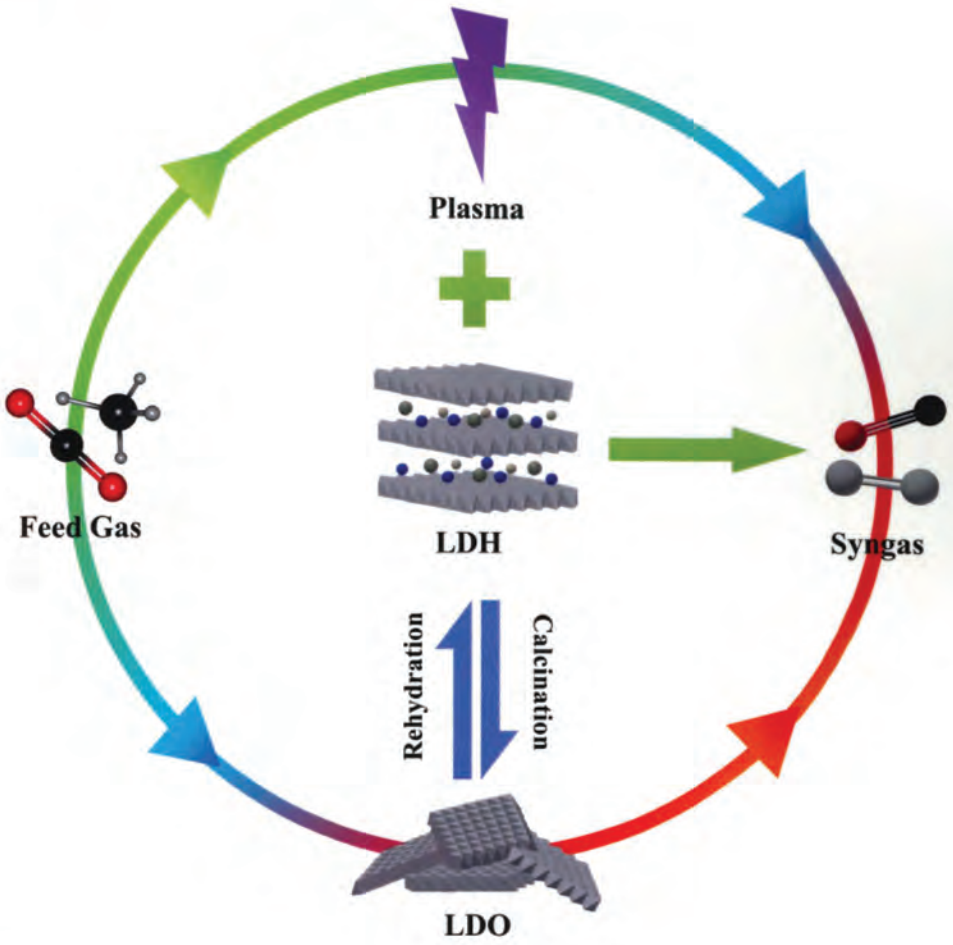

Supervisors **Prof. Dr. Vera Meynen | Prof. Dr. Annemie Bogaerts | Prof. Dr. Vladimir V. Galvita**

Thesis submitted for the degree of

Doctor of Science: Chemistry
Faculty of Science Departement Chemistry, Antwerp, 2023

Doctor of: Chemical Engineering
Faculty of Engineering and Architecture, Ghent

University of Antwerp

GHENT UNIVERSITY

Faculty of Science

Department of Chemistry

Faculty of Engineering and Architecture
Department of Materials, Textiles and Chemical Engineering

Plasma-Catalytic DRM: Study of LDH-Derived Catalyst for DRM in a GAP Plasma System

Proefschrift voorgelegd tot het behalen van de graad van
doctor in de wetenschappen: chemie aan de Universiteit Antwerpen
en de graad van
doctor in de ingenieurswetenschappen: chemische technologie aan de Universiteit Gent
te verdedigen door

Wencong Xu

Supervisors:
Prof. dr. Vera Meynen; Prof. dr. Annemie Bogaerts; Prof. dr. Vladimir V. Galvita

Antwerp, 2023

Faculteit Wetenschappen

Departement Chemie

Faculteit Ingenieurswetenschappen
en Architectuur
Vakgroep Materialen, Textiel en
Chemische Proceskunde

Plasmakatalytische DRM: studie van LDH-afgeleide katalysator voor DRM in een GAP-plasmasysteem

Proefschrift voorgelegd tot het behalen van de graad van
doctor in de wetenschappen: chemie aan de Universiteit Antwerpen
en de graad van
doctor in de ingenieurswetenschappen: chemische technologie aan de Universiteit Gent
te verdedigen door

Wencong Xu

Supervisors:
Prof. dr. Vera Meynen; Prof. dr. Annemie Bogaerts; Prof. dr. Vladimir V. Galvita

Antwerpen, 2023

Table of Contents

Acknowledgments

Happy time always goes fast. It was like yesterday when I came to Belgium Antwerp. Many things and people goes through my mind. I would like to express my gratitude herein.

Firstly, I would like to thank my supervisors, Prof. Vera Meynen, Prof. Annemie Bogaerts, and Prof. Vladimir V. Galvita. Thank you for giving me the chance to come to University of Antwerp to work and to Ghent University for joint PhD and doing experiments. I still remember the moment when I got offer from Vera and Annemie. It is one of the happiest moments in my life. It is very wonderful experience to work in University of Antwerp and Gent University. Besides this, during the off work time, I also had quite many good times in not only Belgium but also other countries in Europe.

I also very gratefully acknowledge the VLAIO Catalisti Moonshot project D2M and the VLAIO Catalisti transition project CO2PERATE (HBC.2017.0692) for financial support.

I would like to say my sincere thanks to the members of my jury as well. I appreciate your time and help during the period of my pre-defence and public defence. During the four years PhD time, there are also many people to be thanked:

Prof. Pegie Cool, very glad to work with you in the team. Many times your suggestions in the group meeting can help me realize the problems which I may also have.

Gert Nuyts and Thomas Kenis, thank you for helping in the characterizations by SEM and ICP. Your help contributed a lot to make my papers better. Myrjam Mertens from VITO, thank you for helping to test many samples of XRD, which to some degree lay the foundation of my LDO rehydration paper. Elien Derveaux and Prof. Peter Adriaensens from University of Hasselt, your help in ^{27}Al MAS NMR also makes my paper more complete.

Also thank you at Dr. Lukas C. Buelens. Thank you for teaching me in the utilization of the thermal catalytic setup and helping me to deal with this part of the data. Thanks also need to be given to Gilles Van Loon: your help in making many devices truly helped a lot for my experiments.

I like to make new friends. For my Chinese friends and colleagues, working and playing with you all is a very pleasure thing. Although sometimes the language

limited my expression, I would like also to chat and maybe more often to listen to my “foreigner” friends and colleagues.

Thanks at Rui, who started his PhD half a year before me. Your help goes through my whole PhD period. Many times he is the first person I am going to ask when I met some problems in the work or life. His help let me get familiar with the work and life in the university faster.

Thanks at Jinxin, who also started the PhD before me. I felt panic when I came to Antwerp the first time. Thanks at Jinxin to pick me up in the Berchem train station. As we both do research in plasma DRM, discussions with him let me learn a lot. Also thanks to his wife, Kaimin, not only in discussions of research things, but also in answering where Jinxin is when I look for him.

Thanks at Karen and Saskia. Your help in many things, like instruments training, safety training, ordering things for me, and solving instruments problems. I enjoy the chats when we change gas bottles.

Thanks at Rana. You are the mentor who taught me the basic operation of my plasma setup and the GC instrument, which lay the foundation of my later study.

Thanks at Radu, Sander and Iza. Very glad to stay in the same office. Chatting with you and listening you chatting are a very pleasure thing for me.

Thanks at Stefano, Ravi, Jeroen, Diana, Valeria, Wouter, Lore, Hilde, and Mitra. Chatting with you helped me to know more about different cultures. Very glad to know you all.

Thanks at Shangkun, Jian and Peng. Discussing scientific things and travelling with you are very pleasant. Besides this, I'm very glad to finish the half marathon running in Antwerp with Shangkun and Peng.

Thanks at Yuwei, my girlfriend. We had a difficult time staying in different countries and having no chance to meet each other during the Covid-19 period. However, finally, we get through it. Your support, understanding and encouragement helped a lot to decrease my stress in both work and life. I love you!

Last but not the least, I thank my parents very much. You are always the courage and support of mine to purse a PhD. Covid-19 made everything become more difficult than usual. Impossible to go back to China made me homesick, while chatting with you two always relaxes me. You're my support, I can eventually finish my PhD well. Thank you two very much. I love you two!

List of abbreviations

CCU	Carbon capture and utilization
DRM	Dry reforming of methane
LDH	Layered double hydroxide
GA	Gliding arc
GAP	Gliding arc plasmatron
LDO	Layered double oxide
DBD	Dielectric barrier discharge
MO	Metal oxide
T-bed	Tray-type catalyst bed
RH	Relative humidity
N-bed	Newly designed catalyst bed
NOAA	National Oceanic and Atmospheric Administration
IPC	In-plasma catalysis
PPC	Post-plasma catalysis
TOS	Time on-stream
RWGS	Reverse water gas shift reaction
TG	Thermogravimetric
3D	Three-dimensional
GHSV	Gas hourly space velocity
DFT	Density functional theory
TPSR	Temperature programmed surface reaction
NSs	Nanosheets
TPD	Temperature-programmed desorption
IR	Infrared spectrometry
HMT	Hexamethylenetetramine

SEI	Specific energy input
AC power source	Alternating current power source
PRF	Pulse repetition frequency
2D	Two-dimensional
RGA	Rotating gliding arc plasmas
PEGP	Parallel wire-plate electrodes gliding arc plasma
RF	Radio frequency
NF	Nickel foam
SEM	Scanning electron microscope
ICP analysis	Inductively coupled plasma analysis
XRD	X-ray diffraction
^{27}Al MAS	^{27}Al magic-angle spinning
NMR	Nuclear magnetic resonance
TG-MS	Thermogravimetric analysis - mass spectrometry
MS	Mass spectrometry
ICP-MS	Inductively coupled plasma - mass spectrometry
DRIFT	Diffuse Reflectance Infrared Fourier Transform
Re-LDH	Rehydrated-LDH
DTG	Derivative thermogravimetric
DSC	Differential scanning calorimetry
S_{BET}	Specific surface area calculated with BET method
BET	Brunauer-Emmett-Teller
FT-IR	Fourier transformed infrared spectroscopy
DVP	Dual-vortex plasmatron
EC	Energy cost
EE	Energy efficiency
MW	Microwave
DC	Direct current

CEM	Controlled evaporator mixer
GC	Gas chromatography
CFD	Computational fluid dynamics
H_2-TPR	Hydrogen-temperature programmed reduction
O_2-TPO	Oxygen-temperature programmed oxidation
WGSR	Water gas shift reaction
Ni/MO	Ni-based metal oxide

General Introduction

The carbon dioxide (CO_2) concentration increases every year due to human activities, such as burning of fossil fuels, which leads to global warming and has attracted much concern in society. Carbon capture and utilization (CCU) is one of the strategies to mitigate part of the CO_2 emissions, in which CO_2 is captured from exhaust gases and utilized in divers processes. Dry reforming of methane (CH_4) (DRM) with captured CO_2 is one of these CCU technologies with the aim to convert the captured CO_2 together with CH_4 (e.g. from natural supplies or biogas) to syngas (CO and H_2), which in turn can be used to produce a wide variety of chemical building blocks such as via Fischer-Tropsch processes. Traditional thermal catalytic DRM happens at high temperatures over 700 °C. However, next to the requirement of thermal energy, classically obtained via fossil fuel burning, coke deposition and catalyst deactivation are current challenges. Layered double hydroxide (LDH)-derived catalysts are promising for DRM as they possess many advantages such as a high specific surface area, rich basic sites, good active metal dispersion and adjustable active metal loading. As an alternative to thermal DRM, plasma is an attractive technology as it uses (renewable) electric energy as energy source. However, several challenges remain to improve its conversion, energy efficiency and selectivity. Although plasma catalysis has been identified as a

possible solution for this, the integration of catalysts with the plasma process is not straightforward and requires additional knowledge. This PhD focuses on the combination of warm 3D gliding arc (GA) plasmas with post-plasma catalysis using LDH-based catalysts. These catalysts are known to function well in thermal catalytic DRM processes, but we need to evaluate if these catalysts also perform well in combination with a gliding arc plasmatron (GAP) reactor. Therefore, several research questions need to be answered such as: 1) what are the key factors used in the GAP process that influence the post-plasma catalysis with respect to temperature and gas composition at the plasma exhaust, that influence the post-plasma catalytic process and 2) what are the key performance indicators and reactor configurations that determine and enhance the post-plasma catalytic DRM performance.

Chapter 1 gives a general introduction of LDH-derived catalysts, plasma and their combination for DRM. In this chapter, the impact of LDH-derived layered double oxide (LDO) properties on catalytic (DRM) performance is discussed. Subsequently, two types of plasma, dielectric barrier discharge (DBD) and gliding arc (GA), are introduced, which are typical examples representative of non-thermal plasma (DBD) and warm plasma (GA) and the concepts of choosing for in-plasma or post-plasma catalysis are provided. Their application for DRM assisted with or without LDH or LDH-derived catalyst is given. Finally, the challenges and aims of this PhD are discussed.

In Chapter 2, the properties of MgAl-LDH (molar ratio of Mg:Al = 3) materials and the LDH-derived LDO, also named metal oxides (MO), as a function of calcination temperature (600-900 °C) are discussed. This temperature range was chosen as it is the expected exhaust gas temperature of the GAP plasma for which it will be used. To understand the stability of the LDO materials towards water, their rehydration was studied in both vapour and liquid water environment at room temperature. Several characterization techniques were used to study the as-synthesized LDH and the rehydrated LDH obtained after rehydration of LDO calcined at different temperatures. Results proved that the rehydration of the LDO into the LDH resulted in a new LDH rather than reconstructing it into the original LDH. This part of research gives suggestions for the careful storage of LDH-derived samples even after calcination at high temperatures of 600-900 °C.

In Chapter 3, we studied the influence of operating conditions for a gliding arc plasmatron (GAP) system, such as gas flow rate, gas composition (N_2/CO_2, and $N_2/CO_2/CH_4$ with different CO_2/CH_4 ratios) and addition of H_2O on the conversion, selectivity, energy cost and temperature of the exhaust gas. Furthermore, the temperature in different positions after the plasma was measured, which can offer suggestions for the further synergistic application of post-plasma catalytic system.

In Chapter 4, the catalyst is added via a tray-type catalyst bed (T-bed) into the GAP reactor forming a post-plasma catalytic system. The impact of various parameters such as catalyst amount, distance of the catalyst from the plasma (2-4 cm), external heating with a temperature range of 100-250 °C, and addition of H_2O with relative humidity (RH) from 0% to 100% was studied with the aim to identify key aspects that influence the catalyst performance.

As no or limited catalyst performance improvement was obtained in Chapter 4, it was hypothesized that heat transfer and flow behavior were crucial aspects to improve. Therefore, a newly designed tubular catalyst bed (N-bed) was proposed in Chapter 5. Utilizing the N-bed, even when only filling material of α-Al_2O_3 was used, the conversion of CO_2 and CH_4 increased and further enhancement was achieved upon the addition of Ni/MO catalysts. Next to conversion and selectivity, the impact of the N-bed on energy cost was evaluated.

CHAPTER 1

LDH-derived catalysts for DRM: Can their excellent performance in thermal catalysis also be exploited in plasma catalysis?

This chapter is adapted from the paper "LDH-derived catalysts for DRM: Can their excellent performance in thermal catalysis also be exploited in plasma catalysis?; Wencong Xu, Vladimir V. Galvita, Vera Meynen, Annemie Bogaerts", to be submitted to Catalysts.

1.1 Introduction

Among the greenhouse gases, carbon dioxide (CO_2) and methane (CH_4) attract much concern due to their impact on global warming. The CO_2 concentration increases every year among others due to burning of fossil fuels. The "National Oceanic and Atmospheric Administration (NOAA) Global Monitoring Laboratory" (https://gml.noaa.gov/ccgg/trends/) data showed that the global annual mean CO_2 amount reached about 422 ppm in July 2023, with a growth rate of around 2.4 ppm per year during the decade 2012-2022. Moreover, reducing greenhouse emissions is one of the priority initiatives in the European Green Deal (https://commission.europa.eu/strategy-and-policy/priorities-2019-2024/european-green-deal_en). One of its goals is to curb temperature pathways by 2050. For this reason, it becomes imperative to decrease the amount of CO_2 and CH_4 emissions, which needs the collaborative efforts of both researchers and governments from all over the world. Many technologies, for example, CO_2 capture, storage and conversion, are under investigation, to solve this problem in recent years [1–9].

Studies have shown that CO_2 is the largest greenhouse gas contributor, followed by CH_4 [10]. At the same time, an abundant amount of natural gas reserves [11] and the CH_4-rich biogas, e.g. produced from the anaerobic digestion of organic matter, make the dry reforming of methane (DRM) reaction an attractive route to

convert CO_2 and CH_4 simultaneously into syngas (CO and H_2) [12]. Indeed, if carbon capture and utilization is envisioned, useful products need to be produced from CO_2 such as construction materials or chemical building blocks. The majority of these chemical building blocks have hydrogen atoms as part of their molecular structure, necessitating the use of a hydrogen source to produce them from CO_2. Next to hydrogen itself, water and methane can serve as examples of such a hydrogen source, the latter via the DRM reaction. This is a complex process which consists of several reactions. The main reactions are shown below [13–15]:

$$CH_4 + CO_2 \rightarrow 2CO + 2H_2 \quad \Delta H^0 = 247\ \mathrm{kJ/mol} \tag{1.1}$$

$$CH_4 \rightarrow C_{(s)} + 2H_2 \quad \Delta H^0 = 75\ \mathrm{kJ/mol} \tag{1.2}$$

$$CO_2 + H_2 \rightarrow H_2O + CO \quad \Delta H^0 = 41\ \mathrm{kJ/mol} \tag{1.3}$$

$$2CO \rightarrow C_{(s)} + CO_2 \quad \Delta H^0 = -172\ \mathrm{kJ/mol} \tag{1.4}$$

The CO_2 requires a significant amount of energy for activation, necessitating high temperatures above 700°C in conventional thermal catalytic DRM [16–18]. Additionally, carbon formation as described in Eq.(1.2) and Eq.(1.4) increases the risk of catalyst deactivation due to carbon deposition on the catalyst. Therefore, to increase the conversion of CO_2 and/or CH_4 and the selectivity of desired products, it is crucial to employ catalysts that are not only highly active but also possess stable active sites and resistance to carbon deposition.

Nickel and noble metals like Pt, Ru, and Rh, renowned for their high catalytic activity and resistance to carbon formation, are extensively studied in dry reforming [18–20]. Despite their effectiveness, the high cost and limited availability of these noble metals restrict their industrial application. As a viable alternative, nickel-based catalysts have been considered; however, they are prone to deactivation due to sintering and carbon encapsulation under reforming conditions [20–22]. Enhancing the activity and stability of nickel catalysts thus becomes a critical area of research, with a focus on the impact of supports, promoters, and additional metals.

Aluminum oxide (Al_2O_3) is a common catalyst support, and other materials like MgO, ZrO_2, La_2O_3, TiO_2, SiO_2, and SiO_2-Al_2O_3 have also been explored [23–26]. The choice of support materials significantly influences the DRM process. For catalysts on inert supports such as SiO_2, the process follows a monofunctional pathway with limited CO_2 activation leading to catalyst deactivation. In contrast, on acidic (Al_2O_3) or basic (La_2O_3, CeO_2, MgO) supports, a bifunctional mechanism is observed, enhancing activity and stability [23,24].

Layered double hydroxide (LDH), or hydrotalcite, and its derivative, layered double oxide (LDO), are promising due to their active surface area, basic properties, and adjustable metal loading [19,27–29]. LDHs are versatile, allowing composition changes through different metals and anions. After calcination, LDOs enhanced

with additional metals exhibit improved stability and activity, attributed to a synergistic effect [19].

Apart from the development of improved LDH-derived catalysts for DRM, different technologies are being perfected or generated [30]. Among them, plasma technology with its versatility, is garnering growing interest, particularly as it is an electrically driven process [31–35]. In general, plasma, often referred to as “the fourth state of matter”, is an ionized gas that can be artificially generated by supplying electric energy to a gas [8,36]. This method of plasma production aligns well with the evolving demand for electrically driven processes in the chemical industry [37]. Moreover, plasma technology can be synergistically combined with catalysts in two distinct ways: directly form (in-plasma catalysis, IPC) or in hybrid form (post-plasma catalysis, PPC). Considering that nascent stage of plasma-assisted catalytic DRM systems, LDH-derived catalysts, as a type of promising catalyst for thermal-catalytic DRM, are worth investigating for their synergistic effect in a plasma-based DRM. These catalysts, with their high active surface area, abundance of basic and active sites and tunable structure and metal composition, may enhance IPC systems, where the catalyst is integrated into the plasma discharge zone. IPC is typically applied in dielectric barrier discharge reactors, operating near room temperature and at pressures of 1 to 3 bar [31,38–41]. Conversely, in PPC systems, the catalyst is located outside the plasma discharge area, near the plasma exhaust. This setup is typically used in warm plasmas, which

reach temperatures of 3000 K or more in the discharge zone (e.g. gliding arcs and microwave plasmas) [37,42–44]. The gas exiting the plasma cools down with distance from the plasma exhaust, reaching several hundred degrees. This feature allows for the recovery of heat produced by the plasma to preheat the catalyst, facilitating the conversion of unreacted CO_2 and CH_4 molecules into syngas or converting the plasma exhaust gases to other products, depending on the catalyst. Nevertheless, the majority of the PPC processes require additional heating or insulation to achieve sufficient catalytic performance [42,44,45]

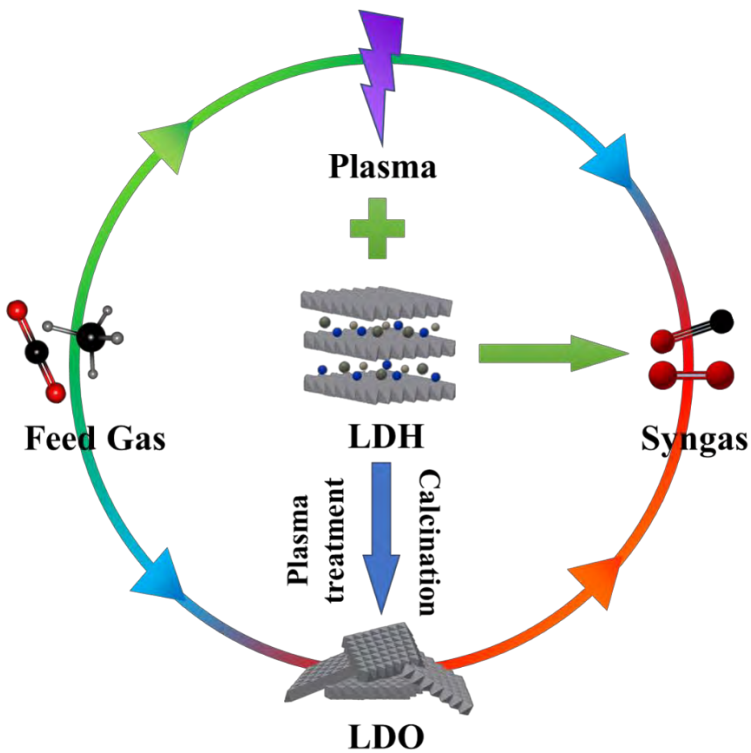

Fig. 1.1. Schematic diagram of the utilization of LDH/LDO and plasma in DRM in this chapter.

In the past several years, there has been a rapid growth in publications related to the catalytic application of LDH-derived catalysts for DRM, as well as for plasma-

based DRM with or without catalysis [19,46–53]. However, no review on the combination of LDH-derived catalysts and plasma for DRM has been reported yet. Herein, the chapter first discusses the applications of recently reported LDH-derived metal oxides catalysts and plasma technology for DRM to syngas production separately. Then the combination of LDH-derived metal oxides in plasma catalysis is generally introduced. The schematic structure of the chapter is shown in Fig 1.1. In the following section, the LDH-derived catalysts are divided into LDH-derived catalysts without Ni, Ni-containing LDH-derived catalysts, and promoted Ni LDH-derived catalysts. Based on the promoted metals used, the last part is divided into three subsections: transition metal bimetallic Ni LDH-derived catalyst, lanthanides metal binary Ni LDH-derived catalyst, and other metal binary and multi-metals Ni LDH-derived catalyst. Subsequently, two commonly used plasma types, i.e., dielectric barrier discharge plasma (DBD) and gliding arc (GA) plasma, and their solo application in DRM are introduced, which are representative of non-thermal plasma (DBD) and warm plasma (GA). Finally, the integration of plasma with LDH or LDO catalysts for DRM is introduced, encompassing two parts: DBD plasma-assisted LDH/LDO catalysis, typically implemented as 'IPC' for DRM, and GA plasma-assisted LDH/LDO catalysis, usually conducted as 'PPC' for DRM. Each main section includes brief theoretical notes and discussions. Lastly, a conclusion and future outlook are provided, offering research recommendations.

1.2 LDH-derived catalyst for DRM

As mentioned above, the DRM route is of great interest as it involves the conversion of two major greenhouse gases, namely CO_2 and CH_4. After the reaction, syngas (i.e., a mixture of H_2 and CO) is produced, which can be used directly for the production of valuable chemicals such as methanol, ethanol, formic acid etc. [54–56]. Among all the types of materials developed, LDH-derived mixed metal oxide materials (MgAl-LDH as the most commonly used LDH) show some advantages, like tuneability of its composition, abundant basic site and well-distributed active sites. When introducing high active metals, such as Rh, Pt and Ru, into the LDH-derived MgO-Al_2O_3 structure, the catalyst can show good catalytic performance with around 90% conversion of CO_2 and CH_4 at 750 °C for DRM [28,57,58]. Compared with other supports, such as γ-Al_2O_3, MgO, and $MgAl_2O_4$, the Ru catalyst supported on MgAl-LDH derived Mg_3(Al)O showed the highest Ru metal dispersion and catalytic performance [28]. Moreover, the Ru/Mg_3(Al)O catalyst displayed 84% CH_4 conversion and 90% CO_2 conversion at 750 °C for 30 h with no deactivation. However, although noble metals exhibit excellent conversion and coke-resistance properties, they are critical raw materials with a shortage in reserves and are expensive, which puts constrains on their industrial applications. In comparison, catalysts derived from Ni-based LDHs, either alone or promoted with small amounts of other metals, like transition metals, are cost-friendly and have good catalytic activities with about 90% CH_4 conversion

and 95% CO_2 conversion at 750 °C with 15 wt% Ni loading [59], showing considerable application potential in the DRM reaction. Nevertheless, the well-dispersed small Ni nanoparticles, being one of the important reasons for obtaining high catalytic performance, are not stable, as they sinter during the reaction process. Moreover, coke formation from direct CH_4 decomposition and CO disproportionation easily occurs on the catalyst surface, covering the active sites and leading to catalyst deactivation and reactor blocking when the coke deposition is serious. Therefore, more research focusing on enhancing the stability and coke resistance of LDH derived catalysts is highly needed.

This chapter is divided into three parts, dependent on the metals it contains: LDH-derived DRM catalyst without Ni, monometallic Ni LDH-derived DRM catalyst, and promoted Ni LDH-derived DRM catalyst. Based on the promoted metals utilized, the promoted Ni LDH-derived catalyst contains three parts: transition metal promoted binary Ni LDH-derived catalyst, lanthanides metal promoted binary Ni LDH-derived catalyst, and other binary and multi-metal Ni LDH-derived catalyst. The newly reported results in this area are shown and discussed.

1.2.1 LDH-derived DRM catalysts without Ni

Apart from Ni-based catalysts, Co is another low-cost metal attracting more attention in recent years. Attempts have been made to find promising results using a Co-LDH-based catalyst without the addition of Ni. Li's group [60] compared the

short-term and long-term catalytic activity of NiMgAl-LDO and CoMgAl-LDO for DRM. The catalysts were prepared via the co-precipitation method with 12 wt% loading of Ni or Co. At a high-temperature of 800 °C with time on-stream (TOS) of 200 h, the experimental results showed conversions of CH_4 and CO_2 of about 88.0% and 93.6%, and a H_2/CO ratio of 0.85 for the NiMgAl-LDO catalyst, and a respective conversion of 86.7% and 92.7%, and a ratio of 0.85 for the CoMgAl-LDO catalyst. Moreover, the stability of the Ni and Co catalysts was similar, with a similar low coke deposition (1.2 wt% for the Ni catalyst, and 2.2 wt% for the Co catalyst) in the 200 h test. However, when the reactions were executed at a lower temperature of 500 °C for a short-term of 25 h, although the Ni and Co catalyst showed similar conversions, the Ni catalyst suffered serious coke deposition with 63.9 wt% weight loss when burning off the coke compared to about 4 wt% for the Co catalyst. The kinetics study for the low-temperature DRM illustrated that the better coke resistance of the Co catalyst is mainly due to its low activity for CH_4 dissociation/decomposition [60]. Here, this research proves the potential application of Co-LDH-derived catalyst in DRM at the low temperature of 500 °C.

To further study the catalytic activity of Co-LDH-based catalysts, LDHs with different metal compositions of Co, Mg or/and Al were synthesized, calcined, and then reduced for DRM at 700 °C [61]. The three catalysts, namely Co/MgAl, Co/MgO, and Co/Al_2O_3, were first tested at a TOS of 5 h. The Co/MgAl catalyst had the best initial activity (around 60% CH_4 conversion and 72% CO_2 conversion)

and outstanding stability (with a slight decrease in both CH_4 and CO_2 conversion for 5 h). The initial activity of Co/MgO had the lowest CH_4 and CO_2 conversion of about 40% and 60%, but it gradually increased to 45% and 63% during the whole test. However, although the Co/Al_2O_3 catalyst exhibited relatively good initial activity, it had an obvious deactivation as time went on. For the long-term stability test with TOS of 48 h, the conversion of the Co/MgAl catalyst slightly decreased from 58.6% to 55.7%, for CH_4 conversion and from 72% to 70% for CO_2 conversion presenting comparable catalytic performance as reported fora Ni catalyst with the same catalyst support [62]. Structural analysis demonstrated that the excellent initial catalytic activity of Co/MgAl was attributed to the high specific area (168 m^2/g), large amount of medium basic sites and small size (6.8 nm) of Co nanoparticles, while the long-term stable performance was related to the formation of a CoMgO solid solution improving its sintering- and coke- resistance.

Halliche et al. [63] used Fe as the element to replace Al forming CoFe-LDH. Compared with the CoAl-LDO catalyst, the activity of the CoFe-LDH was slightly lower (66.4% CH_4 conversion and 70.3% CO_2 conversion for the CoAl-LDO catalyst and 54.5% CH_4 conversion and 60.2% CO_2 conversion for the CoFe-LDO catalyst) due to the presence of iron, which favoured to react with water produced from the side reaction of reverse water-gas shift reaction (RWGS). However, the deposited coke was removed by the iron oxide formed by the RWGS step.

The comparable catalytic performance of the Co metal in DRM especially at relatively low temperatures (usually < 600 °C) offers a choice for the utilization of LDH-derived catalysts. Besides this, the coke-resistance property of Co with low CH_4 decomposition activity makes it favourable for long-term industrial production. When promoted with other metals, like Fe, which can help to suppress coke formation as well, the stability will be further improved, giving Co-LDH-based catalysts a broad research and application prospect.

1.2.2 Monometallic Ni LDH-derived catalyst

For the Ni catalyst derived from LDH, the Ni can be incorporated into the brucite-like structure of the catalyst by co-precipitation or simply through impregnation, forming a mixed hydroxide precursor [27]. After calcination, Ni containing mixed metal oxides are formed with controlled interaction between the Ni phase and its carrier, preventing the sintering of active material of Ni. Although depending on different preparation methods, there may be some differences in the particular chemical and physical properties of the obtained catalysts, the monometallic Ni-LDH-derived catalysts show satisfying performance in DRM, as shown in Table 1.1.

Different amounts of Ni used in the catalysts can have various effects on the Ni particle's size, distribution and interaction with the support, which eventually affects the catalytic performance and stability of the catalysts. Lin et al. [64]

investigated the influence of the Ni loading amount (3 wt% to 18 wt%) on the NiMgAl-LDH-derived catalyst for DRM. The catalysts were prepared via a co-precipitation method, forming NiMgAl-LDH precursors with different Ni amounts and were ready for reaction after calcination at 800 °C. The conversion of both CO_2 and CH_4 increased as the reaction temperature increased and with increasing amounts of Ni up to 9 wt%. The catalysts with 9 wt% and 12 wt% Ni had similar catalytic activity. In the case of 15 wt% loadings, the activity reached the highest value. However, serious coke deposition appeared on the catalyst with 18 wt% Ni loading, leading to the blocking of the reactor. Both the Ni loading and reaction temperature were found to affect the long-term stability [64]. At a high temperature of 750 °C, the catalytic activity increased as the loading amount increased, while the stability decreased for all the catalysts at a relatively lower temperature of 600 °C. This phenomenon was attributed to the carbon deposition that became more serious at 600 °C than at 750 °C, which was proven by the higher thermogravimetric (TG) loss (attributed to the carbon) of the catalyst after the reaction. Moreover, the deposited amount of coke increased with increasing Ni loading at both 600 °C and 750 °C. The coke deposition, especially encapsulating carbon, was considered to be the main reason for the deactivation of the catalysts.

Another study by Zhan et al. [65] reported on the influence of reduction temperature on the DRM reaction. Ni particles with an average size of 4 nm to 7.3 nm were obtained when changing the reduction temperature from 650 °C to 800 °C.

Generally, increasing the reduction temperature increased the Ni particle size. Since the Ni^{2+} species were incorporated into Mg(Ni, Al)O and were expected to disperse uniformly throughout the entire catalyst particle from surface to core, upon reduction, only those Ni^{2+} species at or close to the surface could be reduced. However, as the reduction temperature increased, more Ni^{2+} species were reduced, forming more Ni particles of larger size. All of the reduced samples had a good catalytic performance at high temperatures of 700 °C and 800 °C, while their low-temperature performance varied. At relatively low temperatures of 500 °C and 600 °C, the catalysts obtained at a reduction temperature of 700 °C exhibited stable CH_4 conversion which was close to the equilibrium levels (20% at 500 °C and 50% at 600 °C). In contrast, the catalyst reduced at 650 °C showed lower CH_4 conversion (initial around 5% to final about 0% at 500 °C and initial around 20% to finial around 30% at 600 °C) and deactivated at 500 °C because of Ni oxidation, while catalysts reduced at 750 °C and 800 °C suffered sintering and serious coking. In summary, they found that coke deposition is proportional to the Ni particle size and this trend ceases when the particle size is around or below 6.2 nm. Therefore, a critical size of about 6 nm of the Ni particles is essential to effectively inhibit coke deposition. The study reported by Kalai and co-workers [66] was consistent with this conclusion. They found that compared with catalysts prepared via the incipient wetness method (Ni loaded on γ-Al_2O_3), the NiMgAl-LDH-derived catalysts with the same Ni loading had smaller particle size, showing better activity and stability.

Apart from the Ni content and Ni particle size, the amount of basic sites also has a great effect on the catalytic performance of the catalyst [19]. Furthermore, by modifying NiMgAl-LDH with varying concentrations of NaOH, the modified LDH-derived catalyst showed an obvious increase in the stability of CH_4 conversion [67]. After modification, partial amounts of Al were dissolved with increasing NaOH amount, increasing the (M^{2+}/M^{3+}) molar ratio, as well as the basicity. The specific surface area (decreased from 231 to 212 m^2/g when the amount of NaOH increased) and pore volume (0.31-0.35 cm^3/g) were both higher than the raw NiMgAl-LDH (173 m^2/g and 0.26 cm^3/g). These variations eventually improved the catalytic performance and coke-resistance. The catalyst Ni/LDO-0.2 modified with 0.2 M NaOH solution was found to have the highest (initially around 91.6% CH_4 and 98% CO_2 conversion) and most stable (final around 90.8% CH_4 and 97% CO_2 conversion) activity within 8 h DRM, whereas Ni/LDO-0 (no modification) had the lowest initial around 88% CH_4 conversion and fastest activity decrease (final about 84% CH_4 conversion). However, when the modified catalysts were applied in a 28 h long-term stability test, the Ni/LDO-0.1 exhibited a higher activity and stability than the Ni/LDO-0.2. The CH_4 and CO_2 conversions for Ni/LDO-0.1 remained about 91% and 96%, while those for Ni/LDO-0.2 decreased from about 91% and 95% to around 86% and 91%. Besides this, it was found that enhancing the CO_2/CH_4 molar ratio benefits the resistance to coke deposition and Ni sintering of the Ni/LDO-0.1 catalyst. A similar study was done by Xu et al. [68]

by using urea to adjust the NiAl-LDH structural properties. Typically, catalysts were synthesized via an in-situ growth method on Al_2O_3 with different amounts of urea (molar ratio of urea/Ni = 2, 4, 6, 8, and catalysts were denoted as Ni-2, Ni-4, Ni-6 and Ni-8). The theoretical content of Ni was 12 wt% for all the samples and a benchmark catalyst with the same Ni content was prepared by the traditional impregnation method (catalyst denoted as Ni-IMP). The performance of the catalysts varied with the different amounts of urea used. Ni-2 showed a slight increase in CH_4 conversion, while Ni-4, Ni-6 and Ni-8 showed similar catalytic activity (around 70% initial CH_4 conversion). Moreover, the Ni-6 catalyst exhibited higher stability (about 65% final CH_4 conversion) than the other two catalysts (both final CH_4 conversion below 65%). Moreover, the catalyst Ni-6 exhibited remarkably improved catalytic performance in CH_4 conversion, which increased 16% compared to the Ni-IMP material while only 6.3 wt% carbon deposition was observed after 50 h reaction at 800 °C (25.3 wt% carbon deposition on the Ni-IMP catalyst). The improvement in activity is due to both the unique structure of LDH and the modification with urea, producing a catalyst with enhanced Ni dispersion and strong Ni-support interactions that inhibited sintering. Moreover, by varying the molar ratio of Mg/Al, the amount of basic sites could be adjusted as well [69]. To evaluate this, three types of supports, namely γ-Al_2O_3, 70MgAl-LDH (MgO/Al_2O_3 mass ratio 70:30), and 30MgAl-LDH (MgO/Al_2O_3 mass ratio 30:70), were firstly calcined at 1200 °C to get stable supports, which were subsequently loaded with 5.7 wt% Ni via incipient wetness impregnation. It

was found that the final Ni/70MgAl catalyst presented a better catalytic performance (CO_2 and CH_4 conversion both kept around 80% over 50 h, while the other two catalysts had lower CO_2 and CH_4 conversion around 30-40%), with a lower deactivation rate (0.004%/h) than the other two catalysts (deactivation rate around 0.7%/h for Ni/Al catalyst, and 0.4%/h for Ni/30MgAl catalyst). This was mainly attributed to the higher amount of strong basic sites and might also be due to the presence of solid solution, preventing the sintering of Ni particles and the formation of carbon. Nguyen-Phu and Kim [70] systematically studied the effect of the Mg/Al molar ratio on the catalytic activity of the NiMgAl-LDO catalyst by synthesizing NiMgAl-LDH with different Mg/Al ratios. It was found that the Ni-$Mg_{1.5}AlO_x$ catalyst (Mg/Al ratio of 1.5), with more basic sites and enhanced Ni reducibility, had the highest activity of around 60% CH_4 conversion and the best stability, with negligible change in reactivity at a reaction temperature of 727 °C for 120 h. Besides this, it seems that slight amounts of Mg (0.42 wt%) introduced into the NiAl-LDO catalyst did not change the Ni particle size and the base strength, as reported by Feng's group [71], but the promoted Ni-Mg/Al catalyst exhibited better activity and stability than the parent Ni/Al catalyst, possibly due to improved CO_2 dissociation. In another research, NiMgAl-LDH (MNA-2.0) with a composition of Mg:Ni:Al = 2.0:1:1.5 was prepared and evaluated for 100 h in DRM at 850 °C [72]. The MNA-2.0 catalyst possessed excellent feed gas conversions of about 90% for CH_4 and 99% for CO_2. During an extended long-term test of 200 h, no considerable deactivation was observed. Analysis of the spent catalyst

suggested that the large amount of basic sites played an important role in the high initial activities while the strong interacting Ni particles formed from the $NiAl_2O_4$ spinel were deemed crucial for the long time stability.

Some other attempts to enhance either the catalytic performance or the stability of the catalysts in the DRM reaction were also studied. A $(NiMg)_2Al$-LDH was obtained by freeze drying at -20 °C [73]. Compared to the oven-dried catalysts whose LDH's 3D platelet scaffold collapsed because of capillary pressure, the freeze drying helped to keep the 3D morphology of the LDH. After calcination at the same temperature, the freeze-drying samples obtained Ni particles with average sizes of about 7.5 ± 1.2 nm, which were uniformly dispersed on well-defined hexagonal platelets. In contrast, the oven-dried samples had Ni particles with slightly smaller sizes of 6.2 ± 1.2 nm, aggregated on irregularly shaped supports. The DRM results showed that the freeze-dried catalysts had higher activities and stability (CH_4 and CO_2 conversion dropped from around 90% and 94% to about 70% and 80%, while for oven dried catalyst the CH_4 and CO_2 conversion decreased from about 76% and 82% to 39% and 50% during the 40 h test at 800 °C with gas hourly space velocity (GHSV) of 240 $L \cdot CH_4\ g_{cat}^{-1}\ h^{-1}$), which is different from the conclusion reported [65] that 6 nm or below is the required size of Ni to warrant good carbon resistance ability. Therefore, it was thought that the LDH-like 3D structure of the catalyst prepared via the freeze-drying method was indeed the determining factor for high Ni dispersion and subsequently high catalytic activity

[73]. Another trial was done by Mu's group [74] using Ni foam as the substrate to prepare Ni/$MgAlO_x$-LDH-based catalyst in a solar irradiated DRM reaction. Compared to traditional powder catalysts, suffering from aggregation and deactivation, the Ni foam-based catalyst benefits from its high thermal conductivity, providing better temperature uniformity. Therefore, overheating was prevented, contributing to much less coke deposition and aggregation of the active sites. In addition, as reported by Bian et al. [75] coating the Ni oxide with SiO_2 is also an efficient way to protect the Ni particles from sintering and carbon deposition, due to its unique spatial confinement effect. At a low DRM reaction temperature of 550 °C, the Ni-LDH@SiO_2 multi-core@shell catalyst exhibited stable CH_4 (20%) and CO_2 (30%) conversions at 550 °C for 30 h, whereas the LDH catalyst without a coated shell experienced a significant drop in conversion of CH_4 and CO_2 from around 25% and 40% to 14.8% and 16.6%, respectively.

Table 1.1. Different NiMgAl- and NiAl-LDH-derived catalysts for DRM reported in the recent literature, with details on the catalyst properties, thermal catalytic reaction conditions and reaction performance.

Catalyst	Method of LDH synthesis	Cations in LDH	Ni amount (wt%)	M^{2+}/M^{3+} (molar ratio)	Calcination Condition	Reaction Conditions			Conversion [a]		H_2/CO ratio	TOS [b] (h)	Coking $wt\%/g_{cat}$	Ref.
						Temp.	CH_4/CO_2	GHSV (mL g^{-1} h^{-1})	CH_4 (%)	CO_2 (%)				
NiMgAl-LDH	co-precipitation	Ni, Mg, Al	3, 6, 9, 12, 15, 18	3	750 °C, 5 h	800 °C	1	60,000	90	94	0.9	30	4	[64]
NiMgAl-LDH	co-precipitation	Ni, Mg, Al	12	3	650, 700, 750, 800 °C, 5 h	800 °C	1	60,000	~93	~100	~0.9	25	4.5	[65]
						600 °C	1	60,000	~48	~60	~0.78	25	66.7	
NiMgAl-LDH	co-precipitation	Ni, Mg, Al	20	3	600 °C, 6 h	750 °C	1	240,000	~53	~63	0.78	11	ND	[66]
MgAl-LDH, Ni loaded on LDH	commercial LDH	Mg, Al	ND	2	600 °C, 3 h	800	1	48,000	91	96	0.9	28	ND	[67]
MgAl-LDH, Ni loaded on LDH	commercial LDH	Mg, Al	5.7	ND	1200 °C, 5 h for LDH; 700 °C, 3 h for loaded sample	700 °C	1	15,882	~80	~80	ND	50	2	[69]
NiAl-LDH	co-precipitation for NiAl-LDH,	Ni, Al	-	2	700 °C, 1 h for NiAl-LDH;	750 °C	1	36,000	~82	~87	ND	10	0.9	[71]

	rehydration method for NiMgAl-LDH				800 °C, 5 h for MgO loaded sample									
Ni(Li, Na, or K)Al-LDH	co-precipitation	Ni, Al	75-79	1.8	600 °C, 6 h	700 °C	1.5	60,000	~80 to ~50	~90 to ~75	1-1.5	8	~65	[76]
NiMgAl-LDH	co-precipitation	Ni, Mg, Al	19	2 or 1.5	850 °C, 6 h	850 °C	0.5	40,000	91.5	98	1.39	200	ND	[72]
NiAl-LDH	in-situ growth method	Ni, Al	12	ND	550 °C, 4 h	800 °C	1	18,000	~70	~75	~0.9	50	6.3	[68]
Ni loaded on MgAl-LDH	incipient wetness impregnation	Mg, Al	10	ND	800 °C, 6 h	750 °C	1	144,000	78	~85	0.9	ND	ND	[77]
NiMgAl-LDH	co-precipitation	Ni, Mg, Al	5	0.05 (no Mg), 0.4, 1.6, 4, - (no Al)	800 °C, 6 h	1000 K	1	120,000	~60	~70	~0.8	120	17.1	[70]
NiAl-LDH	co-precipitation	Ni, Al	ND	2	450 °C, 6 h	700 °C	1	18,000	75.1	78.3	0.94	5	ND	[78]
NiMgAl-LDH		Ni, Mg, Al							82.2	85.4	0.96			
NiMgAl-LDH	urea hydrolysis method	Ni, Mg, Al	12.5	2	800 °C, 6 h	800 °C	1	400,000	~95	~97	~1	100	ND	[73]
NiMgAl-LDH growth on Ni foam	co-precipitation	Ni, Mg, Al	12	4	800 °C, 6 h	~800 °C	0.9	ND	~60	~60	ND	30	6	[74]

NiMgAl-LDH/FeCrAl-fiber	hydrothermal method	Ni, Mg, Al	13	ND	500 °C, 2 h	800 °C	1	5,000	91	89	0.9	270	14	[79]
NiMgAl-LDH@SiO_2	hydrothermal	Ni, Mg, Al	12	3	750 °C, 4 h	600 °C	1	240,000	30	40	0.7	16	2	[75]

[a] the conversions mentioned are from the best or initial to final results in long-term tests; "ND": no data provided in the literature; "~": approximate value; GHSV: Gas hourly space velocity [b] TOS: Time on stream.

1.2.3 Promoted Ni LDH-derived catalysts

Monometallic Ni-based LDH-derived catalysts have shown promising performance for DRM. Many modifications have been performed to further enhance their activity and lifetime. Yet, the main problems still exist, such as coke deposition and active metal sintering. Therefore, alloying the monometallic Ni catalysts with a second, third, or even fourth metal became one of the strategies to improve their catalytic performance and coke-resistance. Several reviews discussing this topic can be found in the literature [17,19–22,80]. In the last several years, there was also a considerable number of papers reported about alloying Ni LDH-based catalysts (shown in Tables 1.2-1.4). However, the mechanism and the effect of the alloying on the activity and stability are still undetermined. Therefore, in this section, the recently reported papers about alloying Ni LDH-based catalysts for DRM are summarized. Based on the metal elements, the discussion is mainly divided into three parts, namely a part on transition metal addition, lanthanides, and multiple alloys and other metals.

1.2.3.1 Transition metal binary-Ni LDH-derived catalysts

In recent years, the DRM reaction was reported using Ni-LDO catalysts promoted with transition metals, including cheap and readily available metals like Fe, Co, Cu or Zn, noble metals like Rh, Pd or Pt, and rare metals like Ir, V, Zr or Y. These metals were introduced into the catalyst as either metal particles or oxide phases,

resulting in different effects on the catalytic performance. The detailed studies are discussed in the following paragraphs and generally presented in Table 1.2. Apart from the experimental investigations, several theoretical studies have also been reported to predict and explain the effects of the combinations of Ni and these promoting metals on the DRM activity and carbon formation behaviour. As reported by Chatla et al. [81], density functional theory (DFT) calculations accompanied by experiments for catalyst performance and materials characterizations were performed, to obtain the activation mechanism of carbon formation and gasification on monometallic Ni (111) and Cu/Ni (111) surface with different Cu amounts (Fig.1. 2). For the Cu/Ni cases, the total (Ni+Cu) loading amount was fixed at 10 wt% and the Cu:Ni atomic ratio varied by 1:3 (higher Cu loading), 1:8 (medium Cu loading), and 1:10 (lower Cu loading). The final step in the dehydrogenation of methane, CH* → C* + H*, namely the dissociation of CH to elemental C, was considered to be the decisive step towards the deactivation of the catalyst due to coking. Therefore, they calculated the barrier values, as depicted in Fig. 1.2a. It can be easily deduced that the activation barrier of CH* dissociation is 1.41 and 1.45 eV for the pure Ni system and the lower (1:10) Cu/Ni alloy system, respectively. For the medium (1:8) Cu/Ni alloy system, the barrier value of carbon formation increases to 1.89 eV, showing a significant increase of 0.44 to 0.48 eV. Similarly, in Fig. 1.2b, the values of the calculated barriers for carbon gasification from the surface by oxidation with O_2 forming CO are presented. The medium Cu/Ni system has the lowest carbon elimination barrier of 0.53 eV, which is lower

than those of the pure Ni and low Cu/Ni system. Therefore, carbon formation is suppressed in a Cu/Ni alloy system, whereas carbon gasification is enhanced. Experimental evidence confirmed that in the medium Cu/Ni case, the catalyst produced a more amorphous or "active" form of carbon with a total 6.4 wt% weight loss (43 wt% for monometallic Ni catalyst). Tang et al. [82] used DFT calculations to study the reaction mechanisms of CH_4 dissociation on the surface of pure Ni and a Ni-Rh alloy (replacing one Ni atom on the surface, forming a RhNi alloy, and replacing six Ni atoms forming a Rh_6Ni alloy) catalysts. They found that doping Rh atoms provided more adsorption sites on RhNi bimetallic catalysts, which resulted in intermediates that tend to be adsorbed by the active sites near the Rh atoms. Increasing the Rh atoms doping can weaken the adsorption strength of the intermediates on the surface of the catalyst. The adsorption strength followed the order Ni > RhNi > Rh_6Ni. Moreover, the reaction of CH* → C* became difficult after doping Rh atoms, which prevented the formation of C*, therefore eventually reducing the carbon deposition and improving the carbon resistance of the RhNi catalyst.

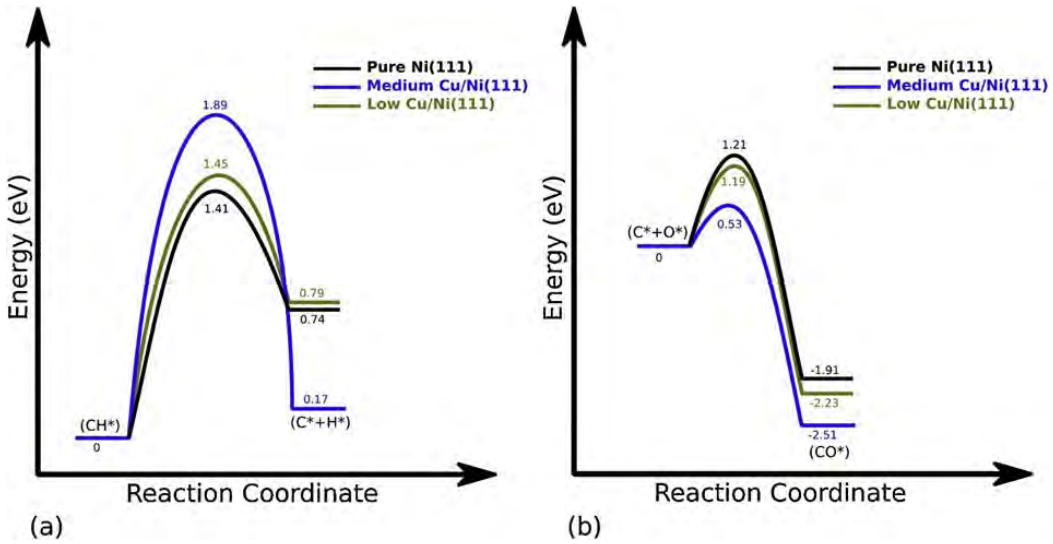

Fig. 1.2. Activation barriers of (a) carbon formation via the CH dissociation pathway and (b) carbon elimination by oxidation with O to form CO [81]. Copyright 2020, Elsevier.

As mentioned in section 1.2.1, Co is another promising metal for the catalytic DRM reaction. Besides this, due to its similar electronic configuration, Co and Ni easily form bimetallic alloy nanoparticles [83]. Moreover, compared with the monometallic catalyst, the Co/Ni alloy catalyst had superior performance with an activity of 4.97 mol CH_4 $mol_{Ni}^{-1}s^{-1}$ for the DRM reaction at 800 °C. It was active at lower temperatures as well, and near-thermodynamic equilibrium conversion was achieved as low as 350 °C, which is one of the challenges in DRM catalysis [17,84–86]. Tanios and co-workers [84] investigated the effect of different amounts of Co on the catalytic performance of DRM in a NiMgAl-LDO catalyst. Their research demonstrated that at high temperatures of 700 – 800 °C, the conversion of CH_4 exhibited little differences for catalysts with or without various contents of Co, while at temperatures between 500 °C and 600 °C the

$CO_2Ni_2Mg_2Al_2800$ generally showed higher activity (CH_4 conversions were about 40% at 500 °C, 65% at 550 °C, and 80 % at 600 °C) than the $Ni_2Mg_4Al_2800$ (CH_4 conversions were about 25% at 500 °C, 55% at 550 °C, and 70% at 600 °C) catalyst. Subsequently, they studied the stability of the $CO_2Ni_2Mg_2Al_2800$ catalyst in DRM at 800 °C for 20 h, showing constant conversion of CH_4 (97%) and waved conversion of CO_2 (between 91-93.5%) [85]. In another recent paper, Duan's group [86] studied the doping of Co into Ni_{12}/MgAlO, forming a Ni_3Co_9/MgAlO catalyst together with catalysts with other Ni/Co ratios, while evaluating their corresponding DRM performances at 600 °C. It was observed that although there were slight decreases in the CH_4 and CO_2 conversions, the coke deposition problem improved significantly, forming only 15 wt% carbon deposition on Ni_3Co_9/MgAlO after 25 h reaction, whereas 75 wt% carbon was deposited on Ni_{12}/MgAlO coinciding with severe carbon filaments accumulated in the reactor.

Fe, Cu, and Zn, as cheap and readily available metals, were also widely studied in promoting Ni-LDO-based catalysts for the DRM reaction [87–95]. Wan et al. [89] found that with a certain additional amount (12 wt%) of Fe into the NiMgAl-LDO and after reduction at temperatures of 700 °C, 800 °C and 900 °C, all the obtained NiFe catalysts showed relative stable activity with little deactivation for DRM in a temperature range of 500 °C to 800 °C. Furthermore, catalysts reduced at 700 °C exhibited the lowest coke deposition amount, especially at a reaction temperature of 600 °C, because of its smaller particle size of about 5.8 nm (7.3 nm and 8.2 nm

at reduction temperatures of 800 °C and 900 °C). Theofanidis et al. [96] gave a detailed mechanistic explanation for the enhancement of coke resistance, which is shown in Fig. 1.3. Concretely, during the DRM reaction, CO_2 can oxidize Fe, forming CO and FeO_x, while CH_4 was dissociated on the Ni sites, forming H_2 and surface carbon. The formed carbon reacted with the lattice oxygen supplied by FeO_x producing CO. Their further study [26] proposed a mechanism of carbon gasification over the Fe-Ni catalyst which included two processes: (1) oxidation of carbon on the surface of the catalyst and (2) migration of FeO_x or/and NiO particles to the carbon depositions which were far from the active sites, where subsequently oxidation can take place by the lattice oxygen supplied by the particles. Similar research was done by Song et al. [91] with Cu. At 600 °C, the CuNi alloy catalyst with Cu/Ni molar ratios of 0.25 to 0.5 exhibited good activity, stability and coke resistance, whereas the catalysts with lower (including pure Ni catalyst) and higher Cu/Ni molar ratios were deactivated due to severe carbon deposition. The optimized catalysts, $Ni_4CuMgAlO_x$ and $Ni_2CuMgAlO_x$, showed only 1/85 to 1/136 carbon deposition amount of the $NiMgAlO_x$ catalyst. Besides this, the high stability and low coke properties were kept at temperatures as low as 450 °C. Xiao et al. [92] observed a different Ni/Cu mass ratio (Ni + Cu total weight percentage was 12 wt% and Ni:Cu ratio was 6:6) associated with best catalytic performance in experiments and conducted DFT calculations to analyze the adsorption of carbon on the surface at various ratios of the NiCu alloy. They first systematically compared LDH catalysts with metal compositions NiAl, NiMg, NiMgAl, and

catalyst consisting of Ni/MgAl, and NiMg/Al prepared by an impregnation method. The amount of Ni loaded was 12 wt% for all the catalysts. The LDH-derived NiMgAl-LDO catalyst exhibited the highest activity and stability in the 6 h reaction at 700 °C, with CH_4 and CO_2 conversions of 89.2% and 90.9%, respectively. Promotion of Cu was added forming a NiCuMgAl-LDH by a hydrothermal method with a (Ni + Cu) content of 12 wt% and a fixed Mg/Al ratio of 1.7. At the same reaction conditions as before, a similar conclusion was drawn that low (Ni9Cu3) and high (Ni3Cu9, and pure Cu) amounts of Cu promotion were unfavourable for improving the NiMgAl catalyst. However, Ni6Cu6 had the highest CH_4 conversion of about 90% and CO_2 conversion of around 93%. Changing reaction conditions (GHSV = 40,000 ml g_{cat}^{-1} h^{-1}) for 70 h, the Ni6Cu6MgAl-LDO catalyst proved its far superior catalytic ability and only a small activity loss of less than 1.5% was observed, whereas the NiMgAl-LDO catalyst could only last for 13 h due to the blocking of the reactor [92]. DFT calculations illustrated that CuNi(111) had the highest C* adsorption energy suggesting its high coke resistance.

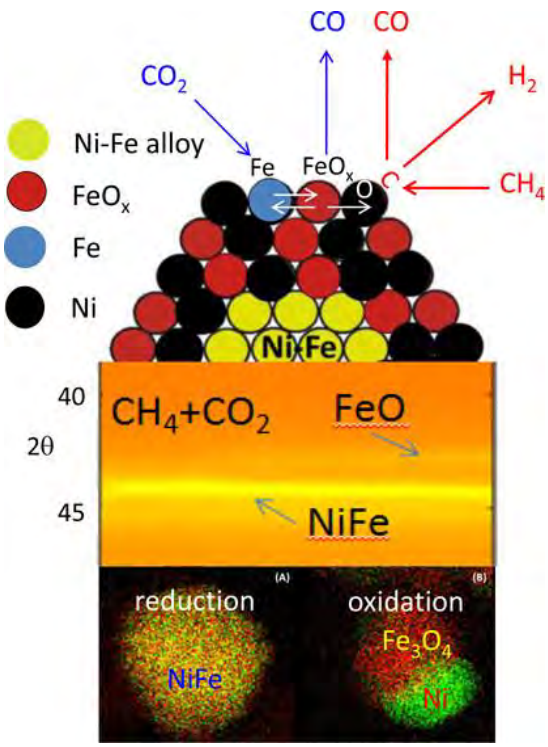

Fig. 1.3. Diagram for the mechanism of Fe addition, enhancing coke resistance of the Ni catalyst. [96]. Copyright 2015. American Chemical Society.

Chatla et al. [94] recently reported a Zn-modified NiMgAl-LDH-derived catalyst with excellent performance for DRM at 650 °C for 100 h. Catalysts with 10 wt% Ni and various amounts of Zn were obtained by calcining and reducing the NiZnMgAl-LDHs, which were synthesized via a simple one-pot co-precipitation method. All the Zn-promoted catalysts showed enhanced reaction rates of CH_4 and CO_2 during a short time reaction of 20 h, and the NiMgAl-3Zn catalyst had the highest reaction rates. Although catalysts with a higher Zn loading (NiMgAl-5Zn and NiMgAl-10Zn) presented better activity than the NiMgAl catalyst as well, the activities declined gradually with time on stream. This could be due to the partial

blocking of active Ni sites by the excess of Zn promotion. TGA results demonstrated trace amounts of coke deposition on NiMgAl-3Zn (0.0043 mgC g_{cat}^{-1} h^{-1}), around 7 times less than the NiMgAl catalyst (0.0292 mgC g_{cat}^{-1} h^{-1}). A further stability test for the NiMgAl-3Zn catalyst for 100 h displayed nearly no decrease in reaction rate. Characterization revealed that the smaller particle sizes of Ni^0 for the Zn-promoted catalyst (NiMgAl-3Zn with Ni^0 size of 10.00 nm and NiMgAl catalyst with Ni^0 size of 13.47 nm) enhanced the metal-support interaction and basicity contributed to the higher performance. Moreover, the Arrhenius plots and CH_4 temperature programmed surface reaction (TPSR) analysis suggested that CH_4 decomposition was more difficult to happen on the Zn-modified surface, explaining its promoting effect. The addition of Cr into the NiAl-LDO catalyst was studied by Hallassi et al. [95] and a comparison to Fe-promoted NiAl-LDO was applied as well. At a low temperature of 500 °C for 1 h, the NiCr catalyst had a relatively stable activity for CH_4 and CO_2, with conversions of around 30% and 15%, respectively. It was better than those of the NiFe catalyst, with conversions of CH_4 and CO_2 of only 4% and 1%. This indicated the promising utilization of promoted CrNi catalysts in the DRM reaction.

Some other, less commonly used transition metals, including Y, Zr, V or Ir, and some noble metals were also applied as promotors to improve the Ni-LDH-based catalyst. Costa's group investigated the promoting effects of Y and Zr in Ni-LDH-derived catalysts [97–101]. Summarizing their reported papers, a conclusion can

be drawn that low (0.2, 0.4, and 0.6 wt%) and medium (1.5, 3, and 4 wt%) contents of Y promotion were beneficial for the enhancement of the catalytic performance of the catalysts, both in activity, stability and coke resistance. A high amount of Y (8 wt%) still facilitated the catalytic stability and coke-resistance (even better than the medium loading amount catalysts), while the activity decreased, which may be because the Y improved the Ni reduction ability and formed larger Ni particles, resulting in lower catalytic Ni particle sites. Promotion with Zr was also studied by varying its amount [100]. Although no enhancement in conversions appeared in the DRM reaction at 550 °C for 5 h, the stability of the NiMgAl catalyst was outstandingly improved. Specifically, for the NiMgAl catalyst, the initial CO_2 and CH_4 conversions were about 45% and 40% and the values changed to about 40% and 47%, while for the ZrNiMgAl catalyst the initial and final conversions of CO_2 and CH_4 were around 37% and 32% with only slight decreases. Therefore, a combination of Y and Zr-promoted NiMgAl-LDO catalyst was subsequently utilized [101]. The catalyst without doubt exhibited higher activity, stability and coke resistance (see Table 1.2). Rather than adding Zr as the promoter, Tathod et al. [102] used ZrO_2 as support and NiMgAl-LDH nanosheets (LDH-NSs) were anchored on it. After calcination, a 2.5Ni/NS/Zr catalyst with 2.5 wt% Ni loading was obtained. In comparison to NiMgAl-LDH, mixed oxide (MO) (also called LDO) was obtained after calcination of MgAl LDH and used as support to prepare 2.5Ni/MO) and Ni/ZrO_2 (2.5Ni/Zr) catalysts with the same amount of Ni. Compared with the other two catalysts, the 2.5Ni/NS/Zr catalyst exhibited a

significantly higher activity, which was more than 2 times more active than 2.5Ni/Zr and around 10 times more active than 2.5Ni/MO after 20 h reaction. Characterization of the catalysts demonstrated that the excellent performance was strongly correlated with the modified metal-support interaction, resulting in a higher active energy barrier for CH_4 and a lower reduction temperature for NiO. This allowed for multiple regenerations of the catalyst and eventually exhibited a total of 240 h on stream with only slight signs of Ni degradation by sintering and only a little coke deposition. This discovery gives a possibility of using low-loading amounts of Ni while obtaining high activity.

In addition, seldomly introduced transition metals Ir and V were investigated as well [103,104]. Huang et al. [103] observed that the addition of Ir failed to improve the catalytic activity, but it promoted the stability of the catalyst due to the suppression in the formation of encapsulated graphitic carbon and the promotion of the oxidation of carbon nanotubes on the surface. However, an appropriate amount of V metal promotion facilitated the NiMgAl-LDO catalyst, as reported by Lu's group [104]. The optimal Ni/V ratio was 10, which acted as the structural promoter, improving the dispersion of Ni sites and declining the Ni particle size. Therefore, the catalyst showed stable catalytic conversion of both CH_4 and CO_2 for 80 h at 750 °C. However, excessive amounts of V promoter caused the collapse of the LDH structure and resulted in lower catalytic activity. By combining CH_4 temperature-programmed desorption (CH_4-TPD) and CH_4-TPSR with DFT

calculations, the mechanism was revealed that the V promoter facilitated the decrease of the CH_4 adsorption energy and the cracking activation energy to form CH_3 and H species and eventually increased the CH_4 adsorption and activation capacity. In addition, in-situ CO_2 infrared spectrometry (CO_2-IR) demonstrated that the V promoter inhibited the formation of nonactivated multidentate carbonate, while it improved the production of the monodentate carbonate species, which was considered to be the intermediate of CO_2 activation. Therefore, the coke deposition could be suppressed.

Compared with other transition metals, although the high cost of noble metals and their presence on the critical raw materials list strictly limits their large-scale utilization, they still can present relatively high catalytic performance and coke resistance ability when loaded in small amounts. Dang et al. [105] loaded around 1 wt% Pd on a NiCaAl-LDO catalyst, which favoured the DRM reaction with 68% CH_4 conversion, 67% CO_2 conversion, and H_2/CO ratio close to unity at a lower temperature of 600 °C for 50 h. It has been found by characterization that the addition of Pd promoted the CH_4 dissociation and CH_4 reformed with $CaCO_3$, achieving a dynamic transformation process between bulk $CaCO_3$ and nano CaO particles, which suppressed Ni sintering. Furthermore, the coke formed was mainly amorphous, which could be removed by $CaCO_3$, ensuring a long-term utilization of the catalyst. Another example of utilizing noble metals was Pt, in which different loading amounts of Pt from 0 to 5.8 wt% were added into a NiMgAl-LDO catalyst

[58]. Among the promoted catalysts, 1.0 wt% Pd loaded catalyst exhibited the best stability and coke resistance, while the un-promoted NiMgAl-LDO catalyst had the highest initial catalytic activity but decreased fast in the 30 h test. DFT calculations and dynamic study revealed that the electronic structure of the PtNi bimetallic catalyst played a crucial role in its performance enhancement. In comparison with solo Pt(111) and Ni(111) metal, the PtNi alloy contributed to the decrease of the adsorption energy of H* and carbon-containing species like CO*, C*, and CH*. Concretely, this bimetal reduced the activation barrier of CO_2 and CH_4, improving the catalytic performance, while simultaneously enhancing O* activity and the surface oxygen amount, which promoted coke removal by oxidization, and weakened H_2 dissociation resulting in higher H_2 amounts and a higher H_2/CO ratio. Schiaroli et al. [57] reported that the addition of a small amount of 0.5 wt% Rh helped to enhance the activity, stability and coke resistance of a NiMgAl catalyst. Compared to the original NiMgAl-LDO catalyst, after modification with Rh, slight increases in conversions of CO_2 from 90% to about 95% and CH_4 from about 85% to 87% were observed. Moreover, the H_2/CO ratio also increased from around 0.85 to about 0.9, and the carbon deposition decreased a lot from 24.9% for the NiMgAl catalyst to 3.3% for the NiRhMgAl catalyst. The enhancement was mainly attributed to the increase of Ni dispersion and its interaction with the support.

Table 1.2. Different transition metal-promoted Ni-LDH-derived thermal catalysts for DRM reported in the recent literature, with details on the catalyst synthesis and composition, reaction conditions and reaction performance.

Catalyst	Method of LDH synthesis	Cations in LDH	Metals amounts (wt%) [a]	M^{2+}/M^{3+}(molar ratio)	Calcination Condition	Reaction Conditions [b]			Conversion [c]		H_2/CO ratio	TOS (h)[d]	Coking $wt\%/g_{cat}$	Ref.
						Temp.	CH_4/CO_2	GHSV (mL g^{-1} h^{-1})	CH_4 (%)	CO_2 (%)				
CoNiMgAl-LDH	co-precipitation	Ni, Co, Mg, Al	Ni:Co:Mg = 1:1:1	3	800 °C, 4 h	800 °C	1	60,000	~97	~92	0.8	20	40	[85]
NiMgAl-LDH	co-precipitation	Ni, Mg, Al	Ni: 12	3	750 °C, 5 h	600 °C	1	120,000	39	~53	~0.6	25	75	[86]
CoNiMgAl-LDH		Ni, Co, Mg, Al	Ni: 3; Co: 9						33.3	~46	0.6		15	
NiFeMgAl-LDH	co-precipitation	Ni, Fe, Mg, Al	Ni:Fe = 4:1	2	800 °C, 5 h	650 °C	1	270,000	~20 mmol g^{-1}_{cat} min^{-1}	ND	~0.55	10	21	[87]
Fe loaded on calcined NiMgAl-LDH	commercial LDH	Ni, Mg, Al	Ni: 10; Fe: 1	2	500 °C, 5 h for LDH; 600 °C, 3 h for loaded catalyst	750 °C	1	48,000	76 to 69	75 to 71	0.93	80	~18	[88]
NiFeMgAl-LDH	co-precipitation	Ni, Fe, Mg, Al	Ni:Fe = 4:1	3	800 °C, 5 h	600 °C	1	60,000	49.5	61	~0.77	25	0.28 mg C g_{cat}^{-1} h^{-1}	[89]
NiFeMgAl-LDH	co-precipitation	Ni, Fe, Mg, Al	Ni:Fe = 3:1	2	800 °C, 5 h	650 °C	1	120,000	~27	~33	~0.6	20	10.2	[90]
NiFeCuMgAl-LDH		Ni, Fe, Cu, Mg, Al	Ni:Fe:Cu = 3:1:1						~27	~32	~0.6	20	5.4	
NiCuMgAl-LDH	co-precipitation	Ni, Cu, Mg, Al	Ni:Cu = 4:1	3	800 °C, 5 h	600 °C	1	60,000	47.9	~57	~0.67	25	1.4	[91]
NiMgAl-LDH	hydrothermal	Ni, Mg, Al	Ni: 12	Mg/Al = 1.7	650 °C, 4 h	700 °C	1	24,000	89.2	90.9	~0.9	5	ND	[92]

NiCuMgAl-LDH		Ni, Cu, Mg, Al	Ni: 6; Cu: 6					40,000	89	87	~0.96	70	2.7	
Mg loaded on calcined NiAl-LDH	rehydration method	Ni, Mg, Al	ND	Ni/Al = 2	400 °C, 12 h for NiAl-LDH; 600 °C, 6 h for loaded catalyst	700 °C	1.5	60,000	42	70	1.4	5	76	[93]
Zn loaded on calcined NiAl-LDH		Ni, Zn, Al							48	76	1.4		82	
NiZnMgAl-LDH	co-precipitation	Ni, Zn, Mg, Al	Ni: 10; Zn: 3	3	650 °C, 5 h	650 °C	1	180,000	0.125 mol min^{-1} g_{Ni}^{-1}	0.125 mol min^{-1} g_{Ni}^{-1}	0.87	100	0.0043 mg C g_{cat}^{-1} h^{-1} for 20 h	[94]
NiCr-LDH	co-precipitation	Ni, Cr	Ni:Cr = 2.2	2	500 °C, 4 h	500 °C	1	60,000	~30	~15	~1	1	3.74	[95]
NiFe-LDH		Ni, Fe	Ni:Fe = 0.7						4	1	0	1	7.02	
NiYMgAl-LDH	co-precipitation	Ni, Y, Mg, Al	Ni: 14; Y: 1.5	3	550 °C, 5 h	700 °C	1	20,000 h^{-1}	73.3	77.8	0.92	10	~10	[97]
NiYMgAl-LDH	co-precipitation	Ni, Y, Mg, Al	Ni: 20; Y: 0.2 or 0.4	3	550 °C, 5 h	700 °C	1	20,000 h^{-1}	84	87	~0.99 to ~0.95	5	~25	[98]
NiYMgA-LDH	co-precipitation	Ni, Y, Mg, Al	Ni: 17; Y: 3	3	550 °C, 5 h	700 °C	1	20,000 h^{-1}	85	90	0.99	5	~30	[99]
NiZrMgAl-LDH	co-precipitation	Ni, Zr, Mg, Al	Ni: 17; Zr: 2.5	3	550 °C, 4 h	750 °C	1	20,000 h^{-1}	83	90	0.93	5	ND	[100]
Zr, Y loaded on NiMgAl-LDH	co-precipitation	Ni, Mg, Al	Ni: 15; Zr: 5; Y: 0.4	3	550 °C, 5 h	700 °C	1	20,000 h^{-1}	~82	~82	~0.9	5	~6	[101]
NiMgAl-LDH on ZrO_2	co-precipitation	Ni, Mg, Al	Ni: 2 Zr: ND	4	800 °C, 8 h	800 °C	1	240,000	~46	~60	~0.75	20	0.6	[102]

NiMgAl-LDH		Ni, Mg, Al	Ni: 2						~4	~7	~0.2	20	1.4	
NiIrMgAl-LDH	co-precipitation	Ni, Ir, Mg, Al	NiO: 8; Ni:Ir = 5	3	800 °C, 6 h	850 °C	1	60,000	68.5	~75	~0.75	180	12.9	[103]
NiVMgAl-LDH	hydrothermal	Ni, V, Mg, Al	Ni: 18.2; Ni:V = 10	1.85	800 °C, 2 h	750 °C	1	96,000	90	94	0.91	80	12	[104]
NiPdCaAl-LDH	co-precipitation	Ni, Pd, Ca, Al	Ni: 10; Pd: 1	2.8	800 °C, 4 h	600 °C	1	18,000	68	67	0.95	50	4.1	[105]
Pt loaded on NiMgAl-LDO	co-precipitation	Ni, Mg, Al	Ni: 12; Pt: 1	3	600 °C, 6 h for LDH; 600 °C, 6 h for loaded catalyst	700 °C	1	900,000	ND	~60	~0.9	30	~5	[58]
NiRhMgAl-LDH	co-precipitation	Ni, Rh, Mg, Al	Rh: 0.5	3	900 °C, 6 h	900 °C	1	25,000	~87	~95	~0.9	5	3.3	[57]
NiMgAl-LDH		Ni, Mg, Al	Ni: 10						~85	~90	~0.85		24.9	

[a] the metal loading amount unit is wt%, the ratio is expressed as a molar ratio; [b] GHSV: Gas hourly space velocity; [c] the conversions were from the best or initial to final results in long term tests; "~": approximate value; "ND": no data provided in the literature; [d] TOS: Time on stream;

1.2.3.2 Lanthanides metal binary-Ni LDH-derived catalyst

Lanthanide metals were also widely used as promotors for Ni-LDH-based catalysts due to their high content of oxygen vacancies, reducibility, basic properties and coke removal ability [47]. In this section, we mainly discuss bimetallic lanthanide metal and nickel LDH-derived catalysts for the DRM reaction. The metals include the actively studied La and Ce, and the less investigated metals like Pr, Gd, Sc et al, which are summarized in Table 1.3.

The addition of La was compared with other metals, namely Li, Mg, Ca, Cu, Co, and Zn, by introducing the metal into a NiAl-LDH catalyst by co-precipitation with a molar percentage of 11% [106]. The catalytic performance at different temperatures showed that the CH_4 conversion of La, Cu, and Zn catalysts increased as temperature increased to 700 °C, while for other catalysts it increased to 600 °C and decreased at temperatures above 650 °C, indicating deactivation of these catalysts. However, the CO_2 conversion raised with temperature up to 700 °C for all the catalysts, except for La, suggesting that CH_4 conversion was more favourable at high temperatures for the La-promoted catalyst. Besides this, the results of the DRM reaction driven at 700 °C for 5 h illustrated that although all the catalysts showed fast loss of activity, the La catalyst deactivated slowest for CH_4 conversion from the initial value of about 80% to the final value of around 69%. The presence of more strong acid sites contributed to this. In comparison, Mg

and Ca catalysts showed higher activity and stability for CO_2 conversion from an initial about 92% to a final conversion of 85% (for La catalyst the value decreased from about 90% to around 75%), which was attributed to their higher amount of basic sites. Armbruster and co-workers [107] reported a promising bimetallic NiLa (Ni: 2.5 wt%, La:Ni molar ratio of 0.8) promoted LDH-based catalyst with excellent catalytic performance and stability of 160 h at 700 °C. In detail, a commercial MgAl-LDH was calcined at 550 °C to obtain the bare support. In comparison, a group of Ni or LaNi promotors was directly loaded on the support via wet impregnation, to obtain Ni/MgO.Al_2O_3 and LaNi/MgO.Al_2O_3 catalysts (denoted Ni and LaNi for short) after calcination, whereas another group of Ni or LaNi promotors was introduced in the same way except that a certain amount of citric acid was added as well, to obtain Ni(CA)/MgO.Al_2O_3 and LaNi(CA)/MgO.Al_2O_3 catalysts (denoted Ni(CA) and LaNi(CA) for short) following the same calcination procedure. After reduction and application in the DRM reaction at 630 °C for 8 h, it was found that the activity of the catalysts followed the sequence from high to low: Ni > Ni(CA) > LaNi ≥ LaNi(CA). However, TGA analysis illustrated that the Ni catalyst had the most serious carbon deposition of around 6%, which was almost 10 fold of all the La-promoted catalysts (carbon deposition between 0.44 wt% and 0.77 wt%). A long-term stability test at 750 °C for 160 h exhibited that the citric acid-modified LaNi(CA) catalyst had the highest stability with little deactivation (conversion of CO_2 and CH_4 both stable at around 80%), while other samples showed obvious deactivation. Specifically, for

Ni and LaNi catalysts, the conversion generally decreased from around 80% CO_2 to 50-60% and CH_4 conversion decreased from around 80% to about 70%. Moreover, for the Ni(CA) catalyst, the reactor was blocked due to serious carbon deposition after about 80 h reaction. The negligible carbon amount (below 1.5 wt%) for all the spent catalysts suggested that active site sintering rather than carbon deposition was the main reason for catalyst deactivation. They also studied the impact of calcining the commercial MgAl-LDH at 1000 °C to obtain a $MgAl_2O_4$ spinel, while loading the same amount of Ni and La on it, forming a LaNi(CA)/$Mg_{1.3}AlO_x$.1000 catalyst [108]. The catalyst showed excellent performance at a high CH_4/CO_2 ratio of 2 at 700 °C for 100 h with only about 5 wt% carbon deposition. Their study demonstrated that promotion with La, with assistance from citric acid, provided highly dispersed Ni active sites and easier reducibility, which contributed to its high stability and tolerance to high CH_4 reactions in long-term testing.

Among the various lanthanide metals, Ce is another attracting element because of its unique redox properties, oxygen storage capacity and surface defect sites like oxygen vacancies which can remove coke [109–111]. Besides this, Ce itself also possesses catalytic activity in the DRM reaction [112]. The recently reported Ce or CeO_2-promoted Ni-LDH-derived catalysts are summarized in Table 1.3. Upon analysis of the papers, it was found that the promoted catalyst performance can be affected by the promotion method and phase of Ce. Kalai et al. [29] studied the

effect of a Ce-promoted NiMgAL-LDH derived catalyst in DRM with a high CH_4/CO_2 ratio of 3. They found at a relatively low Ni loading of 12 wt%, that promoted catalysts with 4 wt% Ce had slightly lower initial CH_4 and CO_2 conversion (values were about 20% and 60% for the Ni catalyst, and were about 17% and 55% for the NiCe catalyst), but a higher stability with a total of 18% decrease in CO_2 conversion during 25 h reaction, which was about 27% for the unpromoted Ni catalyst. The catalysts had however a similar declining trend for CH_4 conversion, indicating that CO_2 was the rate-determining reactant. However, at high Ni loading of 20 wt%, the CO_2 conversion increased as the Ce content increased and the 20Ni-8Ce (Ni: 20 wt%, Ce: 8 wt%) catalyst exhibited higher stability, suggesting that the promotion effect of Ce enhanced the adsorption of CO_2, resulting in higher CO_2 activation and improved coke resistance. A similar conclusion was drawn by Lino et al. [113] as well that with a fixed Ce loading amount, higher Ni loading resulted in higher activity but less stability and coke-resistance ability.

The Ce metal can also be introduced into the catalyst by the impregnating method. Niu et al. [114] prepared Ce, Zr, or Zn-promoted NiMgAl-LDO catalysts by incipient wetness impregnation of the metal solution onto calcined NiMgAl-LDH. The DRM test, characterization and DFT calculations demonstrated that the Ce-promoted catalyst had the best performance due to its higher basicity (CO_2 activation on the solid surface was used to test the basicity of catalysts, which

increased in the order NiCe > NiZr > Ni > NiZn) and the decreased electronegativity of the metal element, which improved the CO_2 activation and enhanced the stability of the catalyst. Das et al. [49] reported a NiCo-MgAl@CeO_2 core-shell catalyst incorporating a layered double hydroxide-derived as core and a CeO_2 as shell for DRM. In detail, the precursors of Ni-MgAl-LDH or NiCo-MgAl-LDH were first produced via a hydrothermal method. Then, the dried LDH samples were used to load Ce by incipient wetness impregnation to produce Ni-MgAl@CeO_2 and NiCo-MgAl@CeO_2. In comparison, a Ni-MgAlCe catalyst was prepared by the hydrothermal method. At 600 °C and a CH_4/CO_2 ratio of 1, the reaction of Ni-MgAl, NiCo-MgAl, and Ni-MgAlCe catalysts was forced to stop in around 3 h due to reactor blocking, whereas the other two catalysts prepared via the incipient wetness impregnation method showed excellent stable activity. Specially, only a marginal decrease of 4% in CH_4 conversion and of 5.5% in CO_2 conversion was observed for the Ni-MgAl@CeO_2 catalyst after 165 h testing, while at the same conditions, negligible deactivation appeared on the NiCo-MgAl@CeO_2 catalyst. Characterization attributed its super coke resistance to two aspects: on one hand, the CeO_2 shell changed the nature of the deposited coke, forming more active amorphous carbon which was easier to be removed; on the other hand, CeO_2 provided lattice oxygen to oxidize the carbonaceous intermediates, decreasing carbon formation. Moreover, the authors also studied the H_2S tolerance ability of the catalysts. The results suggested that the presence of Co in the mixed oxide core of NiCo-MgAl@CeO_2 delayed deactivation upon H_2S exposure, whereas addition

of the CeO_2 shell resulted in a higher steady state activity in the presence of H_2S and in a gradual recovery of activity after stopping H_2S in the feed gas.

La and Ce containing Ni-LDH-derived catalysts have attracted more attention due to their relative abundance, easier availability and good improvement in catalytic stability and coke resistance. Despite this, other lanthanide metals were also reported, illustrating their either similar or unique properties. Ojeda-Niño's group [115] investigated the promotion effect of Pr promoted NiMgAl-LDH derived catalyst by mixing all the metal nitrates and varying the amount of Pr used via a microwave-assisted self-combustion method. Compared to the pure Ni, 1 wt% Pr loaded, and 12 wt% Pr loaded catalysts, the 6 wt% loaded PrNi catalyst exhibited the most stable activity and lowest carbon deposition amount at 600 °C, despite its conversions of CH_4 and CO_2 were the lowest among the four catalysts. Its improvement in stability was attributed to the enhancement of the thermal stability of the basic sites and the decrease in Ni^0 particle size (about 11.6 nm, similar to 11.0 nm in the 12 wt% Pr loaded catalyst, and smaller than 18.9 nm for Pr-free Ni catalyst). They also studied how the synthesis methods affected the performance of Pr-promoted catalysts [116]. In comparison to the microwave-assisted self-combustion method (AM for short) and self-combustion method (AC for short), the co-precipitation method (CP for short) produced a catalyst with a relatively higher specific surface area (162 m^2/g of CP > 33 m^2/g of AM >28 m^2/g of AC), CO_2 capture capacity (120 μmol/g of CP > 68 μmol/g of AM > 25 μmol/g of AC),

basic sites and smaller Ni particle size (5.52 nm of CP < 12.4 nm of AM < 17.2 nm of AC), resulting in higher initial and final CH_4 and CO_2 conversion. Nevertheless, they also deactivate the fastest. Furthermore, the microwaves improved the performance of the catalysts prepared by self-combustion. However, all three catalysts suffered from severe coke deposition, which may be due to the low loading amount of Pr, which was proven by the paper they reported before [115].

Ha et al. [117] reported the modification effect of different lanthanide metals (Gd, Sc, and La). All the promotors improved the stability of the NiMgAl-LDO catalyst in the CH_4 rich (CH_4/CO_2 = 2) DRM reaction at 750 °C. Moreover, Sc and Gd-promoted catalysts had less carbon content than the original Ni catalyst, while the La-promoted one produced more carbon deposition. Therefore, the ScNi and GdNi catalysts were applied for a long-term stability test of 100 h at a CH_4/CO_2 ratio of 2, as shown in Fig 1.4. Both catalysts showed stable activity and only slight deactivation of about 16% for the GdNi catalyst and 17% for the ScNi catalyst. Low carbon amounts were obtained on the spent catalysts, around 4 wt% for the GdNi catalyst and 7.5 wt% for the ScNi catalyst, respectively. The unique performance of the two catalysts was considered to be provided by the stabilized Ni dispersion and enhanced CO_2 activation. Similar reasons were also concluded in the reported papers describing Nd and Sm-promoted NiMgAl-LDH-derived catalysts [118,119].

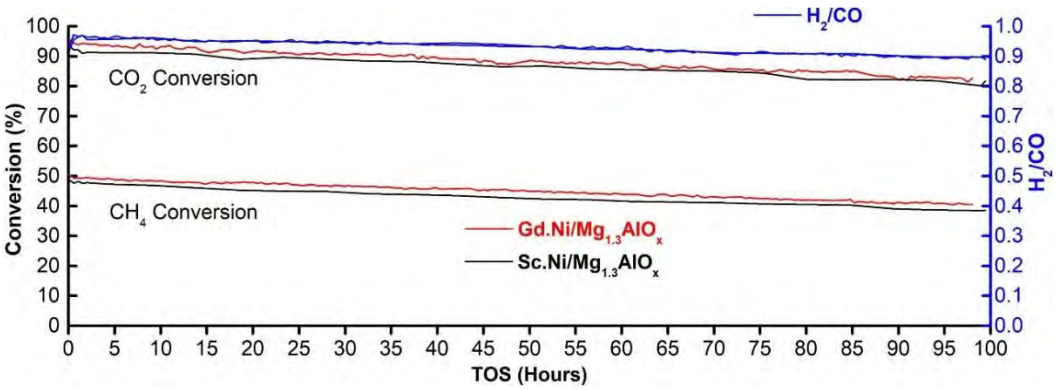

Fig. 1.4. CO_2 and CH_4 conversions and H_2/CO ratio in long-term CH_4 rich DRM with catalysts: $GdNi/MgAlO_x$ and $ScNi/MgAlO_x$ at 750 °C, 1 bar, $CH_4/CO_2 = 2$, GHSV = 170 $Lg_{cat}^{-1}h^{-1}$ [117]. Copyright 2022. Elsevier.

Table 1.3. Different lanthanides metal binary-Ni LDH-derived thermal catalysts for the DRM reaction reported in the recent literature, with details of the catalyst synthesis and composition, reaction conditions and reaction performance.

Catalyst	Method of LDH synthesis	Cations in LDH	Metal amounts (wt%) [a]	M^{2+}/M^{3+} (molar ratio)	Calcination Condition	Reaction Conditions [b]			Conversion [c]		H_2/CO ratio	TOS (h) [d]	Coking $wt\%/g_{cat}$	Ref.
						Temp.	CH_4/CO_2	GHSV (ml g^{-1} h^{-1})	CH_4 (%)	CO_2 (%)				
NiLaMgAl-LDH	co-precipitation	Ni, La, Mg, Al	Ni: 15; La: 4	3	550 °C, 4 h	550 °C	1	20,000 h^{-1}	~40	~37	0.8 - 1.2	~8	87.5	[120]
NiLaMgAl-LDH	co-precipitation	Ni, La, Mg, Al	Ni:Mg:Al:La = 2:4:1.8:0.2	3	800 °C, 4 h	700 °C	1	60,000	~80	~80	~1	14	75	[121]
NiLaMgAl-LDH	co-precipitation	Ni, La, Mg, Al	Ni: 20; La: 4.3	3	600 °C, 4 h	750 °C	1	240,000	~70	~80	~0.6	15	ND	[122]
NiMAl-LDH (M = Mg, Li, Ca, La, Cu, Co, Zn)	co-precipitation	Ni, M, Al (M = Mg, Li, Ca, La, Cu, Co, Zn)	Ni: 55% mol; M: 11% mol (M = Mg, Li, Ca, La, Cu, Co, Zn)	2	600 °C, 6 h	600 °C	2.3	54,000	~55	~70	~3	5	71	[106]
Ni, La loaded on calcined MgAl-LDH	commercial	Mg, Al	Ni: 2.5 molar ratio La:Ni = 0.8	1.3	550 °C 6 h for LDH, 400 °C 3h then 800 °C 6 h for loaded samples	750 °C	1	170,000	~80	~85	~0.7	160	~1.5	[107]
Ni, La loaded on calcined MgAl-LDH	commercial	Mg, Al	Ni: 2.5 molar ratio La:Ni = 0.8	1.3	1000 °C for LDH, 400 °C 3h then 800 °C 6 h for loaded samples	750 °C	2	170,000	~45	~90	~0.9	100	~5	[108]

NiCeMgAl-LDH	co-precipitation	Ni, Ce, Mg, Al	Ni: 10; Ce: 5	3	650 °C, 4 h	650 °C	1.5	70,800	~30	~52	~0.75	6	ND	[113]
NiCeMgAl-LDH	co-precipitation	Ni, Ce, Mg, Al	Ce: 4.7	3	600 °C, 6 h	600 °C	3	144,000	~13	~46	~0.7	25	76	[29]
Ce loaded on calcined NiMgAl-LDH	co-precipitation	Ni, Mg, Al	Ni: 12; Ce: 3	3	600 °C, 6 h	700 °C	1	180,000	ND	~55	ND	30	~4	[114]
CeO_2 covered NiCoMgAl-LDH	urea hydrolysis	Ni, Co, Mg, Al	Ni: 4.2; Co: 4; Ce: 36.1	2.3	CeO2 loaded on LDH then 600 °C, 4 h	600 °C	1	36,000	~55	~62	~0.7	165	2.3 mg $C \cdot h^{-1} g_{cat}^{-1}$	[49]
CeO_2 covered NiMgAl-LDH		Ni, Mg, Al	Ni: 4.8; Ce: 38.5	2	CeO2 loaded on LDH then 600 °C, 4 h				~50	~57	~0.65	165	2.2 mg $C \cdot h^{-1} g_{cat}^{-1}$	
NiCoMgAl-LDH		Ni, Co, Mg, Al	Ni: 6.3; Co: 6.1	2.3	600 °C, 4 h				~57 to ~64	~75 to ~67	~0.8 to ~1	3.5	310 mg $C \cdot h^{-1} g_{cat}^{-1}$	
NiPrMgAl-LDH	microwave-assisted self-combustion	Ni, Pr, Mg, Al	Ni: 51.5; Pr: 5.6	3	700 °C, 4 h	600 °C	1	120,000	~40	~53	1.1	10	30.3	[115]
NiPrMgAl-LDH	co-precipitation								~65 to ~46	~42 to ~36	~1.7 to ~1.1		82.4	
NiPrMgAl-LDH	microwave-assisted self-combustion	Ni, Pr, Mg, Al	Ni/Mg = 2; Pr: 4	3	700 °C, 4 h	600 °C	1	120,000	~51 to ~43	~38 to ~36	~1.3 to ~1.1	10	78.4	[116]
NiPrMgAl-LDH	self-combustion								~44 to ~41	~35 to ~34	~1.2 to ~1.1		71	

NiGd loaded on MgAl-LDH	commercial	Mg, Al	Ni: 2.5; Gd: 5	1.3	550 °C 6 h for LDH, 400 °C 3h then 800 °C 6 h for loaded samples	750 °C	2	170,000	49 to 40	95 to 80	0.98 to 0.9	100	4	[117]
NiSc loaded on MgAl-LDH			Ni: 2.5; Sc: 5						~47 to ~38	~93 to ~77	0.98 to 0.9	100	~7.5	
NiLa loaded on MgAl-LDH			Ni: 2.5; La: 5						~50 to ~45	~95 to ~90	~0.95 to ~0.92	8	~6	
NiNdMgAl-LDH	co-precipitation	Ni, Nd, Mg, Al	Ni: 9.07; Nd: 5.69	Mg:Al = 2.5; total M2+/M3+ = ~2.8	800 °C, 5 h	750 °C	1	48,000	~56 to ~52	~60 to ~62	~0.85 to ~0.8	14	2.4	
		Ni, Nd, Mg, Al	Ni: 8.8; Nd: 7.25						~52 to ~10	~53 to ~11	~0.86 to ~0.76		2.3	
NiMgAl-LDH		Ni, Mg, Al	Ni: 8.46						54.1 to ~44	56.6 to ~56	~0.77 to ~0.36		9.6	
NiSmMgAl-LDH	urea hydrolysis	Ni, Sm, Mg, Al	Ni: 10; Sm: 3	1	freeze-dried, -20 °C, 24 h,	700 °C	1	12,000	~70	ND	~0.9	20	ND	[119]

[a] the unit for loading amount is wt%, the ratio is molar; [b] GHSV: Gas hourly space velocity; [c] the conversions are from the best or initial to final results in long term tests; "~": approximate value; "ND": no data shown in the literature; [d] TOS: Time on stream;

1.2.3.3 Other metal binary-Ni and multi metal-Ni LDH-derived catalyst

As shown in the sections above, promotors of alkali metals, transition elements, and lanthanide metals were widely used to improve the catalysts. Element from other groups, herein namely Ga, can also be introduced into LDH-derived catalysts, showing some unique properties [123,124]. Moreover, as different elements can improve the catalyst in DRM in different ways, the combination of different elements, forming multi metal-Ni LDH (more than one type of promotors) derived catalysts were also investigated, exhibiting promising performance [125–129], which are summarized in Table 1.4.

The promotion effect of Ga was studied by Kim and co-workers [123]. Catalysts Ga/MgO, Ni/MgO, and NMG-600 were synthesized via a modified hydrothermal method (using Ni, Mg, Ga nitrates mixture as the precursor to produce NiMgGa catalyst (shortened as NMG), and all the samples reduced at 600 °C and denoted as NMG-600). Physical mixed Ni/MgO-Ga/MgO and incipient wetness impregnation method synthesized NiGa/MgO were also prepared. For the DRM reaction at 600 °C, the results showed that Ga/MgO had no catalytic effect and Ni/MgO without Ga promotion deactivated rapidly in 12 h, while NMG-600 had almost no deactivation, suggesting the promoting effect of Ga in enhancing stability. Besides this, physically mixed Ni/MgO-Ga/MgO did not prevent the deactivation process of the Ni/MgO catalyst. In comparison with NiG/MgO

catalyst prepared via the traditional impregnation method, which showed good activities (45% for CH_4 and 47% for CO_2) and stability as well at 600 °C for 12 h, the NMG-600 (namely NiMgGa-LDH-derived catalyst with reduction temperature of 600 °C) exhibited superior catalytic performance and less coke deposition. A further 72h long-term DRM test was done on the NMG-600 catalyst, which showed excellent stability with only about 3.5% deactivation for CH_4 and around 4.0% deactivation for CO_2. Characterization helped to explain the possible mechanism that suggested the formation of a Ni_3GaC_x phase during the reaction, which could remove carbon by a reversible exchange between Ni_3Ga and Ni_3GaC_x. The DFT calculations provided the most plausible structure being $Ni_3GaC_{0.25}$ and clarified the reaction mechanism where carbon formed from dissociated CH_4 penetrated into the octahedral interstices of the Ni_3Ga lattice, forming a $Ni_3GaC_{0.25}$ intermetallic carbide, which can easily react with CO_2, resulting in suppression of coke formation on the catalyst surface.

The effect of different promoting metals was studied by Zeng et al. [124] by comparing GaNi, LaNi, and GaLaNi-LDH-derived catalysts in the DRM reaction. In detail, the MgAl-LDH was firstly synthesized via a hydrothermal method, then the LDH was used as support to load GaNi, LaNi, or GaLaNi by impregnation. They first investigated the effects of the Ga content on the activity of the Ni catalyst. It was found that too much Ga addition caused a decrease in the catalyst performance and $Ni_{0.8}Ga_{0.2}$ showed the highest stability and activity (both CO_2 and

CH_4 conversion of about 80% with negligible change in the 6 h test) among the promoted catalysts. In the following test, when using Ga promoted Ni catalyst, only a $Ni_{0.8}Ga_{0.2}$ ratio was applied. A long-term test was done at 700 °C for 50 h for all the catalysts. The results illustrated that when only a single promoting metal Ga or La was present, the LaNi catalyst displayed more effective improvement in both activity and coke resistance. However, when Ga and La were both introduced into the Ni-LDO catalyst, the obtained GaLaNi catalyst exhibited the highest CH_4 and CO_2 conversion and H_2/CO ratio (see Table 1.4), although it slowly decreased as well. Moreover, it also displayed the lowest carbon deposition of 3.8 wt% while it was 8.2 wt% for the GaNi catalyst and 6.6 wt% for the LaNi catalyst. This superior result was attributed to several aspects and the mechanism is shown in Fig 1.5. On one hand, the GaNi alloy and La_2O_3 promoter were highly and adjacently dispersed on the surface of the LDO support. On the other hand, the introduction of Ga formed a GaNi alloy, which produced more electron-rich Ni^0 and electron-deficient Ga^{3+} on the surface, promoting and balancing the CH_4 and CO_2 dissociation during the reaction process. Moreover, the addition of La_2O_3 further activated the adsorption of CO_2 at high temperatures above 600 °C from where the CO_2 can continuously be transferred to Ga^{3+}, allowing reaction with the deposited carbon.

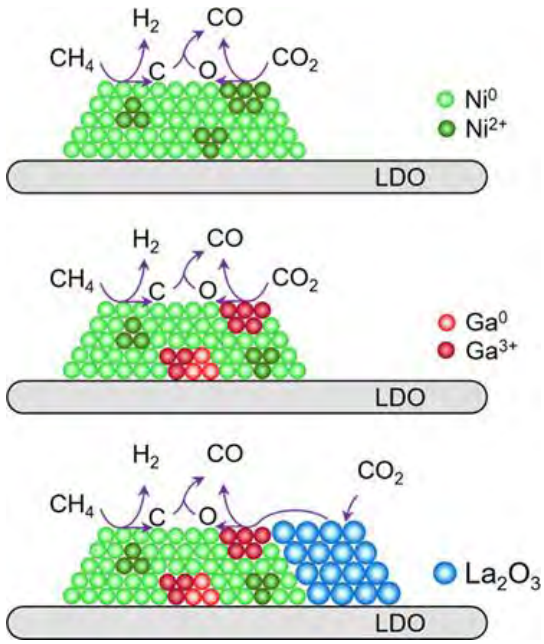

Fig. 1.5. Reaction mechanisms for the DRM reaction with catalysts: Ni/LDO, $Ni_{0.8}Ga_{0.2}$/LDO, and $Ni_{0.8}Ga_{0.2}/La_2O_3$-LDO [124]. Copyright 2021. American Chemical Society.

Costa's group and their co-workers [125–127] prepared a series of CeZr, CeY, and ZrY-promoted Ni-LDH-derived catalysts. Compared with the original Ni-LDH-derived catalyst, the promoted catalysts showed different performance. The CeZr-modified catalyst resulted in a decline in the catalytic performance, while the stability was improved (for the Ni catalyst, the initial CH_4 conversion increased from about 40% to 50% for the final conversion, and the CO_2 conversion decreased from the initial 45% to final 40%; for the CeZr modified Ni catalyst with 4.7 wt% Ce and 2.7 wt% Zr the CH_4 and CO_2 conversion were stable at about 25% and 30% with little deactivation during the 6 h test) and less carbon (about 48 wt% for the Ni catalyst, and 11 wt% for this CeZr modified catalyst) was deposited on the catalyst [125]. The CeY-promoted catalyst exhibited obvious improvement in CH_4

and CO_2 conversions from 75% to 85% and around 88% compared with the unpromoted Ni catalyst, however, carbon deposition (about 28 wt%) was more serious than on the promoted Ni catalyst (about 20 wt%) [126]. The ZrY-modified catalyst produced via the co-precipitation method showed better activity, deactivation resistance and coke resistance than the original Ni-LDO catalyst, while it was less stable and experienced heavier coke deposition than the Ni-LDO catalyst with only Zr modification [127]. Their study demonstrated the high complexity of multi-metals promotion in a Ni-LDH-derived catalyst for DRM reaction.

Li et al. [128] reported a promoted NiMgAl-LDH-derived catalyst with promotors of three different metals, namely Mo, Ce and Zr, which exhibited a remarkable stability of over 600 h with only a small amount of coke deposition (see Table 1.4). The one-pot co-precipitation method (mixing the metal nitrates and ammonium molybdate with deionized water) synthesized Ni/MoCeZr/$MgAl_2O_4$-MgO catalysts prepared at different calcination temperatures of 700 °C, 800 °C, and 900 °C were compared in the DRM reaction at 900 °C. The catalyst calcined at 800 °C exhibited the highest activation with still 95% CH_4 conversion after 658 h, while that of the catalyst calcined at 900 °C decreased to 90% after 105 h and it never exceeded 72% for the catalyst calcined at 700 °C. To study the synergetic effect of the Mo, Ce, and Zr metals, different catalysts were produced using the same conditions except that either one or two metals were introduced into the

original Ni-based catalyst. As shown in Table 1.4 and reference [128], for the Ni/MoZr/$MgAl_2O_4$-MgO, Ni/MoCe/$MgAl_2O_4$-MgO and Ni/CeZr/$MgAl_2O_4$-MgO catalysts, the CH_4 conversion declined to around 90% after 76, 47, and 24 h, respectively. In the case of Ni/$MgAl_2O_4$-MgO, the conversion of CH_4 dropped to about 48% after 28 h, while that of Ni/Mo/$MgAl_2O_4$-MgO declined to about 93% after 130 h and that of Ni/MoCeZr/$MgAl_2O_4$-MgO remained at around 95% after 658 h. Comparing the results, it was obvious that the coexistence of Mo, Ce, and Zr was essential to obtain high activity and super-high stability. Various characterization methods illustrated the joint effects of small Ni nanoparticles of 7.2 nm endowed from the coexistence of the $MgAl_2O_4$ spinel, NiO-MgO solid solution and multiple promoters, more basic sites and reinforced metal-support interactions. High performance and stability were also obtained when they explored a hexamethylenetetramine (HMT) assisted method, which avoided the utilization of alkali metal ions, giving a potential industrial application prospect [129].

Table 1.4. Different lanthanide metal binary-Ni LDH-derived catalysts for the DRM reaction reported in the recent literature, with details of the catalyst synthesis and composition, reaction conditions and reaction performance.

Catalyst	Method of LDH synthesis	Cations in LDH	Metal amounts (wt%) [a]	M^{2+}/M^{3+} (molar ratio)	Calcination Condition	Reaction Conditions [b]			Conversion [c]		H_2/CO ratio	TOS (h) [d]	Coking $wt\%/g_{cat}$	Ref.
						Temp.	CH_4/CO_2	GHSV (mL g^{-1} h^{-1})	CH_4 (%)	CO_2 (%)				
NiGaMg-LDH	hydrothermal	Ni, Ga, Mg	Ni: 13.6; Ga: 17.3	4	600 °C, 5 h with 50% H_2/Ar	600 °C	1	54,000	52 to 48.3	48 to 46.3	ND	72	1.7 for 12 h	[123]
Ni loaded on MgAl-LDH	urea hydrolysis	Mg, Al	Ni: 3.72	2	600 °C, 2 h for LDH; then 600 °C, 2 h for metals loaded samples	700 °C	1	275,000	66.9 to 33.9	73.1 to 38.9	0.71	50	9.8 for 20 h	[124]
NiGa loaded on MgAl-LDH			Ni: 3.4; Ga: 0.6						72.1 to 50.9	74.1 to 59.9	0.72		8.2 for 20 h	
NiLa loaded on MgAl-LDH			Ni: 4.07; La: ND						82.6 to 66.3	83.6 to 71.5	~0.72		6.6 for 20 h	
NiGaLa loaded on MgAl-LDH			Ni: 3.42; Ga: 0.66; La: ND						82 to 75.3	84.3 to 76.4	~0.72		3.8 for 20 h	
NiCeZrMgAl-LDH	co-precipitation	Ni, Zr, Mg, Al	Ni: 20; Zr: 2.7; Ce: 4.7	3	550 °C, 4 h	750 °C	1	20,000 h^{-1}	~83	~90	~0.92	24	~11	[125]
NiMgAl-LDH	co-precipitation	Ni, Mg, Al	Ni: 20	3	550 °C, 5 h	700 °C	1	20,000 h^{-1}	~73	~75	~0.9	5	~25	[126]
NiCeMgAl-LDH		Ni, Ce, Mg, Al	Ni: 25; Ce: 3						~85	~87	~0.97		~20	
Y loaded on NiCeMgAl-LDH		Ni, Ce, Mg, Al	Ni: 23; Ce: 3; Y: 0.2						~77 to ~84	~80 to ~86	~1 to ~0.97		~28	

NiZrMgAl-LDH	co-precipitation	Ni, Zr, Mg, Al	Ni: 23 Zr: 3.6	3	550 °C, 5 h	700 °C	1	20,000 h^{-1}	78.6 to 77.7	82.7 to 82.6	0.99 to 0.98	5	7.3	[127]
Y loaded on NiZrMgAl-LDH		Ni, Zr, Mg, Al	Ni: 25; Zr: 3.5; Y: 0.4						76.9 to 77.1	82.8 to 82	0.9 to 0.88		11.9	
NiZrYMgAl-LDH		Ni, Zr, Y, Mg, Al	Ni: 20; Zr: 4.1; Y: 0.5						84.3 to 90.9	86.3 to 90.2	0.99 to 0.98		20.2	
NiMoCeZrMgAl-LDH		Ni, Mo, Ce, Zr, Mg, Al	Ni: 15.5; Ce: 1.73; Zr: 0.083; Mo: 0.035		800 °C, 6 h				95	~98	~0.97	658	0.015 [e]	
					900 °C, 6 h				90	~92	~0.93	105	0.032 [e]	
					700 °C, 6 h				72	~85	~0.85	72	0.393 [e]	
NiMgAl-LDH	co-precipitation	Ni, Mg, Al	ND	3	800 °C, 6 h	900 °C	1	60,000	48	~64	~0.8	28	4.96 [e]	[128]
NiMoMgAl-LDH		Ni, Mo, Mg, Al							93	~96	~0.9	130	1.45 [e]	
NiMoZrMgAl-LDH		Ni, Mo, Zr, Mg, Al							90	~94	~0.9	76	4.54 [e]	
NiMoCeMgAl-LDH		Ni, Mo, Ce, Mg, Al							90	~92	~0.9	47	1.2 [e]	
NiCeZrMgAl-LDH		Ni, Ce, Zr, Mg, Al							90	~90	~0.7	24	1.11 [e]	
NiMoCeZrMgAl-LDH	hydrothermal	Ni, Mo, Ce, Zr, Mg, Al	Ni: 6; (ZrO_2+CeO_2): 1; MoO_3: 0.6	3	800 °C, 6 h	900 °C	1	60,000	~95	~97	~0.97	610	0.19 [e]	[129]

[a] the unit for loading amount is wt%; [b] GHSV: Gas hourly space velocity; [c] the conversions are from the best or initial to final results in long term tests; "~": approximate value; "ND": no data shown in the literature; [d] TOS: Time on stream; [e] the unit for coking is $mgC \cdot h^{-1} g_{cat}^{-1}$.

1.3 Plasma for DRM

As briefly introduced in the introduction, plasma is one of the promising technologies to reduce CO_2 emissions and use it as the carbon source to form other chemical products. Compared with the conventional thermal-catalytic DRM system, two types of plasma-catalysis (see Fig. 1.6) operation can be distinguished, as mentioned before, being IPC and PPC, in which the latter is closer to conventional thermal catalysis. Both types of plasma catalysis are distinctively different and provide a different plasma-catalyst interaction, therefore creating a different reaction environment at the location of the catalyst bed.

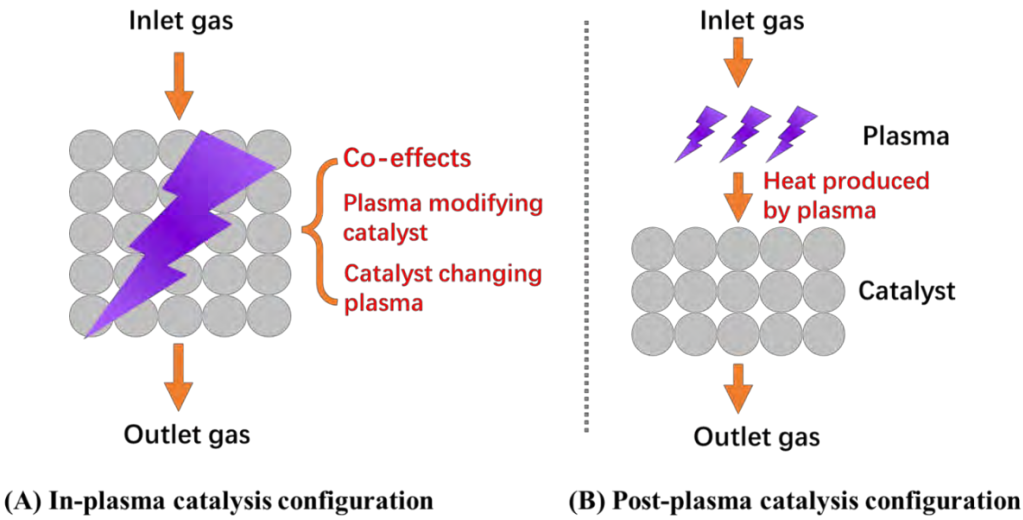

Fig. 1.6. Schematic overview of two plasma catalysis system configurations; (A) in-plasma catalysis (IPC) and (B) post-plasma catalysis (PPC).

Indeed, a PPC bed is positioned after the plasma exhaust and thus has no direct contact with the discharge, but comes in contact with the plasma-treated species

(converted and unconverted) and the exhaust conditions of the plasma (temperature, flow rates and pressure). To allow catalysis to occur in the post-plasma bed, it has to be positioned in such a way that it benefits most from the energy present in the plasma gas mixture at the exhaust, allowing heat recovery and possible use of the energy of the excited/reacted species in the exhaust, if sufficiently long living. Therefore, post-plasma catalysis is mainly applied in combination with warm plasmas such as gliding arcs and microwave plasmas, with the purpose of recovering as much energy as possible provided by the plasma. For the PPC system, which operates (partially) with the heat provided by warm plasmas, it is expected to be more similar to the classical thermal catalytic processes, although the feed stream (plasma exhaust) coming in contact with the catalyst is different. Moreover, both the feed stream and temperature in contact with the catalyst bed are determined by the operating conditions of the plasma, and heat and mass transfer are determined by the design and position of the post-plasma bed, posing challenges to PPC systems.

In contrast, in the case of IPC, the catalyst is placed in the discharge zone and thus has a direct impact on the plasma discharge properties (e.g. change of discharge type) and is in direct contact with all the plasma species. IPC is therefore most often applied in combination with cold plasmas that remain close to ambient temperature such as DBDs, which would not supply sufficient energy post-plasma. In the latter case, finding catalysts that are compatible with the plasma and provide

an enhancing effect on the plasma properties (physically altering the plasma), while also benefiting surface (catalytic) effects, is currently one of the key challenges in IPC DRM. They are essential to allow more energy-efficient processes while enhancing conversion and selectivity.

Many reviews give a comprehensive introduction to plasma-based DRM without catalysts [8,31,37,130] and coupling plasma DRM with catalysts [35,38,131–133], as well as plasma-based pre-treatment of catalysts [133–138]. Considering this, we will not repeat this overview in this chapter, as the reader can obtain this information from the reviews listed before. However, we will focus here specifically on plasma-catalytic DRM in combination with LDH or LDH-derived catalysts. From the previous sections, it is obvious that LDH works very well in thermal catalytic DRM. The question is whether it can also work well in plasma catalysis. For this purpose, in this section, we give a brief description of two types of plasmas that will be discussed further in this chapter. The first is DBD, as an example of typical non-thermal plasma, because it has already been combined with LDH catalysts. The second is GA plasma, as an example of a warm plasma. Although it has not yet been combined with LDH catalysts, we believe it has great potential when LDH catalysts are placed post-plasma, allowing the hot gas from the plasma to heat and activate the catalyst, just like in thermal catalysis.

1.3.1 DBD for DRM

DBD is a typical non-thermal plasma, which can be applied at atmospheric or slightly elevated (e.g. 3 bar) pressure, and temperatures as low as room temperature [41,139,140]. A DBD reactor consists of two parallel electrodes, among which one is covered by a dielectric barrier (see Fig. 1.7A). When producing plasma, one electrode is connected to the high-voltage power supply, providing alternating current and the other one is grounded. The gas flows from one side to the other side through the gap (which varies from 0.1 mm to a few centimetres) between the inner electrode and the dielectric barrier. It is ignited to the plasma phase by the electric potential between the two electrodes, creating a reactive environment that enables the conversion of the species present. Various parameters affect the performance of a DBD plasma, such as the gas flow rate and composition, space-time, and power [53,141–143]. Moreover, the designs parameters of a DBD plasma reactor, such as the dielectric tube dimensions, the electrode length and the gas inlet and outlet position, also have some impact [144–146].

Uytdenhouwen et al. [145] studied how the gas flow design affected the performance of DBD plasma for DRM. Particularly, in a multi-inlets reactor, it was found that the gradual addition of one of the input gases, via a reactor with 14 inlets along the side, enhanced the conversion, which, however, highly depended on the type of main gas and the direction of the additional gas supply via long or short

orientation. In addition, the effect of the discharge gap size was evaluated for DRM in DBD reactors, including the introduction of packing material (non-porous SiO_2 and ZrO_2) as a function of gap size [139]. At a smaller gap size, this resulted in an enhancement in CO_2 conversion due to a higher reduced electric field and specific energy input (SEI). While a different gap-dependent material effect was observed on the apparent partial equilibrium, no apparent synergistic effect or plasma-catalytic behaviour was observed for the non-porous packing materials in the study [139]. Tu et al. [140,147] also found that that the way in which the catalyst was filled into the discharge gap could affect the conversion of CH_4 and CO_2, which indicates that the filling mode changes the discharge mode.

As the DBD reactors for DRM are usually driven by AC power sources, which may lead to overheating and reactor damage when continuously heating the discharge channel, it was thought that pulsed power for a DBD reactor could have several advantages, such as short rise time with considerable energy efficiency and inhibition of overheating, easier separation of the radical generation and the chemical reaction process and so on. This was to some degree evaluated by Wang and co-workers [141], providing data that short pulse rise & fall times slightly improved the conversion and energy conversion efficiencies (the CH_4 and CO_2 conversion increased from about 10% and 30% to 17% and 40%) in a nanosecond pulsed DBD plasma for DRM. Besides this, it was found that a higher pulse repetition frequency (PRF) (increasing from 3 kHz to 10 kHz) was also helpful in

reaching higher conversion (the CH_4 and CO_2 conversion increased from around 10% and 7% to 39% and 22%), which was attributed to the enhancement of the discharge pulse and possible increase of collisions between energetic electrons and molecules.

Apart from the experimental studies on improved DBD configurations that lead to better plasma performance, simulation and theoretical studies were also performed to further understand the mechanism of DRM in the DBD plasma. Uytdenhouwen et al. [142] investigated the kinetic activities of the CO_2 dissociation and CH_4 reforming and their influence on each other when added together in the DRM reaction, by combining experiments and calculations/data fitting. They found that, compared with the CH_4 reforming rate (0.041 s^{-1}), the CO_2 dissociation had a comparatively higher apparent reaction rate (0.120 s^{-1}), while CH_4 reforming obtained higher partial equilibrium conversions (82% compared to 53.6% for CO_2 dissociation). A combination of CO_2 and CH_4, forming a DRM reaction, resulted in intermediate results of an apparent reaction rate of 0.088 s^{-1} and a total conversion of 75.4%. Further investigation revealed that CO_2 promoted the loss reactions in a DRM reaction, while CH_4 suppressed the back reactions. In another study combining experimental validation and kinetic modelling [148], the conclusion was drawn that the CH_4 molecule was relatively easier dissociated than the CO_2 molecule due to its lower threshold energy, explaining the higher conversion of CH_4 in the DRM reaction in a DBD reactor. This is in contrast to

what is often observed in thermal catalytic DRM with LDH-derived catalysts as summarized in Table 1.1-1.4, where CO_2 is converted more than CH_4. The RWGS reaction in the thermal catalysis DRM process may be a possible reason for this, so that some CO_2 can react with the produced H_2, thereby producing CO [80,149].

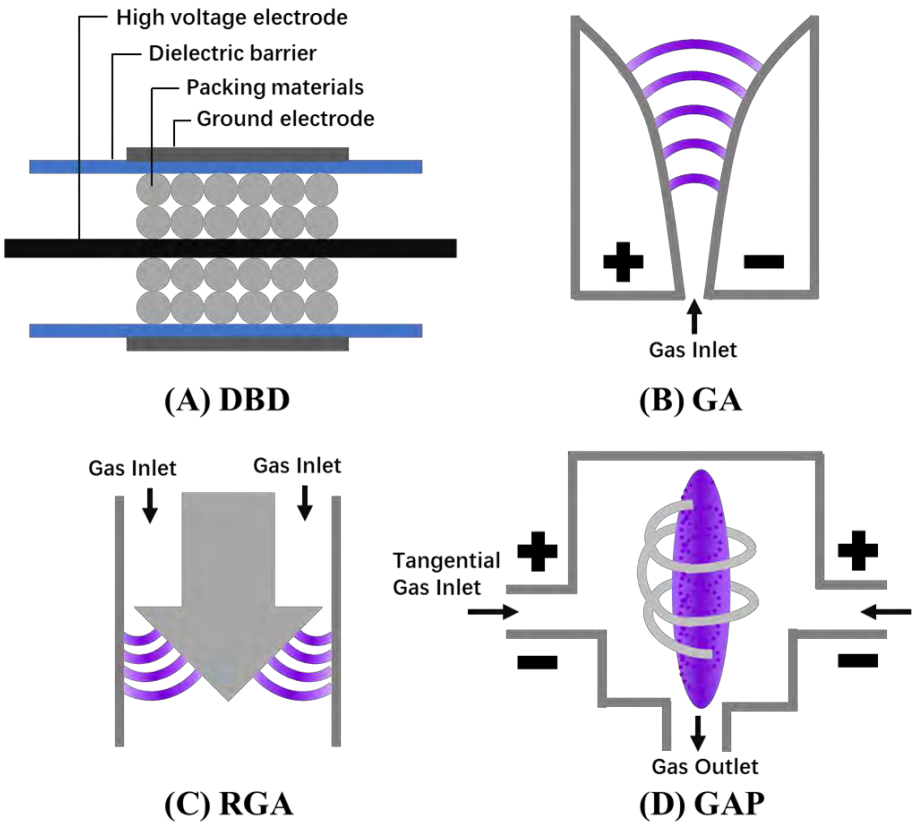

Fig. 1.7. Schematic of the (A) DBD, (B) classical two-dimensional knife-type electrodes GA, (C) rotating gliding arc (RGA), and (D) gliding arc plasmatron (GAP). The schematic image of the GAP was adapted from Bogaerts' group setup reported in ref. [150]. Copyright 2017. The Royal Society of Chemistry.

Different from the plasma alone cases, packing with catalysts causes significant effects on the properties of a DBD plasma, such as a drop in the discharge (gap) volume (i.e., the distance between the electrodes allowing gas to go through) and

feed gas space velocity and changes in the discharge behaviour and residence time. Besides this, the properties of the catalysts, like the supports utilized, the specific surface area, particle and pore sizes and morphologies, and the types of active metal(s) used, can also have an impact on the discharge process and eventually affect the DRM process and results [32,151,152]. Moreover, when the catalyst is present inside the plasma, the plasma can also affect the catalyst, resulting in modification of the catalyst. The physical and chemical interactions between plasma and catalysts are well summarized in a recently reported review by Bogaerts's group (see Fig. 1.8) [153].

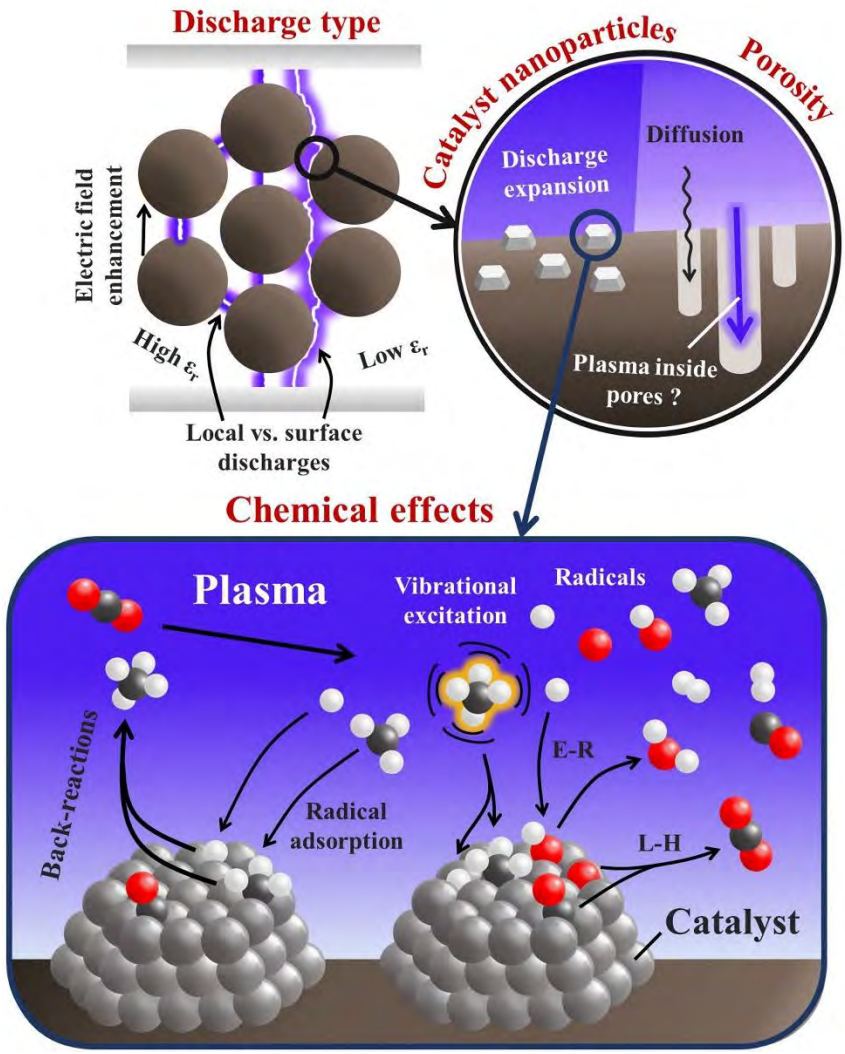

Fig. 1.8. The various physical and chemical plasma-catalytic interactions. E-R and L-H are abbreviations for Eley-Rideal and Langmuir-Hinshelwood reactions, respectively. ε_r: dielectric constant of the packing [153]. Copyright 2023. Elsevier.

The plasma makes the DRM reaction possible at lower gas temperatures than what is normally needed in thermal catalytic conditions, as the electrons are accelerated while the gas remains at relatively lower temperatures. Although this is an advantage, IPC is a complex process and is far more complex than the simple addition or combination of plasma and catalyst, causing either a positive or

negative overall effect [153]. As introduced before, plasma and catalyst can affect each other, and some of the effects of their interaction may be positive, while some are neutral and some may be negative, compared with the plasma alone process or the normal catalytic process and the overall effect will then be the sum of all these different interactions. Therefore, catalysts with good catalytic activity, herein, LDH-derived catalysts as introduced before, are worth to be evaluated towards their effect on the plasma performance in DRM.

1.3.2 GA plasma for DRM

A classical GA plasma can be produced at the shortest point between two flat electrodes (Fig. 1.7B). After being generated, the arc can glide to the other side of the electrode, guided by the gas flow. Then the arc will extinguish in the large gap part of the electrode, while at the same time a new arc will be generated at the shortest gap part and be pushed by the gas flow, forming continuous gliding arcs. The GA plasma possesses the advantages of both thermal plasma and non-thermal plasma conditions. It is an intermediate plasma type and is often called a warm plasma because the gas temperature can reach up to 3000 K, which is higher than non-thermal plasma that remains close to room temperature, but still lower than thermal plasmas (> 4000K) [154–158]. Although relatively simple and reliable, the classical two-dimensional (2D) (usually knife-type electrodes) GA plasmas [159–163] have a limitation in the sense that the plasma arc is formed in a limited region between the flat electrodes, leading to a large fraction of gas that will flow around

the electrodes without being converted. Therefore, other types of GA plasma reactors have also been developed, such as 3D reverse vortex flow gliding arc plasmatrons (GAP) (Fig. 1.7D) [164–167], rotating gliding arc plasmas (RGA) (Fig. 1.7C) [168–170], dual-vortex plasmatrons [171], and magnetic field co-driven GAs [172–174]. These 3D GA plasmas, with a cylindrical electrode design, overcome the problem of a large gas fraction not being treated in 2D GA plasmas, by stabilising the arc in the center, which promotes a longer residence time for the gas molecules in the discharge and improves the gas conversion [156].

Similar to the DBD plasma, whose performance can be affected by the reactor design, the structure of the gliding arc plasma setups can influence their performance to some degree as well. For example, instead of using thin knife electrodes, Ghorbanzade and Rahmati [175] used a pair of parallel wire-plate electrodes for the gliding arc plasma (PEGP) setup. In comparison with conventional GA plasma, the PEGP provided higher plasma mobility within the volume of the parallel electrodes, giving more gliding time for molecule dissociation. Moreover, the energy of the mobile plasma part was generally dissipated in the layers of fresh reactant gas rather than overheating or re-dissociating the products. The advantages in these two aspects resulted in high conversions of CO_2 and CH_4 (about 55% and 65%, respectively) and over 60% in energy efficiency. Besides this, the angles and the external-electrode lengths can also affect the GA plasma performance [169]. As shown in Fig. 1.9, the angle and

length of the internal electrode were changed. They found a summit angle of 45° was more favourable for achieving higher CH_4 and CO_2 conversions. The energy efficiencies increased by 25% and 22% compared with the RGA with electrode angles of 30° and 60°. With the angle of 45°, the longer external electrode RGA showed higher CO_2 and CH_4 increase due to the improvement of arc extension.

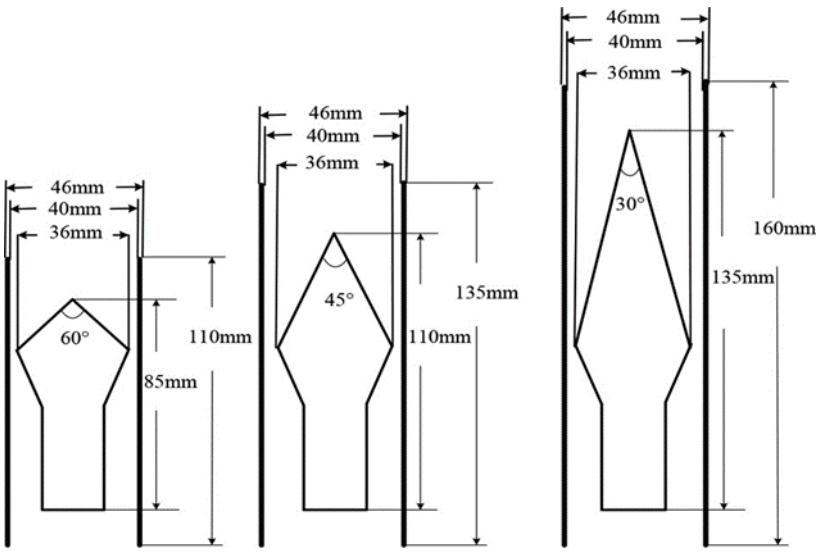

Fig. 1.9. Internal electrodes with summit angles of 60°, 45° and 30° [169]. Copyright 2018, Elsevier.

Irrespective of the design of the gliding arc plasmas, the gas itself is intrinsically heated by the plasma reactions, reaching temperatures up to a few 1000K for GA plasma. [32,167] This not only allows for thermal conversion to occur in the plasma zone but also offers a possibility for thermal catalysis after the plasma zone. However, this high temperature also puts constraints on the type of materials that can be put in the plasma discharge zone as shrinkage, loss of porosity and sintering will take place in the majority of materials used in thermal catalysis. Therefore, in

the case of warm plasmas, such as gliding arcs, PPC is the main choice of plasma catalysis configurations, as material choices for IPC are limited, and strategies attempting to recover at least part of the heat and thus energy can be pursued, with processes and mechanisms closer to what is known in thermal catalysis, which avoids to some extent the complexity of IPC. Nevertheless, PPC seems to have not been found straightforwardly. Trying to find out the reasons, some research about the PPC will be given in section 4.2, which may give some clues.

1.4 Plasma catalysis with LDH/LDO catalysts

This section focuses on the application of LDH-derived catalysts in combination with plasma in the DRM field. This section contains two parts: (i) DBD-assisted LDH/LDO catalysis for DRM, which is a typical IPC system, and (ii) GA plasma-assisted LDH/LDO catalysis for DRM, which is a typical PPC system.

1.4.1 DBD-assisted LDH/LDO catalysis for DRM

The number of studies related to the application of DBD plasma catalysis with LDH/LDO catalysts is limited so far [176–179]. Shao and co-workers [176] applied radio frequency (RF) plasma to modify a NiCoMgAl-LDH, which was synthesized via the in-situ growth method on nickel foam (NF), with the aim to create more oxygen vacancies and promote the dispersion of active nano-particles in the catalyst. They then applied the catalyst in a DBD reactor for DRM. The catalyst synthesis routes, treatment by the plasma, and SEM images of the obtained

catalysts are shown in Fig. 1.10. In comparison, catalysts with different metals and without plasma treatment were utilized as well in a plasma-driven DRM reaction. The experimental results illustrate that the plasma-modified catalyst P-CoMgAl/NF had the highest activation of CO_2 and CH_4 conversion of around 11% and 16% due to the co-existence of the MgAlO phase and Ov, which could more easily capture CO_2 molecules and then break the C=O bond. Thus, the CO_2 protonation/hydrogenation routes, and the OH(g) as well as O(g) radicals promotion routes can be remarkably strengthened via the essentially barrierless E-R mechanism (< 0.1 eV) [176]. Besides this, the discharge waveforms measured from different catalysts only showed slight changes, suggesting that the composition of the catalysts had an almost negligible impact on the plasma discharge behaviour. This was confirmed by the similar wall temperature of the plasma reactor (about 120 °C).

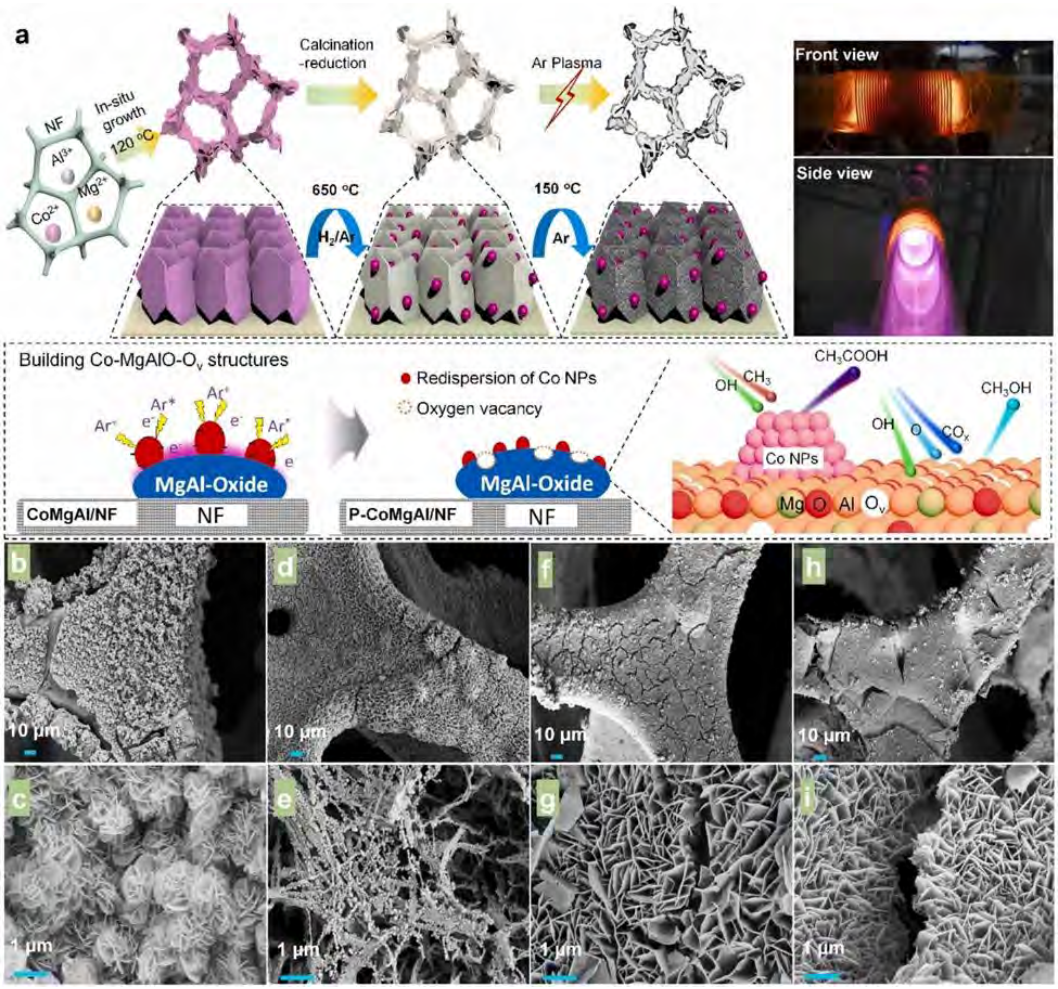

Fig. 1.10. Procedure of producing the catalyst treated by RF plasma and SEM images of the catalysts. (a) Schematic of the synthesis routes and catalytic roles for the Co-MgAlO-Ov multiphase structures; SEM of (b, c) NiMgAl/NF, (d, e) CoAl/NF, (f, g) CoMgAl/NF and (h, i) plasma-treated P-CoMgAl/NF (80 W, 30 min) [176]. Copyright 2022, Elsevier.

Further investigation of the synergetic effect of LDH-derived catalysts with plasma was also done by Shao and co-workers [177]. A series of Ni-based LDH-derived catalysts, which were grown on nickel foam (NF), were synthesized. It was found that for the DBD plasma-catalytic IPC system, the microstructure, surface composition (valency states) and reducibility were crucial for the selectivity of

liquid oxygenate products. The Ni^0-based catalysts Ni/NF and NiGa/NF (catalysts obtained by calcination of NiAl-LDH/NF in H_2/Ar gas at 500 °C) exhibited higher total liquid selectivity (> 30%) with CH_3COOH (> 15%) as dominant product, while the Ni^{2+} based catalyst NiO/NF (obtained by calcination of NiAl-LDH/NF in air at 500 °C) showed a comparable selectivity for CH_3OH (8.9%) and CH_3COOH (9.6%). Notably, the NiAl-LDH/NF catalyst gave the highest CH_3OH selectivity of 12.3% and almost no carbon deposition appeared after the reaction. Systematic analysis suggested that the large number of -OH groups on the surface of NiAl-LDH might play an important role in reacting with the interfacial CH_3* species. Moreover, the NiAl-LDH possessed inferior electron affinity for carbon atoms. These two catalyst properties promoted its high CH_3OH selectivity and coke resistance. Wang et al. [178] systematically compared the catalytic performances of NiZnAl-LDH with different Ni loading amounts for DRM by three different experimental modes: DBD plasma alone, catalysis alone, and DBD in-plasma catalysis. Considering that the plasma was operated at low temperatures of 30–60 °C, the catalysis-alone reaction was also executed at this temperature, resulting in the absence of catalytic performance. When the plasma was applied without the LDH catalysts (plasma alone), the conversions of CH_4 and CO_2 reached about 43.4% and 33.8%, respectively, while when catalyst was packed into the plasma reactor, the highest conversions of CH_4 and CO_2 were enhanced to around 68.9% and 54.3% with 20 wt% Ni loading. Interestingly, the catalytic activity of LDH-derived

ZnO/Al_2O_3 without loading of Ni was close to those of the plasma alone case, indicating the catalyst support can hardly impose any catalytic behaviors. Moreover, the 20 wt% Ni loading LDH-derived catalyst also had the highest CO and H_2 selectivity of 74.5% and 62.5%. Furthermore, a long-term test of DRM for 10 h was done with the same catalyst for plasma catalysis and thermal catalysis at 650 °C. Although the conversions of plasma catalysis were lower than for thermal catalysis (i.e., around 70% CH_4 conversion and 60% CO_2 conversion for plasma catalysis, while for thermal catalysis the initial CH_4 and CO_2 conversions were around 89% and 83%, and the final CH_4 and CO_2 conversions were around 81% and 74%), the activity stability of the plasma-catalytic system was higher with only around 1% deactivation after 10 h reaction, while this was about 9% for the thermal catalysis mode. Besides this, the energy yield for thermal catalysis alone (650 ℃) and plasma alone was only about 0.022 mmol/kJ and 0.20 mmol/kJ, respectively, whereas the value was increased to about 0.36 mmol/kJ for plasma catalysis. Not only the Ni loading can affect the activity in a DBD plasma-catalytic DRM system, also the amount of promoting metal has some impact.

To further understand the function of promoted active metals, Diao et al. [180] recently reported Ni-, Fe-, and NiFe- loaded LDH-derived catalysts (named Ni/MgAlO, Fe/MgAlO, and NiFe/MgAlO) for DRM involved with DBD plasma. In detail, three experiments were conducted, namely thermal catalysis (500 °C), thermal catalysis (500 °C) coupled with 60 W DBD plasma, and the 60 W DBD

plasma alone. Firstly, the Ni/MgAlO catalyst was applied in the three configurations. They found that for the thermal catalysis case only 22.2% CO_2 conversion and 16.0% CH_4 conversion were obtained, which were lower than for the 60 W DBD plasma alone (23.4% for CO_2 and 38.1% for CH_4). However, when the thermal catalysis (500 °C) system was coupled with the DBD plasma configuration, high conversions of 71.0% for CO_2 and 64.8% for CH_4 were achieved, suggesting the significant beneficial effect of plasma on DRM in this system. Moreover, experiments with Ni/MgAlO, Fe/MgAlO, and NiFe/MgAlO were carried out to investigate how the promoted metals affect the results. It was found that only 4.7% CO_2 conversion and 1.2% CH_4 conversion were obtained in the Fe/MgAlO configuration, implying that the Fe atom had almost no catalytic effect on the DRM. However, the NiFe/MgAlO catalyst showed higher activity of CO_2 and CH_4 conversions of 80.5% and 73.8%, higher than those of Ni/MgAlO mentioned before. This may be because the addition of Fe can improve the dispersion of Ni particles, which was already reported in the traditional thermal DRM system [181]. The stability performance of the Ni/MgAlO and NiFe/MgAlO catalysts was done for 20 h in the thermal catalysis system coupled with the DBD plasma. The NiFe/MgAlO catalyst showed better stability, because the conversions of CO_2 and CH_4 remained at 81.2% and 72.5%, while those of CO_2 and CH_4 for the Ni/MgAlO catalyst decreased to 55.6% and 67.8% from 72.2% and 73%, respectively. A longer test of 100 h was performed with NiFe/MgAlO catalyst, and the CO_2 and CH_4 conversions still remained at 71% and 75%. This could be

attributed to two reasons. Firstly, the plasma enabled the DRM reaction to occur at 500 °C and maintained high conversions of CO_2 and CH_4. Secondly, the addition of Fe increased the surface oxygen and enhanced the CO_2 adsorption, and adjacent Fe promotion improved the carbon elimination reaction between the adsorbed CO_2 and deposited carbon which was produced by CH_4 cracking.

1.4.2 GA plasma-assisted LDH/LDO catalysis for DRM

Compared with non-thermal plasma like DBD and corona plasmas, the electron temperature of GA can be lower. However, the GA plasmas have a higher electron density and higher gas temperature, making them more energy-efficient for the activation of CO_2 in DRM [182,183]. Different from the DBD plasma-catalytic system, which is a typical IPC, the catalysts in a GA plasma-catalytic system are typically put after the plasma, in so-called PPC, to avoid the destruction of catalysts by the excessive heat produced by the plasma. PPC requires the catalyst distance to be meticulously investigated. Indeed, considering that the reactive plasma species densities decrease fast and can almost totally disappear at a distance of 2.5 mm from the arc centre [156], the PPC system acts more as in thermal catalysis, which can make use of the heat produced by the plasma to further convert the CO_2 and CH_4 molecules in the afterglow of the plasma or convert the products formed by the plasma.

As discussed before, LDH-derived catalysts show attractive performance in thermal catalytic DRM, providing high potential for its combination with GA plasma. However, even though there are some papers about GA plasma coupled with catalysts for DRM, unfortunately, catalysts derived from LDH were not found among them. Therefore, in this section, we introduce several discoveries in this area, giving a prospect description for the combination of LDH-derived catalysts and GA plasma.

As described above, for PPC which performs more like thermal catalysis, the temperature is crucial for the catalyst to work, which is highly related to the position of the catalyst after the plasma. Li et al. [42] studied how the catalyst bed position affected the reforming results in a heat-insulated plasma catalysis reactor. It was found that as the distance of the catalyst to the plasma reduced from 11 cm to 4 cm, the CH_4 and CO_2 conversions increased from 82% and 4% to 92% and 20%. The catalyst mid-bed temperature elevated from 647 °C to 779 °C due to the decrease in heat loss when approaching the plasma zone. Higher temperature, which was suitable for the catalyst to work, was the main reason for the increasing conversions.

In another study, Liu and co-workers [184] exhibited an enhancing effect on the GA plasma-catalytic DRM reaction when extra heating was applied to the reactor. Without extra heating, the performance of the GA plasma and the GA plasma

catalysis showed almost the same results in conversion, selectivity, energy cost and efficiency. Although traditional thermal catalysis proved that the Ni-based catalyst ($Ni/CeO_2/Al_2O_3$) had good performance in DRM, no contribution was found in the plasma-catalytic system without extra heating. The reason could be attributed to the low gas temperature of the plasma effluent, which was only in the range of 300 °C to 500 °C, at which the catalyst was inactive for the DRM reaction. When keeping the reactor at the same temperature of 850 °C, compared with thermal catalysis with about 45% CH_4 conversion and about 62% CO_2 conversion, the plasma-catalytic case with extra heating resulted in higher conversions, around 60% for CH_4 and around 71% for CO_2, respectively. As the reactor temperature was the same, the rise in conversion could be ascribed to the synergetic effect of plasma and catalyst. However, considering LDH-derived catalysts can provide high potential to improve the catalytic performance for thermal catalytic DRM, it allows lower and more suitable extra heating temperatures to be investigated, which can promote the energy efficiency of the whole PPC system.

The reported papers above suggest the possibility of using traditional thermal catalysts to further improve the performance of DRM in a PPC system. Considering this, the LDH-derived catalyst can be a potential catalyst. Moreover, as the idea of PPC is to make full use of the heat produced by the plasma gas, which is economical, a good design of a PPC reactor system which can keep more heat from

the plasma on the catalyst bed, or requires less (external) heating will be a possible way to make PPC with LDH/LDO catalyst more powerful.

1.5 Conclusion

This chapter generally summarizes the development of DRM catalyzed by LDH-derived catalyst, DBD and GA plasma, and their combination effect. The first part involves a detailed overview of new studies in LDH synthesis and catalytic performance of monometallic, bimetallic promoted, and multi-metallic Ni-LDH-based catalysts in DRM. Plasma DBD or GA reactions for CO_2 and CH_4 conversion without the presence of catalysts were shortly introduced as well. Finally, recent investigations in plasma catalysis using LDH/LDO catalysts for DRM were reported.

As summarized in the tables, the co-precipitation method is the most commonly applied method to prepare LDH-based catalysts, while other methods such as hydrothermal, microwave-assisted or ultrasonication-assisted methods, can be utilized as well, either alone or in combination with some other methods. Based on the research needs, the morphology, crystal size, and even the basicity of the LDH can be adjustable by the synthesis method. Besides this, in-situ growth of LDH on metal foam or other substrates with good properties has attracted increasing attention.

For DRM converting CO_2 and CH_4, LDH-derived mixed metal oxide catalysts are favoured due to many advantages, such as a large surface area, adjustable metal types and contents and an abundant number of basic sites. Among them, catalysts containing Ni are most widely studied, as they show high catalytic activity and are readily available. However, deactivation still exists due to the agglomeration of active sites and coke deposition on the particles. Promotion with noble metal(s), transition metal(s) or some other metal elements, forming bimetallic, trimetallic, or multi-metallic Ni-LDH-based catalysts, can improve the stability and anti-coking ability.

Plasma technology is attracting increasing interest for DRM, as plasma is an electrically driven process that can effectively supply energy to ionize gaseous species, creating a reactive environment able to excite and dissociate relatively stable molecules efficiently. Depending on the type of plasma, i.e. in cold plasma such as DBDs, these reactions can proceed near room temperature and atmospheric pressure. Additional advantages are that plasma can easily be switched on and off, and allows the rapid activation of the reaction, making it compatible with fluctuating energy supply. When applied together with LDH/LDO catalysts, improvements were achieved in an IPC system.

Although great progress has been made in DRM with LDH-derived catalysts, mainly in thermal catalysis, and recently also combined with plasma, some challenges remain, and further improvement is necessary:

1) For DRM with Ni-LDH-based catalysts, a remaining challenge is that the investigation is still limited to laboratory scale, with long-term time on stream tests of a maximum of 100-200 hours. Longer-term stability tests over weeks with shaped catalysts are necessary to be able to further scale up the technology and allow future implementation in the industry. In addition, several experimental attempts were made at a laboratory scale to alter the promoting metals in the LDH/LDO materials to achieve, for example, better stability and coke resistance. However, the repeatability of these experiments towards scaled-up amounts has not been reported. Besides this, fewer studies were focused on the regeneration of these catalysts and their performance in reaction.

2) The possible synergetic effect between plasma and catalyst has been demonstrated in recent years, however, the detailed mechanisms still need to be revealed. Specifically for LDH-derived catalysts, only a few papers were reported for DBD plasma catalysis. Finally, no paper about GA plasma coupled with LDH-derived catalyst has been reported so far. However, we believe this combination has a lot of potential when placing the catalyst post-plasma, as the heat produced by the plasma can be used to activate the LDH/LDO similar to thermal catalysis, although the feed stream, in casu the plasma exhaust mixture, will be different from the thermal process and might require further adjusted catalysts compared to the

current classical thermal DRM catalysts. Furthermore, it requires well-designed GA plasma-catalytic reactor configurations, allowing effective heat recovery and mass transfer. It is in this second part that we aim to progress the state-of-the-art with this PhD.

1.6 Aim of the work and outline of the thesis

LDH-derived catalysts are promising for the dry reforming of methane (DRM), a chemical process that is able to convert captured CO_2, together with CH_4 (originating from e.g. natural gas reserves and/or biogas). However, this thermal catalytic process requires high temperatures (> 700 °C) to achieve sufficiently high CO_2 and CH_4 conversion, generally above 60%. Plasma technology offers an alternative, enabling the DRM reaction at atmospheric pressure using (renewable) electrical energy. Nevertheless, in the current plasma processes, challenges remain to enhance CO_2 and CH_4 conversion, selectivity and energy efficiency. Catalysts are envisioned to be a part of the solution but knowledge on how to integrate catalysts with different types of plasma processes to achieve this enhanced performance is still lacking. Among various plasma technologies, gliding arc plasma (GAP) can provide high temperatures in the range of 400-1000°C in the post-plasma zone, which poses opportunities to recover the plasma energy to serve as a heat source for catalytic processes. However, to put this hypothetical opportunity into practice, several knowledge steps need to be taken in order to fit

the plasma exhaust and its properties with the catalytic process taking place in direct connection to the exhaust of the plasma process. Several questions can be asked, of which 2 main questions have been defined at the start of this PhD: 1) How does plasma operation and feed gas composition influence the temperature of the exhaust gas and its composition and thus feed gas of the catalytic process and heat transfer. 2) Can well performing LDH-derived catalysts used in thermal processes also enhance post-plasma DRM and what are the critical determining factors in reactor configuration and plasma operation that influence this PPC performance. To answer these questions, the work has been divided in several chapters, providing the state-of-the-art (Chapter 1), important knowledge on properties and stability of the LDH-derived catalysts towards liquid water and moist (Chapter 2), correlation of operating conditions of the plasma and its influence on exhaust gas composition and temperature (Chapter 3) and identification of key aspects when coupling GAP with post-plasma catalysis (Chapter 4 and 5).

Chapter 1 provides a comprehensive overview of the state-of-the-art in LDH-based materials for DRM, an introduction to plasma catalytic technology and the application of LDH-based materials in plasma catalytic technology. The objectives are primarily addressed in Chapter 1 of the study: evaluate the efficiency of LDH-derived catalysts in DRM; explore plasma technology as an alternative in DRM; explore the potential of plasma technology in facilitating the DRM reaction at

atmospheric pressure using renewable electrical energy, and to identify ways to improve the limited conversion of CO_2 and CH_4 and energy efficiency and enhance selectivity currently achieved through this method.

However, to our knowledge, limited achievements have been obtained till now concerning DRM with PPC GA reactors. Therefore, attempts to figure out a solution for the improvement of PPC for DRM, connected to the GAP system were carried out.

Before combining the plasma and catalyst, properties of the LDH and derived LDO materials and the optimal plasma configurations for DRM were investigated. Specifically, **Chapter 2** describes the synthesis, properties and rehydration of the LDH-derived LDO materials. In **Chapter 3**, optimal operation parameters for the GAP plasma DRM without catalysts, like gas flow rate, gas composition, and addition of H_2O, were investigated. Moreover, the temperatures at different positions post-plasma in relation to the gas composition applied, were recorded during the plasma reaction process. Based on this knowledge, information on the feed gas composition (plasma exhaust) contacting the catalysts and temperature at the catalyst bed is obtained. The latter aids in determining the distance of the catalyst bed position required for efficient utilization of heat and sufficient catalytic performance.

After this, **Chapter 4** discusses attempts to improve plasma-catalytic DRM with a traditional tray-type catalyst bed (T-bed). This part aims to study which factors influence the catalytic process. It focuses among others on the amount of catalyst used, deactivation by carbon deposits and the impact of the heat transferred from plasma to catalyst. The results of this chapter provide recommendations on ways to improve the performance of the PPC DRM, which are further studied in Chapter 5. Before being utilized for PPC DRM, the catalytic activity of the catalyst was evaluated by thermal catalytic DRM, which suggests that the catalytic performance enhanced as the temperature increased. Varying the distance of the post-plasma catalyst to the plasma exhaust can adjust the temperature (the closer, the higher the temperature) on the catalyst bed. Moreover, adding extra heating at low temperatures (150-250 °C) and wrapping the post-plasma reactor tube with insulation materials seem to be a possible method to enhance the surrounding temperature of the catalyst. Some improvements are achieved with extra heating with a temperature of 250 ℃, suggesting the importance of higher temperature for the catalyst layer. These attempts to improve plasma-catalytic DRM are important for the last chapter (Chapter 5), offering some important suggestions.

In **Chapter 5**, considering the limited effect of the GAP plasma-catalytic DRM with the tray-type T-bed, a newly designed tubular catalyst bed (N-bed) is directly connected to the GAP device, which can transfer the heat from the plasma exhaust

gas as well as via thermal conductivity from the connected GAP device to the catalyst bed body, to heat the catalyst layer. Moreover, also the flow behaviour might be impacted by the presence of the bed and influence the PPC performance. The presence of the N-bed versus the T-bed is thus evaluated in Chapter 5. Also the prensence of α-Al_2O_3 filling material with or without catalyst is evaluated with the purpose of identifying the impact of catalytic versus none-catalytic effects on the performance of the N-bed, providing interesting insights in the above mentioned possible influences in heat transfer, flow behaviour and catalysis. It was found that when the N-bed was applied, both the conversion of CO_2 and CH_4 increased, even though only filling material of α-Al_2O_3 was utilized. Moreover, the addition of a Ni/LDO catalyst proved to further improve the conversion and selectivity and decrease the energy cost. Analysis suggested that differences in the flow behaviour and possibly in quenching, present in the N-bed, together with efficient heat transfer to the catalyst bed, without extra external insulation or heating, are proven to contribute to its better performance.

Finally, the whole work is summarized and an outlook for future research is presented for the GAP plasma-catalytic DRM field at the end of this thesis.

1.7 References

[1] Mustafa, A.; Lougou, B. G.; Shuai, Y.; Wang, Z.; Tan, H. Current Technology Development for CO_2 Utilization into Solar Fuels and Chemicals: A Review. J. Energy Chem. 2020, 49, 96–123. https://doi.org/10.1016/j.jechem.2020.01.023.

[2] Weng, W.; Tang, L.; Xiao, W. Capture and Electro-Splitting of CO_2 in Molten Salts. J. Energy Chem. 2019, 28, 128–143. https://doi.org/10.1016/j.jechem.2018.06.012.

[3] Ramos, A. E.; Maiti, D.; Daza, Y. A.; Kuhn, J. N.; Bhethanabotla, V. R. Co, Fe, and Mn in La-Perovskite Oxides for Low Temperature Thermochemical CO_2 Conversion. Catal. Today 2019, 338 (November 2018), 52–59. https://doi.org/10.1016/j.cattod.2019.04.028.

[4] Lee, W. J.; Li, C.; Prajitno, H.; Yoo, J.; Patel, J.; Yang, Y.; Lim, S. Recent Trend in Thermal Catalytic Low Temperature CO_2 Methanation: A Critical Review. Catal. Today 2021, 368 (November 2019), 2–19. https://doi.org/10.1016/j.cattod.2020.02.017.

[5] Gür, T. M. Carbon Dioxide Emissions, Capture, Storage and Utilization: Review of Materials, Processes and Technologies. Progress in Energy and Combustion Science. 2022, p 100965. https://doi.org/10.1016/j.pecs.2021.100965.

[6] Parvez;, A. M.; Afzal;, M. T.; Hebb;, T. G. V.; Schmid;, M. Utilization of CO_2 in Thermochemical Conversion of Biomass for Enhanced Product Properties: A Review. J. CO_2 Util. 2020, 40, 101217.

[7] Desport;, L.; Selosse;, S. An Overview of CO_2 Capture and Utilization in Energy Models. Resour. Conversvation Recycl. 2022, 180, 106150.

[8] Snoeckx, R.; Bogaerts, A. Plasma Technology-a Novel Solution for CO_2 Conversion? Chem. Soc. Rev. 2017, 46 (19), 5805–5863. https://doi.org/10.1039/c6cs00066e.

[9] Cui, Z.; Meng, S.; Yi, Y.; Jafarzadeh, A.; Li, S.; Neyts, E. C.; Hao, Y.; Li, L.; Zhang, X.; Wang, X.; Bogaerts, A. Plasma-Catalytic Methanol Synthesis from CO_2 Hydrogenation over a Supported Cu Cluster Catalyst: Insights into the Reaction Mechanism. ACS Catal. 2022, 12 (2), 1326–1337. https://doi.org/10.1021/acscatal.1c04678.

[10] Oki, M.; Galadima, A. A Review on Coke Management during Dry Reforming of Methane. Int. J. Energy Res. 2015, 39, 1196–1216. https://doi.org/10.1002/er.

[11] Arora, S.; Prasad, R. An Overview on Dry Reforming of Methane: Strategies to Reduce Carbonaceous Deactivation of Catalysts. RSC Adv. 2016, 6 (110), 108668–108688. https://doi.org/10.1039/c6ra20450c.

[12] Hussien, A. G. S.; Polychronopoulou, K. A Review on the Different Aspects and Challenges of the Dry Reforming of Methane (DRM) Reaction. Nanomaterials. 2022. https://doi.org/10.3390/nano12193400.

[13] Aramouni, N. A. K.; Touma, J. G.; Tarboush, B. A.; Zeaiter, J.; Ahmad, M. N. Catalyst Design for Dry Reforming of Methane: Analysis Review. Renew. Sustain. Energy Rev. 2018, 82 (December 2016), 2570–2585. https://doi.org/10.1016/j.rser.2017.09.076.

[14] Michielsen, I.; Uytdenhouwen, Y.; Bogaerts, A.; Meynen, V. Altering Conversion and Product Selectivity of Dry Reforming of Methane in a Dielectric Barrier Discharge by Changing the Dielectric Packing Material; 2019; Vol. 9. https://doi.org/10.3390/catal9010051.

[15] Abdulrasheed, A.; Jalil, A. A.; Gambo, Y.; Ibrahim, M.; Hambali, H. U.; Shahul Hamid, M. Y. A Review on Catalyst Development for Dry Reforming of Methane to Syngas: Recent Advances. Renew. Sustain. Energy Rev. 2019, 108 (March), 175–193. https://doi.org/10.1016/j.rser.2019.03.054.

[16] de Medeiros, F. G. M.; Lopes, F. W. B.; Rego de Vasconcelos, B. Prospects and Technical Challenges in Hydrogen Production through Dry Reforming of Methane. Catalysts 2022, 12 (4), 363. https://doi.org/10.3390/catal12040363.

[17] Yentekakis, I. V.; Panagiotopoulou, P.; Artemakis, G. A Review of Recent Efforts to Promote Dry Reforming of Methane (DRM) to Syngas Production via Bimetallic Catalyst Formulations. Appl. Catal. B Environ. 2021, 296, 120210. https://doi.org/10.1016/j.apcatb.2021.120210.

[18] Hambali Umar, H.; Aishah Abdul, J.; Abdulrahman A. Abdulrasheed; Tan Ji Siang; Yahya Gambo;; Ahmad Abulfathi Umar; Zeolite and Clay Based Catalysts for CO_2 Reforming of Methane to Syngas： A Review. Int. J. Hydrogen Energy 2022, 47, 30759–30787.

[19] Dewangan, N.; Hui, W. M.; Jayaprakash, S.; Bawah, A. R.; Poerjoto, A. J.; Jie, T.; Jangam, A.; Hidajat, K.; Kawi, S. Recent Progress on Layered Double Hydroxide (LDH) Derived Metal-Based Catalysts for CO_2 Conversion to Valuable Chemicals. Catal. Today 2020, 356, 490–513. https://doi.org/10.1016/j.cattod.2020.06.020.

[20] Baharudin, L.; Rahmat, N.; Othman, N. H.; Shah, N.; Syed-Hassan, S. S. A. Formation, Control, and Elimination of Carbon on Ni-Based Catalyst during $CO_2$and CH_4 conversion via Dry Reforming Process: A Review. J. CO_2 Util. 2022, 61 (April), 102050. https://doi.org/10.1016/j.jcou.2022.102050.

[21] Gao, X.; Li, J.; Zheng, M.; Cai, S.; Zhang, J.; Askari, S.; Dewangan, N.; Ashok, J.; Kawi, S. Recent Progress in Anti-Coking Ni Catalysts for Thermo-Catalytic Conversion of Greenhouse Gases. Process Saf. Environ. Prot. 2021, 156, 598–616. https://doi.org/10.1016/j.psep.2021.10.051.

[22] le Saché, E.; Reina, T. R. Analysis of Dry Reforming as Direct Route for Gas Phase CO_2 Conversion. The Past, the Present and Future of Catalytic DRM Technologies. Progress in Energy and Combustion Science. 2022. https://doi.org/10.1016/j.pecs.2021.100970.

[23] Qin, Z.; Chen, J.; Xie, X.; Luo, X.; Su, T.; Ji, H. CO_2 Reforming of CH_4 to Syngas over Nickel-Based Catalysts. Environ. Chem. Lett. 2020, 18 (4), 997–1017. https://doi.org/10.1007/s10311-020-00996-w.

[24] Yusuf, M.; Farooqi, A. S.; Keong, L. K.; Hellgardt, K.; Abdullah, B. Contemporary Trends in Composite Ni-Based Catalysts for CO_2 Reforming of Methane. Chem. Eng. Sci. 2021, 229, 116072. https://doi.org/10.1016/j.ces.2020.116072.

[25] Buelens, L. C.; Galvita, V. V.; Poelman, H.; Detavernier, C.; Marin, G. B. Super-Dry Reforming of Methane Intensifies CO_2 Utilization via Le Chatelier's Principle. Science (80-.). 2016, 354 (6311), 449–452. https://doi.org/10.1126/science.aah7161.

[26] Theofanidis, S. A.; Batchu, R.; Galvita, V. V.; Poelman, H.; Marin, G. B. Carbon Gasification from Fe-Ni Catalysts after Methane Dry Reforming. Appl. Catal. B Environ. 2016, 185, 42–55. https://doi.org/10.1016/j.apcatb.2015.12.006.

[27] Dębek, R.; Motak, M.; Grzybek, T.; Galvez, M. E.; Da Costa, P. A Short Review on the Catalytic Activity of Hydrotalcite-Derived Materials for Dry Reforming of Methane. Catalysts. 2017. https://doi.org/10.3390/catal7010032.

[28] Li, D.; Li, R.; Lu, M.; Lin, X.; Zhan, Y.; Jiang, L. Carbon Dioxide Reforming of Methane over Ru Catalysts Supported on Mg-Al Oxides: A Highly Dispersed and Stable Ru/Mg(Al)O Catalyst. Appl. Catal. B Environ. 2017, 200, 566–577. https://doi.org/10.1016/j.apcatb.2016.07.050.

[29] Kalai, D. Y.; Stangeland, K.; Tucho, W. M.; Jin, Y.; Yu, Z. Biogas Reforming on Hydrotalcite-Derived Ni-Mg-Al Catalysts: The Effect of Ni Loading and Ce Promotion. Journal of CO_2 Utilization. 2019, pp 189–200. https://doi.org/10.1016/j.jcou.2019.05.011.

[30] Le Saché, E.; Reina, T. R. Analysis of Dry Reforming as Direct Route for Gas Phase CO_2 Conversion. The Past, the Present and Future of Catalytic DRM Technologies. Prog. Energy Combust. Sci. 2022, 89 (December 2021). https://doi.org/10.1016/j.pecs.2021.100970.

[31] Bogaerts, A.; Neyts, E. C. Plasma Technology: An Emerging Technology for Energy Storage. ACS Energy Lett. 2018, 3 (4), 1013–1027.

[32] Feng, J.; Sun, X.; Li, Z.; Hao, X.; Fan, M.; Ning, P.; Li, K. Plasma-Assisted Reforming of Methane. Adv. Sci. 2022, 9 (34), 1–36. https://doi.org/10.1002/advs.202203221.

[33] Chen, G.; Snyders, R.; Britun, N. CO_2 Conversion Using Catalyst-Free and Catalyst-Assisted Plasma-Processes: Recent Progress and Understanding. J.

CO_2 Util. 2021, 49 (May), 101557. https://doi.org/10.1016/j.jcou.2021.101557.

[34] Vermeiren, V.; Bogaerts, A. Plasma-Based CO_2 Conversion: To Quench or Not to Quench?.Pdf. J. Phys. Chem. C 2020, 124 (34), 18401–18415.

[35] George, A.; Shen, B.; Craven, M.; Wang, Y.; Kang, D.; Wu, C.; Tu, X. A Review of Non-Thermal Plasma Technology: A Novel Solution for CO_2 Conversion and Utilization. Renew. Sustain. Energy Rev. 2021, 135, 109702. https://doi.org/10.1016/j.rser.2020.109702.

[36] Wang, W.; Snoeckx, R.; Zhang, X.; Cha, M. S.; Bogaerts, A. Modeling Plasma-Based CO_2 and CH_4 Conversion in Mixtures with N_2, O_2, and H_2O: The Bigger Plasma Chemistry Picture. Journal of Physical Chemistry C. 2018, pp 8704–8723. https://doi.org/10.1021/acs.jpcc.7b10619.

[37] Klemm, E.; Lobo, C. M. S.; Löwe, A.; Schallhart, V.; Renninger, S.; Waltersmann, L.; Dietrich, A. S. R.; Costa, R.; Möltner, L.; Meynen, V.; Sauer, A.; Friedrich, K. A. CHEMampere : Technologies for Sustainable Chemical Production with Renewable Electricity and CO_2,N_2, O_2, and H_2O. Can. J. Chem. Eng. 2022, 100 (10), 2736–2761. https://doi.org/doi.org/10.1002/cjce.24397.

[38] Bogaerts, A.; Tu, X.; Whitehead, J. C.; Centi, G.; Lefferts, L.; Guaitella, O.; Azzolina-Jury, F.; Kim, H. H.; Murphy, A. B.; Schneider, W. F.; Nozaki, T.; Hicks, J. C.; Rousseau, A.; Thevenet, F.; Khacef, A.; Carreon, M. The 2020 Plasma Catalysis Roadmap. J. Phys. D. Appl. Phys. 2020, 53 (44), 443001. https://doi.org/10.1088/1361-6463/ab9048.

[39] Bogaerts, A.; Neyts, E. C.; Guaitella, O.; Murphy, A. B. Foundations of Plasma Catalysis for Environmental Applications. Plasma Sources Sci. Technol. 2022, 31 (5). https://doi.org/10.1088/1361-6595/ac5f8e.

[40] Adamovich, I.; Baalrud, S. D.; Bogaerts, A.; Bruggeman, P. J.; Cappelli, M.; Colombo, V.; Czarnetzki, U.; Ebert, U.; Eden, J. G.; Favia, P.; Graves, D. B.; Hamaguchi, S.; Hieftje, G.; Hori, M.; Kaganovich, I. D.; Kortshagen, U.; Kushner, M. J.; Mason, N. J.; Mazouffre, S.; Thagard, S. M.; Metelmann, H. R.; Mizuno, A.; Moreau, E.; Murphy, A. B.; Niemira, B. A.; Oehrlein, G. S.; Petrovic, Z. L.; Pitchford, L. C.; Pu, Y. K.; Rauf, S.; Sakai, O.; Samukawa, S.; Starikovskaia, S.; Tennyson, J.; Terashima, K.; Turner, M. M.; Van De Sanden, M. C. M.; Vardelle, A. The 2017 Plasma Roadmap: Low Temperature Plasma Science and Technology. J. Phys. D. Appl. Phys. 2017, 50 (32), 323001. https://doi.org/10.1088/1361-6463/aa76f5.

[41] George, A.; Shen, B.; Craven, M.; Wang, Y.; Kang, D.; Wu, C.; Tu, X. A Review of Non-Thermal Plasma Technology: A Novel Solution for CO_2 Conversion and Utilization. Renew. Sustain. Energy Rev. 2021, 135 (August 2020), 109702. https://doi.org/10.1016/j.rser.2020.109702.

[42] Li, K.; Liu, J. L.; Li, X. S.; Zhu, X.; Zhu, A. M. Warm Plasma Catalytic Reforming of Biogas in a Heat-Insulated Reactor: Dramatic Energy

Efficiency and Catalyst Auto-Reduction. Chem. Eng. J. 2016, 288, 671–679. https://doi.org/10.1016/j.cej.2015.12.036.

[43] Zhu, F.; Zhang, H.; Yan, X.; Yan, J.; Ni, M.; Li, X.; Tu, X. Plasma-Catalytic Reforming of CO_2-Rich Biogas over Ni/γ-Al_2O_3 Catalysts in a Rotating Gliding Arc Reactor. Fuel 2017, 199, 430–437. https://doi.org/10.1016/j.fuel.2017.02.082.

[44] Liu, J. L.; Li, Z.; Liu, J. H.; Li, K.; Lian, H. Y.; Li, X. S.; Zhu, X.; Zhu, A. M. Warm-Plasma Catalytic Reduction of CO_2 with CH_4. Catal. Today 2019, 330 (December 2017), 54–60. https://doi.org/10.1016/j.cattod.2018.05.046.

[45] Lian, H. Y.; Wei, Z.; Yun, S.; Jing, R.; Liu, L. Warm Plasma Catalytic Coreforming of Dilute Bioethanol and Methane for Hydrogen Production. Plasma Process. Polym. 2023, 1–9. https://doi.org/10.1002/ppap.202300062.

[46] Dębek, R.; Azzolina-Jury, F.; Travert, A.; Maugé, F. A Review on Plasma-Catalytic Methanation of Carbon Dioxide – Looking for an Efficient Catalyst. Renew. Sustain. Energy Rev. 2019, 116, 109427. https://doi.org/10.1016/j.rser.2019.109427.

[47] Salaev, M. A.; Liotta, L. F.; Vodyankina, O. V. Lanthanoid-Containing Ni-Based Catalysts for Dry Reforming of Methane: A Review. Int. J. Hydrogen Energy 2022, 47 (7), 4489–4535. https://doi.org/10.1016/j.ijhydene.2021.11.086.

[48] Li, P.; Yu, F.; Altaf, N.; Zhu, M.; Li, J.; Dai, B.; Wang, Q. Two-Dimensional Layered Double Hydroxides for Reactions of Methanation and Methane Reforming in C1 Chemistry. Materials. 2018. https://doi.org/10.3390/ma11020221.

[49] Das, S.; Lim, K. H.; Gani, T. Z. H.; Aksari, S.; Kawi, S. Bi-Functional CeO_2 Coated NiCo-MgAl Core-Shell Catalyst with High Activity and Resistance to Coke and H_2S Poisoning in Methane Dry Reforming. Appl. Catal. B Environ. 2023, 323. https://doi.org/10.1016/j.apcatb.2022.122141.

[50] Sheng, Z.; Watanabe, Y.; Kim, H. H.; Yao, S.; Nozaki, T. Plasma-Enabled Mode-Selective Activation of CH_4 for Dry Reforming: First Touch on the Kinetic Analysis. Chemical Engineering Journal. 2020. https://doi.org/10.1016/j.cej.2020.125751.

[51] Wanten, B.; Maerivoet, S.; Vantomme, C.; Slaets, J.; Trenchev, G.; Bogaerts, A. Dry Reforming of Methane in an Atmospheric Pressure Glow Discharge: Confining the Plasma to Expand the Performance. Journal of CO_2 Utilization. 2022. https://doi.org/10.1016/j.jcou.2021.101869.

[52] Michielsen, I.; Uytdenhouwen, Y.; Pype, J.; Michielsen, B.; Mertens, J.; Reniers, F.; Meynen, V.; Bogaerts, A. CO_2 Dissociation in a Packed Bed DBD Reactor: First Steps towards a Better Understanding of Plasma Catalysis. Chemical Engineering Journal. 2017, pp 477–488. https://doi.org/10.1016/j.cej.2017.05.177.

[53] Wang, Y.; Chen, Y.; Harding, J.; He, H.; Bogaerts, A.; Tu, X. Catalyst-Free Single-Step Plasma Reforming of CH_4 and CO_2 to Higher Value Oxygenates under Ambient Conditions. Chem. Eng. J. 2022, 450, 137860.

[54] Zhou, D.; Zhang, Q.; Wang, S.; Jia, Y.; Liu, W.; Duan, H.; Sun, X. Hollow-Structured Layered Double Hydroxide: Structure Evolution Induced by Gradient Composition. Inorganic Chemistry. 2020, pp 1804–1809. https://doi.org/10.1021/acs.inorgchem.9b03005.

[55] Li, Y.; Gao, W.; Peng, M.; Zhang, J.; Sun, J.; Xu, Y.; Hong, S.; Liu, X.; Liu, X.; Wei, M.; Zhang, B.; Ma, D. Interfacial Fe_5C_2-Cu Catalysts toward Low-Pressure Syngas Conversion to Long-Chain Alcohols. Nature Communications. 2020. https://doi.org/10.1038/s41467-019-13691-4.

[56] Yu, H.; Wang, C.; Lin, T.; An, Y.; Wang, Y.; Chang, Q.; Yu, F.; Wei, Y.; Sun, F.; Jiang, Z.; Li, S.; Sun, Y.; Zhong, L. Direct Production of Olefins from Syngas with Ultrahigh Carbon Efficiency. Nat. Commun. 2022, 13, 5987. https://doi.org/10.1038/s41467-022-33715-w.

[57] Schiaroli, N.; Lucarelli, C.; Sanghez de Luna, G.; Fornasari, G.; Vaccari, A. Ni-Based Catalysts to Produce Synthesis Gas by Combined Reforming of Clean Biogas. Appl. Catal. A Gen. 2019, 582, 117087. https://doi.org/10.1016/j.apcata.2019.05.021.

[58] Niu, J.; Wang, Y.; Liland, S. E.; Regli, S. K.; Yang, J.; Rout, K. R.; Luo, J.; Rønning, M.; Ran, J.; Chen, D. Unraveling Enhanced Activity, Selectivity, and Coke Resistance of Pt-Ni Bimetallic Clusters in Dry Reforming. ACS Catal. 2021, 11 (4), 2398–2411. https://doi.org/10.1021/acscatal.0c04429.

[59] Lin, X.; Li, R.; Lu, M.; Chen, C.; Li, D.; Zhan, Y.; Jiang, L. Carbon Dioxide Reforming of Methane over Ni Catalysts Prepared from Ni-Mg-Al Layered Double Hydroxides: Influence of Ni Loadings. Fuel 2015, 162, 271–280. https://doi.org/10.1016/j.fuel.2015.09.021.

[60] Li, D.; Xu, S.; Song, K.; Chen, C.; Zhan, Y.; Jiang, L. Hydrotalcite-Derived Co/Mg(Al)O as a Stable and Coke-Resistant Catalyst for Low-Temperature Carbon Dioxide Reforming of Methane. Appl. Catal. A Gen. 2018, 552, 21–29. https://doi.org/10.1016/j.apcata.2017.12.022.

[61] Guo, Y.; Lu, J.; Liu, Q.; Bai, X.; Gao, L.; Tu, W.; Wang, Z. jun. Carbon Dioxide Reforming of Methane over Cobalt Catalysts Supported on Hydrotalcite and Metal Oxides. Catal. Commun. 2018, 116, 81–84. https://doi.org/10.1016/j.catcom.2018.08.017.

[62] Zhang, L.; Zhang, Q.; Liu, Y.; Zhang, Y. Dry Reforming of Methane over Ni/MgO-Al_2O_3 Catalysts Prepared by Two-Step Hydrothermal Method. Appl. Surf. Sci. 2016, 389, 25–33.

[63] Aider, N.; Touahra, F.; Bali, F.; Djebarri, B.; Lerari, D.; Bachari, K.; Halliche, D. Improvement of Catalytic Stability and Carbon Resistance in the Process of CO_2 Reforming of Methane by CoAl and CoFe Hydrotalcite-Derived Catalysts. Int. J. Hydrogen Energy 2018, 43 (17), 8256–8266. https://doi.org/10.1016/j.ijhydene.2018.03.118.

[64] Lin, X.; Li, R.; Lu, M.; Chen, C.; Li, D.; Zhan, Y.; Jiang, L. Carbon Dioxide Reforming of Methane over Ni Catalysts Prepared from Ni-Mg-Al Layered Double Hydroxides: Influence of Ni Loadings. Fuel 2015, 162, 271–280. https://doi.org/10.1016/j.fuel.2015.09.021.

[65] Zhan, Y.; Song, K.; Shi, Z.; Wan, C.; Pan, J.; Li, D.; Au, C.; Jiang, L. Influence of Reduction Temperature on Ni Particle Size and Catalytic Performance of Ni/Mg(Al)O Catalyst for CO_2 Reforming of CH_4. Int. J. Hydrogen Energy 2020, 45 (4), 2794–2807. https://doi.org/10.1016/j.ijhydene.2019.11.181.

[66] Kalai, D. Y.; Stangeland, K.; Jin, Y.; Yu, Z. Active and Stable Hydrotalcite Derived Ni Catalysts for CO_2 Reforming of Methane: Comparison with Catalysts by Incipient Wetness. J. CO_2 Util. 2018, 25, 346–355. https://doi.org/10.1016/j.jcou.2017.12.018.

[67] Jin, L.; Ma, B.; Zhao, S.; He, X.; Li, Y.; Hu, H.; Lei, Z. Ni/MgO–Al_2O_3 Catalyst Derived from Modified [Ni,Mg,Al]-LDH with NaOH for CO_2 Reforming of Methane. Int. J. Hydrogen Energy 2018, 43 (5), 2689–2698. https://doi.org/10.1016/j.ijhydene.2017.12.087.

[68] Xu, Y.; Du, X.; Shi, L.; Chen, T.; Wan, H.; Wang, P.; Wei, S.; Yao, B.; Zhu, J.; Song, M. Improved Performance of Ni/Al_2O_3 Catalyst Deriving from the Hydrotalcite Precursor Synthesized on Al_2O_3 Support for Dry Reforming of Methane. Int. J. Hydrogen Energy 2021, 46, 14301–14310.

[69] Rego de Vasconcelos, B.; Pham Minh, D.; Lyczko, N.; Phan, T. S.; Sharrock, P.; Nzihou, A. Upgrading Greenhouse Gases (Methane and Carbon Dioxide) into Syngas Using Nickel-Based Catalysts. Fuel 2018, 226, 195–203. https://doi.org/10.1016/j.fuel.2018.04.017.

[70] Nguyen-Phu, H.; Kim, T.; Kim, Y.; Kang, K. H.; Cho, H.; Kim, J.; Ro, I. Role of Phase in NiMgAl Mixed Oxide Catalysts for CO_2 Dry Methane Reforming (DRM). Catal. Today 2022. https://doi.org/10.1016/j.cattod.2022.08.036.

[71] Feng, X.; Feng, J.; Li, W. Insight into MgO Promoter with Low Concentration for the Carbon-Deposition Resistance of Ni-Based Catalysts in the CO_2 Reforming of CH_4. Chinese J. Catal. 2018, 39 (1), 88–98. https://doi.org/10.1016/S1872-2067(17)62928-0.

[72] Abbas, M.; Sikander, U.; Mehran, M. T.; Kim, S. H. Exceptional Stability of Hydrotalcite Derived Spinel Mg(Ni)Al_2O_4 Catalyst for Dry Reforming of Methane. Catal. Today 2022, 403, 74–85. https://doi.org/10.1016/j.cattod.2021.08.029.

[73] Huang, J.; Yan, Y.; Saqline, S.; Liu, W.; Liu, B. High Performance Ni Catalysts Prepared by Freeze Drying for Efficient Dry Reforming of Methane. Applied Catalysis B: Environmental. 2020. https://doi.org/10.1016/j.apcatb.2020.119109.

[74] Mu, Z.; Liu, X.; Shi, H.; Song, C.; Dang, C.; Gao, K.; Sun, N.; Tian, C.; Zheng, H.; Wang, X.; Xuan, Y. A Highly Efficient Solar-Driven CO_2

Reforming of Methane on Ni/MgAlOx-LDH Loaded Ni Foam Reactors with Heat Recovery: Experimental Measurements and Numerical Simulations. Chem. Eng. J. 2022, 446, 137437. https://doi.org/10.1016/j.cej.2022.137437.

[75] Bian, Z.; Deng, S.; Sun, Z.; Ge, T.; Jiang, B.; Zhong, W. Multi-Core@Shell Catalyst Derived from LDH@SiO_2 for Low- Temperature Dry Reforming of Methane. Renew. Energy 2022, 200, 1362–1370. https://doi.org/10.1016/j.renene.2022.10.046.

[76] Rosset, M.; Féris, L. A.; Perez-Lopez, O. W. Biogas Dry Reforming over Ni-M-Al (M = K, Na and Li) Layered Double Hydroxide-Derived Catalysts. Catal. Today 2021, 381, 96–107. https://doi.org/10.1016/j.cattod.2020.08.018.

[77] Song, D. H.; Jung, U. H.; Kim, Y. E.; Im, H. B.; Lee, T. H.; Lee, K. B.; Koo, K. Y. Influence of Supports on the Catalytic Activity and Coke Resistance of Ni Catalyst in Dry Reforming of Methane. Catalysts. 2022. https://doi.org/10.3390/catal12020216.

[78] Abdelsadek, Z.; Holgado, J. P.; Halliche, D.; Caballero, A.; Cherifi, O.; Gonzalez-Cortes, S.; Masset, P. J. Examination of the Deactivation Cycle of NiAl- and NiMgAl-Hydrotalcite Derived Catalysts in the Dry Reforming of Methane. Catalysis Letters. 2021, pp 2696–2715. https://doi.org/10.1007/s10562-020-03513-4.

[79] Chai, R.; Fan, S.; Zhang, Z.; Chen, P.; Zhao, G.; Liu, Y.; Lu, Y. Free-Standing NiO-MgO-Al_2O_3 Nanosheets Derived from Layered Double Hydroxides Grown onto FeCrAl-Fiber as Structured Catalysts for Dry Reforming of Methane. ACS Sustain. Chem. Eng. 2017, 5 (6), 4517–4522. https://doi.org/10.1021/acssuschemeng.7b00717.

[80] Wang, L.; Wang, F. Design Strategy, Synthesis, and Mechanism of Ni Catalysts for Methane Dry Reforming Reaction: Recent Advances and Future Perspectives. Energy and Fuels 2022, 36 (11), 5594–5621. https://doi.org/10.1021/acs.energyfuels.2c01007.

[81] Chatla, A.; Ghouri, M. M.; Wissam, O.; Hassan, E.; Mohamed, N.; Prakash, A. V; Elbashir, N. O. An Experimental and First Principles DFT Investigation on the Effect of Cu Addition to Ni/Al_2O_3 Catalyst for the Dry Reforming of Methane. Appl. Catal. A Gen. 2020, 602, 117699. https://doi.org/10.1016/j.apcata.2020.117699.

[82] Tang, L.; Huang, X.; Ran, J.; Guo, F.; Niu, J.; Qiu, H.; Ou, Z.; Yan, Y.; Yang, Z.; Qin, C. Density Functional Theory Studies on Direct and Oxygen Assisted Activation of C–H Bond for Dry Reforming of Methane over Rh–Ni Catalyst. Int. J. Hydrogen Energy 2022, 47 (71), 30391–30403. https://doi.org/10.1016/j.ijhydene.2022.07.002.

[83] Wu, Z.; Yang, B.; Miao, S.; Liu, W.; Xie, J.; Lee, S.; Pellin, M. J.; Xiao, D.; Su, D.; Ma, D. Lattice Strained Ni-Co Alloy as a High-Performance Catalyst

for Catalytic Dry Reforming of Methane. ACS Catal. 2019, 9 (4), 2693–2700. https://doi.org/10.1021/acscatal.8b02821.

[84] Tanios, C.; Bsaibes, S.; Gennequin, C.; Labaki, M.; Cazier, F.; Billet, S.; Tidahy, H. L.; Nsouli, B.; Aboukaïs, A.; Abi-Aad, E. Syngas Production by the CO_2 Reforming of CH_4 over Ni–Co–Mg–Al Catalysts Obtained from Hydrotalcite Precursors. Int. J. Hydrogen Energy 2017, 42 (17), 12818–12828. https://doi.org/10.1016/j.ijhydene.2017.01.120.

[85] Tanios, C.; Gennequin, C.; Labaki, M.; Tidahy, H. L.; Aboukaïs, A.; Abi-Aad, E. Evaluation of a Catalyst Durability in Absence and Presence of Toluene Impurity: Case of the Material $Co_2Ni_2Mg_2Al_2$ Mixed Oxide Prepared by Hydrotalcite Route in Methane Dry Reforming to Produce Energy. Materials (Basel). 2019, 12 (9), 1362. https://doi.org/10.3390/ma12091362.

[86] Duan, X.; Pan, J.; Yang, X.; Wan, C.; Lin, X.; Li, D.; Jiang, L. Nickel–cobalt Bimetallic Catalysts Prepared from Hydrotalcite-like Compounds for Dry Reforming of Methane. Int. J. Hydrogen Energy 2022, 47 (58), 24358–24373. https://doi.org/10.1016/j.ijhydene.2022.05.211.

[87] Kim, S. M.; Abdala, P. M.; Margossian, T.; Hosseini, D.; Foppa, L.; Armutlulu, A.; Van Beek, W.; Comas-Vives, A.; Copéret, C.; Müller, C. Cooperativity and Dynamics Increase the Performance of NiFe Dry Reforming Catalysts. J. Am. Chem. Soc. 2017, 139 (5), 1937–1949. https://doi.org/10.1021/jacs.6b11487.

[88] Wang, P.; Jin, L.; Hu, H. CO_2 Reforming of Methane over Fe-Modified Ni-Based Catalyst for Syngas Production. Energy Technol. 2020, 8, 1900231. https://doi.org/10.1002/ente.201900231.

[89] Wan, C.; Song, K.; Pan, J.; Huang, M.; Luo, R.; Li, D.; Jiang, L. Ni-Fe/Mg(Al)O Alloy Catalyst for Carbon Dioxide Reforming of Methane: Influence of Reduction Temperature and NieFe Alloying on Coking. Int. J. Hydrogen Energy 2020, 45, 33574–33585.

[90] Jin, F.; Fu, Y.; Kong, W.; Wang, J.; Cai, F.; Zhang, J.; Xu, J. Dry Reforming of Methane over Trimetallic NiFeCu Alloy Catalysts. Chem. Phys. Lett. 2020, 750, 137491. https://doi.org/10.1016/j.cplett.2020.137491.

[91] Song, K.; Lu, M.; Xu, S.; Chen, C.; Zhan, Y.; Li, D.; Au, C.; Jiang, L.; Tomishige, K. Effect of Alloy Composition on Catalytic Performance and Coke-Resistance Property of Ni-Cu/Mg(Al)O Catalysts for Dry Reforming of Methane. Appl. Catal. B Environ. 2018, 239, 324–333. https://doi.org/10.1016/j.apcatb.2018.08.023.

[92] Xiao, Z.; Hou, F.; Zhang, J.; Zheng, Q.; Xu, J.; Pan, L.; Wang, L.; Zou, J.; Zhang, X.; Li, G. Methane Dry Reforming by Ni-Cu Nanoalloys Anchored on Periclase-Phase MgAlOx Nanosheets for Enhanced Syngas Production. ACS Appl. Mater. Interfaces 2021, 13 (41), 48838–48854. https://doi.org/10.1021/acsami.1c14918.

[93] Rosset, M.; Féris, L. A.; Perez-Lopez, O. W. Biogas Dry Reforming Using Ni–Al-LDH Catalysts Reconstructed with Mg and Zn. Int. J. Hydrogen Energy 2021, 46 (39), 20359–20376. https://doi.org/10.1016/j.ijhydene.2021.03.150.

[94] Chatla, A.; Abu-Rub, F.; Prakash, A. V.; Ibrahim, G.; Elbashir, N. O. Highly Stable and Coke-Resistant Zn-Modified Ni-Mg-Al Hydrotalcite Derived Catalyst for Dry Reforming of Methane: Synergistic Effect of Ni and Zn. Fuel. 2022. https://doi.org/10.1016/j.fuel.2021.122042.

[95] Hallassi, M.; Benrabaa, R.; Cherif, N. F.; Lerari, D.; Chebout, R.; Bachari, K.; Rubbens, A.; Roussel, P.; Vannier, R. N.; Trentesaux, M.; Löfberg, A. Characterization and Syngas Production at Low Temperature via Dry Reforming of Methane over Ni-M (M = Fe, Cr) Catalysts Tailored from LDH Structure. Catalysts 2022, 12, 1507. https://doi.org/10.3390/catal12121507.

[96] Theofanidis, S. A.; Galvita, V. V.; Poelman, H.; Marin, G. B. Enhanced Carbon-Resistant Dry Reforming Fe-Ni Catalyst: Role of Fe. ACS Catal. 2015, 5 (5), 3028–3039. https://doi.org/10.1021/acscatal.5b00357.

[97] Świrk, K.; Gálvez, M. E.; Motak, M.; Grzybek, T.; Rønning, M.; Da Costa, P. Yttrium Promoted Ni-Based Double-Layered Hydroxides for Dry Methane Reforming. J. CO_2 Util. 2018, 27, 247–258. https://doi.org/10.1016/j.jcou.2018.08.004.

[98] Świrk, K.; Motak, M.; Grzybek, T.; Rønning, M.; Da Costa, P. Effect of Low Loading of Yttrium on Ni-Based Layered Double Hydroxides in CO_2 Reforming of CH_4. React. Kinet. Mech. Catal. 2019, 126 (2), 611–628. https://doi.org/10.1007/s11144-018-1515-9.

[99] Świrk, K.; Zhang, H.; Li, S.; Chen, Y.; Rønning, M.; Motak, M.; Grzybek, T.; Da Costa, P. Carbon-Resistant NiO-Y_2O_3-Nanostructured Catalysts Derived from Double-Layered Hydroxides for Dry Reforming of Methane. Catal. Today 2021, 366, 103–113. https://doi.org/10.1016/j.cattod.2020.03.032.

[100] Dębek, R.; Motak, M.; Galvez, M. E.; Grzybek, T.; Da Costa, P. Promotion Effect of Zirconia on Mg(Ni,Al)O Mixed Oxides Derived from Hydrotalcites in CO_2 Methane Reforming. Applied Catalysis B: Environmental. 2018, pp 36–46. https://doi.org/10.1016/j.apcatb.2017.06.024.

[101] Swirk, K.; Galvez, M. E.; Motak, M.; Grzybek, T.; Ronning, M.; Costa, P. Da. Dry Reforming of Methane over Zr- and Y-Modified Ni/Mg/Al Double-Layered Hydroxides. Catal. Commun. 2018, 117, 26–32.

[102] Tathod, A. P.; Hayek, N.; Shpasser, D.; Simakov, D. S. A.; Gazit, O. M. Mediating Interaction Strength between Nickel and Zirconia Using a Mixed Oxide Nanosheets Interlayer for Methane Dry Reforming. Appl. Catal. B Environ. 2019, 249, 106–115. https://doi.org/10.1016/j.apcatb.2019.02.040.

[103] Huang, Y.; Li, X.; Zhang, Q.; Vinokurov, V. A.; Huang, W. Enhanced Carbon Tolerance of Hydrotalcite-Derived Ni-Ir/Mg(Al)O Catalysts in Dry Reforming of Methane under Elevated Pressures. Fuel Process. Technol. 2022, 237, 107446. https://doi.org/10.1016/j.fuproc.2022.107446.

[104] Lu, Y.; Kang, L.; Guo, D.; Zhao, Y.; Zhao, Y.; Wang, S.; Ma, X. Double-Site Doping of a v Promoter on Nix-V-MgAl Catalysts for the DRM Reaction: Simultaneous Effect on $CH_4$and CO_2Activation. ACS Catal. 2021, 11 (14), 8749–8765. https://doi.org/10.1021/acscatal.1c01299.

[105] Dang, C.; Luo, J.; Yang, W.; Li, H.; Cai, W. Low-Temperature Catalytic Dry Reforming of Methane over Pd Promoted Ni–CaO–$Ca_{12}Al_{14}O_{33}$ Multifunctional Catalyst. Ind. Eng. Chem. Res. 2021, 60 (50), 18361–18372. https://doi.org/10.1021/acs.iecr.1c04010.

[106] Calgaro, C. O.; Perez-Lopez, O. W. Biogas Dry Reforming for Hydrogen Production over Ni-M-Al Catalysts (M = Mg, Li, Ca, La, Cu, Co, Zn). International Journal of Hydrogen Energy. 2019, pp 17750–17766. https://doi.org/10.1016/j.ijhydene.2019.05.113.

[107] Ha, Q. L. M.; Armbruster, U.; Kreyenschulte, C.; Atia, H.; Lund, H.; Vuong, H. T.; Wohlrab, S. Stabilization of Low Nickel Content Catalysts with Lanthanum and by Citric Acid Assisted Preparation to Suppress Deactivation in Dry Reforming of Methane. Catal. Today 2019, 334, 203–214. https://doi.org/10.1016/j.cattod.2018.11.021.

[108] Ha, Q. L. M.; Lund, H.; Kreyenschulte, C.; Bartling, S.; Atia, H.; Vuong, T. H.; Wohlrab, S.; Armbruster, U. Development of Highly Stable Low Ni Content Catalyst for Dry Reforming of CH_4-Rich Feedstocks. ChemCatChem 2020, 12 (6), 1562–1568. https://doi.org/10.1002/cctc.201902066.

[109] Montini, T.; Melchionna, M.; Monai, M.; Fornasiero, P. Fundamentals and Catalytic Applications of CeO_2-Based Materials. Chem. Rev. 2016, 116 (10), 5987–6041. https://doi.org/10.1021/acs.chemrev.5b00603.

[110] Chang, K.; Zhang, H.; Cheng, M. J.; Lu, Q. Application of Ceria in CO_2 Conversion Catalysis. ACS Catal. 2020, 10 (1), 613–631. https://doi.org/10.1021/acscatal.9b03935.

[111] Rosli, S. N. A.; Abidin, S. Z.; Osazuwa, O. U.; Fan, X.; Jiao, Y. The Effect of Oxygen Mobility/Vacancy on Carbon Gasification in Nano Catalytic Dry Reforming of Methane: A Review. Journal of CO_2 Utilization. 2022. https://doi.org/10.1016/j.jcou.2022.102109.

[112] Laosiripojana, N.; Assabumrungrat, S. Catalytic Dry Reforming of Methane over High Surface Area Ceria. Appl. Catal. B Environ. 2005, 60 (1–2), 107–116. https://doi.org/10.1016/j.apcatb.2005.03.001.

[113] Lino, A. V. P.; Assaf, E. M.; Assaf, J. M. Hydrotalcites Derived Catalysts for Syngas Production from Biogas Reforming: Effect of Nickel and Cerium Load. Catal. Today 2017, 289, 78–88. https://doi.org/10.1016/j.cattod.2016.08.022.

[114] Niu, J.; Liland, S. E.; Yang, J.; Rout, K. R.; Ran, J.; Chen, D. Effect of Oxide Additives on the Hydrotalcite Derived Ni Catalysts for CO_2 Reforming of Methane. Chem. Eng. J. 2019, 377, 119763. https://doi.org/10.1016/j.cej.2018.08.149.

[115] Ojeda-Niño, O. H.; Gracia, F.; Daza, C. Role of Pr on Ni-Mg-Al Mixed Oxides Synthesized by Microwave-Assisted Self-Combustion for Dry Reforming of Methane. Ind. Eng. Chem. Res. 2019, 58 (19), 7909–7921. https://doi.org/10.1021/acs.iecr.9b00557.

[116] Ojeda-Niño, O. H.; Gallego, J.; Daza, C. E. Pr-Promoted Ni Exsolution from Ni–Mg–Al (O) as Catalysts for Syngas Production by Dry Reforming of Methane. Results Eng. 2023, 17, 100821. https://doi.org/10.1016/j.rineng.2022.100821.

[117] Ha, Q. L. M.; Atia, H.; Kreyenschulte, C.; Lund, H.; Bartling, S.; Lisak, G.; Wohlrab, S.; Armbruster, U. Effects of Modifier (Gd, Sc, La) Addition on the Stability of Low Ni Content Catalyst for Dry Reforming of Model Biogas. Fuel 2022, 312, 122823. https://doi.org/10.1016/j.fuel.2021.122823.

[118] Yuan, X.; Li, B.; Wang, X.; Li, B. Synthesis Gas Production by Dry Reforming of Methane over Neodymium-Modified Hydrotalcite-Derived Nickel Catalysts. Fuel Process. Technol. 2022, 227, 107104. https://doi.org/10.1016/j.fuproc.2021.107104.

[119] Taherian, Z.; Shahed Gharahshiran, V.; Khataee, A.; Orooji, Y. Anti-Coking Freeze-Dried NiMgAl Catalysts for Dry and Steam Reforming of Methane. J. Ind. Eng. Chem. 2021, 103, 187–194. https://doi.org/10.1016/j.jiec.2021.07.032.

[120] Liu, H.; Wierzbicki, D.; Debek, R.; Motak, M.; Grzybek, T.; Da Costa, P.; Gálvez, M. E. La-Promoted Ni-Hydrotalcite-Derived Catalysts for Dry Reforming of Methane at Low Temperatures. Fuel 2016, 182, 8–16. https://doi.org/10.1016/j.fuel.2016.05.073.

[121] Dahdah, E.; Abou Rached, J.; Aouad, S.; Gennequin, C.; Tidahy, H. L.; Estephane, J.; Aboukaïs, A.; Abi Aad, E. CO_2 Reforming of Methane over $Ni_xMg_{6-x}Al_2$ Catalysts: Effect of Lanthanum Doping on Catalytic Activity and Stability. Int. J. Hydrogen Energy 2017, 42 (17), 12808–12817. https://doi.org/10.1016/j.ijhydene.2017.01.197.

[122] Kalai, D. Y.; Stangeland, K.; Jin, Y.; Tucho, W. M.; Yu, Z. Biogas Dry Reforming for Syngas Production on La Promoted Hydrotalcite-Derived Ni Catalysts. Int. J. Hydrogen Energy 2018, 43 (42), 19438–19450. https://doi.org/10.1016/j.ijhydene.2018.08.181.

[123] Kim, K. Y.; Lee, J. H.; Lee, H.; Noh, W. Y.; Kim, E. H.; Ra, E. C.; Kim, S. K.; An, K.; Lee, J. S. Layered Double Hydroxide-Derived Intermetallic $Ni_3GaC_{0.25}$ Catalysts for Dry Reforming of Methane. ACS Catal. 2021, 11, 11091–11102.

[124] Zeng, F.; Wei, B.; Lan, D.; Ge, J. Highly Dispersed NixGay Catalyst and La2O3Promoter Supported by LDO Nanosheets for Dry Reforming of

Methane: Synergetic Catalysis by Ni, Ga, and La_2O_3. Langmuir 2021, 37 (32), 9744–9754. https://doi.org/10.1021/acs.langmuir.1c01162.

[125] Dębek, R.; Motak, M.; Galvez, M. E.; Grzybek, T.; Da Costa, P. Influence of Ce/Zr Molar Ratio on Catalytic Performance of Hydrotalcite-Derived Catalysts at Low Temperature CO_2 Methane Reforming. Int. J. Hydrogen Energy 2017, 42 (37), 23556–23567. https://doi.org/10.1016/j.ijhydene.2016.12.121.

[126] Świrk, K.; Rønning, M.; Motak, M.; Beaunier, P.; Da Costa, P.; Grzybek, T. Ce-and Y-Modified Double-Layered Hydroxides as Catalysts for Dry Reforming of Methane: On the Effect of Yttrium Promotion. Catalysts. 2019. https://doi.org/10.3390/catal9010056.

[127] Świrk, K.; Rønning, M.; Motak, M.; Grzybek, T.; Da Costa, P. Synthesis Strategies of Zr- and Y-Promoted Mixed Oxides Derived from Double-Layered Hydroxides for Syngas Production via Dry Reforming of Methane. International Journal of Hydrogen Energy. 2021, pp 12128–12144. https://doi.org/10.1016/j.ijhydene.2020.04.239.

[128] Li, X.; Huang, Y.; Zhang, Q.; Luan, C.; Vinokurov, V. A.; Huang, W. Highly Stable and Anti-Coking Ni/MoCeZr/$MgAl_2O_4$-MgO Complex Support Catalysts for CO_2 Reforming of CH_4: Effect of the Calcination Temperature. Energy Convers. Manag. 2019, 179, 166–177. https://doi.org/10.1016/j.enconman.2018.10.067.

[129] Li, X.; Huang, Y.; Zhang, Q.; Zuo, Z.; Wang, X.; Vinokurov, V. A.; Wang, Z.; Huang, W. Hexamethylenetetramine-Assisted Hydrothermal Synthesis of Efficient and Stable Ni-MoCeZr-MgAl(O) Catalysts for Dry Reforming of CH_4: Effect of Ni Content. Fuel 2019, 254, 115562. https://doi.org/10.1016/j.fuel.2019.05.145.

[130] Wang, Y.; Wang, N.; Harding, J.; Chen, G.; Tu, X. Plasma Technology for Syngas Production; Elsevier Inc., 2023. https://doi.org/10.1016/B978-0-323-91871-8.00014-3.

[131] Neyts, E. C.; Ostrikov, K. (Ken); Sunkara, M. K.; Bogaerts, A. Plasma Catalysis: Synergistic Effects at the Nanoscale. Chem. Rev. 2015, 115, 13408–13446.

[132] Gao, X.; Lin, Z.; Li, T.; Huang, L.; Zhang, J.; Askari, S.; Dewangan, N.; Jangam, A.; Kawi, S. Recent Developments in Dielectric Barrier Discharge Plasma-Assisted Catalytic Dry Reforming of Methane over Ni-Based Catalysts. Catalysts 2021, 11 (4). https://doi.org/10.3390/catal11040455.

[133] Ye, Z.; Zhao, L.; Nikiforov, A.; Giraudon, J. M.; Chen, Y.; Wang, J.; Tu, X. A Review of the Advances in Catalyst Modification Using Nonthermal Plasma: Process, Mechanism and Applications. Adv. Colloid Interface Sci. 2022, 308 (August), 102755. https://doi.org/10.1016/j.cis.2022.102755.

[134] Di, L.; Zhang, J.; Zhang, X. A Review on the Recent Progress, Challenges, and Perspectives of Atmospheric-Pressure Cold Plasma for Preparation of

Supported Metal Catalysts. Plasma Processes and Polymers. 2018. https://doi.org/10.1002/ppap.201700234.

[135] Wang, Z.; Zhang, Y.; Neyts, E. C. .; Cao, X.; Zhang, X.; Jang, B. W.-L. .; Liu, C. Catalyst Preparation with Plasmas: How Does It Work? ACS Catal. 2018, 8 (3), 2093–2110.

[136] Xu, J.; Xia, P.; Zhang, Q.; Guo, F.; Xia, Y.; Tian, H. Coke Resistance of Ni-Based Catalysts Enhanced by Cold Plasma Treatment for CH_4–CO_2 Reforming: Review. Int. J. Hydrogen Energy 2021, 46 (45), 23174–23189. https://doi.org/10.1016/j.ijhydene.2021.03.245.

[137] Di, L.; Zhang, J.; Zhang, X.; Wang, H.; Li, H.; Li, Y.; Bu, D. Cold Plasma Treatment of Catalytic Materials: A Review. J. Phys. D. Appl. Phys. 2021, 54 (33). https://doi.org/10.1088/1361-6463/ac0269.

[138] Khoja, A. H.; Mazhar, A.; Saleem, F.; Mehran, M. T.; Naqvi, S. R.; Anwar, M.; Shakir, S.; Saidina Amin, N. A.; Sajid, M. B. Recent Developments in Catalyst Synthesis Using DBD Plasma for Reforming Applications. Int. J. Hydrogen Energy 2021, 46 (29), 15367–15388. https://doi.org/10.1016/j.ijhydene.2021.02.043.

[139] Uytdenhouwen, Y.; Bal, K. M.; Michielsen, I.; Neyts, E. C.; Meynen, V.; Cool, P.; Bogaerts, A. How Process Parameters and Packing Materials Tune Chemical Equilibrium and Kinetics in Plasma-Based CO_2 Conversion. Chem. Eng. J. 2019, 372, 1253–1264. https://doi.org/10.1016/j.cej.2019.05.008.

[140] Tu, X.; Whitehead, J. C. Plasma-Catalytic Dry Reforming of Methane in an Atmospheric Dielectric Barrier Discharge: Understanding the Synergistic Effect at Low Temperature. Appl. Catal. B Environ. 2012, 125, 439–448. https://doi.org/10.1016/j.apcatb.2012.06.006.

[141] Wang, X.; Gao, Y.; Zhang, S.; Sun, H.; Li, J.; Shao, T. Nanosecond Pulsed Plasma Assisted Dry Reforming of CH_4: The Effect of Plasma Operating Parameters. Appl. Energy 2019, 243 (March), 132–144. https://doi.org/10.1016/j.apenergy.2019.03.193.

[142] Uytdenhouwen, Y.; Bal, K. M.; Neyts, E. C.; Meynen, V.; Cool, P.; Bogaerts, A. On the Kinetics and Equilibria of Plasma-Based Dry Reforming of Methane. Chem. Eng. J. 2021, 405 (August 2020), 126630. https://doi.org/10.1016/j.cej.2020.126630.

[143] Mei, D.; Zhang, P.; Duan, G.; Liu, S.; Zhou, Y.; Fang, Z.; Tu, X. CH_4 Reforming with CO_2 Using a Nanosecond Pulsed Dielectric Barrier Discharge Plasma. J. CO_2 Util. 2022, 62 (May), 102073. https://doi.org/10.1016/j.jcou.2022.102073.

[144] Mei, D.; Duan, G.; Fu, J.; Liu, S.; Zhou, R.; Zhou, R.; Fang, Z.; Cullen, P. J.; Ostrikov, K. (Ken). CO_2 Reforming of CH_4 in Single and Double Dielectric Barrier Discharge Reactors: Comparison of Discharge Characteristics and Product Distribution. J. CO_2 Util. 2021, 53 (July), 101703. https://doi.org/10.1016/j.jcou.2021.101703.

[145] Uytdenhouwen, Y.; Hereijgers, J.; Breugelmans, T.; Cool, P.; Bogaerts, A. How Gas Flow Design Can Influence the Performance of a DBD Plasma Reactor for Dry Reforming of Methane. Chemical Engineering Journal. 2021. https://doi.org/10.1016/j.cej.2020.126618.

[146] Chen, X.; Kim, H. H.; Nozaki, T. Plasma Catalytic Technology for CH_4 and CO_2 Conversion: A Review Highlighting Fluidized-Bed Plasma Reactor. Plasma Process. Polym. 2023. https://doi.org/10.1002/ppap.202200207.

[147] Tu, X.; Gallon, H. J.; Twigg, M. V.; Gorry, P. A.; Whitehead, J. C. Dry Reforming of Methane over a Ni/Al_2O_3 Catalyst in a Coaxial Dielectric Barrier Discharge Reactor. J. Phys. D. Appl. Phys. 2011, 44 (27), 274007. https://doi.org/10.1088/0022-3727/44/27/274007.

[148] Sun, J.; Chen, Q.; Guo, Y.; Zhou, Z.; Song, Y. Quantitative Behavior of Vibrational Excitation in AC Plasma Assisted Dry Reforming of Methane. J. Energy Chem. 2020, 46, 133–143. https://doi.org/10.1016/j.jechem.2019.11.002.

[149] Usman, M.; Daud, W. M. A. W.; Abbas, H. F. Dry Reforming of Methane: Influence of Process Parameters-A Review. Renew. Sustain. Energy Rev. 2015, 45, 710–744.

[150] Snoeckx, R.; Bogaerts, A. Plasma Technology – a Novel Solution for CO_2 Conversion? Chem. Soc. Rev. 2017, 46, 5805.

[151] Khoja, A. H.; Tahir, M.; Amin, N. A. S. Recent Developments in Non-Thermal Catalytic DBD Plasma Reactor for Dry Reforming of Methane. Energy Convers. Manag. 2019, 183 (September 2018), 529–560. https://doi.org/10.1016/j.enconman.2018.12.112.

[152] Chen, S.; Wang, H.; Dong, F. Activation and Characterization of Environmental Catalysts in Plasma-Catalysis: Status and Challenges. Journal of Hazardous Materials. 2022, p 128150. https://doi.org/10.1016/j.jhazmat.2021.128150.

[153] Loenders, B.; Michiels, R.; Bogaerts, A. Is a Catalyst Always Beneficial in Plasma Catalysis? Insights from the Many Physical and Chemical Interactions. J. Energy Chem. 2023, 85, 501–533. https://doi.org/10.1016/j.jechem.2023.06.016.

[154] Rutberg, P. G.; Nakonechny, G. V.; Pavlov, A. V.; Popov, S. D.; Serba, E. O.; Surov, A. V. AC Plasma Torch with a $H2O/CO_2/CH_4$ Mix as the Working Gas for Methane Reforming. J. Phys. D. Appl. Phys. 2015, 48 (24). https://doi.org/10.1088/0022-3727/48/24/245204.

[155] Trenchev, G.; Kolev, S.; Bogaerts, A. A 3D Model of a Reverse Vortex FLow Gliding Arc Reactor. Plasma Sources Sci. Technol 2016, 25, 035014.

[156] Trenchev, G.; Kolev, S.; Wang, W.; Ramakers, M.; Bogaerts, A. CO_2 Conversion in a Gliding Arc Plasmatron: Multidimensional Modeling for Improved Efficiency. J. Phys. Chem. C 2017, 121 (39), 24470–24479. https://doi.org/10.1021/acs.jpcc.7b08511.

[157] Ramakers, M.; Trenchev, G.; Heijkers, S.; Wang, W.; Bogaerts, A. Gliding Arc Plasmatron: Providing an Alternative Method for Carbon Dioxide Conversion. ChemSusChem 2017, 10, 2642–2652. https://doi.org/doi.org/10.1002/cssc.201700589.

[158] Cleiren, E.; Heijkers, S.; Ramakers, M.; Bogaerts, A. Dry Reforming of Methane in a Gliding Arc Plasmatron To a Better Understanding of the Plasma Chemistry. ChemSusChem 2017, 10, 4025–4036.

[159] Tan, Z.; Ai, P. CO_2 Reforming of Biogas to Obtain Synthesis Gas Using Non-Thermal Plasma. J. Energy Inst. 2017, 90 (6), 864–874. https://doi.org/10.1016/j.joei.2016.08.008.

[160] Xia, Y.; Lu, N.; Wang, B.; Li, J.; Shang, K.; Jiang, N.; Wu, Y. Dry Reforming of CO_2–CH_4 Assisted by High-Frequency AC Gliding Arc Discharge: Electrical Characteristics and the Effects of Different Parameters. Int. J. Hydrogen Energy 2017, 42 (36), 22776–22785. https://doi.org/10.1016/j.ijhydene.2017.07.104.

[161] Pornmai, K.; Suvachitanont, S.; Chavadej, S. Reforming of CO_2-Containing Natural Gas with Steam in AC Gliding Arc Discharge for Hydrogen Production. Int. J. Green Energy 2018, 15 (7), 441–453. https://doi.org/10.1080/15435075.2018.1475285.

[162] Liu, M.; Liu, Y.; Lu, N.; Wang, S.; Sun, G. Effect of Flow Rate on the Characteristics of Atmospheric-Pressure AC Constant-Current Powered Gliding Arc Discharge. IEEE Trans. Plasma Sci. 2021, 49 (10), 3113–3120. https://doi.org/10.1109/TPS.2021.3107456.

[163] Rabinovich, A.; Nirenberg, G.; Kocagoz, S.; Surace, M.; Sales, C.; Fridman, A. Scaling Up of Non-Thermal Gliding Arc Plasma Systems for Industrial Applications. Plasma Chem. Plasma Process. 2022, 42 (1), 35–50. https://doi.org/10.1007/s11090-021-10203-5.

[164] Ramakers, M.; Trenchev, G.; Heijkers, S.; Wang, W.; Bogaerts, A. Gliding Arc Plasmatron: Providing an Alternative Method for Carbon Dioxide Conversion. ChemSusChem 2017, 10, 2642–2652. https://doi.org/doi.org/10.1002/cssc.201700589.

[165] Slaets, J.; Aghaei, M.; Ceulemans, S.; Van Alphen, S.; Bogaerts, A. CO_2 and CH_4 Conversion in “Real” Gas Mixtures in a Gliding Arc Plasmatron: How Do N_2 and O_2 Affect the Performance? Green Chem. 2020, 22 (4), 1366–1377. https://doi.org/10.1039/c9gc03743h.

[166] You, T.; Wang, C.; Yang, C.; Wang, F.; Xia, W. Experimental Study of the Discharge Characteristics of a 3D Vortex Gliding Arc Plasmatron. Contrib. to Plasma Phys. 2022, No. July, 1–13. https://doi.org/10.1002/ctpp.202200120.

[167] Van Alphen, S.; Slaets, J.; Ceulemans, S.; Aghaei, M.; Snyders, R.; Bogaerts, A. Effect of N_2 on CO_2-CH_4 Conversion in a Gliding Arc Plasmatron: Can This Major Component in Industrial Emissions Improve the Energy

Efficiency? J. CO_2 Util. 2021, 54, 101767. https://doi.org/10.1016/j.jcou.2021.101767.

[168] Martin-del-Campo, J.; Coulombe, S.; Kopyscinski, J. Influence of Operating Parameters on Plasma-Assisted Dry Reforming of Methane in a Rotating Gliding Arc Reactor. Plasma Chem. Plasma Process. 2020, 40 (4), 857–881. https://doi.org/10.1007/s11090-020-10074-2.

[169] Lu, N.; Sun, D.; Xia, Y.; Shang, K.; Wang, B.; Jiang, N.; Li, J.; Wu, Y. Dry Reforming of CH_4–CO_2 in AC Rotating Gliding Arc Discharge: Effect of Electrode Structure and Gas Parameters. Int. J. Hydrogen Energy 2018, 43 (29), 13098–13109. https://doi.org/10.1016/j.ijhydene.2018.05.053.

[170] Dinh, D. K.; Choi, S.; Lee, D. H.; Jo, S.; Kim, K. T.; Song, Y. H. Energy Efficient Dry Reforming Process Using Low Temperature Arcs. Plasma Process. Polym. 2018, 15 (5). https://doi.org/10.1002/ppap.201700203.

[171] Trenchev, G.; Bogaerts, A. Dual-Vortex Plasmatron: A Novel Plasma Source for CO_2conversion. J. CO_2 Util. 2020, 39 (March), 101152. https://doi.org/10.1016/j.jcou.2020.03.002.

[172] Cunha, A. G.; Ribeiro, R. P.; Ribeiro, V. A.; Zucolotto, C. G.; Cevolani, M. B.; Schettino, M. A.; Khalifa, E. A.; Marchiori, E.; Labanca, A. R.; Emmerich, F. G. Increased Arc Length and Stability in a Magnetic Gliding Arc Discharge Using a Cylindrical Notched Cathode. Plasma Sources Sci. Technol. 2020, 29 (5). https://doi.org/10.1088/1361-6595/ab876f.

[173] Li, L. L.; Zhang, H.; Li, X.; Huang, J.; Kong, X.; Xu, R.; Tu, X. Magnetically Enhanced Gliding Arc Discharge for CO_2 Activation. J. CO_2 Util. 2020, 35 (May), 28–37. https://doi.org/10.1016/j.jcou.2019.08.021.

[174] Ivanov, V.; Paunska, T.; Lazarova, S.; Bogaerts, A.; Kolev, S. Gliding Arc/Glow Discharge for CO_2conversion: Comparing the Performance of Different Discharge Configurations. J. CO_2 Util. 2023, 67 (August 2022), 102300. https://doi.org/10.1016/j.jcou.2022.102300.

[175] Rahmati, H.; Ghorbanzadeh, A. Parallel Electrodes Gliding Plasma: Working Principles and Application in Dry Reforming of Methane. Energy 2021, 230, 120753. https://doi.org/10.1016/j.energy.2021.120753.

[176] Dou, L.; Liu, Y.; Gao, Y.; Li, J.; Hu, X.; Zhang, S.; Ostrikov, K. (Ken); Shao, T. Disentangling Metallic Cobalt Sites and Oxygen Vacancy Effects in Synergistic Plasma-Catalytic CO_2/CH_4 Conversion into Oxygenates. Appl. Catal. B Environ. 2022, 318 (July), 121830. https://doi.org/10.1016/j.apcatb.2022.121830.

[177] Li, J.; Dou, L.; Gao, Y.; Hei, X.; Yu, F.; Shao, T. Revealing the Active Sites of the Structured Ni-Based Catalysts for One-Step CO_2/CH_4 Conversion into Oxygenates by Plasma-Catalysis. J. CO_2 Util. 2021, 52 (May), 101675. https://doi.org/10.1016/j.jcou.2021.101675.

[178] Wang, H.; Yang, Y.; Li, Z.; Kong, X.; Martin, P.; Cui, G.; Wang, R. Plasma-Assisted Ni Catalysts: Toward Highly-Efficient Dry Reforming of Methane

at Low Temperature. Int. J. Hydrogen Energy 2023, 48, 8921–8931. https://doi.org/10.1016/j.ijhydene.2022.11.287.

[179] Tao, X.; Yang, C.; Huang, L.; Xu, D. DBD Plasma Combined with Catalysts Derived from NiMgAlCe Hydrotalcite for CO_2 Reforming of CH_4. Mater. Chemsitry Phys. 2020, 250, 123118.

[180] Diao, J. F.; Zhang, T.; Xu, Z. N.; Guo, G. C. The Atomic-Level Adjacent NiFe Bimetallic Catalyst Significantly Improves the Activity and Stability for Plasma-Involved Dry Reforming Reaction of CH_4 and CO_2. Chem. Eng. J. 2023, 467 (February), 143271. https://doi.org/10.1016/j.cej.2023.143271.

[181] Zhang, T.; Liu, Z.; Zhu, Y. A.; Liu, Z.; Sui, Z.; Zhu, K.; Zhou, X. Dry Reforming of Methane on Ni-Fe-MgO Catalysts: Influence of Fe on Carbon-Resistant Property and Kinetics. Appl. Catal. B Environ. 2020, 264 (November 2019), 118497. https://doi.org/10.1016/j.apcatb.2019.118497.

[182] Trinh, Q. H.; Dinh, D. K.; Lee, D. H.; Nguyen, D. B.; Mok, Y. S.; Lee, W. G. Combination of Atmospheric Pressure Plasma with Catalysts for Dry Reforming of Methane to Value-Added Chemicals, First Edit.; Elsevier Ltd., 2022. https://doi.org/10.1016/B978-0-323-85586-0.00009-3.

[183] Shi, C.; Wang, S.; Ge, X.; Deng, S.; Chen, B.; Shen, J. A Review of Different Catalytic Systems for Dry Reforming of Methane: Conventional Catalysis-Alone and Plasma-Catalytic System. J. CO_2 Util. 2021, 46 (January), 101462. https://doi.org/10.1016/j.jcou.2021.101462.

[184] Liu, J. L.; Li, Z.; Liu, J. H.; Li, K.; Lian, H. Y.; Li, X. S.; Zhu, X.; Zhu, A. M. Warm-Plasma Catalytic Reduction of CO_2 with CH_4. Catal. Today 2019, 330 (December 2017), 54–60. https://doi.org/10.1016/j.cattod.2018.05.046.

CHAPTER 2

Can high temperature calcined Mg-Al layered double hydroxides (LDHs) fully rehydrate at room temperature in vapour or liquid condition?

This chapter is published as “Can high temperature calcined Mg–Al layered double hydroxides (LDHs) fully rehydrate at room temperature in vapour or liquid condition?; Wencong Xu, Myrjam Mertens, Thomas Kenis, Elien Derveaux, Peter Adriaensens, and Vera Meynen Mater. Chem. Phys. 2023, 295, 127113”.

Abstract

The rehydration behaviour of metal oxides (LDOs) derived from calcination of Mg-Al layered double hydroxides (LDHs) at high temperatures of 600-900 °C was studied in the presence of deionized water under vapour or liquid conditions. XRD reflections showed that the LDO metal oxides obtained from thermally treated LDHs can rehydrate into LDHs at room temperature even after calcination as high as 900 °C, both in vapour and liquid conditions, although faster in the latter. Only when the calcination temperature was increased to 900 °C, an additional spinel phase appeared, which remained in the particles under both vapour and liquid rehydration conditions. This is proven by ^{27}Al MAS NMR showing the presence of a peak representing tetrahedral Al. Differences between the as-synthesized LDHs and rehydrated LDOs were observed via additional analysis with FT-IR, SEM and nitrogen sorption. This illustrated that the process of the rehydration of the LDO into the LDH resulted in a new LDH rather than reconstructing it into the former LDH. Based on the results, it is suggested that even after high temperature calcination (600-900 °C), samples need to be stored carefully to avoid rehydration reactions to altered LDH materials, occurring at room temperature under an ambient, moist-containing atmosphere.

2.1 Introduction

Layered double hydroxides (LDHs), a group of well-known materials with hydrotalcite structure, have been attracting attention because of their applications in various fields, such as adsorbents, anion exchangers and controlled release, separation and membrane technology, catalysts and catalyst supports [1–5]. LDHs can be synthesized by various methods including hydrothermal synthesis, so-gel synthesis, co-precipitation and urea hydrolysis methods [6–11]. Some of these methods, such as co-precipitation and urea hydrolysis, are straightforward, which gives an advantage for industrial-scale-up [12]. Generally, LDHs have at least one divalent and one trivalent cation. They can be expressed by the general formula $[M^{II}_{1-x}M^{III}_{x}(OH)_2]^{x+}(A^{n-})_{x/n}\cdot mH_2O$, where the most typical divalent metal cation (M^{II}) is Mg^{2+} and Al^{3+} the most common trivalent metal cation (M^{III}). The value of x represents the molar ratio of $M^{III}/(M^{II} + M^{III})$ [12,13] and A^{n-} is an anion such as CO_3^{2-}, NO_3^-, or Cl^- that resides in the interlayers [14].

When LDHs are calcined, the layered structure is destroyed due to the progressive loss of physically adsorbed water molecules, dehydration of interlaminar water molecules, dehydroxylation and loss of anions in the layers. The specific collapsing temperature of an LDH is different depending on the metal cations and ratios of the metal cations [15–17]. For Mg/Al-CO_3 LDH, a typical example of a widely researched and applied LDH, generally, dehydroxylation and decarbonisation

occur in the temperature range of 240 °C and 480 °C, resulting in a mixed oxide phase of periclase (MgO structure). A spinel phase ($MgAl_2O_4$) appeared when the calcination temperature increased above 800 °C [18]. The layered double oxides (LDOs) derived from the LDHs at a calcination temperature of 450 ℃ and 550 ℃ can rehydrate into the layered structure when they are brought in contact with an anion-containing aqueous solution, water or a moist environment [19–22]. This rehydration property gives LDOs a high advantage in many applications especially when used as absorbents [23–26].

Some papers focusing on the rehydration of metal oxide compounds to form LDHs, well-known as the 'memory effect', were reported. Millange et al. [18] synthesized Mg/Al-LDH (Mg:Al = 3:1) via a co-precipitation method and prepared the LDO by calcining the LDH at 400 °C for 2 h. The rehydration process was studied via in-situ Energy-Dispersive X-ray diffraction by putting the calcined products in a sodium carbonate solution. The results indicated that carbonate in the liquid provided efficient means for the rehydration of low crystalline LDO. Mokhtar et al. [19] compared the rehydration of Mg/Al-LDO (Mg:Al = 3:1) in moist gas (gas flow of H_2O/N_2) and in Na_2CO_3 solution. Different from the liquid condition, where the LDO was put in a Na_2CO_3 aqueous solution for 1 h to rehydrate, in the moist gas phase hydration, the LDO kept its less ordered phase even after 52 h. Furthermore, Kikhtyanin et al. [21] studied the rehydration of Mg/Al-LDO with a metal molar ratio of 3 (Mg:Al = 3:1). After calcination at 450 °C for 3 h, the freshly

prepared mixed oxide was added and stirred in water at room temperature for 0-2 h. Characterization results showed that the rehydration of the layered LDH structure occurred quickly, within several seconds, in pure liquid water while stirring. In addition, the Mg/Al ratio can also affect the thermokinetic rehydration process of the calcined MgAl-LDH [15]. Interestingly, at ratios of 2.5 and 3.0, the LDOs had the fastest H_2O adsorption and this adsorption process was more temperature-dependent when the relative humidity was low. To further study the mechanism of the LDO rehydration process, MgAl-LDH was formed by physically mixing MgO and Al_2O_3 oxides via hydrothermal treatment [27]. It was found that the formation of LDH was strongly affected by the initial pH of the suspension solution. Neutral conditions were beneficial for the formation of MgAl-LDH with $Mg(OH)_2$ as a minor impurity, while in basic conditions, MgO was the major impurity and did not hydrate even after 10 days of heating at 110 °C. Nevertheless, although the rehydration of Mg/Al-LDOs have been studied, many of these reports are more focused on the rehydration of LDOs obtained after calcination of the LDHs at relatively low calcination temperature (usually lower than 600 °C). Few studies investigated the relationship between rehydration time and high calcination temperature (> 600 °C) . Besides this, when calcined at high (> 600 °C) temperature less attention has been given to the rehydration conditions in pure liquid water or humid air atmosphere. The latter is however of practical significance, providing

recommendations towards the storage of calcined LDH, i.e. LDO product, which might rehydrate into LDH (Re-LDH) materials with different features.

In this work, we studied the rehydration of LDOs which were obtained after high temperature calcination from 600 °C to 900 °C. Pure water was used as a liquid rehydration solution and compared to humid gas atmosphere rehydration, obtained via a sealed desiccator with pure water at the bottom. We prepared Mg/Al-LDH with a molar ratio of Mg:Al = 3:1 (as confirmed by ICP analysis) via a co-precipitation method at room temperature. After calcining at different temperatures, the samples were divided into two parts: one was added into pure deionized water and reacted at room temperature while stirring; the other part was put into the sealed desiccator and adsorbed water from the humid ambient air (vapour phase). The phase changes of the materials were characterized by X-ray diffraction (XRD). ^{27}Al magic-angle spinning (MAS) nuclear magnetic resonance (NMR) was accomplished to look for changes after calcination at different temperatures and rehydration behaviour in the two water phases. Apart from this, thermal analytical measurements coupled to a mass spectrometer (TG-MS), scanning electron microscopy (SEM), infrared spectroscopy (IR) and N_2 sorption isotherms were done to investigate whether the structure, composition and specific surface area of the rehydrated LDO were affected by the rehydration conditions and time.

2.2 Experimental

2.2.1 Synthesis of Mg/Al-LDH

The Mg/Al-LDH used in this work was synthesized by a co-precipitation method at room temperature. Typically, 75 mmol $Mg(NO_3)_2 \cdot 6H_2O$ (≥ 99.0%, Sigma Aldrich) and 25 mmol $Al(NO_3)_3 \cdot 9H_2O$ (≥ 98.5%, Merck) were dissolved in 100 mL deionized water. In two separate flasks, 50 mmol Na_2CO_3 (≥ 99.95% dry basis, Sigma Aldrich) was dissolved in 100 mL deionized water and 180 mmol NaOH (98.5%, ACROS Organics) was dissolved in 50 mL deionized water. Then, the mixed metal solution and NaOH solution were dropwise and simultaneously added to the Na_2CO_3 solution while vigorously stirring. As the original Na_2CO_3 solution has a pH higher than 10, the addition of metal solution was put faster than that of NaOH in the first several minutes. When the pH reached 10, the addition speed of the metal solution was adjusted to keep the pH of the solution around 10 ± 0.1. Once the addition process was finished, the white mixture was aged at room temperature (20 °C) for 24 h under vigorous stirring. Then, the final white suspension was isolated by filtration, washed with 500 mL of deionized water and dried at 80 °C overnight. The white solid product was ground into powder for utilization.

2.2.2 Conversion to Mg/Al-LDO

To convert the as-synthesized Mg/Al-LDH to LDO, it was heated at 600 °C, 700 °C, 800 °C or 900 °C in ambient air atmosphere for 6 h with a heating rate of 5 °C/min. The obtained Mg/Al-LDOs were denoted as C600-LDO, C700-LDO, C800-LDO and C900-LDO.

2.2.3 Rehydration in water vapour

The obtained LDOs were put into a sealed desiccator with deionized water at the bottom. They were kept in the desiccator at room temperature for 6 h, 12 h, 24 h or 48 h. The sample names are as follows: C*T*-LDO-*t*, where *T* represents the calcination temperature and *t* indicates the time for the rehydration. It has to be noted that the desiccator was not flushed with an inert gas. Hence, some CO_2 was present. This was particularly done to mimic storage conditions in ambient laboratory conditions.

2.2.4 Rehydration in liquid water

As a comparison, LDOs were added into deionized water at room temperature under vigorous stirring for 6 h to 48 h. Then, the final products were isolated by centrifugation and dried in air at 80 °C overnight. The white samples obtained were crushed and ground into powder. The liquid water rehydrated samples are denoted

as Re-C*T*-*t*, where *T* and *t* indicate calcination temperature and rehydration time, respectively.

2.2.5 Characterization techniques

The thermalgravimetric analysis (TG) was performed on a Mettler Toledo TGA/SDTA851e thermal balance. Typically, the sample was heated to 1000 °C under a flow of argon with a heating rate of 10 °C/min. The volatile decomposed products during the TG process were analyzed by a Hiden HPR-20 R&D Mass Spectrometer (MS), operating at conditions with an argon flow of 50 ml/min and a heating rate of 10 °C/min. The MS signal was collected for m/z within the range of 2 to 100.

The metal elemental composition of the LDHs was determined by ICP-MS (Agilent 7500, Agilent, Santa Clara, California USA). Each sample was destructed in trace metal grade nitric acid (Fluka, Buchs, Switzerland) and diluted with Milli-Q Type 1 water. Calibration standards were made by diluting purchased 10000 ppm standards (Alfa Aesar, Kandel, Germany).

X-ray diffraction (XRD) was performed using an X'Pert Pro X-ray generator. The incident beam went through a Soller slit with a width of 0.04° combined with a programmable divergence slit with an irradiated length of 10.0 mm. The diffracted beam system has an automatic anti-scatter slit (observed length: 10.0 mm and

height 0.3 mm), after which there is another Soller slit with 0.04 radians. Behind the Soller slit, a graphite monochromator and a proportional detector were present. Samples were ground in an agate mortar, placed in a monocrystal holder and mounted on a sample stage, which is a spinner. The samples were spinning with a revolution time of one second. It was operated at 40 kV and 40 mA with CuK_{α} radiation in the 2θ scanning range of 5-70° with a step size of 0.04° and 4 s/step. The measurements were done under atmospheric conditions at room temperature.

^{27}Al solid-state MAS NMR experiments were performed with an Agilent VNMRS Direct Drive 400 MHz spectrometer (9.4 T wide bore magnet) equipped with a T3HX 3.2 mm probe. The experiments were carried out using magic angle spinning (MAS) at 14 kHz in ceramic rotors of 3.2 mm (22 µl). $AlCl_3$ was used to calibrate the aluminium chemical shift scale (0 ppm). Acquisition parameters used were: a spectral width of 420 kHz, a 75° pulse of 2.5 µs, an acquisition time of 10 ms, a recycle delay time of 3 s, a line-broadening of 150 Hz and around 2000 accumulations.

The specific surface area was deduced from the isotherms recorded on a Quantachrome Quadrasorb SI automated gas adsorption system. Before analysis, all the samples were degassed at 80 °C (which is also the temperature for drying the samples) or 200 °C (at which the interlayer and physically adsorbed water can be removed) for 16 h under high vacuum condition. As the samples used for 80 °C

and 200 ℃ degassing conditions were from different batches, the difference in the specific surface area should only be interpreted in view of trends in changes in specific surface area as a function of treatment (temperature or/and hydration condition) rather than comparing absolute values at different degassing temperatures. Multipoint BET was used to determine the apparent surface area.

Diffuse Reflectance Infrared Fourier Transform (DRIFT) spectra were measured on a Nicolet 6700 Fourier Transform IR spectrometer (Thermo Scientific). For each spectrum, a wavenumber region of 500-4000 cm^{-1} was detected and 200 scans were collected. The sample was diluted in KBr to form a 2 wt% uniform mixture which was loaded in the Harrick DRIFT accessory. Before it was measured, a vacuum condition was applied for 15 minutes with a rotation pump at room temperature to remove excess physically adsorbed water and/or CO_2.

Scanning electron microscopy (SEM) was used to observe the morphology and particle size of all the samples. They were examined with a Field Emission Gun – Environmental Scanning Electron Microscope (FEG-ESEM) equipped with an Energy Dispersive X-ray (EDX) detector (FEI Quanta 250, USA; at AXES and EMAT research groups, University of Antwerp), using an accelerating voltage of 20 kV, a take-off angle of 30°, a working distance of 10 mm and a sample chamber pressure of 10^{-4} Pa.

2.3 Results and Discussion

2.3.1 Elemental chemical analysis (ICP)

ICP analysis was used to determine the chemical composition of as-synthesized LDH. The analysis showed that the ratio of Mg^{2+}/Al^{3+} was 3, which is the same as the theoretical value. This result confirmed the effective synthesis of LDH via the co-precipitation method.

2.3.2 X-ray diffraction

The XRD patterns of as-synthesized LDH are shown in Fig. 2.1A. The sharp reflections of (003), (006), (012) and wide reflections of (015), and (018) showed successful synthesis of the LDH compound. The (110) and (113) reflections were easily recognized, although they showed overlap between 60.5º and 61.7º 2θ. The (00l) reflections, namely (003) and (006), were characterized by high intensities with broad baseline shapes, which indicates that the as-synthesized LDH had relatively high crystallinity but with small crystallites.

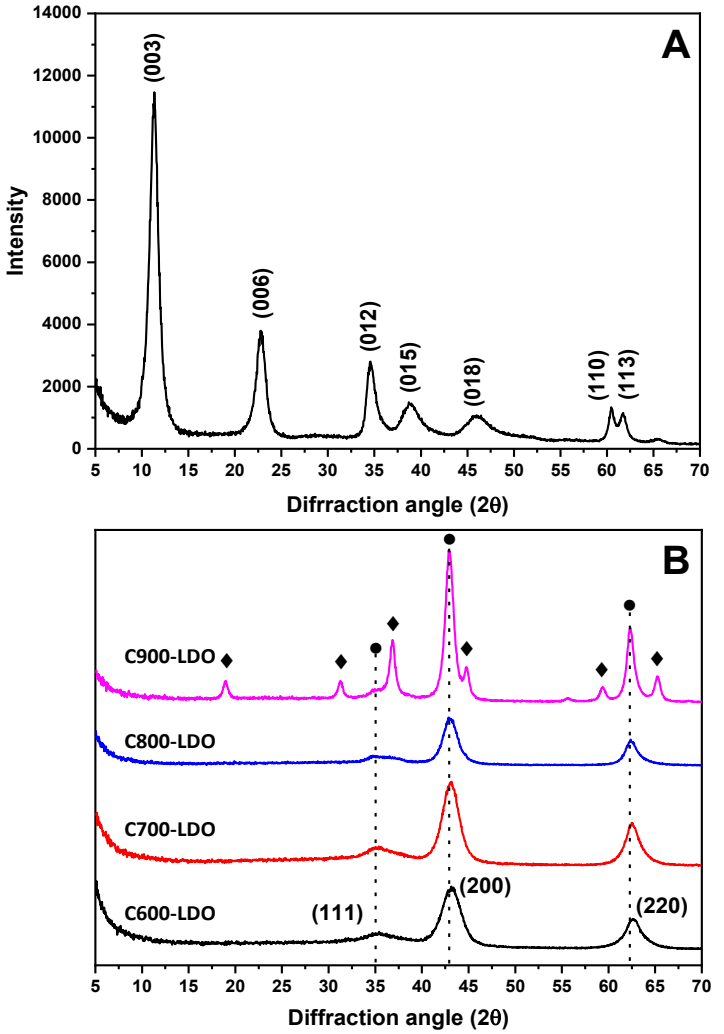

Fig. 2.1. XRD patterns of as-synthesized Mg/Al-LDH (A) and LDOs obtained at different temperatures (B). MgO (●), Mg-Al Spinel (♦).

After calcination at different temperatures between 600 °C and 900 °C, X-ray diffraction, exhibiting reflections at 2θ of 35°, 43° and 62°, suggested that calcination of the LDH at temperatures between 600 °C and 800 °C only results in the formation of a periclase (MgO) phase (Fig. 2.1B). However, when the temperature was increased to 900 °C, an extra phase of $MgAl_2O_4$ spinel was formed.

Putting these samples into a water vapour or liquid water condition at room temperature for 6–48 h, some changes occurred in these samples, which were recognized by XRD (Fig. 2.2). The XRD patterns of the samples indicated a rapid (partial) rehydration of the LDO into LDHs (Re-LDHs) within 6 h for all the high-temperature (600-900 °C) calcined LDOs. This observation was different from the rehydration reported in the literature using a Mg/Al-LDH with a Mg/Al ratio of 2 [28]. This could be explained by former literature, stating that higher Mg/Al molar ratios of 2.5 and 3.0 in the LDHs had better absorption ability of H_2O, which was crucial in the rehydration process [15]. Samples reported here, which were calcined at higher temperatures, showed similar rehydration ability compared to the reported low-temperature (≤ 600 °C) calcined ones [18,19,21]. Generally, LDOs rehydrated for 48 h in both vapour and liquid conditions (Re-LDHs obtained at temperatures of 600 °C, 700 °C, and 800 °C) exhibited sharper and stronger reflections than as-synthesized LDH at all reflections (Fig. A.1). The reflections of C600-LDO-48h and Re-C600-48h were the highest, suggesting that the samples rehydrated from C600-LDO had the best crystallinity. Compared with as-synthesized LDH, the rehydrated C900-LDO featured lower reflections both in vapour and water conditions, due to the stable crystalline of spinel phase present in the sample. Therefore, it is suggested that the ability for rehydration and the crystallinity of the rehydrated samples are dependent on the calcination temperature of the LDOs and to some degree dependent on the rehydrating conditions like water phase and time.

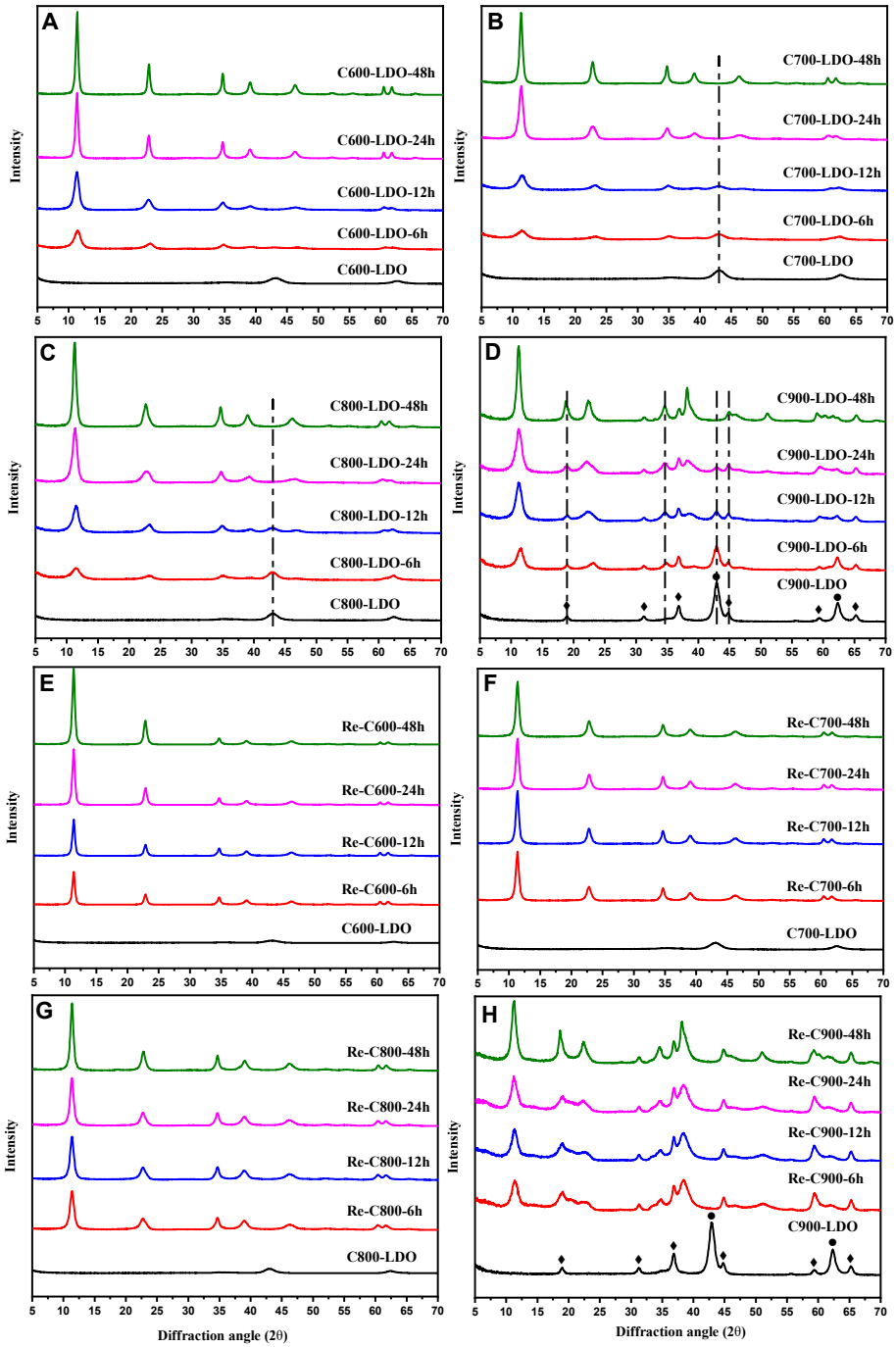

Fig. 2.2. XRD patterns of rehydrated C600-LDO, C700-LDO, C800-LDO and C900-LDO in water vapour (A-D) and liquid water (E-H). MgO (●), Mg-Al Spinel (♦).

When comparing the rehydration process of C600-LDO in water vapour (Fig. 2.2A), there was a progressive change of the XRD pattern intensity and sharpness of the reflections when prolonging the rehydrating time from 6 h to 48 h in vapour condition. However, sharper and more intense reflections were already formed in the liquid water after 6 h (Fig. 2.2E). Similar trends as rehydrated C600-LDO also appeared in the rehydration process of the C700-LDO and C800-LDO (Fig. 2.2B and 2.2F, Fig. 2.2C and 2.2G, respectively). Nevertheless, the reflection of MgO at $2\theta = 42.9°$ already disappeared in the C600-LDO sample (Fig. 2.2A) after exposure to water vapour for 6 h, while it remained visible even after 12 h in the samples of C700-LDO (Fig. 2.2B) and C800-LDO (Fig. 2.2C), and stayed present for 24 h in the sample of C900-LDO (Fig. 2.2D) in the vapour condition. The intensity of the MgO reflection decreased as time increased, which indicated that the magnesium oxide was involved in the rehydration reaction. Moreover, comparing liquid water versus vapour rehydration for samples calcined at the same temperature, showed a faster rehydration process in liquid water as can be deduced from the existence or disappearance of the reflection of MgO at $2\theta = 42.9°$. This was also visible from data in Table 2.1, where larger crystals of the Re-LDHs were formed at lower exposure time in liquid water versus water vapour. Only in the case of samples rehydrated from C800-LDO and C900-LDO, still an increase in crystal size is visible as a function of time in liquid water conditions.

When the calcination temperature was 900 °C, an obvious spinel phase appeared in the C900-LDO compounds, next to MgO (Fig. 2.1B and Fig. 2.2D and 2.2H). The spinel remained to exist even after a 48 h rehydration reaction in both vapour and liquid conditions. Also, the spinel signals seem to increase in intensity as a function of rehydration time as visible in the reflection at $2\theta = 18.9°$, for which the increase also seems stronger in the liquid water than in water vapour. For the reflections at $2\theta = 59.3°$ and $65.3°$ this seems less obvious for vapour phase rehydration, although the relative intensity to the reflection at $2\theta = 18.9°$ appears similar after vapour or liquid water rehydration (Fig. 2.2D and Fig. 2.2H). All these reflections seem to increase with time in a similar manner, which implies that the spinel phase can still be formed in the rehydration process, although it is obvious that the growth appears faster in liquid water than in water vapour.

To have a direct comparison of the absolute intensity of Re-LDHs as a function of their preparation temperature, the XRD reflections of samples rehydrated for 24 h and 48 h were collected in Fig. A.1 (see Appendix A). Compared with samples obtained in water vapour condition, the intensities of samples with calcination temperatures of 700 °C and 800 °C rehydrated in liquid water were more intense and sharper, while there was no difference for the 600 °C sample. In contrast, after calcination at 900 °C, rehydration in liquid water (Re-C900-24h) resulted in lower XRD reflections than in water vapour (C900-LDO-24h). In addition, the intensity and sharpness of the XRD reflections of samples rehydrated under the same

condition decreased with increasing calcination temperature, Note that the intensity of reflections was weaker than the as-synthesized LDH as the temperature reached 900 °C (Fig. A.1). These phenomena indicated that, although LDOs were obtained at temperatures as high as 800 °C, they could completely rehydrate into LDH, but with a calcination temperature dependent rehydration rate (slower at a higher temperature) and a coinciding difference in crystal size and crystallinity.

Table 2.1 Crystalline size and d_{003} parameter of as-synthesized LDH, calcined and rehydrated samples based on XRD reflections.

Sample	Crystal Size (nm)	d_{003} (Å)	Sample	Crystal Size (nm)	d_{003}(Å)
LDH	10.4	7.80			
C600	8.7	-	C800	9.1	-
C600-6h	9.9	7.74	C800-6h	9.8	7.71
C600-12h	11.9	7.80	C800-12h	10.8	7.69
C600-24h	17.6	7.80	C800-24h	10.9	7.77
C600-48h	20.2	7.77	C800-48h	14.9	7.83
Re-C600-6h	19.3	7.74	Re-C800-6h	12.7	7.77
Re-C600-12h	19.7	7.77	Re-C800-12h	13.4	7.74
Re-C600-24h	19.1	7.77	Re-C800-24h	13.9	7.77
Re-C600-48h	18.7	7.77	Re-C800-48h	15.8	7.77
C700	8.6	-	C900	10.8	-
C700-6h	8.7	7.69	C900-6h	10.7	7.64
C700-12h	9.6	7.71	C900-12h	10	7.88
C700-24h	12.5	7.80	C900-24h	10.1	7.91
C700-48h	16.2	7.82	C900-48h	13.5	7.88
Re-C700-6h	15.6	7.80	Re-C900-6h	10	7.80
Re-C700-12h	16.2	7.77	Re-C900-12h	10.6	7.82
Re-C700-24h	15.6	7.74	Re-C900-24h	11	7.88
Re-C700-48h	15.4	7.77	Re-C900-48h	11.8	7.83

[a] Calcined sample size was calculated based on the (200) reflection of the LDO. [b] Rehydrated sample size was calculated based on (003) reflection of the LDH.

Table 2.1 and Table A.1 display the effect of rehydration on the crystalline sizes and crystal lattice parameters of the as-synthesized LDH, LDOs and Re-LDHs. The crystalline sizes were calculated based on XRD reflections by Scherrer's equation. The d_{003} value of 7.69 to 7.91 Å demonstrated that the interlayer anions should be CO_3^{2-} and H_2O molecules [14,29], which was confirmed by the TG-MS in Fig. A.2. An average *c*-axis parameter of around 3.05 Å and 3.11 Å and a lattice parameter equal to about 23 Å were calculated and shown in Table A.1. Combining this information with the XRD diffraction peaks of (012), (015) and (018), a polytype of $3R_1$ was assumed for the as-synthesized and Re-LDHs [14,30–32]. Furthermore, the lattice *a* parameters increased from 3.05 Å in the rehydrated samples produced by LDOs calcined at 600-800 °C to 3.11 Å when calcined at 900 °C, which might be due to a slight change of the Mg/Al molar ratio in the LDH phase. Besides this, the spinel phase which still existed after the rehydration process may also contribute to the lattice increase to some degree. Compared with the crystalline size of the as-synthesized LDH (10.4 nm), after calcination, the obtained crystal sizes of the LDOs became smaller when the temperature was between 600-800 ℃ (8.7 nm, 8.6 nm, and 9.1 nm, respectively). This was as expected due to the collapse of the layered structure. However, when the temperature arrived at 900 ℃, the crystalline size increased somewhat to 11 nm because of the formation of the observed spinel phase in the sample. Moreover, upon rehydration, the crystalline size of all rehydrated samples increased compared to the LDOs and most were also larger than the original LDH. The size showed an evident increasing trend as the

rehydration process evolved in time in the presence of water vapour. Different from that, samples rehydrated in liquid water kept unchanged or only changed a little (C800-LDO and C900-LDO) in the crystalline size, confirming the faster and more complete rehydration process in liquid water. Besides this, for samples rehydrated in liquid water, the crystalline size of samples rehydrated for the same length of time decreased as the calcination temperature increased. In the water vapour condition, this phenomenon happened after rehydration for 24 h and 48 h. Whereas, for shorter rehydration times (6 h and 12 h), the samples calcined at different temperatures had almost the same crystalline size. These results suggested that rehydration in liquid water can aid in achieving maximum crystal sizes of rehydrated LDHs faster than in water vapour. Another conclusion that could be drawn was that the crystallinity and crystal growth of the LDH was facilitated upon rehydration compared to the as-synthesized LDH obtained via a room-temperature co-precipitation method.

2.3.3. ^{27}Al solid-state MAS NMR

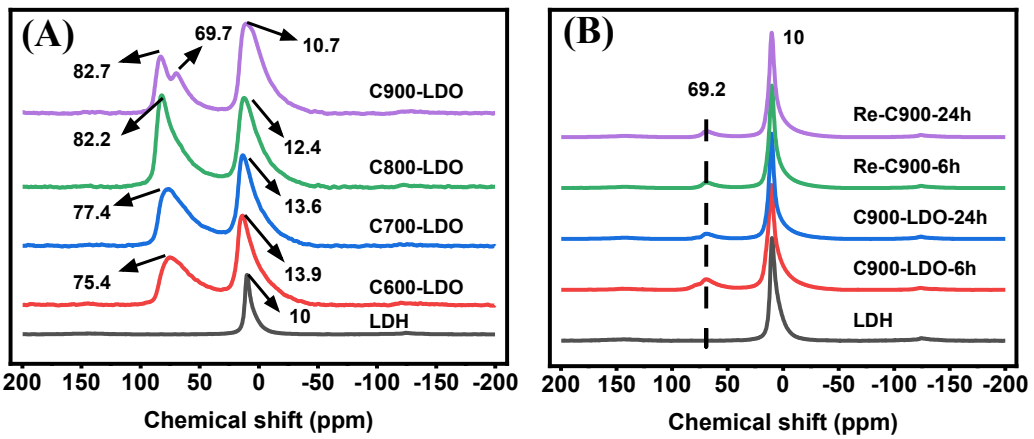

Fig. 2.3. ^{27}Al MAS NMR spectra of (A) as-synthesized LDH and LDOs calcined at different temperatures, and (B) as-synthesized LDH, and Re-LDHs of C900-LDO rehydrated in water vapour (C900-LDO-6h and 24h) or liquid water (Re-C900-6h and 24h) for 6 h or 24 h.

The ^{27}Al MAS NMR spectra of as-synthesized LDH, LDOs obtained at different temperatures and rehydrated C900-LDOs are shown in Fig. 2.3. As shown in Fig. 2.3A., the as-synthesized LDH only shows a single sharp resonance at 10 ppm in the ^{27}Al spectrum, indicating that the Al appears predominantly in octahedral sites [33,34]. After calcination at 600 °C, with the loss of interlayer water, a broad peak was observed at 75.4 ppm which can be assigned to tetrahedral sites of Al. This resonance becomes stronger and shifts downfield (from 75.4 ppm to 82.2 ppm) upon calcination at 800 °C, coinciding with the formation of the periclase (MgO) phase as observed in XRD (Fig 2.1B), causing simultaneous changes in the alumina phase, next to changes induced by progressive dehydroxylation in function of temperature (see section 2.3.4 TG coupled to mass spectrometry). At a calcination temperature of 900 °C, it splits into two peaks (69.7 ppm and 82.7 ppm). A similar

situation was described in the literature, but with a somewhat smaller downfield shift from 74.0 ppm to 76.1 ppm, claimed to be correlated to aluminium oxide phases such as cubic structures (γ-, δ-, and θ- alumina) and/or hexagonal phases (χ- and κ-alumina), although no XRD detectable alumina phase was observed upon calcination [35]. However, although no alumina phases were detected in XRD, the peak appearing at 69.7 ppm in ^{27}Al NMR (Fig. 2.3A) seems to correlate to the XRD visible $MgAl_2O_4$, spinel phase that appears at 900 °C calcination. This correlation was also confirmed by literature [34–36]. Hence, based on XRD and ^{27}Al NMR data, the signals between 75 and 83 ppm are expected to correlate to tetrahedral Al sites in (disordered/distorted) phases of aluminium oxide that are not detectable in XRD and change with temperature, whereas the signal at 69.7 ppm seems to originate from a nanostructured ordered spinel phase with tetrahedral Al in a more defined spinel lattice when calcining at 900 °C [36]. Moreover, the peak representing octahedral Al shifted from 10 ppm for LDH to 13.9 ppm for C600-LDO, while it moved upfield as temperature increased and reached a chemical shift of 10.7 ppm for C900-LDO. This trend was also reported in the literature, demonstrating that the unheated LDH showed a single resonance at 9 ppm which shifted downfield to 10.2 ppm at a calcination temperature of 700 °C and then shifted back upfield to 10 ppm after calcination at 900 °C [34]. Comparing the spectra of the rehydrated samples obtained from C900-LDO with the spectrum of as-synthesized LDH, all spectra showed a sharp peak at 10 ppm, representative of the LDH phase, but all rehydrated C900-LDO samples also show an additional

tetrahedral peak at 69.2 ppm (Fig 2.3B) that is most probably originating from the spinel ($MgAl_2O_4$) phase as it also remained present in the XRD (Fig. 2.2D and 2.2H). This confirms that the rehydration of the sample calcined at 900 °C was incomplete which was also confirmed by the XRD results in section 2.3.2. Besides this, no significant differences were observed between Re-C900-6h and Re-C900-24h, which is in accordance with the XRD results (Fig. 2.2H). However, comparing C900-LDO-6h and C900-LDO-24h, a difference is observed in the tetrahedral/octahedral ratio which is also reflected in the XRD patterns (Fig. 2.2D).

2.3.4. TG coupled with mass spectrometry

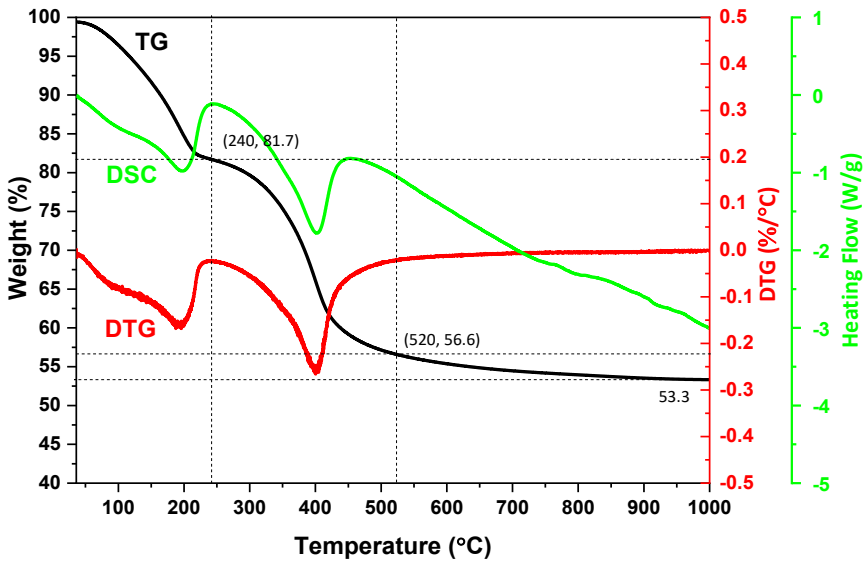

Fig. 2.4. Thermal analysis of the as-synthesized Mg/Al-CO_3-LDH: TG (black line)/DTG (red line)/DSC (green line) analysis of LDH.

The thermal decomposition of the LDH (Fig. 2.4) generally proceeded in three mass loss stages in the temperature regions of 35-240 °C, 240-520 °C, and 520-

1000 °C, coinciding with two obvious endothermic peaks with a maximum heat flow (DSC curve, green line) at about 200 °C and 400 °C. The asymmetric nature of the DSC and DTG peaks indicates that multiple mass loss processes were ongoing, spread over a wide temperature range with a maximum at the endothermic maxima of the DSC curve. The mass loss till 240 °C included the removal of physical adsorbed H_2O, the interlayer water and a trace amount of CO_2, as visible in the MS (Fig. A.2), which in total accounts for 18.3 wt%. As reported in the literature [37], the interlayer water started to be removed above 70 °C. The same could be assumed here, visible as a weakly resolved peak in DTG and DSC curves, with a mass loss of ~ 1.5%, attributed to physical adsorbed water, while the total mass loss for interlayer water was about 16.8% (temperature range 70 °C to 240 °C). In the temperature range from 240 °C to 520 °C, the mass spectrometric data indicated the removal of both CO_2 and H_2O (Fig. A.2), which represented a 25.1% mass change.

Table 2.2 Mass loss based on TG for samples of as-synthesized LDH, C600-LDO and its rehydrated samples at two different rehydration conditions (vapour and liquid) for different hours.

Sample	Temperature Range (°C) & Mass Loss (%)				
	RT-70	70-240	240-520	520-1000	Total
LDH[a]	1.5	16.8	25.1	3.3	46.7
C600-LDO[a]	0.1	3.8	2	2.3	8.2
C600-LDO-6h[a]	0.9	9.9	13.3	2.4	26.5
C600-LDO-12h	3	18.2	18.9	2.4	42.5
C600-LDO-24h[a]	6.6	20.3	20.1	2.5	49.5
C600-LDO-48h	6.6	27.5	18.7	2.1	54.9
Re-C600-6h[a]	1.5	14.5	26.4	2.2	44.6

Re-C600-12h	0.5	15.1	26	2.3	43.9
Re-C600-24h[a]	0.5	14.6	26.3	2.3	43.7
Re-C600-48h	0.5	14.6	26.3	2.4	43.8

[a] Mass spectrometer was connected with the TG for these samples.

Table 2.2 summarizes the TG results for as-synthesized LDH, C600-LDO and Re-LDHs obtained from C600-LDO. As shown before, for as-synthesized LDH, in addition to the ~1.5% physically adsorbed water, the interlayer loss of CO_2 and H_2O was about 16.8% and another ~ 25.1% mass loss appeared between ~ 240 °C to ~ 520 °C due to the dehydroxylation of the brucite structure as well as the decomposition of carbonates. The same three temperature ranges were used to study the changes in the rehydrated samples. Typically, C600-LDO showed about 3.8% evolution of interlayer water loss and 2% dehydroxylation related water loss, which suggested that there was still a small amount of layered H_2O-containing structure and OH-groups in the structure which probably was left after calcination or that already reappeared as the start of the rehydration process. When C600-LDO was rehydrated in the water vapour, as the reaction time increased from 6 h to 48 h, both the physically adsorbed water (room temperature to 70 °C in the TG curve) and the interlayer water (70-240 °C) content increased from ~ 0.9% to ~ 6.6% and ~ 9.9% to ~ 27.5%, respectively. The physical adsorbed water seemed to reach its maximum amount at 24 h, while the content of interlayer water increased further till 48 h. The amounts of physically adsorbed and interlayer water were also higher than that of the original as-synthesized LDH. The amount of dehydroxylated water and CO_2 increased in the first 12 hours but then remained almost unchanged, which

was in accordance with the XRD results where the periclase reflections disappeared and rehydrated into LDH after 12 h. Nevertheless, it did not reach its original amount of dehydroxylated water of 25% nor the 3% related to OH-group condensation 520-1000 °C. However, samples rehydrated in liquid water exhibited a stable value of interlayer water ~ 15% and dehydroxylation water and CO_2 ~ 26% after 6 h. Moreover, these two values were also closer to the values of the as-synthesized LDH, suggesting a similar chemical composition. Different from the as-synthesized LDH, it adsorbed less physical water when rehydrating more than 12 h, which was opposite to rehydration in water vapour.

TG-MS analysis of the as-prepared LDH, C600-LDO, C600-LDO-6h, C600-LDO-24h, Re-C600-6h, and Re-C600-24h provided information on the amount of both H_2O and CO_2 species evolved from the samples by dehydration, dehydroxylation or/and decarboxylation (Fig. A.3A-E). The TG-MS curves show that the rehydrated samples have a similar dehydroxylation of the brucite-like layers and decarboxylation of CO_3^{2-} in the temperature range of 240-520 °C with the as-synthesized LDH. However, some differences can be observed. Specifically, the signals of interlayer H_2O increased as the rehydration time increased in both water vapour and liquid water rehydration conditions. Besides this, the relative intensity of the H_2O signal at 50-240 °C and 240-500 °C for all the four rehydrated C600-LDO samples illustrated the increase of the amount of both interlayer water and the OH^- group in the brucite-like layers. Compared with as-synthesized LDH (Fig.

A.2), which had only one resolved peak between 130 °C and 240 °C, the rehydrated samples (Fig. A.3) had two peaks in this temperature range. Moreover, this temperature range increased to about 289 °C for Re-C600 -24h. This could be caused by both weakly and strongly physically adsorbed water in the samples and points to a difference in surface chemistry or interaction. Besides, the CO_2 signal in the MS (m/z 44) of as-synthesized LDH (Fig. A.2) moved left from about 302-499 °C to 257-460 °C (in water vapour) and 264-450 °C (in liquid water) for 6 h rehydrated samples under both conditions. However, this range became more narrow and closer to the maximum temperature of CO_2 release of the as-synthesized LDH for 24 h samples, 364-480 °C for water vapour condition and 371-496 °C for liquid water condition, respectively. The phenomena suggested that for the CO_3^{2-} anion in the rehydrated samples, time is the more important factor for its formation rather than the type of water phase for rehydration.

2.3.5. Specific surface area

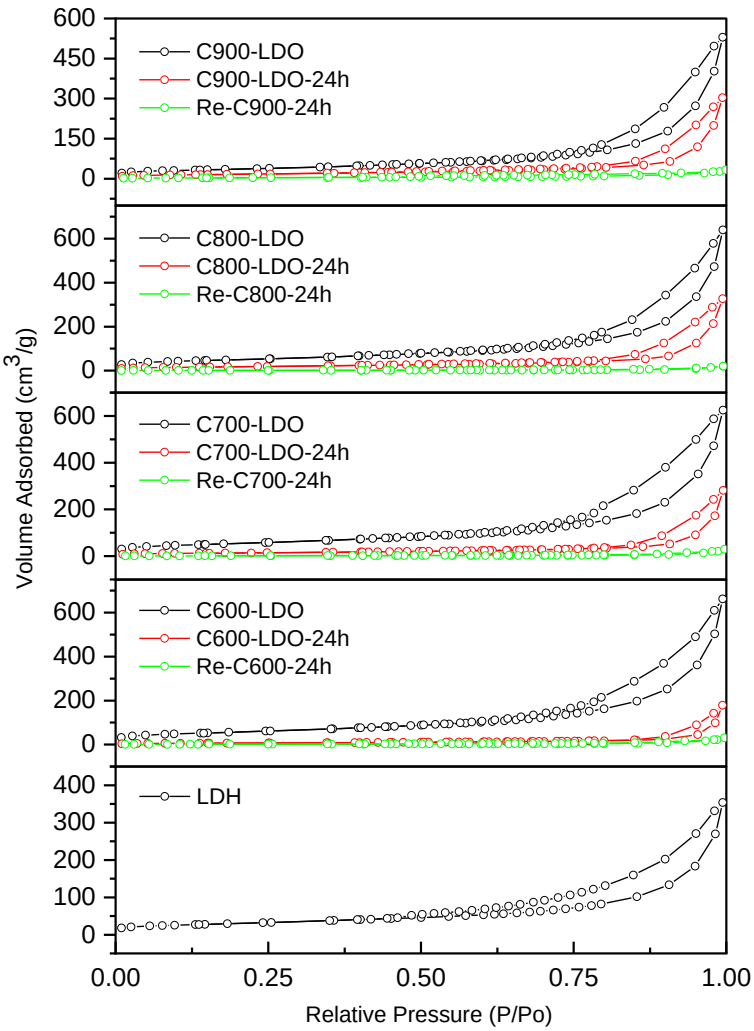

Fig. 2.5. Nitrogen adsorption-desorption isotherms at -196 °C of the as-synthesized LDH, LDO calcined at different temperatures, and LDHs rehydrated in water vapour and liquid water conditions with degassing temperature at 80 °C.

The alterations of disorder and crystalline changes caused by calcination and rehydration are considered to be the reason for the variation in the specific surface area [38–40]. According to the nitrogen adsorption-desorption isotherms (Fig. 2.5

and Fig. A.4), as-synthesized LDH, LDOs and rehydrated LDHs showed generally type II isotherms with H3 hysteresis loops representative for non-rigid aggregation of plate-like particles or incompletely filled macropores [41,42].

Table 2.3 Specific surface area (degassing at 80 °C for 16 h) of samples obtained at different calcination temperatures and rehydration conditions.

Sample	S_{BET} (m^2/g)	Sample	S_{BET} (m^2/g)	Sample	S_{BET} (m^2/g)	Sample	S_{BET} (m^2/g)
LDH	108	-	-	-	-	-	-
C600-LDO	204	C700-LDO	194	C800-LDO	177	C900-LDO	128
C600-LDO-6h	111	C700-LDO-6h	113	C800-LDO-6h	95	C900-LDO-6h	88
C600-LDO-24h	24	C700-LDO-24h	48	C800-LDO-24h	62	C900-LDO-24h	58
Re-C600-6h	5	Re-C700-6h	4	Re-C800-6h	4	Re-C900-6h	12
Re-C600-24h	5	Re-C700-24h	5	Re-C800-24h	4	Re-C900-24h	11

The as-synthesized LDH has a specific surface area (S_{BET}) of 108 m^2/g. Once it is calcined, this value increases as a result of the porous structure with holes created by the loss of interlayer CO_3^{2-}, -OH and the collapse of the layered structure [43,44]. At 600 °C, the C600-LDO exhibited the highest S_{BET} of 204 m^2/g. As the calcination temperature increased further, the values of S_{BET} decreased to 194 m^2/g, 177 m^2/g and 128 m^2/g at 700 °C, 800 °C and 900 °C, respectively. However, when the samples were rehydrated in water vapour or liquid water, the values of S_{BET} of all these samples decreased and remained much lower than the LDOs and original LDH. After being rehydrated in water vapour for 6 h, C600-LDO-6h and C700-LDO-6h displayed almost the same S_{BET}, 111 m^2/g and 113 m^2/g, respectively.

Moreover, when prolonging the exposure time to 24 h, both of their S_{BET} decreased quickly. Samples calcined at 800 °C and 900 °C showed a similar decreasing tendency. Nonetheless, the S_{BET} of C800-LDO-24h (62 m^2/g) and C900-LDO-24h (58 m^2/g) were higher than those of C600-LDO-24h (24 m^2/g) and C700-LDO-24h (48 m^2/g). A possible reason could be that samples with a lower calcination temperature featured a better rehydration effect (as shown in XRD, Fig. 2.2) while being exposed to the same rehydration time. Therefore, the rehydrated samples kept more hydroxyl groups and water molecules in the interlayer after degassing, which could lead to a decrease in the adsorption ability of N_2 during the characterization process.

In addition, when the samples were rehydrated in liquid water, the final S_{BET} of samples with calcination temperatures of 600 °C, 700 °C and 800 °C were around 5 m^2/g, no matter the calcination temperature and rehydration time. Only the Re-C900-6h and Re-C900-24h samples showed somewhat higher S_{BET} values of 12 and 11 m^2/g, respectively. These low specific surface areas were comparable with those reported for rehydrated LDO samples, whose specific surface areas were only 6.6 and 4.3 m^2/g [45].

As suggested by the TG results, at 200 °C the interlayer and physically adsorbed water can be removed. To study how the water in the rehydrated samples affected S_{BET}, a higher degassing temperature of 200 °C was used. As another batch of

materials was used for 200 °C degassing, the results obtained should only be interpreted towards the trends in function of treatment conditions, rather than comparing the absolute value differences in surface areas for the different degassing temperatures. As shown in Fig. A.4-6, the adsorption/desorption isotherms of the LDH were both type II. This suggested that increasing the degassing temperature from 80 °C to 200 °C had little effect on the pore properties of as-synthesized LDHs. After calcination, the S_{BET} of LDOs (Table A.2) was higher than the as-synthesized LDH and showed a decreasing trend as the calcining temperature increased, which was the same as LDOs samples measured at a low degassing temperature of 80 °C. Besides this, in both 80 °C and 200 °C degassing conditions, the Re-LDHs produced in water vapour showed an obvious decrease trend in S_{BET}. Furthermore, in both degassing temperatures, Re-LDHs obtained in liquid water conditions showed quite small S_{BET}. Although at both 80 °C and 200 °C degassing conditions, the S_{BET} has decreased significantly after 24h rehydration in water vapour for all samples, a difference in trend is visible after only 6 h degassing at 200 °C (versus 80 °C). Generally, samples rehydrated in water vapour featured larger specific surface area than those rehydrated in liquid water no matter if the interlayered and physically adsorbed water was removed (degas at 200 °C) or not (degas at 80 °C). Combing the N_2 sorption data with the SEM images shown in Fig. 2.8 and Fig. A.7, it can be figured out that, after rehydration no matter in water vapour or liquid water, samples aggregated together forming irregular layers or lumps with larger particle sizes. However, it led to the

decrease in the amount of cavities between particles, resulting in the decrease of S_{BET}. This can also be confirmed by the loss of interstitial porosity visible in N_2 sorption at relative pressures above 0.75, as shown in Fig. 2.5.

2.3.6. Fourier transformed infrared spectroscopy (FT-IR)

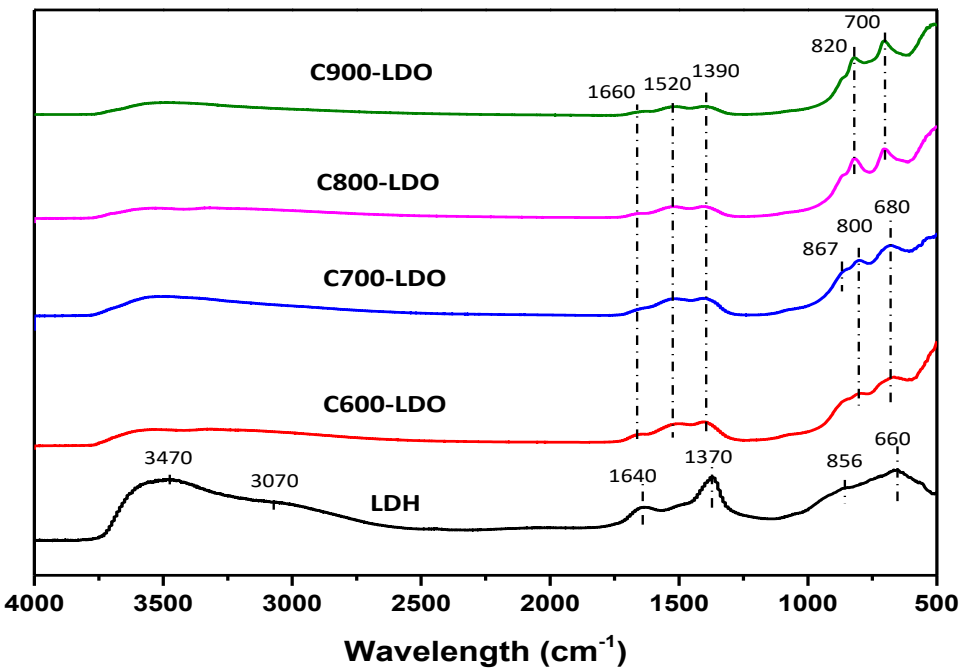

Fig. 2.6. DRIFT spectra of LDH and LDO calcined at different temperatures.

To better understand the changes in the LDH, calcined LDOs and rehydrated LDOs, FT-IR was used to reveal chemical bond information. Comparing the LDH before and after calcination at different temperatures (Fig. 2.6) indicates a weakening of the band at about 3470 cm^{-1} in the calcined samples due to the vibration of physically adsorbed water and structural OH^- groups in the LDH sample, illustrating their loss during the calcination process. Specifically, the wide,

unresolved band at around 3470 cm^{-1} can be correlated to multiple contributions: hydrogen-bonded interlayer water typically expected around 3300 cm^{-1} and, in addition, different stretching modes of M-OH (3470 cm^{-1} belongs to the Al-OH bond and 3600 cm^{-1} was assigned to Al- or Mg-OH bond) [46]. At about 3070 cm^{-1}, a wide band attributed to the CO_3^{2-}- H_2O bridging modes of carbonate and interlayer water of the LDH sample was visible [18]. This band almost disappeared after calcination. A bending vibration band of interlayer water was visible near 1640 cm^{-1} whose intensity decreased significantly with increasing calcination temperature and shifted to 1660 cm^{-1} in the calcined samples. In the LDH sample, the obvious FT-IR signals at 1370 cm^{-1}, 856 cm^{-1} and 660 cm^{-1} were due to the CO_3^{2-} vibration [37,47]. The other bands below 1000 cm^{-1} generally belonged to the M-O skeletal vibrations. After calcination, signals around 680-700 cm^{-1} and 800-867 cm^{-1} appeared, depending on the calcination temperature and were ascribed to the stretching vibration of Mg-O and the stretching vibrations of tetrahedral AlO_4 and octahedral AlO_6 [48]. They became stronger with calcination temperature. Moreover, the shift in peak positions of the tetrahedral (> 760 cm^{-1}) and octahedral alumina stretching vibrations (400-800 cm^{-1}) confirms the suggested changes in the alumina phase upon dehydroxylation that were hypothesized based on the shift in the ^{27}Al NMR chemical shifts between 75-82.7 ppm (tetrahedral alumina) and between 10-13.9 ppm (octahedral alumina). However, their positions were somewhat different from those reported in the

literature, in which the LDO was obtained at temperatures between 200-800 °C and the bands of Al-O were around 713 cm^{-1} and 797 cm^{-1} [49].

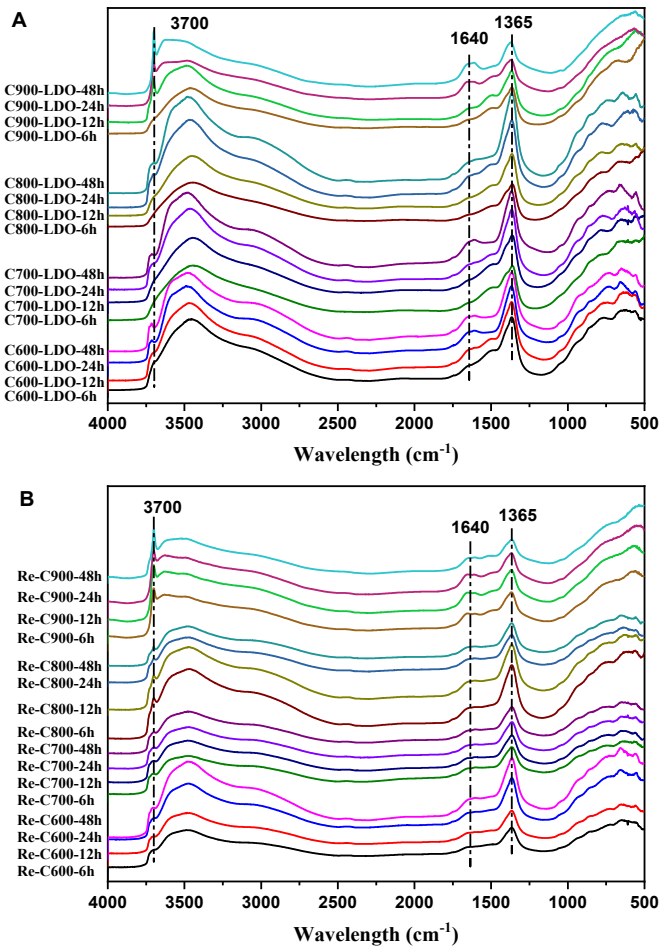

Fig. 2.7. DRIFT spectra of rehydrated LDOs in water vapour (A) and liquid water (B).

Fig. 2.7A shows the FT-IR results of rehydrated samples in the condition of water vapour and in Fig. 2.7B those of rehydration in water. After rehydration in water vapour or liquid water, the bands of physically adsorbed water and interlayer water were clearly present. The appearance of bands at 3470 cm^{-1} and 1365 cm^{-1} in all

the samples, which belong to OH stretching of water molecules and carbonate ions [50], suggested that some H_2O and CO_3^{2-} anions were integrated into the structure during the rehydration process of the samples, which could be adsorbed from the air or/and liquid water. However, compared with other rehydrated samples at 600–800 °C under both water vapour and liquid water, the samples rehydrated from C900-LDO showed relatively lower and less sharp bands at 3470 cm^{-1} and 1365 cm^{-1}. This suggested the relatively weak ability of adsorbing CO_2 and H_2O for C900-LDO, coinciding with the observed lower rehydration tendency of the C900-LDO samples. In addition, different from the as-synthesized LDH, an obvious band at about 3700-3710 cm^{-1} appeared, which belongs to the brucite ($Mg(OH)_2$) phase [27]. Moreover, it is sharper for materials rehydrated after calcination at higher temperatures. The same bands are observed in the rehydrated LDO in liquid condition as shown in Fig. 2.7B, illustrating the fact that the same functional groups were formed, even though the reactions happen in a different water phase.

2.3.7. SEM images

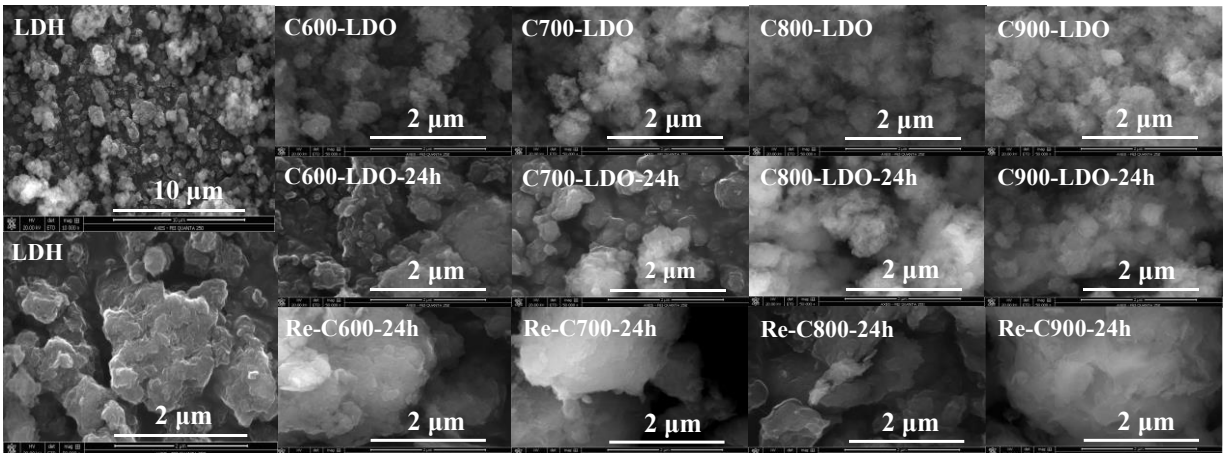

Fig. 2.8. SEM images of LDH, calcined LDO, and 24 h rehydrated samples in different conditions.

SEM images (Fig. 2.8 and Fig. A.7) described the morphological changes of the LDH after calcination and rehydration for 24 h and 6h. The micrograph of synthesized LDH illustrated that aggregation occurred with small pieces of irregular layered structures forming small lumps of micrometre size. After calcination at 600 °C, the layered structure collapsed into smaller size particles. Increasing calcination temperature to 700–900 °C, C700-LDO, C800-LDO and C900-LDO resulted in similar morphology with no obvious differences, namely a spongy appearance in accordance with its porous nature. Rehydrated in water vapour for 24 h, the C600-LDO-24h and C700-LDO-24h samples formed aggregates of smaller plate-like particles, which were smoother on the surface than the C600-LDO-6h and C700-LDO-6h (Fig. A.7E and F); C800-LDO-24h and C900-LDO-24h showed another typical LDH morphology, consisting of large

amounts of loosely cumulated layered flake-like particles. The particles were more tightly integrated than those rehydrated for 6 h (Fig. A.7G and H). For samples rehydrated in liquid water, larger aggregates of crystal plate-like particles with layered structures appeared in all the samples at different rehydration hours (Fig. 2.8 and Fig. A.7A-E), which were generally packed more closely than in the situation of water vapour. The conglomerated system affected the adsorption properties of samples [51]. The morphology differences could explain the lower specific surface areas of the samples rehydrated for 24h and the somewhat higher specific surface area for C800-LDO-24h and C900-LDO-24h. Nevertheless, the changes in the morphology with different rehydration times and water conditions seemed to have no obvious effect on the crystallographic characteristics of the rehydrated LDH as proven by XRD (Fig. 2.2).

2.4. Conclusions

MgAl-LDH (molar ratio Mg:Al = 3:1) and its derived mixed metal oxide are widely applied in different fields. However, after calcination even at high temperatures up to 900 °C, the metal oxides obtained could rehydrate into LDH, although with different properties, which could affect their application. We created a water vapour phase condition which was close to atmospheric storage conditions, to study the differences between moist vapour-rehydrated samples with those rehydrated in liquid water. XRD measurements provided direct evidence for the

rehydration of the LDO calcined at high temperatures (600–900 °C) in both water vapour and liquid water conditions. The LDH phase could be formed from all these LDOs after (possibly less than) 6 h rehydration. Based on the disappearance of the MgO reflection, the vapour phase hydration was found as fast as the liquid phase in the case of LDO calcined at 600 °C. However, at higher calcination temperatures of 700-900 °C, the vapour phase hydration showed a slower rehydration rate than the liquid phase. In addition, the rehydrated samples featured different properties from the as-synthesized LDH. The infrared spectra after rehydration display extra signals due to $Mg(OH)_2$ formation. Moreover, the specific surface areas, morphologies, crystal sizes and thermal decomposition behaviour of all the rehydrated samples were, at least partially, different from the as-synthesized samples, which suggested that, although the process of rehydration created a similar LDH, it doesn't include a full memory effect, rehydrating it exactly into the former LDH with the same properties. Moreover, the difference in these properties was found to be dependent on the applied calcination temperature and the conditions of rehydration being vapour or liquid phase. TG-MS showed that the rehydration process also includes the adsorption of CO_2 from the air or dissolved in liquid water to form LDHs containing carbonate, like the as-synthesized LDH. Finally, it was shown that the rehydration happens slowly, but occurs within hours after LDO formation, even under atmospheric water vapour and room temperature conditions, which were close to the environment for putting unsealed, non-purged samples under atmospheric conditions in the lab. Therefore, it is recommended to

store calcined LDH (LDO) samples carefully in a moist-free environment, preventing their progressive change into an altered structure. As in this paper, only metals of Mg and Al with a ratio of 3 have been studied, it does not warrant extrapolation of the results to LDH-derived LDOs with other compositions. Nevertheless, based on the results, we recommend evaluating the rehydration behaviour under gas and if needed liquid phase conditions with respect to application, but also under storage conditions (i.e. room temperature and humid air).

2.5 References

[1] Yang, Z.; Wei, J.; Zeng, G.; Zhang, H.; Tan, X.; Ma, C.; Li, X.; Li, Z. hao; Zhang, C. A Review on Strategies to LDH-Based Materials to Improve Adsorption Capacity and Photoreduction Efficiency for CO_2. Coord. Chem. Rev. 2019, 386, 154–182. https://doi.org/10.1016/j.ccr.2019.01.018.

[2] Gao, F.; Wang, J.; Jiang, M.; Du, X.; Ma, X.; Hao, X.; Yue, X.; Guan, G. A Novel Unipolar Pulsepotential Oscillation System Based on HKUST-1(C)@CoAl LDH Film for Selective Separation of Dodecyl Sulfonate Ions. Sep. Purif. Technol. 2021, 265, 118488. https://doi.org/10.1016/j.seppur.2021.118488.

[3] Wang, Y.; Zhang, N.; Wu, H.; Ren, Y.; Yang, L.; Wang, X.; Wu, Y.; Liu, Y.; Zhao, R.; Jiang, Z. Exfoliation-Free Layered Double Hydroxides Laminates Intercalated with Amino Acids for Enhanced CO_2 Separation of Mixed Matrix Membrane. J. Memb. Sci. 2021, 618, 118691. https://doi.org/10.1016/j.memsci.2020.118691.

[4] Xu, S.; Chansai, S.; Shao, Y.; Xu, S.; Wang, Y.; Haigh, S.; Mu, Y.; Jiao, Y.; Stere, C. E. .; Chen, H.; Fan, X.; Hardacre, C. Mechanistic Study of Non-Thermal Plasma Assisted CO_2 Hydrogenation over Ru Supported on MgAl Layered Double Hydroxide. Appl. Catal. B Environ. 2020, 268, 118752. https://doi.org/10.1016/j.apcatb.2020.118752.

[5] Hussein, A. M. A.; Burra, K. G.; Bassioni, G.; Hammouda, R. M.; Gupta, A. K. Production of CO from CO_2 over Mixed-Metal Oxides Derived from

Layered-Double-Hydroxides. Appl. Energy 2019, 235 (October 2018), 1183–1191. https://doi.org/10.1016/j.apenergy.2018.11.040.

[6] Chaillot, D.; Bennici, S.; Brendlé, J. Layered Double Hydroxides and LDH-Derived Materials in Chosen Environmental Applications: A Review. Environmental Science and Pollution Research. 2021, pp 24375–24405. https://doi.org/10.1007/s11356-020-08498-6.

[7] Dewangan, N.; Hui, W. M.; Jayaprakash, S.; Bawah, A. R.; Poerjoto, A. J.; Jie, T.; Jangam, A.; Hidajat, K.; Kawi, S. Recent Progress on Layered Double Hydroxide (LDH) Derived Metal-Based Catalysts for CO_2 Conversion to Valuable Chemicals. Catal. Today 2020, 356, 490–513. https://doi.org/10.1016/j.cattod.2020.06.020.

[8] Fang, X.; Chen, C.; Jia, H.; Li, Y.; Liu, J.; Wang, Y.; Song, Y.; Du, T.; Liu, L. Progress in Adsorption-Enhanced Hydrogenation of CO_2 on Layered Double Hydroxide (LDH) Derived Catalysts. J. Ind. Eng. Chem. 2021, 95, 16–27. https://doi.org/10.1016/j.jiec.2020.12.027.

[9] Prinetto, F.; Ghiotti, G.; Graffin, P.; Tichit, D. Synthesis and Characterization of Sol-Gel Mg/Al and Ni/Al Layered Double Hydroxides and Comparison with Co-Precipitated Samples. Microporous and Mesoporous Materials. 2000, pp 229–247. https://doi.org/10.1016/S1387-1811(00)00197-9.

[10] Rivera, J. A.; Fetter, G.; Bosch, P. Microwave Power Effect on Hydrotalcite Synthesis. Microporous Mesoporous Mater. 2006, 89 (1–3), 306–314. https://doi.org/10.1016/j.micromeso.2005.10.041.

[11] Benito, P.; Guinea, I.; Labajos, F. M.; Rocha, J.; Rives, V. Microwave-Hydrothermally Aged Zn,Al Hydrotalcite-like Compounds: Influence of the Composition and the Irradiation Conditions. Microporous Mesoporous Mater. 2008, 110 (2–3), 292–302. https://doi.org/10.1016/j.micromeso.2007.06.013.

[12] Miyata, S. Physico-Chemical Properties of Synthetic Hydrotalcites in Relation to Composition. Clays Clay Miner. 1980, 28 (1), 50–56. https://doi.org/10.1346/ccmn.1980.0280107.

[13] Taylor, H. F. W. Crystal Structures of Some Double Hydroxide Minerals. Mineral. Mag. 1973, 39 (304), 377–389. https://doi.org/doi.org/10.1180/minmag.1973.039.304.01.

[14] Cavani, F.; Trifirò, F.; Vaccari, A. Hydrotalcite-Type Anionic Clays: Preparation, Properties and Applications. Catal. Today 1991, 11 (2), 173–301. https://doi.org/10.1016/0920-5861(91)80068-K.

[15] Pfeiffer, H.; Martínez-Dlcruz, L.; Lima, E.; Flores, J.; Vera, M. A. .; Valente, J. S. . Influence of Mg/Al Ratio on the Thermokinetic Rehydration of Calcined Mg-Al Layered Double Hydroxides. J. Phys. Chem. C 2010, 114 (18), 8485–8492. https://doi.org/10.1021/jp1011457.

[16] Valente, J. S.; Hernandez-Cortez, J.; Cantu, M. S.; Ferrat, G.; López-Salinas, E. Calcined Layered Double Hydroxides Mg-Me-Al (Me: Cu, Fe, Ni, Zn)

as Bifunctional Catalysts. Catalysis Today. 2010, pp 340–345. https://doi.org/10.1016/j.cattod.2009.08.020.

[17] Cherepanova, S. V.; Leont'Eva, N. N.; Arbuzov, A. B.; Drozdov, V. A.; Belskaya, O. B.; Antonicheva, N. V. Structure of Oxides Prepared by Decomposition of Layered Double Mg-Al and Ni-Al Hydroxides. J. Solid State Chem. 2015, 225, 417–426. https://doi.org/10.1016/j.jssc.2015.01.022.

[18] Millange, F.; Walton, R. I. .; O'Hare, D. Time-Resolved in Situ X-Ray Diffraction Study of the Liquid-Phase Reconstruction of Mg-Al-Carbonate Hydrotalcite-like Compounds. J. Mater. Chem. 2000, 10, 1713–1720. https://doi.org/doi.org/10.1039/B002827O.

[19] Mokhtar, M.; Inayat, A.; Ofili, J.; Schwieger, W. Thermal Decomposition, Gas Phase Hydration and Liquid Phase Reconstruction in the System Mg/Al Hydrotalcite/Mixed Oxide: A Comparative Study. Applied Clay Science. 2010, pp 176–181. https://doi.org/10.1016/j.clay.2010.07.019.

[20] Pfeiffer, H.; Lima, E.; Lara, V.; Valente, J. S. . Thermokinetic Study of the Rehydration Process of a Calcined MgAl-Layered Double Hydroxide. Langmuir 2010, 26 (6), 4074–4079. https://doi.org/10.1021/la9035248.

[21] Kikhtyanin, O.; Tišler, Z.; Velvarská, R.; Kubička, D. Reconstructed Mg-Al Hydrotalcites Prepared by Using Different Rehydration and Drying Time: Physico-Chemical Properties and Catalytic Performance in Aldol Condensation. Appl. Catal. A Gen. 2017, 536, 85–96. https://doi.org/doi.org/10.1016/j.apcata.2017.02.020.

[22] Li, J.; Zhou, X.; Wang, F.; Ning, X.; Wen, Y.; Song, B.; Yang, C.; Wu, D.; Ke, X.; Peng, L. Insights into Memory Effect Mechanisms of Layered Double Hydroxides with Solid-State NMR Spectroscopy. Nat. Commun. 2022, 13, 6093.

[23] Zhu, Y.; Zhu, R.; Chen, Q.; Laipan, M.; Zhu, J.; Xi, Y.; He, H. Calcined Mg/Al Layered Double Hydroxides as Efficient Adsorbents for Polyhydroxy Fullerenes. Appl. Clay Sci. 2018, 151, 66–72. https://doi.org/10.1016/j.clay.2017.10.018.

[24] Besharatlou, S.; Anbia, M.; Salehi, S. Optimization of Sulfate Removal from Aqueous Media by Surfactant-Modified Layered Double Hydroxide Using Response Surface Methodology. Mater. Chem. Phys. 2021, 262, 124322. https://doi.org/10.1016/j.matchemphys.2021.124322.

[25] Zhao, J.; Zhang, L.; Zhang, S.; Yuan, W.; Fang, X.; Yu, Q.; Qiu, X. Remediation of Chromium-Contaminated Soil Using Calcined Layered Double Hydroxides Containing Different Divalent Metals: Temperatures and Mechanism. Chem. Eng. J. 2021, 425, 131405. https://doi.org/10.1016/j.cej.2021.131405.

[26] Zhang, L.; Xiong, Z.; Li, L.; Burt, R.; Zhao, X. S. Uptake and Degradation of Orange II by Zinc Aluminum Layered Double Oxides. J. Colloid Interface Sci. 2016, 469, 224–230. https://doi.org/10.1016/j.jcis.2016.02.005.

[27] Xu, Z. P.; Guo, Q. L. Hydrothermal Synthesis of Layered Double Hydroxides (LDHs) from Mixed MgO and Al_2O_3: LDH Formation Mechanism. Chem. Mater. 2005, 17 (5), 1055–1062. https://doi.org/10.1021/cm048085g.

[28] Rocha, J.; Del Arco, M.; Rives, V.; Ulibarri, M. A. Reconstruction of Layered Double Hydroxides from Calcined Precursors: A Powder XRD and ^{27}A1 MAS NMR Study. J. Mater. Chem. 1999, 9 (10), 2499–2503. https://doi.org/10.1039/a903231b.

[29] Ogawa, M.; Hiramine, M. Direct Correlation between Nanostructure and Particle Morphology during Intercalation. Cryst. Growth Des. 2014, 14 (4), 1516–1519. https://doi.org/10.1021/cg401684u.

[30] Bookin, A. S.; Drits, V. A. Polytype Diversity of the Hydrotalcite-like Minerals I. Possible Polytypes and Their Diffraction Features. Clays Clay Miner. 1993, 41 (5), 551–557. https://doi.org/10.1346/CCMN.1993.0410504.

[31] Newman, S. P.; Jones, W.; O'Connor, P.; Stamires, D. N. Synthesis of the 3R2 Polytype of a Hydrotalcite-like Mineral. J. Mater. Chem. 2002, 12 (2), 153–155. https://doi.org/10.1039/b110715c.

[32] Prestopino, G.; Arrabito, G.; Generosi, A.; Mattoccia, A.; Paci, B.; Perez, G.; Verona-Rinati, G.; Medaglia, P. G. Emerging Switchable Ultraviolet Photoluminescence in Dehydrated Zn/Al Layered Double Hydroxide Nanoplatelets. Scientific Reports. 2019. https://doi.org/10.1038/s41598-019-48012-8.

[33] Cheah, L. A.; Manohara, G. V.; Maroto-Valer, M. M.; Garcia, S. Layered Double Hydroxide (LDH)-Derived Mixed Metal Oxides (MMOs): A Systematic Crystal-Chemical Approach to Investigating the Chemical Composition and Its Effect on High Temperature CO_2 Capture. ChemistrySelect 2020, 5 (19), 5587–5594. https://doi.org/10.1002/slct.201904447.

[34] MacKenzie, K. J. D.; Meinhold, R. H.; Sherriff, B. L.; Xu;, Z. ^{27}Al and ^{25}Mg Solid-State Magic-Angle Spinning Nuclear Magnetic Resonance Study of Hydrotalcite and Its Thermal Decomposition Sequence.Pdf. J. Mater. Chem. 1993, 3 (12), 1263–1269.

[35] A. Aramendía, M.; Avilés, Y.; Borau, V.; M. Luque, J.; M. Marinas, J.; R. Ruiz, J.; J. Urbano, F. Thermal Decomposition of Mg/Al and Mg/Ga Layered-Double Hydroxides: A Spectroscopic Study. J. Mater. Chem. 1999, 9 (7), 1603–1607. https://doi.org/10.1039/A900535H.

[36] Sepelak, V.; Bergmann, I.; Indris, S.; Feldhoff, A.; Hahn, H.; Becker, K. D.; Grey, C. P. ; Heitians, P. High-Resolution 27Al MAS NMR Spectroscopic Studies of the Response of Spinel Aluminates to Mechanical Action. J. Mater. Chem. 2011, 21, 8332.

[37] Yang, W.; Kim, Y.; Liu, P. K. T.; Sahimi, M.; Tsotsis, T. T. A Study by in Situ Techniques of the Thermal Evolution of the Structure of a Mg-Al-CO_3

Layered Double Hydroxide. Chem. Eng. Sci. 2002, 57 (15), 2945–2953. https://doi.org/10.1016/S0009-2509(02)00185-9.

[38] Kim, B. K.; Gwak, G. H.; Okada, T.; Oh, J. M. Effect of Particle Size and Local Disorder on Specific Surface Area of Layered Double Hydroxides upon Calcination-Reconstruction. J. Solid State Chem. 2018, 263 (December 2017), 60–64. https://doi.org/10.1016/j.jssc.2018.03.041.

[39] Ahmed, A. A. A.; Talib, Z. A.; Hussein, M. Z. Bin; Zakaria, A. Improvement of the Crystallinity and Photocatalytic Property of Zinc Oxide as Calcination Product of Zn-Al Layered Double Hydroxide. J. Alloys Compd. 2012, 539, 154–160. https://doi.org/10.1016/j.jallcom.2012.05.093.

[40] Ye, H.; Liu, S.; Yu, D.; Zhou, X.; Qin, L.; Lai, C.; Qin, F.; Zhang, M.; Chen, W.; Chen, W.; Xiang, L. Regeneration Mechanism, Modification Strategy, and Environment Application of Layered Double Hydroxides: Insights Based on Memory Effect. Coord. Chem. Rev. 2022, 450, 214253. https://doi.org/10.1016/j.ccr.2021.214253.

[41] Thommes, M.; Kaneko, K.; Neimark, A. V.; Olivier, J. P.; Rodriguez-Reinoso, F.; Rouquerol, J.; Sing, K. S. W. Physisorption of Gases, with Special Reference to the Evaluation of Surface Area and Pore Size Distribution (IUPAC Technical Report). Pure Appl. Chem. 2015, 87 (9–10), 1051–1069. https://doi.org/10.1515/pac-2014-1117.

[42] Schlumberger, C.; Thommes, M. Characterization of Hierarchically Ordered Porous Materials by Physisorption and Mercury Porosimetry—A Tutorial Review. Adv. Mater. Interfaces 2021, 8 (4), 2002181. https://doi.org/10.1002/admi.202002181.

[43] Navajas, A.; Campo, I.; Moral, A.; Echave, J.; Sanz, O.; Montes, M.; Odriozola, J. A.; Arzamendi, G.; Gandía, L. M. Outstanding Performance of Rehydrated Mg-Al Hydrotalcites as Heterogeneous Methanolysis Catalysts for the Synthesis of Biodiesel. Fuel 2018, 211, 173–181. https://doi.org/10.1016/j.fuel.2017.09.061.

[44] Zhang, S. T.; Dou, Y.; Zhou, J.; Pu, M.; Yan, H.; Wei, M.; Evans, D. G.; Duan, X. DFT-Based Simulation and Experimental Validation of the Topotactic Transformation of MgAl Layered Double Hydroxides. ChemPhysChem 2016, 2754–2766. https://doi.org/10.1002/cphc.201600354.

[45] Pavel, O. D.; Zăvoianu, R.; Bîrjega, R.; Angelescu, E. The Effect of Ageing Step Elimination on the Memory Effect Presented by $Mg_{0.75}Al_{0.25}$ Hydrotalcites (HT) and Their Catalytic Activity for Cyanoethylation Reaction. Catalysis Communications. 2011, pp 845–850. https://doi.org/10.1016/j.catcom.2011.02.005.

[46] Kloprogge, J. T.; Frost, R. L. Fourier Transform Infrared and Raman Spectroscopic Study of the Local Structure of Mg-, Ni-, and Co-Hydrotalcites. J. Solid State Chem. 1999, 146 (2), 506–515. https://doi.org/10.1006/jssc.1999.8413.

[47] Prinetto, F.; Ghiotti, G.; Durand, R.; Tichit, D. Investigation of Acid-Base Properties of Catalysts Obtained from Layered Double Hydroxides. J. Phys. Chem. B 2000, 104 (47), 11117–11126. https://doi.org/10.1021/jp002715u.

[48] Boumaza, A. .; Favaro, L. .; Le´dion, J. .; Sattonnay, G. .; Brubach, J. B. .; Berthet, P. .; Huntz, A. M. .; Roy, P. .; Te´tot, R. . Transition Alumina Phases Induced by Heat Treatment of Boehmite: An X-Ray Diffraction and Infrared Spectroscopy Study. J. Solid State Chem. 2009, 182, 1171–1176.

[49] Kloprogge, J. T.; Frost, R. L. Infrared Emission Spectroscopic Study of the Thermal Transformation of Mg-, Ni- and Co-Hydrotalcite Catalysts. Applied Catalysis A: General. 1999, pp 61–71. https://doi.org/10.1016/s0926-860x(99)00084-8.

[50] Resini, C.; Montanari, T.; Barattini, L.; Ramis, G.; Busca, G.; Presto, S.; Riani, P.; Marazza, R.; Sisani, M.; Marmottini, F.; Costantino, U. Hydrogen Production by Ethanol Steam Reforming over Ni Catalysts Derived from Hydrotalcite-like Precursors: Catalyst Characterization, Catalytic Activity and Reaction Path. Applied Catalysis A: General. 2009, pp 83–93. https://doi.org/10.1016/j.apcata.2008.11.029.

[51] Pavel, O. D.; Bîrjega, R.; Che, M.; Costentin, G.; Angelescu, E.; Şerban, S. The Activity of Mg/Al Reconstructed Hydrotalcites by “Memory Effect” in the Cyanoethylation Reaction. Catalysis Communications. 2008, pp 1974–1978. https://doi.org/10.1016/j.catcom.2008.03.027.

CHAPTER 3

Effect of Gas Composition on Temperature and CO_2 Conversion in a Gliding Arc Plasmatron reactor: Insights for Post-plasma Catalysis from Experiments and Computation

This chapter is adapted from the paper "Effect of Gas Composition on Temperature and CO_2 Conversion in a Gliding Arc Plasmatron reactor: Insights for Post-plasma Catalysis from Experiments and Computation; Wencong Xu, Senne Van Alphen, Vladimir V. Galvita, Vera Meynen, Annemie Bogaerts", to be submitted to Fuel.

Abstract

Plasma-based CO_2 conversion has attracted increasing interest. In this chapter, we investigate different conditions by introducing additional gases such as N_2, N_2/CH_4 and $N_2/CH_4/H_2O$ into the CO_2 feed gas within a gliding arc plasmatron. We aim to provide valuable insights for potential synergistic applications in post-plasma catalysis (PPC) systems for which the temperature and plasma exhaust gas compositions are crucial as they are the feed gas conditions for the post-plasma catalysis and thus determine the design of the PPC system, adjusted to the plasma conditions applied and the catalytic reactions envisioned. To achieve this, we measured the temperature at various points after the plasma discharge. Adding only N_2 to CO_2 improves the CO_2 absolute conversion from 4% (with 100% CO_2) to 13% (with 20% CO_2), while the addition of CH_4 resulted in a further dramatic increase in CO_2 conversion to 44% (in a $CO_2/CH_4/N_2$ mixture of 1:1:8) at a total flow rate of 10 L/min. This conversion can be further enhanced upon decreasing the gas flow rate, reaching 61% at a flow rate of 6 L/min. By varying the CO_2/CH_4 ratio from 0.6 to 1.67 while keeping N_2 at 80% and a gas flow rate of 8 L/min, the CO_2 conversion slightly increased from 51% ($CO_2/CH_4 = 0.78$) to 58% ($CO_2/CH_4 = 0.6$). However, the addition of H_2O (at a gas flow rate of 8 L/min and $CO_2/CH_4 = 1$) reduced the CO_2 conversion from 55% (0% relative humidity, RH) to 22% (100% RH). In contrast, the H_2/CO ratio showed an increasing trend from 1.45 to 2, demonstrating the benefit of H_2O addition for downstream processing of the

formed syngas. Moreover, the addition of H_2O was also beneficial to reduce the energy cost (EC) from 5.8 (0% RH) to 3 (40% RH) kJ/L. Regarding the temperature at 4.9 cm from the outlet of the plasma, the addition of N_2 was favourable as it resulted in higher temperatures, albeit with reduced plasma flame stability. A slight increase in temperature was also observed with higher gas flow rates, but the CO_2/CH_4 ratio had no significant effect on temperature. The obtained temperature profiles provide insights into the impact of feed composition on plasma exhaust gas temperature and where to position a post-plasma catalysis bed, in order to benefit from heat recovery by integrating post-plama catalysis with warm plasma-based processes.

3.1 Introduction

In the past decades, accumulating evidence has demonstrated that the increasing emission of greenhouse gases is leading to global warming [1]. Specifically, the concentration of CO_2 in the atmosphere has risen significantly, surging from 362 ppm at the end of the last century to 420 ppm in June 2023, based on the data from the "National Oceanic and Atmospheric Administration (NOAA) Global Monitoring Laboratory" (https://gml.noaa.gov/ccgg/trends/). Therefore, numerous techniques are being developed to capture CO_2 and convert it into value-added fuels or chemical products [2–6]. Several different chemical processes, including CO_2 splitting (Eq.(3.1)), CO_2 methanation with H_2 (Eq.(3.2)), and CO_2 dry reforming of methane (DRM) (Eq.(3.3), have been investigated for the conversion of CO_2 either directly or in combination with other molecules like CH_4, H_2, or/and H_2O [7–9]. However, as a relatively stable molecule, the activation of CO_2 remains a significant challenge for many (catalytic) reactions. Thermally, direct CO_2 splitting is energy-consuming and only favourable at quite high temperatures. For instance, at 2000 K, it is estimated that to achieve a CO_2 conversion of 1.5%, the energy cost (EC) will be about 7.9 MJ/mol and the final energy efficiency (EE) is just 4.4% [10].

$$CO_2 \rightarrow CO + 1/2\ O_2,\ \ \Delta H^0 = 283 kJ/mol \quad (3.1)$$

$$CO_2 + \ 4H_2 \rightarrow CH_4 + 2H_2O,\ \ \Delta H^0 = -165 kJ/mol \quad (3.2)$$

$$CO_2 + CH_4 \rightarrow 2CO + 2H_2,\ \ \Delta H^0 = 247.3 kJ/mol \quad (3.3)$$

In recent years, plasma technology has been widely applied in CO_2 conversion because it can activate the gas molecules by electron impact excitation, ionization and dissociation via electrical energy supply. This creates excited species, ions and radicals that can form new molecules [10,11]. Compared with conventional thermal approaches, electrical energy is transferred to the gas, making it a promising technology for the ongoing energy transition in chemical production [12–17]. Furthermore, plasma can be integrated with catalysts to create a hybrid plasma catalysis process, which holds promise for enhancing CO_2 conversion, improving energy efficiency and chemical product selectivity [14,18–20]. A lot of research on CO_2 conversion is performed with various kinds of plasmas, including a dielectric barrier discharge (DBD) [21], microwave (MW) [22] and spark or gliding arc (GA) discharge [11,23]. Among these plasma techniques, gliding arc plasma is promising, because it operates at atmospheric pressure and is known as one of the most energy-efficient plasma reactors (electron energy ~ 1 eV, which is ideal to activate CO_2 [11]). Moreover, the GA creates heat in the plasma zone, with temperatures up to a few 1000 K [24,25], which influences the reactions and allows for post-plasma catalysis in the exhaust stream of the plasma reactor, recovering (at least part of) the heat of the plasma process [26–28].

Several different types of GA plasmas have been designed, e.g. classical 2D GA [29], 3D rotating gliding arc (RGA) [30,31], 3D gliding arc plasmatron (GAP) [11] and dual-vortex plasmatron (DVP) [25]. The classical 2D GA plasma is widely studied, however, it exhibits some drawbacks, as it is incompatible with industrial applications because of its 2D flat electrodes. Furthermore, not all the gas passes through the arc, and thus it is not fully activated. Finally, a relatively high gas flow rate is needed to sustain the arc gliding process, which gives rise to a short gas residence time in the plasma. To overcome these problems, several 3D gliding arc plasma reactor designs have been developed over the years, as mentioned above, in which the gas flows tangentially into the reactor, forming a stable vortex gas flow [11,30,32]. Furthermore, recently, a novel DVP reactor was designed and tested, enabling to separate the arc into two directions with longer residence time and highly turbulent flow [25].

Ramakers et al. studied the conversion of CO_2 in the GAP reactor, yielding as highest CO_2 conversion 8.6% and an energy efficiency EE of 30% at an energy cost EC of 39 kJ/L [11]. The group PLASMANT also investigated DRM in the GAP, achieving absolute CO_2 and CH_4 conversions of about 24% and 42%, or effective conversions of about 18% and 10%, respectively, at a CH_4 fraction of 25% in the gas flow, corresponding to an EC of 10 kJ/L and an EE of 66% [23]. In a later study, the same group reported DRM upon the addition of N_2 and O_2 in the

same GAP reactor, and obtained absolute CO_2 conversions between 31% and 52%, and CH_4 conversions between 55 and 99%, corresponding to a total EC of 13 – 20 kJ/L (or 3.4 - 5.0 eV/molecules), depending on the gas mixture [33]. Recently, the addition of only N_2 to the DRM process was studied, and it was found that 20% N_2 addition yields CO_2 and CH_4 absolute conversions of 29 and 36%. However, these values rise notably upon N_2 addition, up to 48% for CO_2 and 61% for CH_4 at 80% N_2 [34]. However, although the influence of gas composition on conversion and energy efficiency was described, the impact on temperature generated in the plasma exhaust was not experimentally measured in relation to the feed gas composition. This is however important when integrating plasma with post-plasma catalysis.

To fully make use of the heat produced by GA plasma, research has been focused on establishing synergistic effects of heterogeneous catalysis in combination with the plasma. Zhang et al. reported a combination of GA plasma with a post-plasma catalyst bed with TiO_2 for CO_2 splitting [35]. Simulation of the addition of a post-plasma catalyst bed indicated that a strong backflow was formed and experiments confirmed an enhancement in reaction performance. Notably, when the distance between the plasma reactor outlet and the catalyst bed was only 5 mm, fluctuations in CO_2 conversion and EE occurred at flow rates lower than 4 L/min. A synergistic effect was observed because the presence of TiO_2 enhanced the CO_2 conversion

from 4.6 to 10.8% and the EE from 5.4 to 12.6% at a gas flow rate of 2 L/min. In another study, a 25% increase in CH_4 conversion, a 20% increase in CO_2 conversion, around 30% increase in H_2 yield and about 22% increase in EE were achieved when combining a NiO/Al_2O_3 catalyst with a GA plasma in DRM [36]. Significant improvements were obtained when a GA plasma was combined with $Ni/CeO_2/Al_2O_3$ catalyst post-plasma and extra heating was supplied to the catalyst by a tubular furnace [37]. However, when there was no extra heating, the performance of the plasma with the catalyst was almost the same as the plasma alone. This could be explained because of the low temperature (around 300-500 °C) of the plasma gas effluent, at which range the catalyst was inactive for DRM. When the tubular furnace was heated, a synergistic effect of plasma and catalyst resulted in an increase in CO_2 and CH_4 conversion from about 25% to 59% and from 39% to 70%, respectively. Hence, apart from the importance of the plasma exhaust gas composition serving as feed gas to the post-plasma catalyst bed, the temperature at the outlet of the plasma GAP reactor is also important when combining it with a post-plasma catalysis bed. Nevertheless, to our knowledge, little literature reported on the variation of temperature after plasma in relation to the gas composition used.

In this chapter, we employed a GAP setup, which was reported before [38], to investigate the impact of additional gases, such as N_2, CH_4, and H_2O vapour on the CO_2 conversion on both exhaust gas composition as well as exhaust gas

temperature as a function of distance to the GAP. We aim to provide suggestions for selecting optimal conditions for the DRM reaction in our later research, combining GAP with post-plasma catalysis (see next chapters). Here, both exhaust gas composition, serving as feed gas for the catalytic reaction post-plasma, as well as heat transferred to the catalyst bed, are important features, which should be optimized simulataneously. Moreover, we recorded the temperature after the plasma, offering insights into where to position the catalyst to optimally transfer the heat originating from the plasma to the catalyst, enabling it to catalyze the conversion of remaining unreacted reactants and/or products (e.g. syngas) in the plasma exhaust to useful chemicals in the post-plasma system.

3.2 Experimental

3.2.1 Gliding arc setup

The GAP setup used in the experiments was previously reported in detail, although some changes in the tubular post-plasma reactor tube part have been made [11,38]. Generally, it is a 3D gliding arc plasmatron in which the gas flow enters through several tangential inlets and forms a vortex flow. The vortex flow helps to stabilize the arc formed inside the reactor and forces the gas to first flow in a forward vortex (till the closed end of the reactor), after which it forms a smaller reverse vortex that flows through the plasma [38]. The cathode and anode are separated by an insulator made of Teflon and alumina ceramics. The post-plasma reactor tube is made of

quartz with a length of 200 mm and a diameter of 64 mm. Three tubes with a diameter of 10 mm are connected at the side of the reactor for thermocouples to be inserted at different positions (Fig. 3.1). The power supply for the reactor is a DC source type (APS – Advanced Plasma Solutions). The plasma voltage and current were measured by a high-voltage probe (Pintek HVP-15HF) and a current sense resistor of 3 Ω, respectively. The signals of voltage and current were collected by a two-channel digital storage oscilloscope (Tektronix TDS 2012C). The current was fixed at 0.25 A.

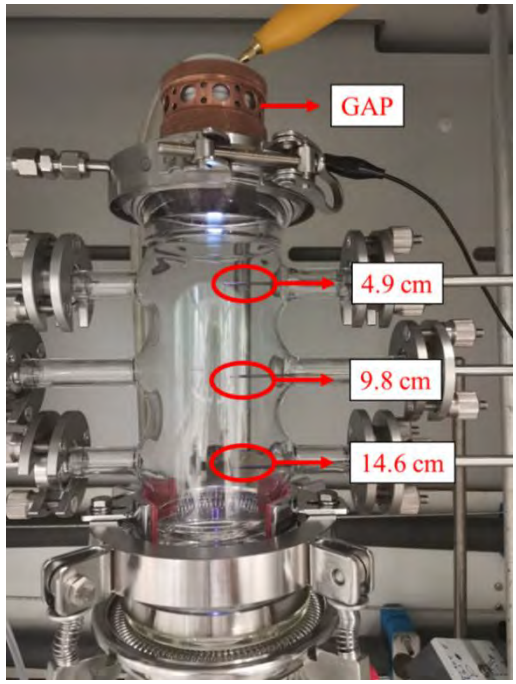

Fig. 3.1. Photograph of the GAP set up with plasma on (gas flow rate:10 L/min, $CO_2/N_2 = 1$) and thermocouples at different positions (4.9 cm, 9.8 cm and 14.6 cm).

3.2.2 Temperature collection

Three thermocouples, which were placed at different positions (4.9 cm, 9.8 cm, and 14.6 cm) after the GAP reactor outlet (Fig. 3.1), were inserted into the post-plasma reactor tube to measure the temperature post-plasma. A four-channel datalogger thermometer (HH-521BT) was used to collect the temperature values.

3.2.3 Gas flows

Mass-flow controllers (Bronkhorst) were used to control the amount of CO_2, CH_4, and N_2 entering into the GAP. The purity of CO_2 and CH_4 is 99.5% and that of N_2 is 99.999%. When the mixture of CO_2/N_2 was used, the total gas flow rate was 10 L/min and the CO_2 amount varied from 0 to 10 L/min. When using the gas mixture of $CO_2/CH_4/N_2$, the total gas flow rate varied between 6 L/min and 12 L/min. The gas ratio of CO_2/CH_4 was changed from 0.6 to 1.67, keeping the mixture gas flow rate and N_2 flow rate fixed at 8 L/min and 6.4 L/min, respectively.

Considering H_2O dissociation can produce oxygen atoms and possibly H_2 in the plasma, the H_2O is introduced to the DRM feed gas, aiming at increasing the H_2 fraction in the product mix (leading to a higher syngas ratio, which is beneficial for further Fischer-Tropsh or methanol synthesis [28,39]) and decreasing the possible carbon deposition (coking) [40]. Deionized water was put into a sealed cylinder connected with N_2 and pressed into a controlled evaporator mixer (CEM,

Bronkhorst). The amount of water mixed with the feed gas was controlled by a liquid flow controller. The temperature for heating the H_2O and gas mixture was 70°C and the relative humidity (RH) varied from 0% to 100%. When using mixtures with water, the total gas flow rate was fixed at 8 L/min and the concentrations of CO_2, CH_4 and N_2 were 10%, 10% and 80%, respectively. The H_2O was added in the vapour phase with relative humidity (RH) of 10%, 40%, 70% and 100%, corresponding to 13 g/h, 58 g/h, 113 g/h, and 183 g/h H_2O added through the liquid flow controller. After plasma and before the gas entering into the GC, a condenser tube was used and iced water went through it to stop unconverted H_2O from entering into the GC.

3.2.4 Product analysis

The gas compositions of the feed gas and products at the outlet were analyzed by gas chromatography (GC) (Thermo Scientific, Trace 1300). The results were calculated by the equations below.

3.2.4.1 Gas composition of CO_2/N_2

For the CO_2/N_2 system, the absolute conversion of CO_2, X_{abs,CO_2} and effective conversion of CO_2, X_{eff,CO_2} were calculated with Eq. (3.4) and Eq. (3.5), respectively. $C_{CO_{2,in}}$ was the concentration of CO_2 measured going through the

GAP before the plasma was turned on. $C_{CO_{2,out}}$ was the concentration of outlet gas.

$$X_{abs,CO_2}(\%) = \frac{C_{CO_{2,in}} - C_{CO_{2,out}}}{C_{CO_{2,in}}} \times 100\% \quad (3.4)$$

$$X_{eff,CO_2}(\%) = X_{abs,CO_2}(\%) \cdot Fraction_{CO_2} \quad (3.5)$$

where $Fraction_{CO_2}$ means the concentration of CO_2 in the inlet gas.

A correction factor α was introduced by Eq. (3.6). The correction was done with N_2 as an internal standard to correct for any gas expansion [41]. In our system, as He is the carrier gas in the GC, it cannot be used, and neither can Ar, because its peak overlaps with that of O_2. Therefore, N_2 was used as the internal standard gas. In the mixture in the plasma zone, N_2 was barely converted in the GAP (< 0.05%) and therefore it can be used as internal standard gas [34].

$$\alpha = \frac{N_{2,blank}}{N_{2,plasma}} \quad (3.6)$$

Where $N_{2,blank}$ and $N_{2,plasma}$ represent the amount of N_2 measured before and after igniting the plasma.

Therefore, the $C_{CO_{2,out}}$ was corrected from the GC-measured value of $C_{CO_{2,out,m}}$ by the Eq. (3.7):

$$C_{CO_{2,out}} = \alpha \cdot C_{CO_{2,out,m}} \quad (3.7)$$

The specific energy input (SEI) and energy cost (EC) for converting CO_2 were calculated with Eq. (3.8) and Eq. (3.9).

$$\mathrm{SEI(kJ/L)} = \frac{\text{Plasma Power (kW)} \cdot 60\ \text{(s/min)}}{\text{Total gas flow rate (L/min)}} \tag{3.8}$$

$$\mathrm{EC(kJ/L)} = \frac{\mathrm{SEI\ (kJ/L)}}{\mathrm{X_{eff,CO_2}}} \tag{3.9}$$

3.2.4.2 Gas composition of $CO_2/CH_4/N_2$ and $CO_2/CH_4/N_2/H_2O$

For the calculation of the results in the $CO_2/CH_4/N_2$ and $CO_2/CH_4/N_2/H_2O$ systems, the formulas were used as derived by Pinhao et al. [42]. In the case of adding H_2O, the amount of H_2O utilized in the reaction was hard to quantify. Therefore, the atoms it offered were ignored in the calculation, which allowed us to only qualitatively analyze the effect of H_2O addition. Another correction factor β was used via formula (3.10), which was introduced to account for the change in gas flow rate due to composition variation.

$$\beta = \frac{\mathrm{N_{2,in}}}{\mathrm{CO_{2,in} + CH_{4,in}}} \tag{3.10}$$

where $\mathrm{N_{2,in}}$, $\mathrm{CO_{2,in}}$, and $\mathrm{CH_{4,in}}$ were the gas flow rate of N_2, CO_2, and CH_4 in the feed gas, respectively.

The value of factor α was corrected by β with Eq. (3.11):

$$\alpha = \frac{\mathrm{N_{2,blank}}}{\mathrm{N_{2,plasma}}}(1+\beta) - \beta \tag{3.11}$$

The concentrations were corrected with Eq. (3.12):

$$C_{i,out} = C_{i,out,m}(1 + \beta/\alpha) \quad (3.12)$$

Where $C_{i,out,m}$ means the concentration of sample i, i.e., CH_4, CO_2, CO, and H_2, measured by the GC.

The absolute and effective conversions of CO_2 were calculated the same as equations (3.4 and 3.5), except that the $C_{CO_{2,out}}$ was corrected by two factors (α and β) and calculated by Eq. (3.12). The absolute and effective conversions of CH_4 were calculated by equations (3.13 and 3.14).

$$X_{abs,CH_4}(\%) = \frac{C_{CH_{4,in}} - C_{CH_{4,out}}}{C_{CH_{4,in}}} \times 100\% \quad (3.13)$$

$$X_{eff,CH_4}(\%) = X_{abs,CH_4} \cdot Fraction_{CH_4} \quad (3.14)$$

The C-based selectivity of CO and other chemicals including carbon atoms, the H-based selectivity of H_2, and the yield of CO, and H_2 were calculated with Eq. (3.15) to Eq. (3.19):

$$S_{H_2} = \frac{C_{H_{2,out}}}{2 \times (C_{CH_{4,in}} - C_{CH_{4,out}})} \times 100\% \quad (3.15)$$

$$S_{CO} = \frac{C_{CO_{out}}}{(C_{CH_{4,in}} - C_{CH_{4,out}}) + (C_{CO_{2,in}} - C_{CH_{2,out}})} \times 100\% \quad (3.16)$$

$$S_{C_xH_yO_z} = \frac{x \times C_{C_xH_yO_{z,out}}}{(C_{CH_{4,in}} - C_{CH_{4,out}}) + (C_{CO_{2,in}} - C_{CH_{2,out}})} \times 100\% \quad (3.17)$$

$$Y_{CO} = \frac{Fraction_{CH_4} \times X_{abs,CH_4} + Fraction_{CO_2} \times X_{abs,CO_2}}{\left(C_{CH_{4,in}} - C_{CH_{4,out}}\right) + \left(C_{CO_{2,in}} - C_{CH_{2,out}}\right)} \times S_{CO} \quad (3.18)$$

$$Y_{H_2} = X_{abs,CH_4} \times S_{H_2} \quad (3.19)$$

The SEI was calculated via Eq. (3.8) and EC was calculated by the following Eq. (3.20):

$$EC(kJ/L) = \frac{SEI\ (kJ/L)}{X_{eff,CO_2} + X_{eff,CH_4}} \quad (3.20)$$

3.3 Computational

The simulation of the temperature distribution in the GAP DRM reactor was done by Senne Van Alphen from PLASMANT. The detailed description is shown in the Appendix B4 and B5.

3.4 Results and Discussion

3.4.1 CO_2 and CH_4 conversion

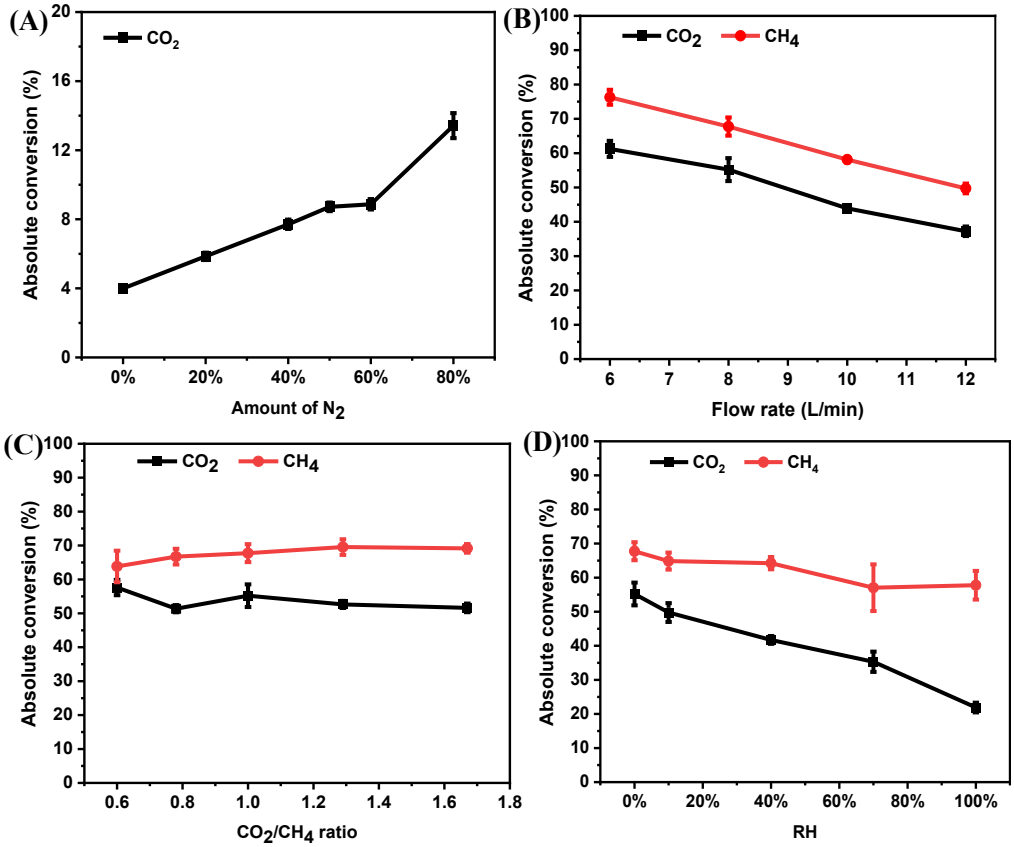

Fig. 3.2. Absolute conversions of CO_2 and CH_4 as a function of gas composition, gas flow rate and RH. (A) CO_2 conversion in CO_2/N_2 mixture: Total gas flow rate = 10 L/min, N_2 fraction varying from 0% to 80%. (B) Total gas flow rate varied from 6 to 12 L/min, $CO_2/CH_4/N_2$ = 1/1/8. (C) Total gas flow rate = 8 L/min, N_2 = 6.4 L/min, CO_2/CH_4 ratio varied between 0.6 and 1.67. (D) Total gas flow rate = 8 L/min, $CO_2/CH_4/N_2$ = 1/1/8, H_2O amount varied between 0% and 100% RH.

To quantify the CO_2 and CH_4 conversions, the absolute and effective conversions of these two gases were defined. The absolute conversion (Fig. 3.2), or simply called "conversion", gives a direct comparison between the different configurations, while the effective conversion (see Appendix, Fig. B.1) considers

the dilution of CO_2 or CO_2/CH_4 in N_2, which is relevant for application and economics as this limits and dilutes the product that is formed.

Fig. 3.2 presents the absolute conversions of CO_2 and CH_4 in different gas mixtures. In the CO_2/N_2 gas composition, a significant increase in absolute conversion of CO_2 is observed when N_2 was added into CO_2 from 0% to 80%, as shown in Fig. 3.2A. The value especially increases significantly when the N_2 fraction rises from 60% to 80%. A maximum absolute conversion of 13% was obtained for a N_2 fraction of 80%. Therefore, N_2 in the feed gas is beneficial for converting CO_2. The reason for this was explained already in literature: the CO_2 conversion in a GAP is most effective through the vibrational levels and the high N_2 vibrational levels help to populate the CO_2 vibrational levels [38]. It is interesting to note that at N_2 fractions of 50% and 60%, the CO_2 absolute conversion remained almost the same. A possible explanation might be that the gas temperature (Fig, 3.7A) also remained almost unchanged, as the N_2 fraction increased only 10% from 50% to 60%. Moreover, as the N_2 fraction was above 60%, the CO_2 conversion increased much more. The temperature data, as shown in Fig. 3.7A, shows a similar trend. It seems that the N_2 promotion effect at fractions below 50% is weaker than at fractions above 60%. For the fraction between 50% and 60%, a combined effect results in the CO_2 conversion and gas temperature remaining almost the same, which is probably because the energy transfer from N_2 for increasing the gas temperature

(the mechanism for it is explained in the temperature part in section 3.4.4) compensates the energy needed for the rise in CO_2 conversion.

For the effective conversion of CO_2, however, because of the decreasing CO_2 fraction in the mixture, it shows the opposite trend (see Appendix B, Fig. B.1A), with first a slight increase from 4% to 4.7% up to 20% N_2 fraction, and then a drop to 2.7% with increasing N_2 fraction. As the N_2 fraction is lower than 50%, the increase in absolute CO_2 conversion can, to some extent, compensate for the lower concentration of CO_2, but with a higher N_2 fraction, the rise in conversion is not enough to compensate for the drop of CO_2 conversion [38].

At the same gas flow rate of 10 L/min, once CH_4 is added into the mixture (Fig. 3.2B), the absolute conversion of CO_2 increases to 43%, more than three times the maximum value in the CO_2/N_2 mixture. Moreover, the conversion of CO_2 increases upon decreasing gas flow rate, reaching its highest value of 61% at a flow rate of 6 L/min. The reason that the highest conversion is obtained at the lowest flow rate is due to the longer residence time, giving sufficient time for more gas molecules to react in the plasma region. Besides this, the conversion of CH_4 is always higher than that of CO_2, because the energy needed for the plasma-based decomposition of CH_4 is lower than that for CO_2, due to the lower bond strength to break the C-H vs C=O bond (i.e., 4.48 eV vs 5.52 eV) [33]. This is different from what is observed

in a thermal catalytic DRM, in which the CO_2 conversion rate is usually higher than that of CH_4 due to the reverse water-gas shift reaction (RWGS, $CO_2 + H_2 \rightarrow CO + 2H_2O,\ \Delta H^0 = 41 kJ/mol$), consuming CO_2 from the feedstock [43]. Since the ratio of CO_2/CH_4 did not change in Fig. 3.2B, the effective conversions of both CO_2 and CH_4 show the same trend as the absolute conversions, but the values are lower. As shown in Fig. 3.3B, although a higher CO_2 conversion was obtained at lower flow rates, the cathode can be seriously damaged. Therefore, we used a gas flow rate of 8 L/min, at which the cathode was safe, to study how the CO_2/CH_4 ratio affects the conversion results.

Fig. 3.2C illustrates that a higher CO_2/CH_4 ratio slightly increases the absolute conversion of CH_4 from 64% to 69%, while the conversion of CO_2 first decreases a bit from about 58% (CO_2/CH_4 ratio of 0.6) to 51% (CO_2/CH_4 ratio of 0.78) and then stays generally constant. However, different from the absolute conversion, the effective conversion of CH_4 decreases significantly from 40% to 26% as the CO_2 fraction increases, while the CO_2 effective conversion shows an obvious increase from 22% to 32%. These conversion values are in line with previous results obtained for the GAP in $CO_2/CH_4/N_2$ mixtures [34], but they give additional insights into how to adjust the CO_2/CH_4 ratio to achieve better results.

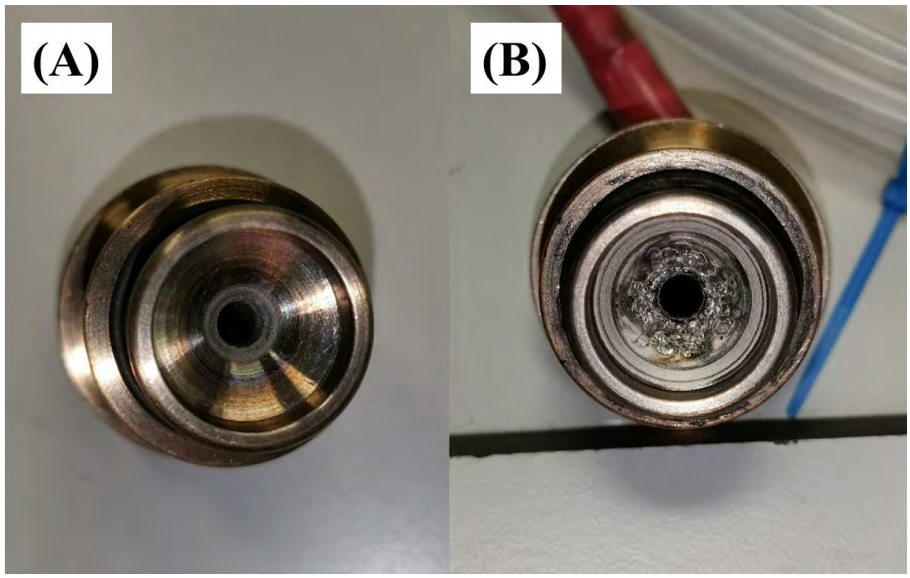

Fig. 3.3. Photographs of (A) clean reactor cathode, and (B) after reaction with a gas flow rate of 6 L/min, indicating clear damage of the cathode.

Compared with DRM without water, adding water causes a serious drop in the absolute conversion of CO_2, from 55% to 22% for RH ranging from 0% to 100% (Fig. 3.2D). This is attributed to the drop in electron density, as water is trapping the electrons [40]. Another reason is probably that the OH radicals produced by water splitting react with CO, forming CO_2 again, as revealed by detailed chemical kinetics modelling for DBD plasma, where a similar effect was observed [44]. The CH_4 conversion decreases less, from 68% to 58%. The effective conversions of CO_2 and CH_4 show the same, but less significant decreasing tendency. This is different from the literature, where it was reported that the CH_4 conversion increases as the molar ratio of H_2O molecules to carbon atoms increases from 0 to 0.58 [40]. This may be due to the difference in CO_2/CH_4 ratio. They used a 1.5 times higher ratio than what we used (ratio of 1).

In general, this section investigated the changes in (absolute) conversion of CO_2 when varying a number of parameters, i.e. gas composition, total gas flow rate and addition of H_2O. Compared with the N_2/CO_2 situation, with a maximum CO_2 absolute conversion of 13%, the addition of CH_4, leading to the DRM reaction, can increase its conversion to 43%. Besides this, decreasing the gas flow rate from 10 L/min to 6 L/min can further increase the CO_2 conversion to 61% with a CH_4 conversion of 76%. However, this low gas flow rate (6 L/min) can damage the GAP device. Therefore, a total gas flow rate of 8 L/min is better. Changing the ratio of CO_2/CH_4 in the DRM feed gas has limited influence on the CO_2 and CH_4 conversion, while the addition of H_2O caused a drop in CO_2 conversion. Ultimately, optimal conditions for further GAP DRM are selected based on the conversions with a total gas flow rate of 8 L/min and gas composition of CO_2:CH_4:N_2 of 1/1/8.

3.4.2 Products selectivity and H_2/CO ratio

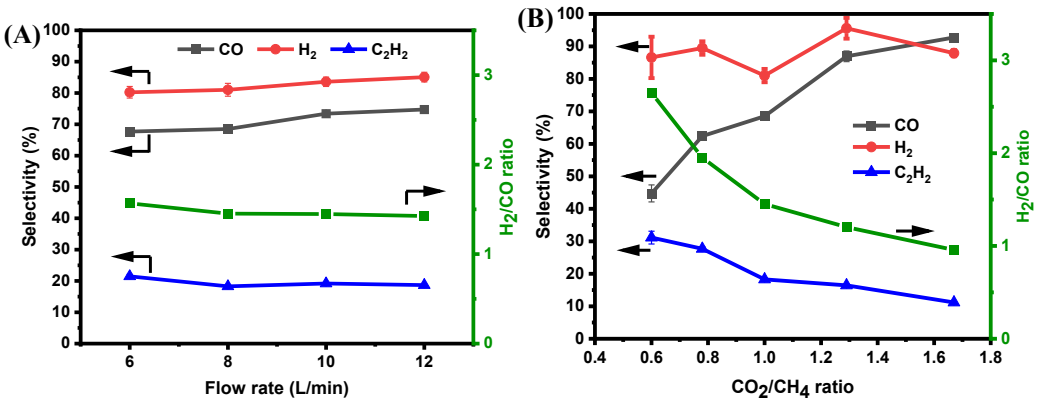

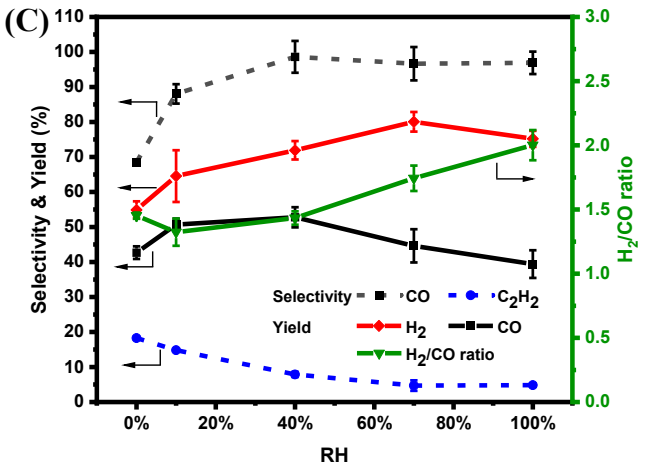

Fig. 3.4. Selectivity of CO, H_2, and C_2H_2 (left y-axes), as well as H_2/CO ratio (green curves; right y-axes), as a function of gas composition, gas flow rate and RH. (A) Total gas flow rate varied from 6 to 12 L/min, $CO_2/CH_4/N_2$ = 1/1/8. (B) Total gas flow rate = 8 L/min, N_2 = 6.4 L/min, CO_2/CH_4 ratio varied between 0.6 and 1.67. (C) Total gas flow rate = 8 L/min, $CO_2/CH_4/N_2$ = 1/1/8, H_2O amount varied between 0% and 100% RH.

As is clear from Fig. 3.4A, the selectivities of CO and H_2 both increase slightly upon increasing the gas flow rate, from 68% to 75%, and from 80% to 85%, respectively. In contrast, the selectivity of C_2H_2 first drops from 22 to 18% and then remains constant at around 19% upon higher gas flow rates. The H_2/CO ratio shows a similar trend, as it decreases firstly from 1.6 to 1.5 and then remains constant at a ratio of 1.4.

As the CO_2/CH_4 ratio increases from 0.6 to 1.67, the selectivity of CO keeps increasing from 45% to 93%, while the selectivity of H_2 remains at a high level above 81% and fluctuates around 90%, and the selectivity of C_2H_2 decreases from 31 to 11% (Fig. 3.4B). In previous research with the GAP [34], a constant CO_2/CH_4

ratio of 1 was used, and the focus was on the optimal effective conversion and EC, which were achieved with 20% N_2. However, the CO and H_2 selectivities were almost the lowest at this N_2 fraction, compared with other N_2 fractions. Our results indicate that these selectivities may be enhanced by increasing the CO_2/CH_4 ratio.

Fig. 3.5 compares photographs of the post-plasma reactor tube when using CO_2/CH_4 ratios of 0.6 and 1.67. With a higher CO_2 fraction, there was no visible carbon deposition on the inside wall of the reactor (Fig. 3.5A), while serious carbon deposition was visible when more CH_4 was added to the feed gas (Fig. 3.5B). We believe this is because the carbon produced from methane ($CH_4 \rightarrow C + 2H_2$, $\Delta H^0 = 75.6\ kJ/mol$) reacts directly with CO_2 or with the oxygen atom produced by CO_2, promoting CO production. Indeed, such reactions were demonstrated to happen also when placing a carbon bed after the GAP plasma reactor, as demonstrated by detailed chemistry modelling [45]. This also explains why the C_2H_2 selectivity decreases, as more C atoms recombine with O atoms to form CO rather than C_2H_2. Raman Spectroscopy, as shown in Fig. B2.1 (see Appendix B), was employed to analyze the composition of the carbon on the reactor's inner wall. Distinct carbon signals were detected at around 1346 cm^{-1} (D band) and 1574 cm^{-1} (G band), with an I_D/I_G value of 0.79. The D band appears due to the defects of the product, and the G band reflects the in-plane sp^2 carbon vibrations. The value of I_D/I_G is used to evaluate the defects of the product: the larger the value, the

smaller the size of the product [46,47]. Additionally, a 2D band at 2678 cm^{-1} was observed, which is typically attributed to the overtone of the D band [47]. Although the conversions of CO_2 and CH_4 change only slightly for different CO_2/CH_4 ratios, relatively more H_2 is produced than CO at a lower CO_2/CH_4 ratio, creating a maximum H_2/CO ratio of 2.7. This is interesting for further use of the syngas via Fischer-Tropsch synthesis, for example, to produce methanol, for which the ideal H_2/CO ratio is equal to 2 [48].

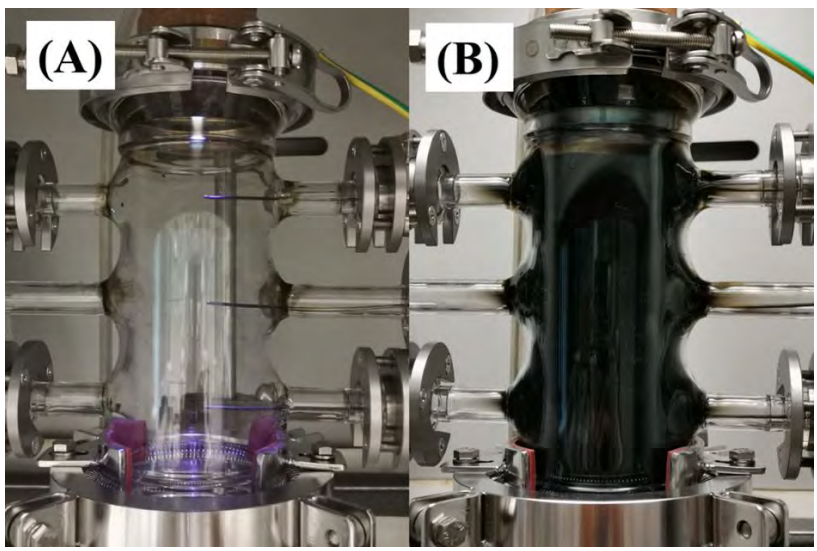

Fig. 3.5. Photographs of the post-plasma reactor tube, at a total gas flow rate of 8 L/min, N_2 = 6.4 L/min, for (A) CO_2/CH_4 = 1.67, and (B) CO_2/CH_4 = 0.6.

The selectivity of CO increases significantly once H_2O is added to the feed gas (Fig. 3.4C). Although it is expected that the CO selectivity will decrease due to the WGSR consuming CO, the results show an increase in CO formation. This can be explained by the higher number of O atoms produced from the H_2O molecules, enhancing the oxidation of carbon-containing species (deposited carbon or

hydrocarbon species) into CO. This results in the general increasing trend of CO selectivity. Vice versa, the C_2H_2 selectivity decreases upon H_2O addition. It has been investigated that the formation of hydrocarbons was strongly affected by the decomposition of CH_4 into CH_3, CH_2, and CH. The addition of H_2O limited the formation of CH, which was proven by optical emission spectrometry [40], leading to less C_2H_2 formation. Although the outlet water was collected, it was impossible to precisely estimate how much water participated in the reaction, because part of the water condensed and adhered to the walls of the cooling device. Therefore, the yield of H_2 was used to exhibit the effect of adding H_2O on the H_2 production. The yield of H_2 increased first from 55% without H_2O to 80% with 70% RH, followed by a drop to 75% when the H_2O percentage was increased further to 100% RH, which was still higher than without H_2O addition. This suggests that, with respect to selectivity, in the case of a CO_2/CH_4 ratio of 1 and a total gas flow rate of 8 L/min with 80% N_2 in the mixture, 70% RH is a reasonable condition for the production of more H_2 and CO. However, the H_2/CO ratio shows a different trend, as it drops at first for 10% RH and then increases with increasing amount of H_2O. This is because, at low H_2O content, the CO yield increases more than that of H_2, leading to a smaller difference in the yield of H_2 and CO. This can be explained by the fact that the addition of a proper amount of H_2O increases the H_2 amount, following the water-gas shift reaction ($CO + H_2O \rightarrow CO_2 + H_2,\ \Delta H^0 = -42.1$ kJ/

mol). At the same time, this also explains the lower CO_2 conversion that was observed (Fig 3.2D).

Generally, in the GAP DRM case, a higher gas flow rate yields a slight increase in the CO and H_2 selectivity. However, increasing the CO_2 amount is beneficial for improving the CO selectivity and reducing carbon deposition. Similarly, the addition of H_2O also benefits the CO selectivity, which can reach around 100% with RH of $\geqslant$40%. Moreover, adding H_2O into the GAP DRM system can yield more H_2 which can be an efficient route to adjust the H_2/CO ratio. However, water addition will negatively impact the CO_2 conversion. In addition, for downstream processes, such as PPC directly connected to the plasma, the presence of water induces important requirements towards hydrolytic stability of the catalyst but limits carbon deposition for the applied catalyst. Hence, when requiring specific H_2/CO ratios, changing the CO_2/CH_4 ratio would be an alternative to consider, possibly in combination with water.

3.4.3 Specific energy input and energy cost

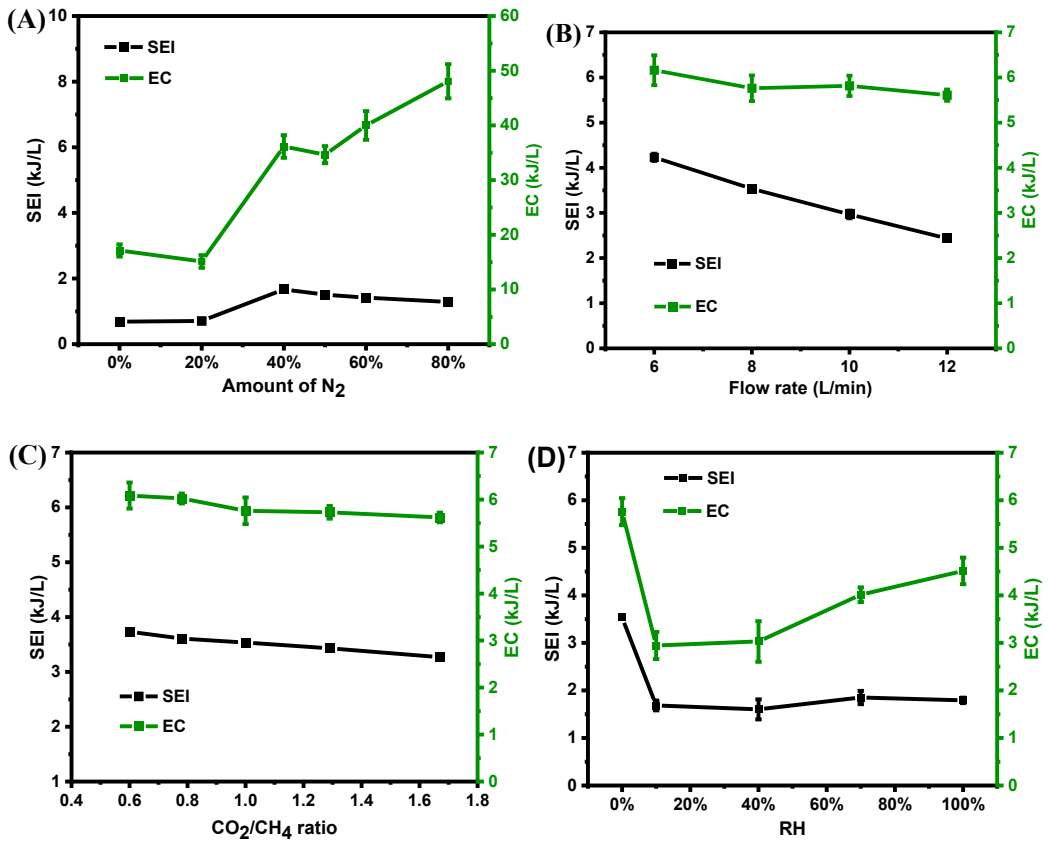

Fig. 3.6. SEI and EC as a function of gas composition, gas flow rate and RH. (A) Total gas flow rate = 10 L/min, N_2 fraction in CO_2 varied from 0% to 80%. (B) Total gas flow rate varied from 6 to 12 L/min, $CO_2/CH_4/N_2$ = 1/1/8. (C) Total gas flow rate = 8 L/min, N_2 = 6.4 L/min, CO_2/CH_4 ratio varied between 0.6 and 1.67. (D) Total gas flow rate = 8 L/min, $CO_2/CH_4/N_2$ = 1/1/8, H_2O amount varied between 0% and 100% RH.

Fig. 3.6 illustrates the specific energy input (SEI) and energy cost (EC) for the various conditions investigated. When only N_2/CO_2 was used for the plasma reaction, the SEI fluctuated between 1.3 and 1.7 kJ/L (Fig. 3.6A), suggesting that the changes in the gas composition had only a small effect on the value of the SEI, as the current was fixed and the power changed only little with gas composition.

Different from the SEI, the EC generally exhibits an increasing tendency. With pure CO_2, the EC is 17.1 kJ/L. This value decreases slightly to 15.1 kJ/L as the fraction of N_2 increases to 20%. It rises however to 36.1 kJ/L at a higher N_2 fraction of 40%, fluctuates around this value up to 60% N_2 and then increases to 48 kJ/L with 80% N_2 used. This is directly correlated to the lower effective CO_2 conversion upon higher N_2 fraction and is most likely due to the higher fraction of energy used to activate the N_2 molecules rather than CO_2.

When increasing the gas flow rate and keeping the gas ratio of $CO_2/CH_4/N_2$ at 1/1/8 (Fig. 3.6B), the SEI decreases linearly, which is logical, as the SEI is inversely proportional to the gas flow rate (see Eq. (3.8)). However, the EC fluctuates between 5.6 and 6.2 kJ/L, with a maximum value at a gas flow rate of 6 L/min. As the EC is relatively stable, the gas flow rate seems to have little effect on the energy needed for molecules to be converted. More or less the same can be concluded about the effect of the CO_2/CH_4 ratio, because the SEI and EC steadily decrease only from 3.7 to 3.2 kJ/L and from 6.1 to 5.6 kJ/L, upon increasing the CO_2/CH_4 ratio (Fig. 3.6C). The effect of different N_2 contents on the EC for DRM, at a CO_2/CH_4 ratio of 1, was also studied in [34], and 20% N_2 addition yielded the lowest EC, in line with our results (Fig. 3.6A). Moreover, the EC can be further slightly reduced by increasing the CO_2/CH_4 ratio, as indicated by our results (Fig. 3.6C).

When H_2O is added, the SEI and EC show similar trends (Fig. 3.6D): they decline significantly from 3.5 kJ/L and 5.8 kJ/L to 1.7 kJ/L and 2.9 kJ/L for 10% RH, followed by an increase to 1.9 kJ/L and 4 kJ/L, for 70% RH. Finally, a small decrease in SEI to 1.8 kJ/L but a slightly higher EC of 4.5 kJ/L is observed with 100% RH. Generally, the introduction of H_2O thus results in a lower SEI and EC for the conversion.

In summary, in a CO_2/N_2 GAP plasma, the addition of N_2 has little effect on the SEI, while the EC increases sharply upon rising N_2 fraction, because some energy is used for the activation of N_2 molecules. In case of DRM, increasing the gas flow rate results in a lower SEI. The EC shows a decreasing trend as well, but this trend is less steep than that of the SEI, due to the lower CO_2 and CH_4 conversion. Changing the CO_2 and CH_4 ratio has only a slight effect on the SEI and EC. However, the addition of H_2O is beneficial for the SEI and EC, which decrease sharply. This seems a good way to optimize the energy utilization of the GAP DRM system when not too high amounts of H_2O are added.

3.4.4 Temperature after the plasma

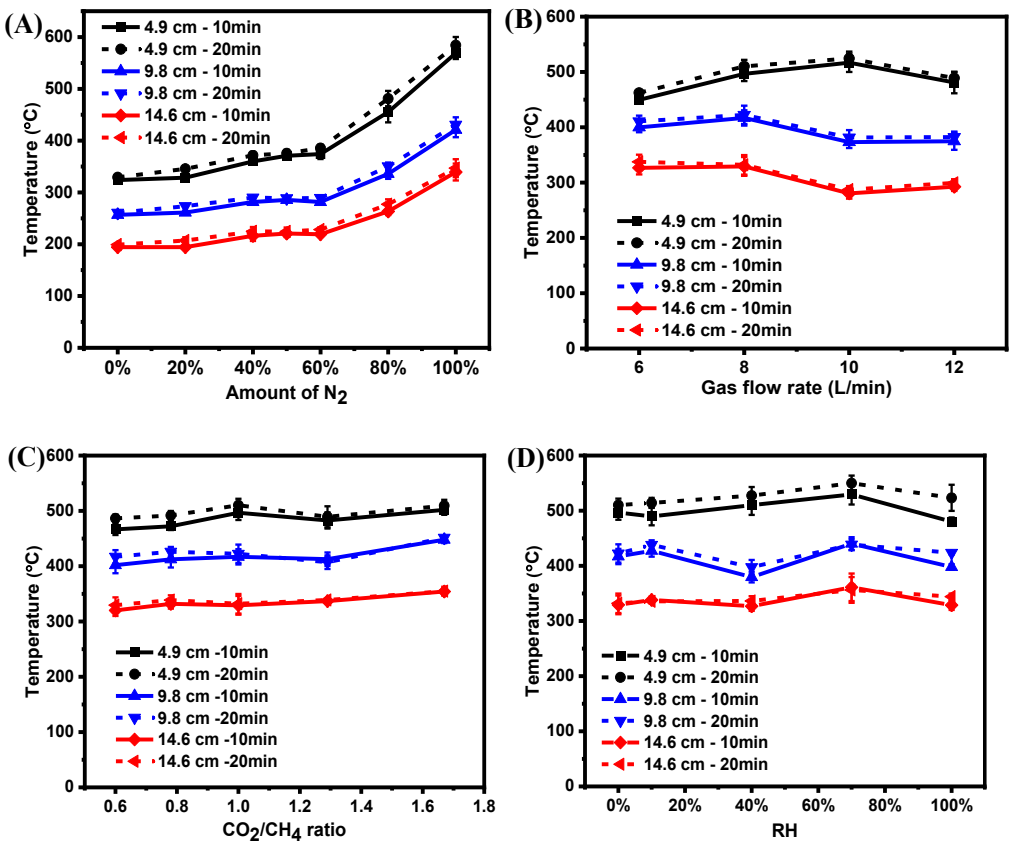

Fig. 3.7. Temperature at 4.9 cm, 9.8 cm, and 14.6 cm after the plasma reactor, for 10 min and 20 min plasma operation, as a function of gas composition, gas flow rate and RH. (A) Total gas flow rate = 10 L/min, N_2 fraction in CO_2 varied from 0% to 100%. (B) Total gas flow rate varied from 6 to 12 L/min, $CO_2/CH_4/N_2$ = 1/1/8. (C) Total gas flow rate = 8 L/min, N_2 = 6.4 L/min, CO_2/CH_4 ratio varied between 0.6 and 1.67. (D) Total gas flow rate = 8 L/min, $CO_2/CH_4/N_2$ = 1/1/8, H_2O amount varied between 0% and 100% RH.

Fig. 3.7 illustrates the measured post-plasma temperature, at three different locations, for all conditions investigated. All experiments were repeated at least three times, and the detailed temperature data as a function of time, as well as more detailed information, are presented in Fig. B3.1-4. The following conclusions can

be drawn from them: (1) The more CO_2 in the N_2/CO_2 system, the more stable are the temperatures measured after plasma, suggesting that CO_2 is beneficial for giving a stable plasma flame. The reason that N_2 addition increases the gas temperature is that the N_2 molecules can acquire energy from the plasma, most of which cannot be used for chemical reaction due to the strong triple bond of N_2, and it can only be vibrationally excited, after which the vibrational levels eventually relax their acquired energy, increasing the gas temperature [34]. (2) Adding CH_4 into the N_2/CO_2 system results in an unstable plasma flame but a generally stable temperature at the same position after the plasma. (3) The addition of H_2O (RH ≥ 40%) makes the plasma flame unstable in the first 10 minutes, resulting in a sudden decrease in temperature. This could be due to condensed H_2O inside the cathode, formed during the flushing time.

The temperatures after 10 and 20 minutes of plasma operation at all different conditions are summarized in Fig. 3.7. When N_2 is added to CO_2 (Fig. 3.7A), the temperatures increase at all three distances from the plasma exhaust. As the N_2 fraction increases, the temperature at 4.9 cm increases significantly from 324 °C with pure CO_2 to 569 °C with pure N_2. Although relatively stable in temperature up to 60% N_2, a sharp increase happens when the N_2 concentration is over 60%. Moreover, the temperatures at 10 and 20 minutes are almost the same, suggesting

that the temperature was stable after 10 minutes of plasma, which was also proven by the data in Fig. B3.1.

Upon adding CH_4 into the CO_2/N_2 mixture and fixing the gas ratio of CO_2/CH_4 to 1 (Fig. 3.7B), the temperature at 4.9 cm first increases upon rising gas flow rate, reaching a maximum value of 516 °C at 10 L/min and then it drops to 481 °C at 12 L/min. However, different from the CO_2/N_2 system, in which the temperature at 9.8 cm and 14.6 cm showed the same trends as at 4.9 cm, the temperature at the lower position (9.8 cm) now drops from 417 °C at 8 L/min to 373 °C at 10 L/min, while at 14.6 cm it drops from about 330 °C at 8 L/min to 280 °C at 10 L/min. The lowest temperature at a distance of 9.8 cm and 14.6 cm was measured at a gas flow rate of 10 L/min. The higher temperature might have contributed to the higher conversions of CO_2 and CH_4 as the dry reforming reaction is endothermic. Besides this, as shown in Fig. 3.3B, the cathode melted at 6 L/min, which could be due to the lower heat loss produced by the plasma at these lower gas flow rates.

At a fixed gas flow rate, changing the CO_2/CH_4 ratio causes some fluctuation in the temperature at 4.9 cm, in the range between 467 °C and 501 °C after 10 min plasma reaction (Fig. 3.7C). After 20 min, at the same positions, the reactions with higher CO_2 fractions had lower temperature differences with the measurements at 10 min, suggesting that more CO_2 present in the gas flow yields more stable

temperatures. This is in accordance with the results in Fig. 3.7A, where higher CO_2 fractions resulted in lower but more stable plasma temperatures.

Finally, upon H_2O addition (Fig. 3.7D), the temperature at 4.9 cm first slightly increases and then decreases once the H_2O content is over 70% RH. This could be due to the high heat capacity of H_2O, which adsorbed more heat. At 100% RH, as shown in Fig. B3.4, the plasma was not stable anymore, leading to lower gas temperatures after the plasma in 10 min. Note that at 9.8 cm, with 40% RH, the temperature dropped from 427 °C to 380 °C (Fig. B3.4). The reason for this is however unclear.

Hence, important conclusions can be drawn with respect to heat transfer when envisioning a combination of the GAP with post-plasma catalysis (see next chapters). The N_2 dilution above 60% was found to affect the post-plamsa temperature significantly, while CH_4 addition and RH have much less affect, although water addition with RH over 70% will cause a temperature drop. For distances to the plasma exhaust of 9.8cm and longer, the temperature drops to ~ 400-450°C at 8 L/min. An important result based on the simulations (see Appendix Fig. B5.1-5.3) was that the heat is concentrated in the center of the tube, which might pose challenges towards uniform heating of the post-plasma catalyst bed.

3.5 Conclusion

We have experimentally investigated the impact of the addition of N_2, N_2/CH_4 (varying gas flow rate and CO_2/CH_4 ratios), and $N_2/CH_4/H_2O$ on the CO_2 (and CH_4) conversion, product selectivity and EC in a GAP. We also measured the temperature at three different distances from the plasma exhaust (4.9 cm, 9.8 cm, and 14.6 cm), and we calculated the temperature distribution inside the GAP and in the post-plasma reactor tube by computational models, to provide insights for potential post-plasma catalyst applications with respect to exhaust gas composition serving as feed gas for the catalytic reaction post-plasma, as well as heat transferred to the catalyst bed.

Generally, the following conclusions can be drawn:

(1) The addition of N_2 enhances the absolute conversion of CO_2 from 4% without N_2 to 13% with 80% N_2, although the effective conversion decreases due to dilution of CO_2. As a result of the latter, the EC increases significantly upon rising N_2 fraction. Considering that industrial gas emissions contain significant amounts of N_2, a mixture with 80% N_2 content, to achieve high absolute CO_2 conversion, is a reasonable choice, while lower N_2 contents may be more beneficial if the higher EC is the most critical parameter. Moreover, the temperature measured at the plasma exhaust is higher above 60% N_2 dilution, providing more heat to the PPC system.

(2) The addition of CH_4 in combination with N_2 results in a more complex situation. At a fixed CO_2/CH_4 ratio of 1, decreasing the gas flow rate from 12 L/min to 6 L/min causes a rise in the CO_2 and CH_4 conversions, selectivity of C_2H_2, ratio of H_2/CO and EC. However, the selectivity of CO and H_2 shows the opposite trend. Moreover, the low gas flow rate of 6 L/min damaged the cathode. Increasing the amount of CO_2 in the mixture, hence increasing the CO_2/CH_4 ratio from 0.6 to 1.67, increased the absolute conversion of CH_4, while the absolute conversion of CO_2 decreased. However, the effective conversion of CH_4 and CO_2 exhibited opposite trends. Besides this, the selectivity of C_2H_2, the H_2/CO ratio, SEI, and EC all decreased with increasing fractions of CO_2. Considering the damage of the GAP device at too low flow rates, and the obtained results for CO_2 and CH_4 conversion, CO and H_2 selectivity, we believe that 8 L/min with $CO_2/CH_4/N_2$ = 1/1/8 is quite an optimal condition. However, when using lower CO_2/CH_4 ratio, a higher H_2/CO ratio for better downstream syngas processing can be reached, although the solid carbon deposition would become a point of attention as it might cause deactivation of a post-plasma catalyst.

(3) The addition of H_2O suppressed the conversion of CO_2 and CH_4, with a more pronounced effect on the former, leading to a decrease in the absolute CO_2 conversion from 55% at 0% RH to 22% at 100% RH. However, as the CH_4

conversion was less affected, this improved the H_2/CO ratio from 1.45 to 2. Furthermore, the SEI and EC both decreased significantly when H_2O was added (between 10 and 40% RH) but then increased as the amount of H_2O increased. Thus, H_2O addition can help to improve the H_2 production, albeit at the expense of CO_2 conversion, which both help to increase the produced H_2/CO ratio. This is beneficial for the further processing of syngas into other chemicals. Moreover, although not shown in this paper, the addition of H_2O can help to decrease carbon deposition, which may help to prolong the lifetime of catalysts in a post-plasma catalytic DRM system. However, the amount of H_2O addition should be carefully studied, as too much H_2O will affect the plasma stability and the post-plasma temperature and will impact CO_2 conversion negatively as well as EC (if above 40%). This is interesting to study in future work.

(4) Our measured temperature data suggest that N_2 dilution above 60% will increase the outlet gas temperature. When adding N_2/CH_4 or N_2/CH_4/H_2O, the exhaust gas temperatures fluctuated a bit, but no dramatic changes were observed, and the temperatures at three distances from the exhaust generally ranged between 470-520 °C at 4.9 cm, 370-440 °C at 9.8 cm, and 330-350 °C at 14.6 cm. To make optimal use of the heat produced by the plasma, for activating post-plasma catalysts, the catalyst bed should thus be placed quite close to the GAP reactor exhaust. However, considering the catalyst stability and the effect of active sites sintering

at too high temperature, the distance should also not be too close to avoid destroying the catalyst. Therefore, the distance of the catalyst (bed) to the plasma exhaust should be carefully studied as well, which will be performed in Chapter 4. Furthermore, as CFD simulation showed concentration of the temperature in the core of the tube, solutions might be needed to distribute the heat more evenly.

In summary, this chapter provides valuable insights into selecting suitable reaction conditions to achieve higher CO_2 (and CH_4) conversion, lower energy costs, and higher syngas production, also important for post-plasma catalysis, as the exhaust gas of the plasma serves as the feed gas for the post-plasma catalytic reaction and the combination of all reaction steps determines the energy cost to produce the end product (not yet including separation costs and energy losses when transferring electrical energy into plasma power). A gas flow rate of 8 L/min with a gas composition of $CO_2/CH_4/N_2$ of 1/1/8 is chosen for the combination of GAP plasma DRM with catalysts. Furthermore, the measured and calculated temperature profiles offer valuable information to design and position a post-plasma catalyst bed, taking the temperature distribution and gradients over the post-plasma reactor tube into account, as well as the impact of gas composition (e.g. dilution) on the post-plasma temperature. It is suggested that the distance of the catalyst bed should be smaller than 4.9 cm, aiming to offer a temperature higher than 500 °C for the

catalyst layer, which may help the catalyst to exhibit its catalytic activity, although this is of course dependent on the reaction envisioned.

We acknowledge Senne Van Alphen for performing the simulations and for writing the corresponding text.

3.6 References

[1] Van der Ploeg, F.; Withageny, C. Global Warming and the Green Paradox: A Review of Adverse Effects of Climate Policies. Rev. Environ. Econ. Policy 2015, 9 (2), 285–303. https://doi.org/10.1093/reep/rev008.

[2] Ashok, J.; Pati, S.; Hongmanorom, P.; Tianxi, Z.; Junmei, C.; Kawi, S. A Review of Recent Catalyst Advances in CO_2 Methanation Processes. Catal. Today 2020, 356 (November 2019), 471–489. https://doi.org/10.1016/j.cattod.2020.07.023.

[3] Gunasekar, G. H.; Park, K.; Jung, K. D.; Yoon, S. Recent Developments in the Catalytic Hydrogenation of CO_2 to Formic Acid/Formate Using Heterogeneous Catalysts. Inorg. Chem. Front. 2016, 3 (7), 882–895. https://doi.org/10.1039/c5qi00231a.

[4] Liu, M.; Yi, Y.; Wang, L.; Guo, H.; Bogaerts, A. Hydrogenation of Carbon Dioxide to Value-Added Chemicals by Heterogeneous Catalysis and Plasma Catalysis. Catalysts 2019, 9 (3). https://doi.org/10.3390/catal9030275.

[5] Pérez-Fortes, M.; Schöneberger, J. C.; Boulamanti, A.; Harrison, G.; Tzimas, E. Formic Acid Synthesis Using CO_2 as Raw Material: Techno-Economic and Environmental Evaluation and Market Potential. Int. J. Hydrogen Energy 2016, 41 (37), 16444–16462. https://doi.org/10.1016/j.ijhydene.2016.05.199.

[6] Aresta, M.; Dibenedetto, A.; Angelini, A. Catalysis for the Valorization of Exhaust Carbon: From CO_2 to Chemicals, Materials, and Fuels. Technological Use of CO_2. Chem. Rev. 2014, 114 (3), 1709–1742. https://doi.org/10.1021/cr4002758.

[7] Mustafa, A.; Lougou, B. G.; Shuai, Y.; Wang, Z.; Tan, H. Current Technology Development for CO_2 Utilization into Solar Fuels and Chemicals: A Review. J. Energy Chem. 2020, 49, 96–123. https://doi.org/10.1016/j.jechem.2020.01.023.

[8] Saeidi, S.; Najari, S.; Fazlollahi, F.; Nikoo, M. K.; Sefidkon, F.; Klemeš, J. J.; Baxter, L. L. Mechanisms and Kinetics of CO_2 Hydrogenation to Value-Added Products: A Detailed Review on Current Status and Future Trends. Renew. Sustain. Energy Rev. 2017, 80 (September 2016), 1292–1311. https://doi.org/10.1016/j.rser.2017.05.204.

[9] Yentekakis, I. V.; Panagiotopoulou, P.; Artemakis, G. A Review of Recent Efforts to Promote Dry Reforming of Methane (DRM) to Syngas Production via Bimetallic Catalyst Formulations. Appl. Catal. B Environ. 2021, 296, 120210. https://doi.org/10.1016/j.apcatb.2021.120210.

[10] Snoeckx, R.; Bogaerts, A. Plasma Technology-a Novel Solution for CO_2 Conversion? Chem. Soc. Rev. 2017, 46 (19), 5805–5863. https://doi.org/10.1039/c6cs00066e.

[11] Ramakers, M.; Trenchev, G.; Heijkers, S.; Wang, W.; Bogaerts, A. Gliding Arc Plasmatron: Providing an Alternative Method for Carbon Dioxide Conversion. ChemSusChem 2017, 10, 2642–2652. https://doi.org/doi.org/10.1002/cssc.201700589.

[12] Di, L.; Zhang, J.; Zhang, X. A Review on the Recent Progress, Challenges, and Perspectives of Atmospheric-Pressure Cold Plasma for Preparation of Supported Metal Catalysts. Plasma Processes and Polymers. 2018. https://doi.org/10.1002/ppap.201700234.

[13] Chen, G.; Snyders, R.; Britun, N. CO_2 Conversion Using Catalyst-Free and Catalyst-Assisted Plasma-Processes: Recent Progress and Understanding. J. CO_2 Util. 2021, 49 (May), 101557. https://doi.org/10.1016/j.jcou.2021.101557.

[14] Anoop, N. .; Sundaramurthy, S.; Jha, J. M.; Chandrabalan, S.; Singh, N.; Verma, J.; Parvatalu, D.; Katti, S. Plasma Catalysis: A Feasible Solution for Carbon Dioxide Valorization? Clean Technol. Environ. Policy 2021, 23 (10), 2789–2811. https://doi.org/10.1007/s10098-021-02203-y.

[15] Abiev, R. S. .; Sladkovskiy, D. A. .; Semikin, K. V. .; Murzin, D. Y. .; Rebrov, E. V. Non-Thermal Plasma for Process and Energy Intensification in Dry Reforming of Methane. Catalysts 2020, 10, 1358.

[16] Suslova, E.; Savilov, S.; Egorov, A.; Shumyantsev, A.; Lunin, V. Carbon Nanotube Frameworks by Spark Plasma Sintering. Microporous Mesoporous Mater. 2020, 293, 109807.

[17] Wang, C.; Li, D.; Lu, Z.; Song, M.; Xia, W. Synthesis of Carbon Nanoparticles in a Non-Thermal Plasma Process. Chem. Eng. Sci. 2020, 227, 115921.

[18] Chung, W. C.; Chang, M. B. Review of Catalysis and Plasma Performance on Dry Reforming of CH_4 and Possible Synergistic Effects. Renew. Sustain. Energy Rev. 2016, 62, 13–31. https://doi.org/10.1016/j.rser.2016.04.007.

[19] Palma, V.; Cortese, M.; Renda, S.; Ruocco, C.; Martino, M.; Meloni, E. A Review about the Recent Advances in Selected NonThermal Plasma

Assisted Solid–Gas Phase Chemical Processes. Nanomaterials 2020, 10, 1596.

[20] Li, S.; Ahmed, R.; Yi, Y.; Bogaerts, A. Methane to Methanol through Heterogeneous Catalysis and Plasma Catalysis. Catalysts. 2021. https://doi.org/10.3390/catal11050590.

[21] Aerts, R.; Somers, W.; Bogaerts, A. Carbon Dioxide Splitting in a Dielectric Barrier Discharge Plasma: A Combined Experimental and Computational Study. ChemSusChem 2015, 8 (4), 702–716. https://doi.org/10.1002/cssc.201402818.

[22] Kim, H.; Song, S.; Tom, C. P.; Xie, F. Carbon Dioxide Conversion in an Atmospheric Pressure Microwave Plasma Reactor: Improving Efficiencies by Enhancing Afterglow Quenching. J. CO_2 Util. 2020, 37 (December 2019), 240–247. https://doi.org/10.1016/j.jcou.2019.12.011.

[23] Cleiren, E.; Heijkers, S.; Ramakers, M.; Bogaerts, A. Dry Reforming of Methane in a Gliding Arc Plasmatron: Towards a Better Understanding of the Plasma Chemistry. ChemSusChem 2017, 10, 4025–4036. https://doi.org/doi.org/10.1002/cssc.201701274.

[24] Feng, J.; Sun, X.; Li, Z.; Hao, X.; Fan, M.; Ning, P.; Li, K. Plasma-Assisted Reforming of Methane. Adv. Sci. 2022, 2203221, 1–36. https://doi.org/10.1002/advs.202203221.

[25] Trenchev, G.; Bogaerts, A. Dual-Vortex Plasmatron: A Novel Plasma Source for CO_2conversion. J. CO_2 Util. 2020, 39 (March), 101152. https://doi.org/10.1016/j.jcou.2020.03.002.

[26] Chen, G.; Snyders, R.; Britun, N. CO_2 Conversion Using Catalyst-Free and Catalyst-Assisted Plasma-Processes Recent Progress and Understanding. J. CO_2 Util. 2021, 49, 101557.

[27] Trinh, Q. H.; Dinh, D. K.; Lee, D. H.; Nguyen, D. B.; Mok, Y. S.; Lee, W. G. Combination of Atmospheric Pressure Plasma with Catalysts for Dry Reforming of Methane to Value-Added Chemicals, First Edit.; Elsevier Ltd., 2022. https://doi.org/10.1016/B978-0-323-85586-0.00009-3.

[28] Wang, Y.; Wang, N.; Harding, J.; Chen, G.; Tu, X. Plasma Technology for Syngas Production; Elsevier Inc., 2023. https://doi.org/10.1016/B978-0-323-91871-8.00014-3.

[29] Sun, H.; Chen, Z.; Chen, J.; Long, H.; Wu, Y.; Zhou, W. The Influence of Back-Breakdown on the CO_2conversion in Gliding Arc Plasma: Based on Experiments of Different Materials and Improved Structures. J. Phys. D. Appl. Phys. 2021, 54 (49). https://doi.org/10.1088/1361-6463/ac2335.

[30] Zhang, H.; Li, L.; Li, X.; Wang, W.; Yan, J.; Tu, X. Warm Plasma Activation of CO_2 in a Rotating Gliding Arc Discharge Reactor. J. CO_2 Util. 2018, 27 (August), 472–479. https://doi.org/10.1016/j.jcou.2018.08.020.

[31] Jardali, F.; Van Alphen, S.; Creel, J.; Ahmadi Eshtehardi, H.; Axelsson, M.; Ingels, R.; Snyders, R.; Bogaerts, A. NOx Production in a Rotating Gliding

Arc Plasma: Potential Avenue for Sustainable Nitrogen Fixation. Green Chem. 2021, 23 (4), 1748–1757. https://doi.org/10.1039/d0gc03521a.

[32] Trenchev, G.; Kolev, S.; Wang, W.; Ramakers, M.; Bogaerts, A. CO_2 Conversion in a Gliding Arc Plasmatron: Multidimensional Modeling for Improved Efficiency. J. Phys. Chem. C 2017, 121 (39), 24470–24479. https://doi.org/10.1021/acs.jpcc.7b08511.

[33] Slaets, J.; Aghaei, M.; Ceulemans, S.; Van Alphen, S.; Bogaerts, A. CO_2 and CH_4 Conversion in "Real" Gas Mixtures in a Gliding Arc Plasmatron: How Do N_2 and O_2 Affect the Performance? Green Chem. 2020, 22 (4), 1366–1377. https://doi.org/10.1039/c9gc03743h.

[34] Van Alphen, S.; Slaets, J.; Ceulemans, S.; Aghaei, M.; Snyders, R.; Bogaerts, A. Effect of N_2 on CO_2-CH_4 Conversion in a Gliding Arc Plasmatron: Can This Major Component in Industrial Emissions Improve the Energy Efficiency? J. CO_2 Util. 2021, 54, 101767. https://doi.org/10.1016/j.jcou.2021.101767.

[35] Zhang, H.; Li, L.; Xu, R.; Huang, J.; Wang, N.; Li, X.; Tu, X. Plasma-Enhanced Catalytic Activation of CO_2 in a Modified Gliding Arc Reactor. Waste Disposal and Sustainable Energy. 2020, pp 139–150. https://doi.org/10.1007/s42768-020-00034-z.

[36] Allah, Z. A.; Whitehead, J. C. Plasma-Catalytic Dry Reforming of Methane in an Atmospheric Pressure AC Gliding Arc Discharge. Catal. Today 2015, 256 (P1), 76–79. https://doi.org/10.1016/j.cattod.2015.03.040.

[37] Liu, J. L.; Li, Z.; Liu, J. H.; Li, K.; Lian, H. Y.; Li, X. S.; Zhu, X.; Zhu, A. M. Warm-Plasma Catalytic Reduction of CO_2 with CH_4. Catal. Today 2019, 330 (December 2017), 54–60. https://doi.org/10.1016/j.cattod.2018.05.046.

[38] Ramakers, M.; Heijkers, S.; Tytgat, T.; Lenaerts, S.; Bogaerts, A. Combining CO_2 Conversion and N2 Fixation in a Gliding Arc Plasmatron. J. CO_2 Util. 2019, 33 (March 2019), 121–130. https://doi.org/10.1016/j.jcou.2019.05.015.

[39] Kim, C.; Yoo, C. J.; Oh, H. S.; Min, B. K.; Lee, U. Review of Carbon Dioxide Utilization Technologies and Their Potential for Industrial Application. J. CO_2 Util. 2022, 65 (July), 102239. https://doi.org/10.1016/j.jcou.2022.102239.

[40] Xia, Y.; Lu, N.; Jiang, N.; Shang, K.; Wu, Y. Combined Steam and CO_2 Reforming of CH_4 for Syngas Production in a Gliding Arc Discharge Plasma. J. CO_2 Util. 2020, 37, 248–259.

[41] Wanten, B.; Vertongen, R.; De Meyer, R.; Bogaerts, A. Plasma-Based CO_2 Conversion: How to Correctly Analyze the Performance? J. Energy Chem. 2023, 86, 180–196. https://doi.org/10.1016/j.jechem.2023.07.005.

[42] Pinhão, N.; Moura, A.; Branco, J. B. .; Neves, J. Influence of Gas Expansion on Process Parameters in Non-Thermal Plasma Plug-Flow Reactors: A

Study Applied to Dry Reforming of Methane. Int. J. Hydrogen Energy 2016, 41 (22), 9245–9255.

[43] Ren, Y.; Ma, Y. Y.; Mo, W. L.; Guo, J.; Liu, Q.; Fan, X.; Zhang, S. P. Research Progress of Carbon Deposition on Ni-Based Catalyst for CO_2-CH_4 Reforming. Catalysts 2023, 13 (4), 647. https://doi.org/10.3390/catal13040647.

[44] Snoeckx, R.; Ozkan, A.; Reniers, F.; Bogaerts, A. The Quest for Value-Added Products from Carbon Dioxide and Water in a Dielectric Barrier Discharge: A Chemical Kinetics Study. ChemSusChem 2017, 10 (2), 409–424. https://doi.org/10.1002/cssc.201601234.

[45] Girard-Sahun, F.; Biondo, O.; Trenchev, G.; van Rooij, G.; Bogaerts, A. Carbon Bed Post-Plasma to Enhance the CO_2 Conversion and Remove O_2 from the Product Stream. Chem. Eng. J. 2022, 442 (P2), 136268. https://doi.org/10.1016/j.cej.2022.136268.

[46] Ma, J.; Chen, X.; Song, M.; Wang, C.; Xia, W. Study on Formation Mechanism of Three Types of Carbon Nanoparticles during Ethylene Pyrolysis in Thermal Plasmas. Diamond and Related Materials. 2021. https://doi.org/10.1016/j.diamond.2021.108445.

[47] Wang, C.; Li, D.; Lu, Z. S.; Song, M.; Xia, W. Synthesis of Carbon Nanoparticles in a Non-Thermal Plasma Process. Chem. Eng. Sci. 2020, 227, 115921. https://doi.org/10.1016/j.ces.2020.115921.

[48] Liu, Y. J.; Cui, N.; Jia, P. L.; Wang, X.; Huang, W. Synergy between Active Sites of Ternary CuZnAlOOH Catalysts in CO Hydrogenation to Ethanol and Higher Alcohols. ACS Sustain. Chem. Eng. 2020, 8 (17), 6634–6646. https://doi.org/10.1021/acssuschemeng.9b07587.

CHAPTER 4

Adjusting the post-plasma catalysis conditions towards improved dry reforming of methane with a gliding arc plasmatron

Effect of distance, catalyst amount, temperature, and H_2O addition

4.1 Introduction

As outlined in the introductory chapter, the transformation of CH_4 and CO_2 typically necessitates processes at high temperatures (> 700 °C), which are achieved through conventional thermal catalysis. Plasma provides an alternative and unique environment where the energy from electrons can be utilized to break the strong bonds in molecules like CH_4 and CO_2. This process can make them more reactive, facilitating chemical reactions. Plasma-assisted catalysis is gaining attention in various fields for its potential to enhance reaction rates and selectivity, while reducing energy consumption and environmental impact [1–3]. The combination of catalyst and plasma can typically be categorized into two modes, as detailed in Chapter 1: in-plasma catalysis (IPC) and post-plasma catalysis (PPC). Given that this PhD research focuses on the use of a gliding arc plasmatron, which is characterized as a warm plasma with temperatures exceeding 700 °C, the PPC mode is particularly relevant and requires adaptation of the catalyst and catalyst bed to the plasma exhaust gas properties. In this context, the plasma acts as an electrically energized pre-converter of reactants, generating more reactive chemicals, which may include end products, and producing heat as a byproduct. Consequently, the design of the catalyst bed should optimize both the utilization of the heat generated by the plasma and the interactions with the reactive plasma-treated mixture.

Existing research on post-plasma catalysis (PPC) for the Dry Reforming of Methane (DRM) reaction provides insightful findings. Martin-del-Campo et al. [4] explored the integration of two different Ni-based catalysts (loaded on Al_2O_3 and SiO_2) with a rotating gliding arc plasma for DRM. Their results indicated that $15NiO/Al_2O_3$ catalyst addition reduced the CO_2 and CH_4 conversion, but increased the selectivity for CO and H_2 marginally (from approximately 80% to 90% for CO and from 70% to 80% for H_2). Zhu et al. [5] observed that adding a 10% Ni-loaded Ni/Al_2O_3 catalyst to the post-plasma stage marginally improved the CH_4 conversion from about 53% to 60%, while the CO_2 conversion remained almost the same. However, introducing heat to the post-plasma reactor positively affected the catalytic performance. Liu and colleagues [6] investigated a warm post-plasma catalytic system with additional heating. The inclusion of a $Ni/CeO_2/Al_2O_3$ catalyst in the warm post-plasma reactor tube, heated by the plasma's exhaust stream without extra heating, showed negligible improvement. However, significant enhancements in conversion – from 40% to 60% for CO_2 and from 25% to 70% for CH_4 – were achieved when external heating raised the post-plasma catalyst bed's temperature to 850 °C. Comparison with the same catalyst for thermal catalytic DRM at 850 °C indicated that the conversion in warm post-plasma surpassed that of conventional thermal catalytic DRM at the same temperature. The studies performed in refs. [4–6] collectively suggest that without extra heating, there is no substantial improvement in CO_2 and CH_4 conversions. This observation forms the core of my research. Therefore, this chapter investigates various

parameters to achieve enhancements in the PPC performance for the DRM reaction, such as catalyst proximity to the plasma (to maximize heat transfer), catalyst quantity (assessing performance at constant catalytic temperatures), addition of extra heating (creating a higher thermal environment for the catalysts), and water addition (to minimize carbon deposition on the catalysts).

4.2 Experimental

4.2.1 Catalyst preparation and characterization

A MgAl-LDH (Mg/Al molar ratio of 3) was used as support material, which was prepared via the co-precipitation method as described in Chapter 2. The 10 wt% Ni ($Ni(NO_3)_2 \cdot 6H_2O$ as the metal source) was loaded on the powder MgAl-LDH (10 g) by mixing them in an aqueous solution (200 mL deionized H_2O) for 24 h under strong stirring. The obtained Ni/MgAl-LDH was dried at 80 ℃ overnight and calcined at 800 °C for 6 h. The obtained Ni-based mixed oxide catalyst was denoted as Ni/MO. The final light green powder was pressed into tablets at 5 MPa, then crushed and sieved with a sieve size of 30 – 40 mesh. Before utilization for plasma-catalytic DRM, the catalyst was reduced at 800 °C for 6 h in a tube furnace with 2% H_2/Ar gas. The same size of filling material of α-Al_2O_3 was prepared by crushing and sieving the α-Al_2O_3 spheres (Alfa Aesar, 3/16 inch). The total weight of the catalyst and filling material (α-Al_2O_3) to be introduced into the catalyst bed was fixed at 5 g. Usually, 1 g of catalyst, mixed with 4 g of α-Al_2O_3 was used.

When testing the effect of catalyst amount, a higher amount, such as 2 g of catalyst mixed with 3 g α-Al_2O_3 was used, keeping the total solid loading in the catalyst bed at 5 g.

X-ray diffraction (XRD) and N_2 sorption, as described in section 2.2.5 (degassing at 80 °C), were performed to determine the crystal phase and specific surface area of the Ni-LDH and Ni/MO. Hydrogen-temperature programmed reduction (H_2-TPR) and oxygen-temperature programmed oxidation (O_2-TPO) were conducted to collect the reduction and oxidation data of the sample. The measurements were performed on a ChemStar TPX Chemisorption Analyzer from Anton Paar. Typically, 50 mg sample was pretreated at 350 °C for 1 h in 50 mL/min He. Subsequently, after cooling down to 50 °C, the O_2-TPO was performed to fully oxidizing the sample with 5% O_2/He gas at a flow rate of 50 mL/min. During the O_2-TPO process, the temperature increased from 50 °C to 800 °C with a rate of 10 °C/min. A maximum temperature of 800 °C was chosen not to exceed the calcination temperature, preventing changes made to the materials during analysis. After the cooling of the sample down to 50 °C by He, the H_2-TPR procedure was conducted to 1000 °C with a rate of 10 °C/min while flowing 5% H_2/Ar at 50 mL/min. After the cooling of the sample down to 50 °C by He, another O_2-TPO was carried out via the same procedure.

4.2.2 Plasma conditions

Fig 4.1 shows the schematic diagram of the experimental setup. As described in Chapter 3, the general gas flow rate for the GAP DRM reaction was fixed to 8 L/min. Herein, a gas composition of $N_2/CH_4/CO_2$ = 8/1/1 was used. The flow rate of each feed gas was controlled by Bronkhorst mass flow controllers. A pressure gauge was connected to the reactant feedgas line entering the GAP, to measure the change of pressure in the feedgas. The plasma in the GAP was generated by a DC power supply (APS – Advanced Plasma Solutions) with a current of 0.25 A and a current sense resistor of 3 Ω. The voltage and current of the plasma were measured by a high-voltage probe (Pintek HVP-15HF). The data of voltage and current were collected by an oscilloscope (Tektronix TDS 2012C). The plasma power was calculated based on the voltage and current data collected.

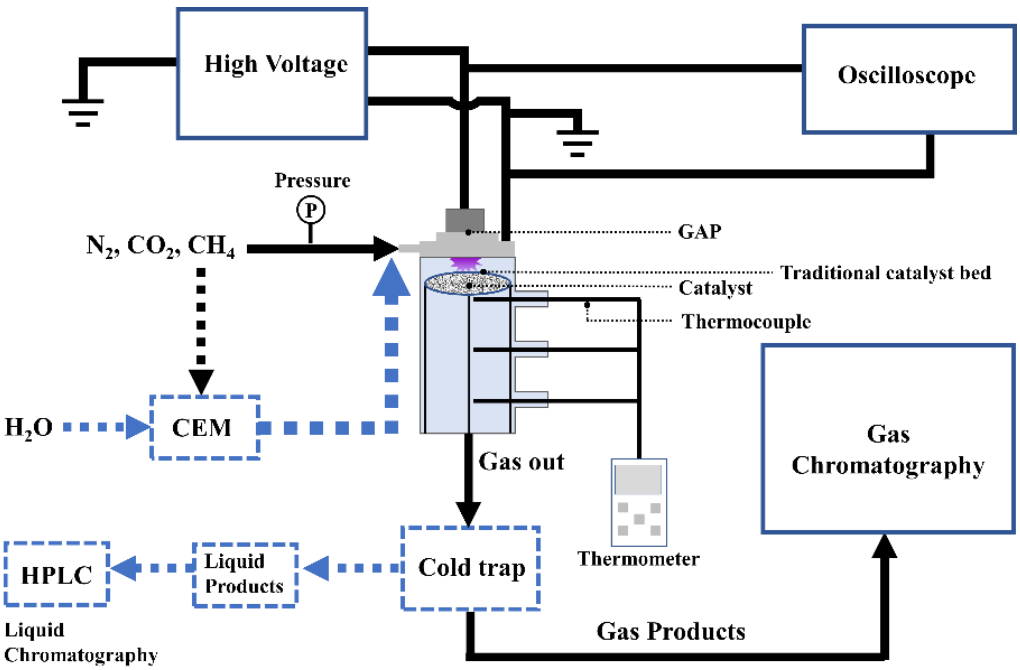

Fig. 4.1 Schematic diagram of the GAP DRM experimental setup. The blue dash lines show the case when H_2O was added via the CEM device.

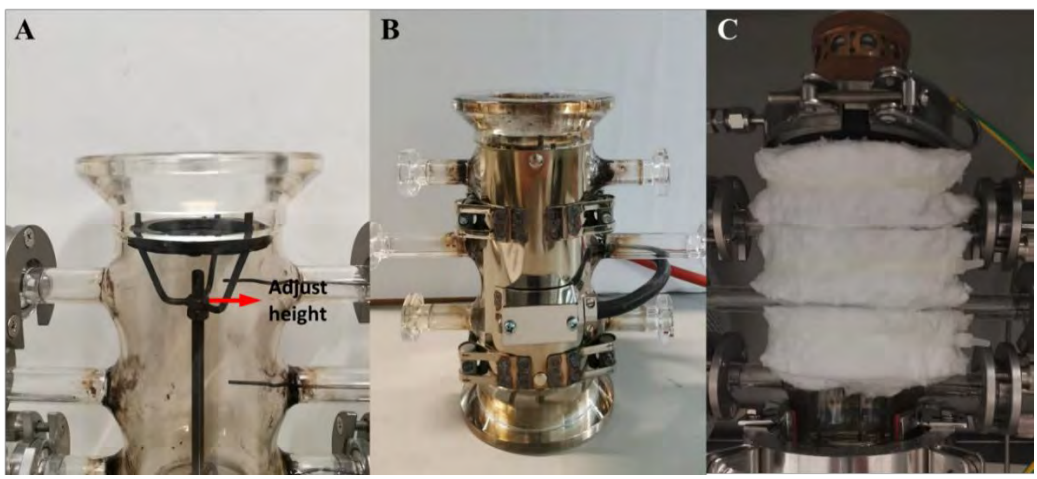

Fig. 4.2. Photograph of (A) a catalyst bed (T-bed), (B) a T-bed with an extra heating jacket, and (C) the insulation wrapped around the heating jacket to keep the heat.

A catalyst bed (T-bed) was used, as depicted in Fig. 4.2A. To load the catalyst bed, a quartz wool layer was first placed on the metal grid of the catalyst bed. The

catalyst and α-Al_2O_3 filling material were mixed in a sample cup and then spread over the quartz wool. Another layer of quartz wool was placed on the top and an additional grid was used to secure it against displacement. The distance of the catalyst bed from the post-plasma was adjustable, ranging from 2 cm to 4 cm.

An extra heating jacket equipped with a temperature control device (HEWID, Heizelemente GmbH) provided additional heat. Aluminium silicate insulation cotton wrapped around the heating jacket was added to maintain the temperature inside the post-plasma reactor tube.

To reduce potential carbon deposition, that could deactivate the catalyst, H_2O was introduced into the feed gas in some experiments, using a controlled evaporator mixer (CEM, Bronkhorst), as shown in Fig. 4.1. A digital mass flow controller (mini CORI-FLOW, Bronkhorst) regulated the H_2O mixing, with a relative humidity range of 0 to 100%. The temperature for the H_2O and mixed gas was set at 70 °C, and the catalyst bed was positioned at 3 cm post-plasma.

The calculations for the performance metrics (such as conversion, selectivity, yield, energy cost, etc.) of the plasma-based DRM under various conditions were the same as those detailed in Chapter 3 and will not be repeated here.

4.2.3 Thermal catalytic DRM conditions

The thermal catalytic activity of the catalyst was assessed in a fixed-bed reactor. The catalyst was uniformly pressed into tablets at 5 MPa, then crushed and sieved to a particle size of 150 – 200 μm. α-Al_2O_3 (Alfa Aesar, 3/16 inch) filling material was prepared to the same size. For the reaction, a combination of 10 mg Ni/MO catalyst and 100 mg α-Al_2O_3 was used, with a GHSV of 480 $L \cdot g_{cat}^{-1} h^{-1}$. A gas flow rate of 80 mL/min, comprising a mixture of Ar/CH_4/CO_2 in an 8/1/1 ratio, was employed. Prior to initiating the reaction, the mixed material was placed in the fixed bed, and a 20% H_2/Ar gas mixture at a flow rate of 80 mL/min was used to reduce the catalyst at 800 °C for 30 minutes. Subsequently, pure Ar gas was flowed through the reactor for an additional 30 minutes to eliminate any residual H_2. While mainting the temperature at 800 °C, the feed gas was switched to 64 mL/min Ar, 8 mL/min CH_4, and 8 mL/min CO_2. The GC then began recording the gases exiting the fixed bed. After over an hour, when the results stabilized, pure Ar was again used to purge any remaining reactants from the reactor while gradually lowering the temperature. Experiments at varying temperatures were subsequently conducted, decreasing from 800 °C to 400 °C.

4.3 Results and Discussion

4.3.1 Catalyst characterization

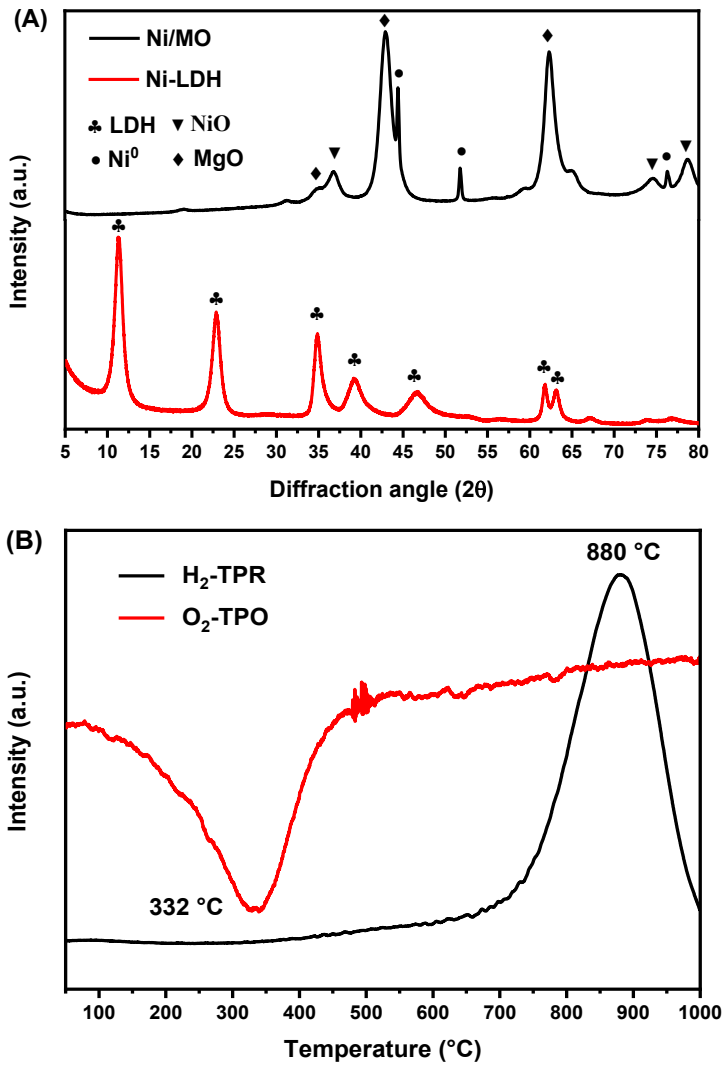

Fig. 4.3. (A) XRD patterns of the Ni-LDH and calcined and reduced Ni/MO and (B) H_2-TPR and O_2-TPO of the calcined Ni/MO.

The XRD patterns of as-prepared Ni-LDH and the Ni/MO catalyst (after calcination and reduction) are shown in Fig. 4.3A. For the Ni-LDH, peaks at 11.3°,

22.9°, 34.8°, 39.3°, 46.6°, 61.8° and 63.1° were noted, confirming the successful synthesis of the Ni-LDH phase. The introduction of Ni did not alter the LDH structure. The Ni/MO catalyst, produced after calcination and reduction, exhibited XRD patterns with peaks of Ni^0 at 2θ values of 44.3°, 51.7° and 76.3°. Additionally, phases of MgO and NiO were detected in the Ni/MO catalyst. The appearance of NiO in the reduced Ni/MO can be due to a partial reoxidation of the Ni during the measurement. The H_2-TPR was conducted to examine the reduction behaviour and the interaction between Ni and the support, as shown in Fig 4.3B. The TPR results revealed a single wide peak centered at approximately 880 °C, attributed to the reduction of Ni^{2+} species in the metal oxide to Ni^0 [7]. The absence of other peaks indicates a uniform distribution of Ni and the lack of bulk crystallite NiO species formation.

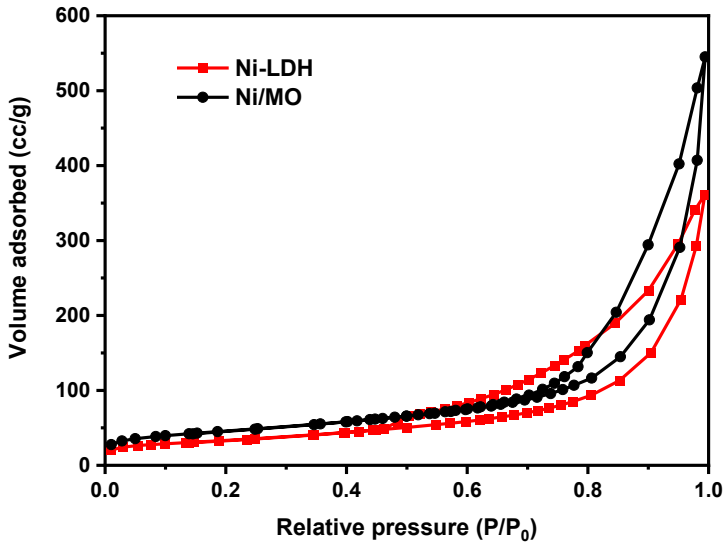

Fig. 4.4 Nitrogen adsorption-desorption isotherms at -196 °C of the as-prepared Ni-LDH and the obtained Ni/MO after calcination.

After calcination to produce the Ni/MO catalyst, the structure of the Ni-LDH changed. Fig. 4.4 shows the N_2 sorption isotherm of the Ni-LDH and Ni/MO samples. The change in hysteresis at relative pressures > P/P_0 0.45 confirm the change in morphology of the particles after calcination from a plate-like morphology to small particles with interstitial porosity. The apparent BET specific surface area of Ni-LDH was 117 m^2/g. After calcination the resulting Ni/MO exhibited a larger specific surface area of 178 m^2/g. As explained in section 2.3.5, this increase is attributed to the collapse of the layered structure and the loss of interlayer molecules or anions.

4.3.2 Thermal catalytic DRM conversions

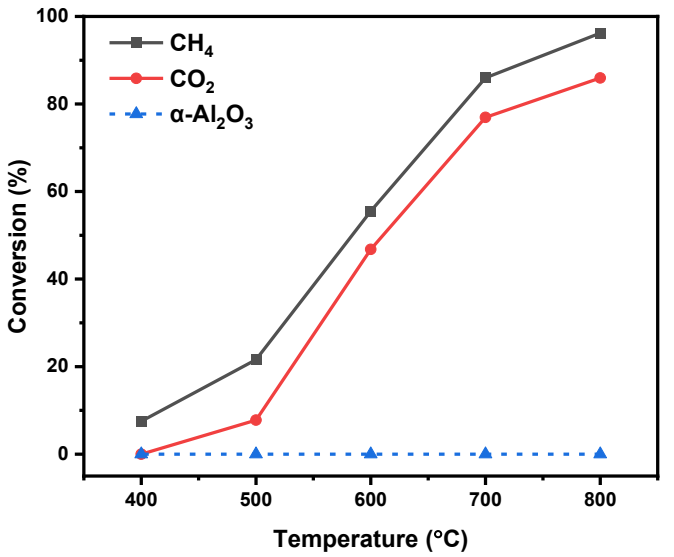

Fig. 4.5. Conversions of the Ni/MO catalyst in the thermal catalytic DRM reaction at different temperatures. As a comparison, the same amount of α-Al_2O_3 filling material was also tested under the same conditions. Experimental conditions: catalyst: 10 mg, gas flow rate: 80 mL/min (GHSV = 480 L·g_{cat}^{-1}·h^{-1}) gas composition: Ar/CO_2/CH_4 = 8/1/1.

As shown in Fig. 4.5, the catalytic activity of the Ni/MO catalyst exhibited an increase with rising temperature. The highest conversion was achieved at 800 °C reaching 86% for CO_2 and 96% for CH_4, respectively. Notably, at all tested temperatures, the conversion of CH_4 consistently exceeded that of CO_2. This higher CH_4 conversion can be attributed to the direct CH_4 decomposition, forming coke, which blocks the active sites needed for CO_2 activation [8]. This is supported by the carbon balance (Table 4.1) which is about 89% at 800 °C. The absence of other hydrocarbon products suggests that the missing carbon likely transitions to a solid carbon phase. Although the carbon balance indicates formation of solid carbon, the amount was too small to be detected with Raman and TGA-MS. Another potential side reaction is the Boudouard reaction ($2CO \rightarrow C + CO_2,\ \Delta H^0 = -172\ kJ/mol$) which also leads to carbon deposition and produces CO_2 which lowers conversion [9,10]. Moreover, a blank experiment with only α-Al_2O_3 as filling material was performed, proving that the filling material is inactive as no conversion of CO_2 and CH_4 was observed, as shown in Fig. 4.5.

Table 4.1. Selectivity, yield, H_2/CO ratio and carbon balance results of DRM with the Ni/MO catalyst in the thermal catalytic reaction

Temperature (°C)	Selectivity (%)		Yield (%)		H_2/CO ratio	C balance
	CO	H_2	CO	H_2		
800	88	100	81	80	0.9	89
700	89	100	73	70	0.9	91
600	92	100	48	41	0.8	96
500	100	100	18	11	0.6	101
400	100	100	3	1	0.3	103

4.3.3 Plasma DRM Results

4.3.3.1 Effect of distance of the catalyst bed after the plasma

The distance between the catalyst and the plasma outlet affects not only the temperature of the catalyst placement area, namely the heat transferred to the catalyst, but also affects the flow dynamics of the plasma gas. Changes in flow can lead to backflow, ultimately affecting the plasma results [11]. It should be noticed that the pressure gauge in the feed gas line did not show an obvious change in values for any of the experiments.

Based on the study in the Chapter 3, the temperature at a distance of 4.9 cm can reach about 500 °C, which, however, is not high enough for the Ni/MO catalyst to show good catalytic performance, as suggested by the thermal catalytic DRM (see Fig, 4.5). Therefore, a shorter distance should be used, which was hypothesized to pass more heat from the plasma to the catalyst layer. Here, as shown in Fig. 4.1A, the distance of the Ni/MO catalyst bed from the plasma outlet was adjusted and varied from 2 cm to 4 cm. i.e. the distance of the bottom grid of the catalyst bed on which the catalyst is put.

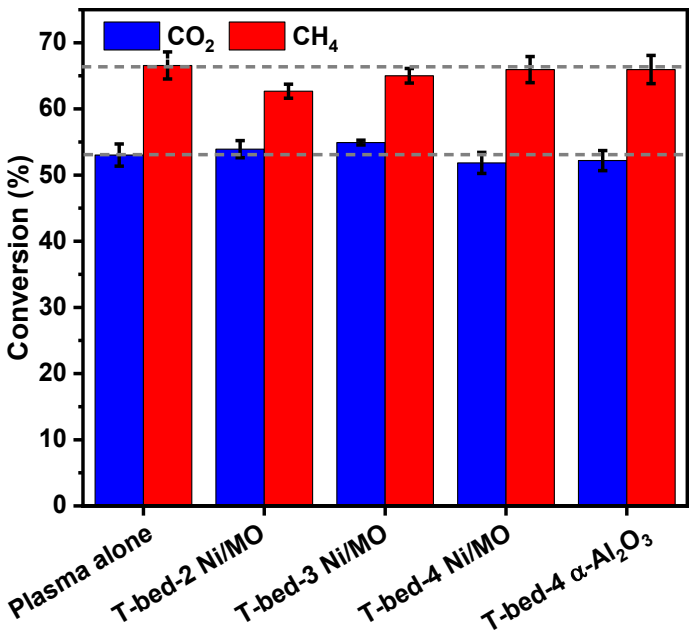

Fig. 4.6. Conversion of CH_4 and CO_2 for DRM in the GAP catalytic system at different distances with Ni/MO catalyst or filling material of α-Al_2O_3. Gas composition: $N_2/CH_4/CO_2$ = 8/1/1, GHSV: 480 $L \cdot g_{cat}^{-1} h^{-1}$.

Fig. 4.6 shows the conversion results in the plasma alone case and the plasma with Ni/MO catalyst at different distances from the plasma outlet (2, 3 and 4 cm) or with α-Al_2O_3 at 4 cm distance. In comparison to the CO_2 conversion in plasma alone, as the distance increased, its conversion fluctuated between 52% and 55% and remained almost the same considering the error. In contrast, with the catalyst, the conversion of CH_4 exhibited an increasing trend as the distance increased. Nevertheless, the addition of Ni/MO catalyst caused a decrease of CH_4 conversion from 67% in plasma alone to 63% in case of a distance of 2 cm. This decrease might be attributed to the fact that the addition of the T-bed close to the plasma caused a stronger backflow or changed the flow behaviour of the gas which

affected the plasma [11], resulting in a decrease in CH_4 conversion This negative effect of the Ni-based catalyst (Ni/Al_2O_3 and Ni/SiO_2) on the CO_2 and CH_4 conversion during the GA plasma DRM system has also been reported [4,12]. Moreover, at a distance of 4 cm, the conversion of both CO_2 and CH_4 over the Ni/MO catalyst and the α-Al_2O_3 filler were almost the same, suggesting that the catalyst had no catalytic effect in this condition.

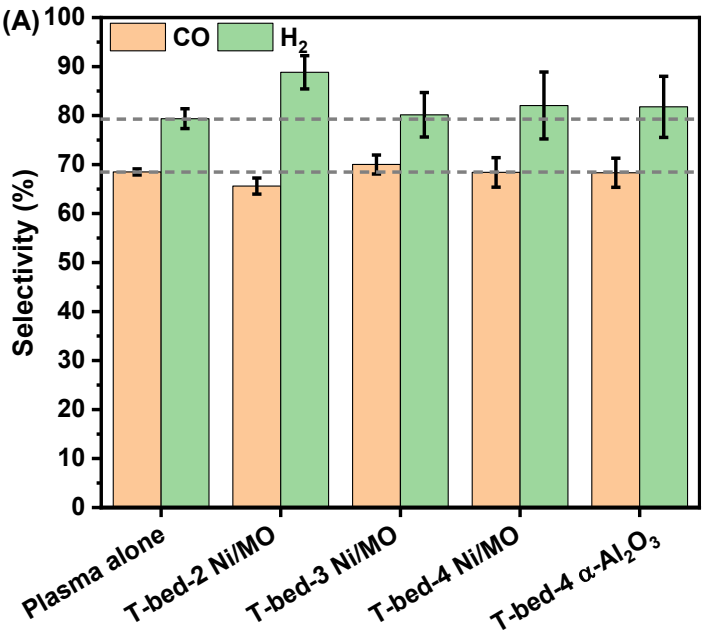

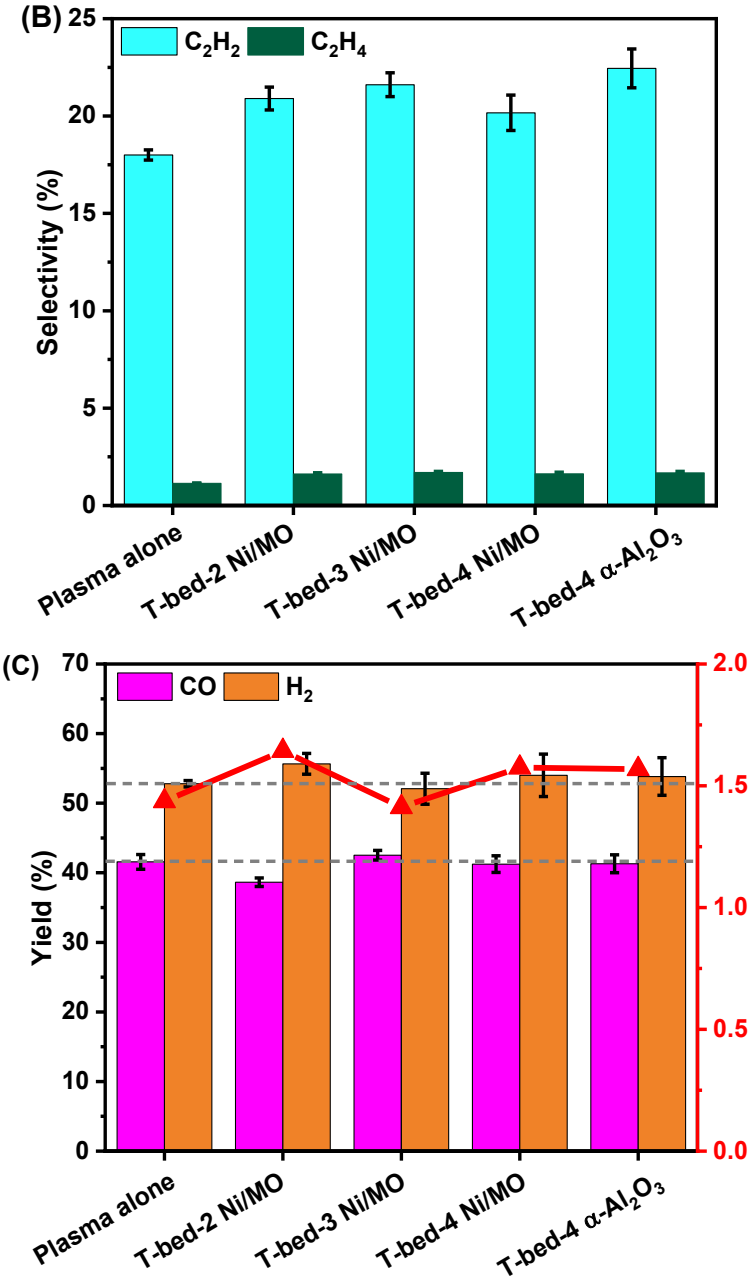
(B)
C_2H_2
C_2H_4
Selectivity (%)
0
5
10
15
20
25
Plasma alone
T-bed-2 Ni/MO
T-bed-3 Ni/MO
T-bed-4 Ni/MO
T-bed-4 α-Al_2O_3
(C)
CO
H_2
Yield (%)
H_2/CO ratio
0
10
20
30
40
50
60
70
0.0
0.5
1.0
1.5
2.0
Plasma alone
T-bed-2 Ni/MO
T-bed-3 Ni/MO
T-bed-4 Ni/MO
T-bed-4 α-Al_2O_3

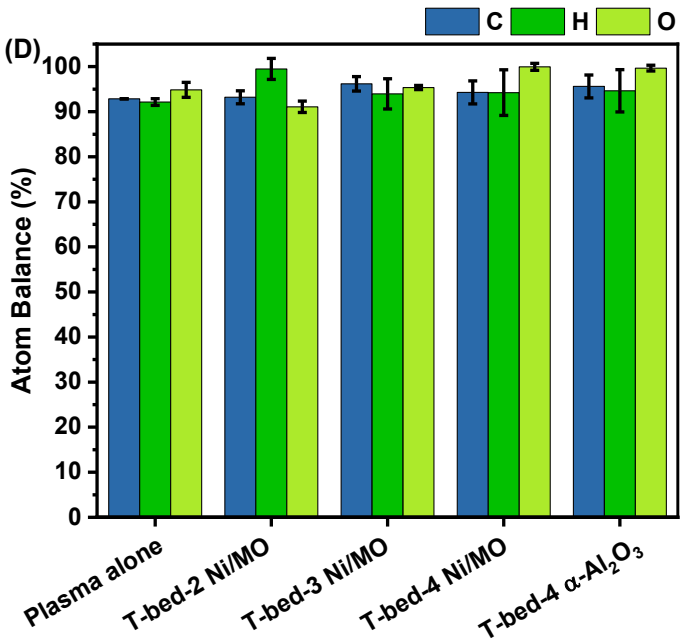

Fig. 4.7. Selectivity, yield, H_2/CO ratio and atom balance for DRM in the GAP catalytic system at different distances with Ni/MO catalyst or filling material of α-Al_2O_3 at 4 cm. (A) selectivity of CO and H_2, (B) Selectivity of C_2H_2 and C_2H_4, (C) Yield of CO and H_2, and H_2/CO ratio, and (D) C, H and O atom balance. (Calculation equations see Chapter 3) Gas composition: $N_2/CH_4/CO_2$ = 8/1/1, GHSV: 480 $L \cdot g_{cat}^{-1} h^{-1}$.

The results of the selectivity of CO, H_2, C_2H_2 and C_2H_4, the yield of H_2 and CO and their ratio are shown in Fig. 4.7(A-C). It is interesting to observe that the addition of the catalyst improved the selectivity of H_2. It first increased from 79% to 89% at 2 cm, and then decreased to a relatively stable range of 80 - 82% upon increasing distance (see Fig. 4.7A). However, when comparing the H_2 and CO selectivity of the Ni/MO catalyst with that of the α-Al_2O_3 filler in the 4 cm case, they were nearly identical. This suggests that at this distance, the catalyst did not enhance their selectivity. Besides this, the addition of the T-bed to the system generally had a positive effect on the C_2H_2 and C_2H_4 selectivity, which increased

a bit from 18% for C_2H_2 and around 1.4% for C_2H_4 in the plasma alone case to a range of 20 - 22% for C_2H_2 and about 1.6 - 1.7% for C_2H_4. However, also in this case, a comparison of these results of the Ni/MO catalyst and α-Al_2O_3 filler suggested that the increase in selectivity of C_2H_2 and C_2H_4 at 4 cm stopped. Due to the slight increase of CH_4 conversion and H_2 selectivity, the yield of H_2 increased from 53% to around 56% as the catalyst was added at a distance of 2 cm, resulting in a fluctuation of the H_2 yield with distance of the catalyst bed, while the selectivity of CO decreased from 42% to 39% as the catalyst was added at a distance of 2 cm and increased to around 42% upon increasing distance. The final H_2/CO ratio showed a similar trend as that of the H_2 yield.

Fig. 4.7D shows the atom balance of carbon, hydrogen and oxygen. The carbon balance in the plasma alone case was 93%, and it remained the same when considering the error in the calculations. In addition, the balance of hydrogen and oxygen was also lower than 100%, which implied the possibility of by-products like H_2O and some other hydrocarbon compounds that could not be analyzed or quantified by our GC.

The SEI is shown in Fig. 4.8 and demonstrates a stable energy input for all cases. A general value of 3.5 – 3.7 kJ/L was achieved. As the conversion of CO_2 was almost unchanged and that of CH_4 fluctuated a bit, the EC of the conversion

exhibited slight fluctuation between 5.9 and 6.3 kJ/L. A slight increase happened in all the cases with the addition of the T-bed with materials.

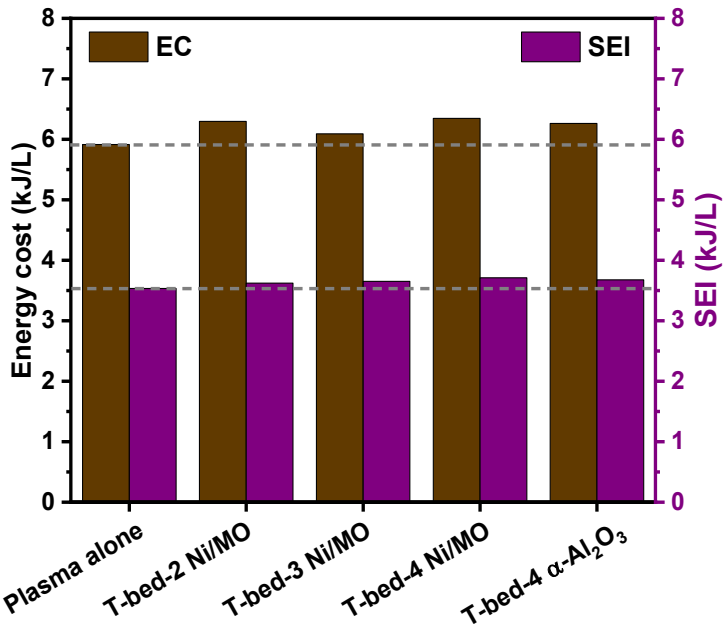

Fig. 4.8. Energy cost (EC, left y-axis) and specific energy input (SEI; right y-axis) (see formulas in Chapter 3) for DRM in the GAP catalytic system at different distances with Ni/MO catalyst or filling material of α-Al_2O_3 at 4 cm. Gas composition: $N_2/CH_4/CO_2$ = 8/1/1, GHSV: 480 $L \cdot g_{cat}^{-1} h^{-1}$.

The data presented in Fig. 4.6-4.8 lead us to conclude that introducing a T-bed with a catalyst has a limited effect on the outcomes, irrespective of distance, particularly in terms of conversions, although some enhancement in H_2 selectivity was noted. However, in the case of the 4 cm distance, a direct comparison between the Ni/MO catalyst and the α-Al_2O_3 filler indicates that the catalyst did not exhibit any catalytic activity under these conditions. Several factors could contribute to this observation: (1) The catalyst quantity might be insufficient, implying that while there is a catalytic effect, it is too minor to be noticeable. (2) The temperature at

the catalyst's location might be inadequate, rendering the catalyst inactive. (3) Potential carbon deposition on the catalyst could lead to its deactivation before reaching its active temperature range (as indicated in Fig. 4.5, the temperature should be above 500 °C) where it can demonstrate catalytic activity. (4) Physical effects such as flow behaviour, including back flow, or quenching effects might be at play. Therefore, to exclude the factors at the levels of the catalyst, the subsequent sections will delve into these three first aspects to further explore ways to enhance the PPC DRM results.

4.3.3.2 Effect of catalyst amount

Increasing the amount catalyst for the DRM reaction, essentially resulting in lower GHSV values, has been shown to enhance the conversion of CO_2 and CH_4 to some extent [6]. Therefore, more Ni/MO was added to evaluate its impact on the DRM results in the PPC system. Besides this, due to the heavy workload to make more catalysts and considering the comparable catalytic performance of Ni-α-Al_2O_3 at high temperatures [13], 10 g Ni-α-Al_2O_3 spheres were tested in this system for DRM as well. The Ni-α-Al_2O_3 catalyst was prepared by impregnating α-Al_2O_3 spheres (Alfa Aesar, 3/16 inch) with the same weight concentration of Ni (10 wt%) using the wet impregnation method. The calcination temperature and reduction process for the Ni-α-Al_2O_3 catalysts were identical to those used for the Ni/MO catalyst. The distance between the T-bed and the plasma was set at 3 cm.

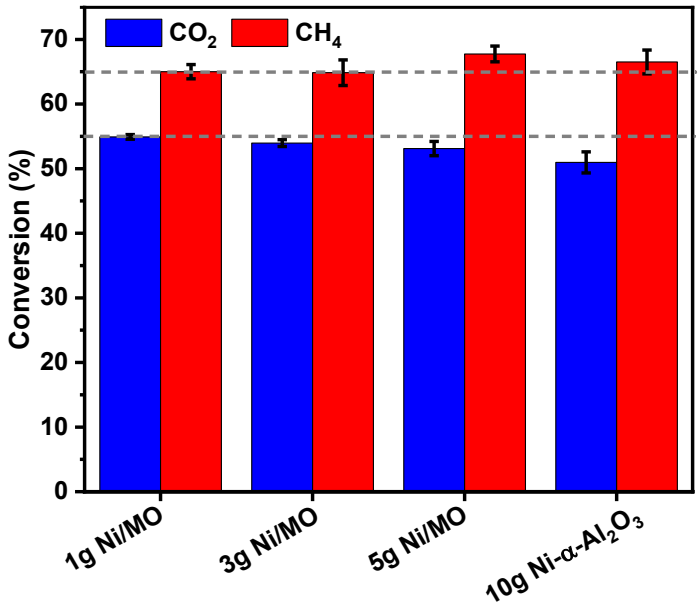

Fig. 4.9. Conversion of CH_4 and CO_2 for DRM in the GAP catalytic system with different amounts of Ni/MO catalyst and 10 g Ni-α-Al_2O_3. Gas composition: $N_2/CH_4/CO_2$ = 8/1/1.

As shown in Fig. 4.9, the addition of Ni/MO catalyst from 1 g to 5 g led to a slight decrease in CO_2 conversion from 55% to 53%, while the CH_4 conversion experienced a minor increase from 65% to 68%. However, the use of 10 g Ni-α-Al_2O_3 resulted in a more notable drop of CO_2 conversion to 51% and a slight decrease in CH_4 conversion to 67%. This outcome can be attributed to a combination of factors. Firstly, since the Ni-α-Al_2O_3 catalyst retained its spherical size of 3/16 inch, the use of 10 g Ni-α-Al_2O_3 catalyst may have led to an uneven distribution on the T-bed, which could have adversely impacted the plasma gas flow and, consequently, the DRM performance. Secondly, the characteristics of the 10 g Ni-α-Al_2O_3, such as Ni distribution, Ni particle size, and the interaction between Ni and the support, might differ, which can influence the catalytic results.

Although it is worth investigating the origin of this difference, the catalytic effect is in any case too limited and thus, other aspects that might have a more substantial impact on the catalytic effect, were deemed more important to evaluate first (see the following sections and Chapter 5). Generally, the enhancement effect of this catalyst was not as significant as expected.

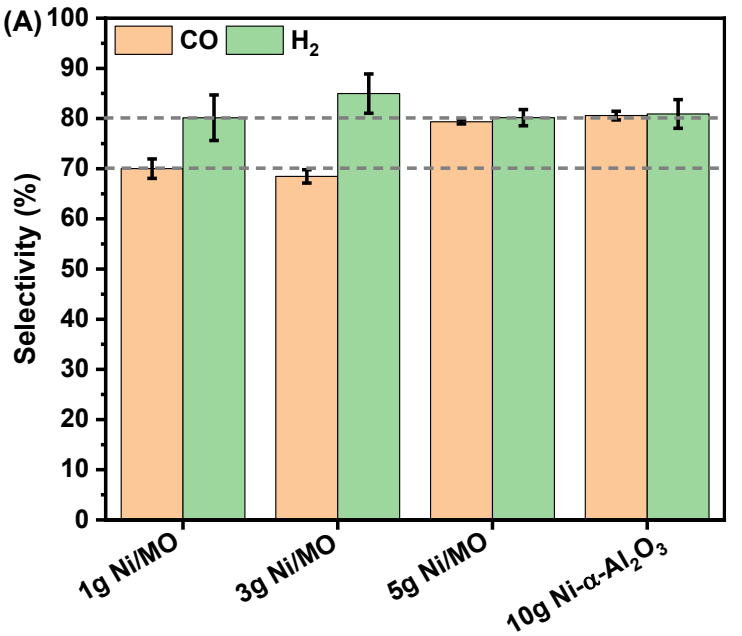

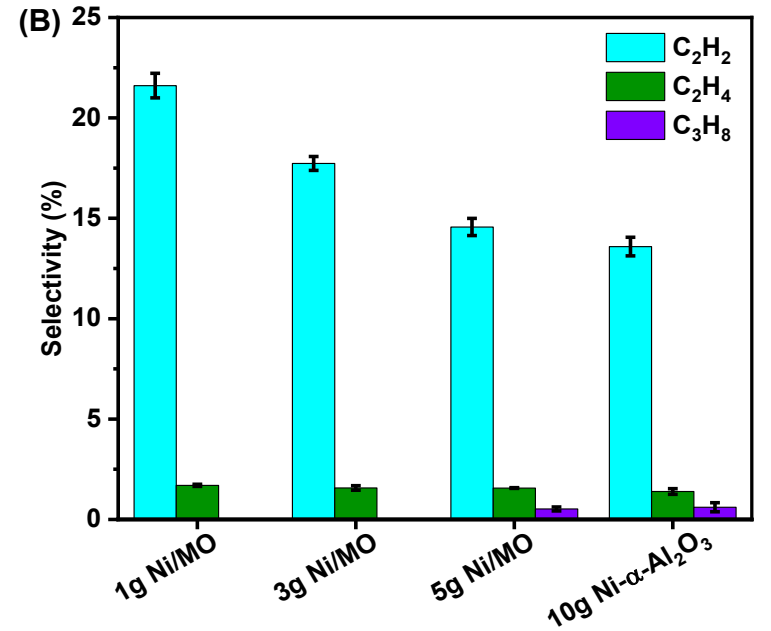
(B)
Selectivity (%)
25
20
15
10
5
0
C2H2
C2H4
C3H8
1g Ni/MO
3g Ni/MO
5g Ni/MO
10g Ni-α-Al2O3

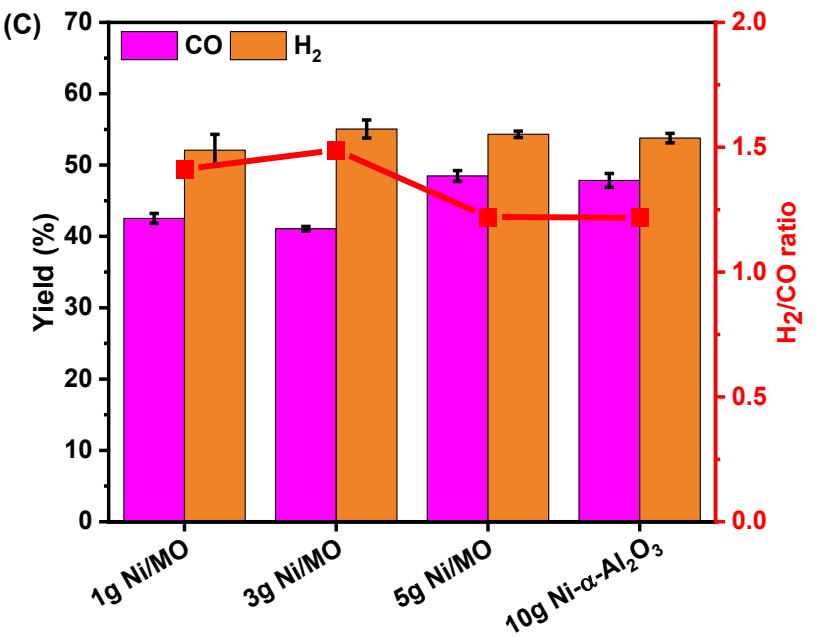
(C)
Yield (%)
70
60
50
40
30
20
10
0
CO
H2
2.0
1.5
1.0
0.5
0.0
H2/CO ratio
1g Ni/MO
3g Ni/MO
5g Ni/MO
10g Ni-α-Al2O3

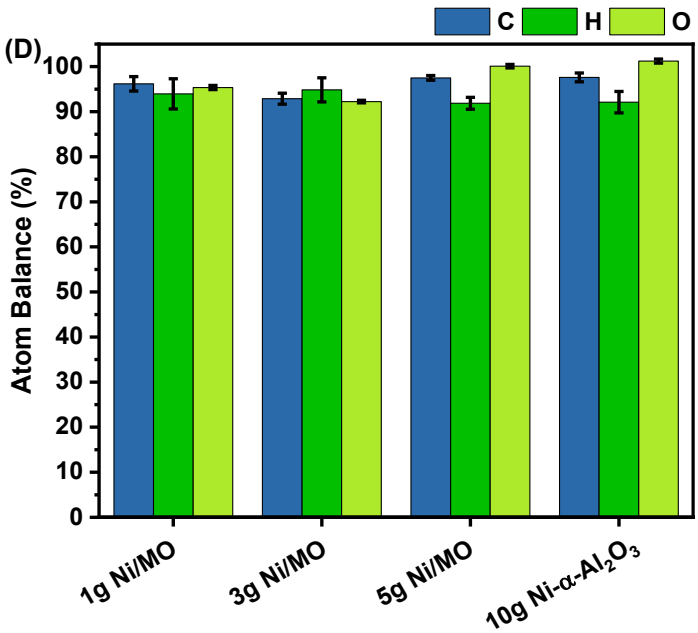

Fig. 4.10. Selectivity, yield, H_2/CO ratio and atom balance for DRM in the GAP catalytic system with different amounts of Ni/MO catalyst or 10 g Ni-α-Al_2O_3. (A) selectivity of CO and H_2, (B) Selectivity of C_2H_2, C_2H_4, and C_3H_8, (C) Yield of CO and H_2, and H_2/CO ratio, and (D) C, H and O atom balance. Gas composition: $N_2/CH_4/CO_2$ = 8/1/1.

When the amount of Ni/MO catalyst increased, the CO selectivity initially remained almost unchanged and then rose to 79%. In contrast, the H_2 selectivity exhibited a different trend, as depicted in Fig. 4.10A. It initially increased from 80% to 85% and then subsequently decreased back to 80%. Hence, when > 5g is used, the CO and hydrogen selectivity become equal while at a lower weight of catalyst, relatively more hydrogen is formed. More catalysts of Ni-α-Al_2O_3 exhibited the same selectivity performance as 5 g Ni/MO, suggesting that increasing the catalyst amount, most likely, cannot enhance the selectivity results in these PPC conditions. As shown in Fig. 4.10B, the selectivity of C_2H_2 showed a decreasing trend as the catalyst amount increased, which was around 22% in the 1 g Ni/MO catalyst case

and declined to 15% in the 5 g Ni/MO case. In addition, it further decreased to 14% as 10 g Ni-α-Al_2O_3 catalyst was used. Moreover, the peak of propane appeared in the GC with selectivity of around 0.5-0.6% as 5 g Ni/MO and 10 g Ni- Ni-α-Al_2O_3 were utilized. Due to the limited changes in the conversions, the yield of CO and H_2 showed a similar trend to the selectivity. The H_2/CO ratio initially increased from 1.4 to 1.5 and then decreased to 1.2. The atom balance showed fluctuations without a clear trend. As shown in Fig. 4.11, the SEI and EC were not affected by the increase of Ni/MO amount, while the EC increased a bit (from 6.1 to 6.4 kJ/L) as the catalyst and its amount changed to 10 g Ni-α-Al_2O_3.

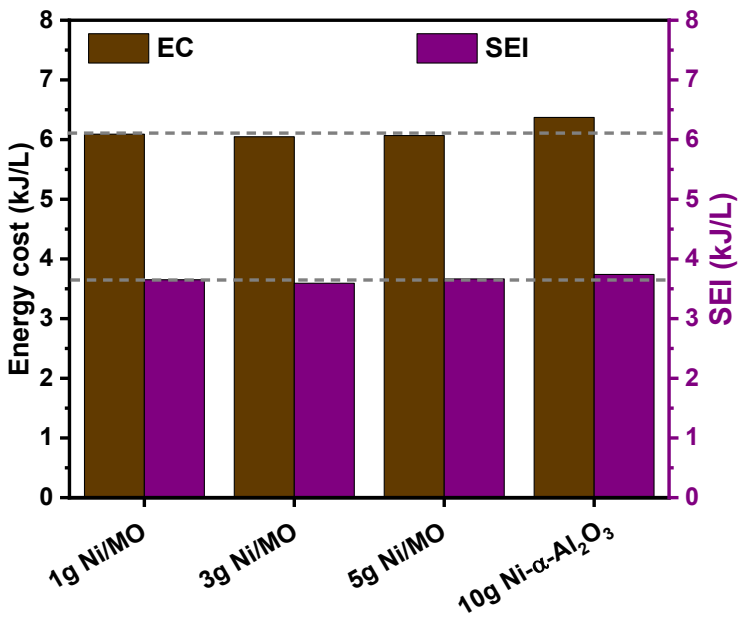

Fig. 4.11. Energy cost (EC) and specific energy input (SEI) for DRM in the GAP catalytic system with different amounts of Ni/MO catalyst or 10 g Ni-α-Al_2O_3. Gas composition: $N_2/CH_4/CO_2$ = 8/1/1.

Generally, although the addition of more Ni/MO catalysts improved the selectivity of CO and decreased the selectivity of by-products like C_2H_2, it had little effect on

the conversions of CO_2 and CH_4 and did not reduce the EC for the reaction. Therefore, the catalyst amount may not be the reason for the limited or even absence of improvement for the PPC DRM, and further study is needed. The other two reasons, namely not enough heat and/or catalyst deactivation will subsequently be investigated.

4.3.3.3 Extra heating effect

The thermal catalytic experiments demonstrated that the temperature plays a crucial role in the activity of the catalyst. Therefore, an extra heating jacket was added to the outside of the reactor, which was wrapped with insulation materials to avoid heat losses (as shown in Fig. 4.2 B-C). In addition, the catalyst bed was moved to 2 cm from the plasma to provide a higher temperature environment for the catalyst. Three temperature points of the heating jacket, 150 °C, 200 °C, and 250 °C, were tested. A thermocouple was bent into the catalyst layer to measure the temperature. The cases with different heating temperatures will be written in short as H-T, where T represents the temperature.

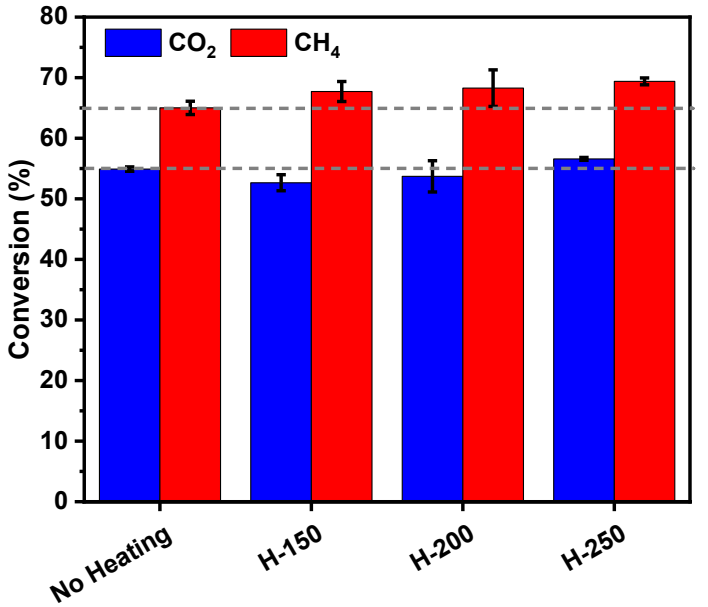

Fig. 4.12. Conversion of CH_4 and CO_2 for DRM in the GAP catalytic system at different extra heating temperatures. Gas composition: $N_2/CH_4/CO_2$ = 8/1/1, GHSV: 480 $L \cdot g_{cat}^{-1} h^{-1}$.

With the application of extra heating, the CO_2 conversion initially decreased from 55% to approximately 53% when heating was added at 150 °C (H-150) and 200 °C (H-200). Subsequently, it increased to 57% as the heating temperature was raised to 250 °C (H-250). Conversely, the conversion of CH_4 showed a consistent upward trend with the increase in temperature, rising from 65% without heating to 69% in the H-250 case.

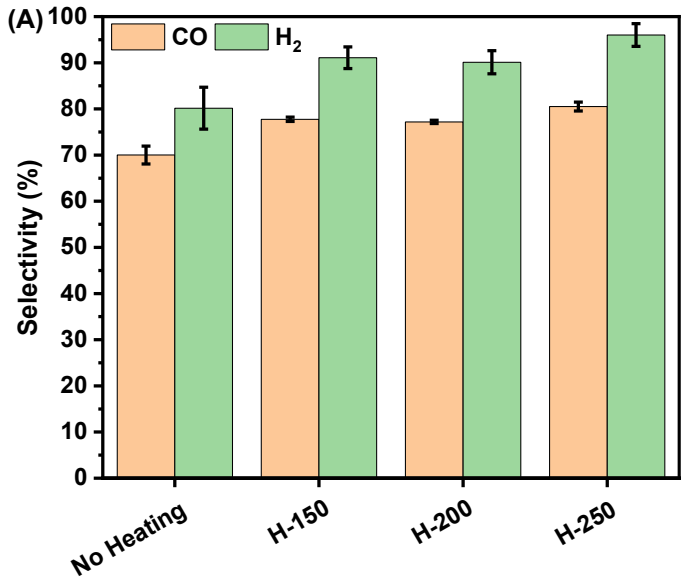
(A)
CO
H2
Selectivity (%)
100
90
80
70
60
50
40
30
20
10
0
No Heating
H-150
H-200
H-250

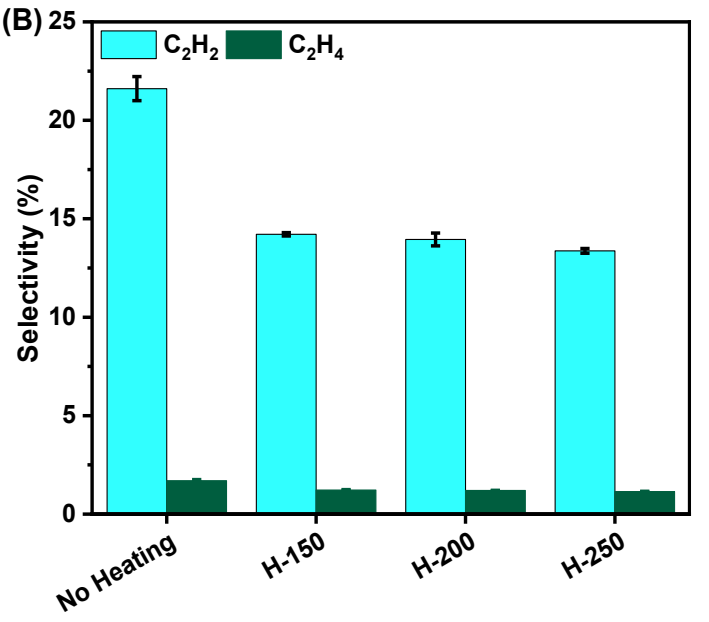
(B)
C2H2
C2H4
Selectivity (%)
25
20
15
10
5
0
No Heating
H-150
H-200
H-250

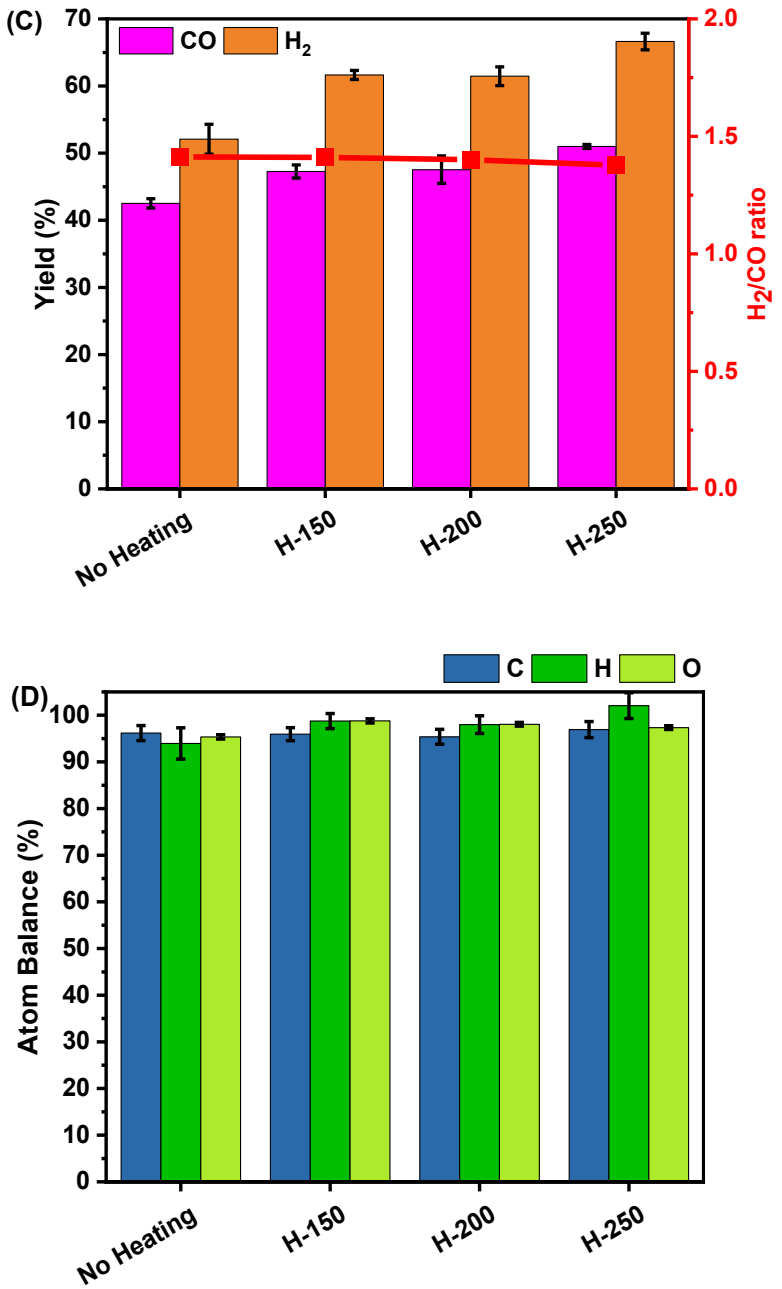

Fig. 4.13. Selectivity, yield, H_2/CO ratio and atom balance for the DRM in the GAP catalytic system at different extra heating temperatures. (A) selectivity of CO and H_2, (B) Selectivity of C_2H_2 and C_2H_4, (C) Yield of CO and H_2, and H_2/CO ratio, and (D) C, H and O atom balance. Gas composition: $N_2/CH_4/CO_2$ = 8/1/1, GHSV: 480 $L \cdot g_{cat}^{-1} h^{-1}$.

An additional interesting observation was the increasing CO and H_2 selectivity with the introduction of extra heating to the system, as shown in Fig. 4.13A. The selectivity for CO rose from 70% to 81%, and for H_2 from 80% to 96%. Moreover, the higher temperature seemed not beneficial for the production of C_2H_2 and C_2H_4 (see Fig. 4.13B). The C_2H_2 selectivity was around 22% without extra heating and it decreased as the temperature increased, reaching 13% in the H-250 case. The selectivity of C_2H_4 exhibited a similar but slightly weaker trend: it was about 1.7% without heating and declined to 1.1% at a heating temperature of 250 °C. A generally stable CO_2 conversion and an increase in CH_4 conversion and selectivity of CO and H_2 contributed to an increase in CO and H_2 yield, which were enhanced from 43% to 51% for CO, and from 52% to 67% for H_2. However, their ratio slightly decreased from 1.41 to 1.38.

The atom balance of C remained stable at around 96% (see Fig. 4.13D) suggesting the existence of carbon deposition and carbon-containing species that were not detected or quantified by our GC in all the cases, and no improvement was observed as the heating temperature was increased. The values of EC and SEI, as shown in Fig. 4.14, both increased as the temperature increased, suggesting a lower energy efficiency resulting from extra heating in this manner, not yet including the EC of adding the heat itself.

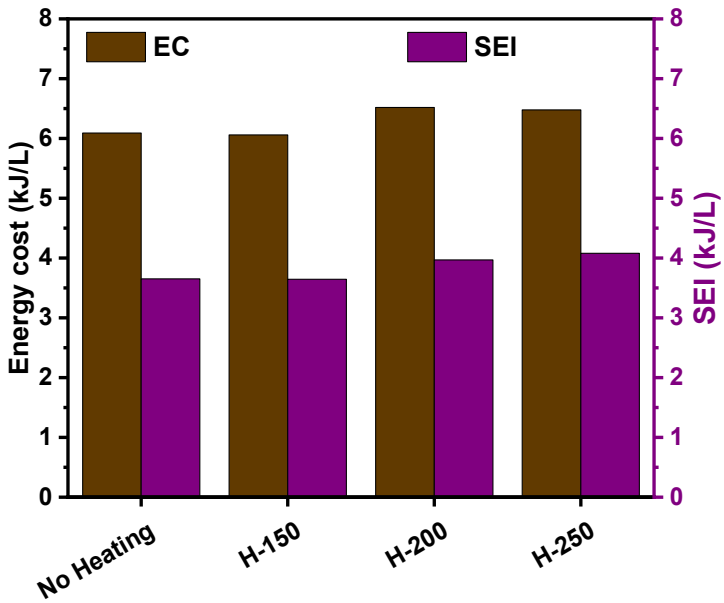

Fig. 4.14. Energy cost (EC) and specific energy input (SEI) for DRM in the GAP catalytic system at different heating temperatures. Gas composition: $N_2/CH_4/CO_2$ = 8/1/1, GHSV: 480 $L \cdot g^{-1}h^{-1}$.

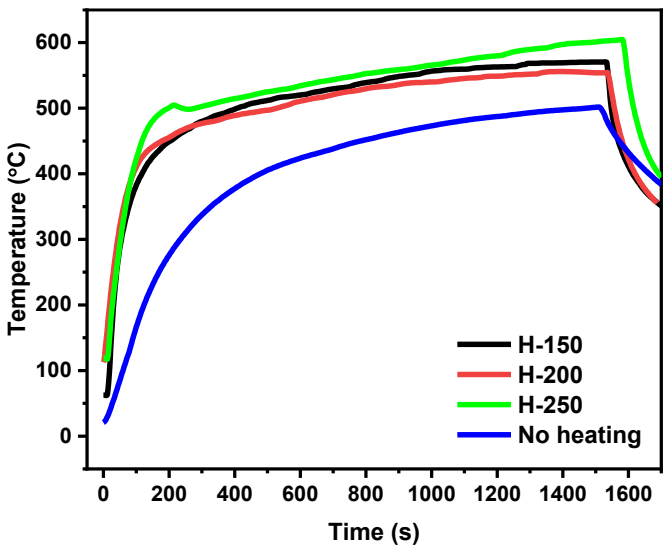

Fig. 4.15. Temperature measured in the catalyst layer in the GAP catalytic DRM system at different external heating temperatures. Gas composition: $N_2/CH_4/CO_2$ = 8/1/1, GHSV: 480 $L \cdot g_{cat}^{-1}h^{-1}$.

In general, in our PPC DRM system, although extra heating can improve the selectivity of CO and H_2 and seems to have some potential to enhance the conversion and selectivity at higher temperatures, the improvement is minor versus the possible economical impact due to the increased EC. Further study revealed that the real temperature was much lower than the set temperature, likely due to the high flow rates taking some heat and the possible low heat transfer effect because of the quartz wall. As shown in Fig. 4.15, introducing extra heating can efficiently enhance the surrounding temperature of the catalyst layer from 500 °C to around 600 °C in the H-250 case. However, the promoting effect was less when the heating temperature was set at lower temperatures of 150 or 200 °C. In addition, before starting the plasma, when extra heating was set at 150 °C, the temperature of the catalyst layer could only reach 60 °C; for extra heating of 250 °C, the temperature increased to about 120 °C, which was much lower than the set temperature and is most likely caused by the high flow rates, as mentioned above. Hence, the extra energy added to the heat from the plasma exhaust is limited. However, the most important result is that these experiments prove that insufficient heat for the catalyst can be the possible reason why there is no or only limited improvement on the PPC DRM system. This suggests a low utilization efficiency of the heat produced by the plasma passing to the catalyst. Therefore, to enhance the conversions and selectivity and to fully utilize the heat from the plasma, a better-designed reactor or catalyst bed is needed, which can either be efficiently combined with an extra heating system or which can collect more heat from the post-plasma

afterglow or a combination of both. Apart from this, the addition of H_2O into the feed gas is still interesting to study, because it may decrease the possible deactivation of the catalyst due to carbon deposition, enabling the catalyst to show catalytic activity at these heat transfer condition.

4.3.3.4 Addition of H_2O

Apart from the possibility of decreasing the catalyst deactivation by reducing the carbon deposition upon oxidation due to H_2O, the addition of H_2O into the dry reforming system can facilitate the production of H_2 [14–17]. Therefore, H_2O was added into the feed gas in the vapour phase by the CEM device as described in section 4.2.2. H_2O in a relative humidity (RH) between 40% and 100% was added. The GHSV was set at 480 $L \cdot g_{cat}^{-1} h^{-1}$. A comparison test with 5 g α-Al_2O_3 was done in both H_2O conditions to get more information about the catalytic effect of the Ni/MO catalyst.

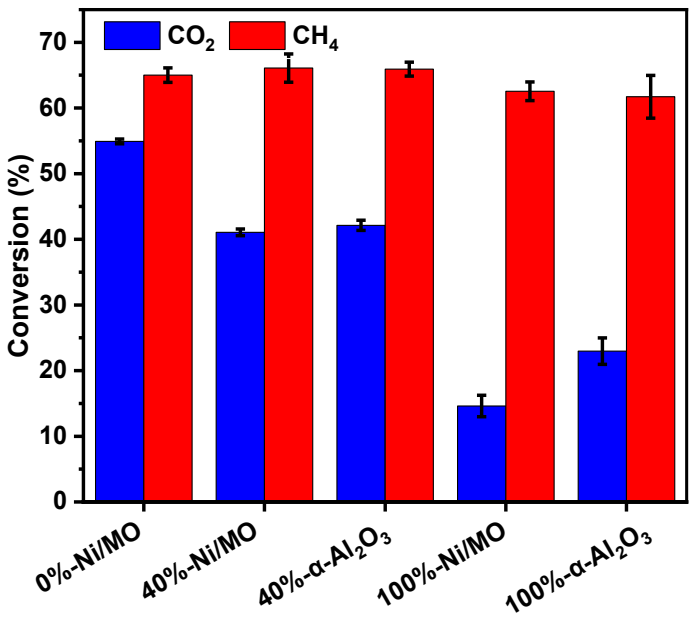

Fig. 4.16. Conversion of CH_4 and CO_2 for DRM in the GAP catalytic system with the addition of different RH. Gas composition: $N_2/CH_4/CO_2$ = 8/1/1, GHSV: 480 $L \cdot g_{cat}^{-1} h^{-1}$.

As shown in Fig. 4.16, the addition of H_2O decreases the conversion of CO_2 and has a small negative effect on the conversion of CH_4 at 100% RH. Specifically, the CO_2 conversion decreased from 55% without H_2O to 41% with the addition of 40% RH with the Ni/MO catalyst. However, comparing it with the α-Al_2O_3 case, the reason for the decline in conversion did not seem to be related to catalytic activity. When adding more H_2O to 100% RH, the CO_2 conversion dropped to 15% with the addition of the Ni/MO catalyst, which was even lower than the value of 23% obtained in the α-Al_2O_3 case. This suggested the detrimental effect of the catalyst in this condition, which can be attributed to the water gas shift reaction (WGSR, $CO + H_2O \rightarrow CO_2 + H_2,\ \Delta H^0 = -41.2 kJ/mol$). For CH_4, a decrease from 65% to around 62% conversion appeared as the H_2O content added increased from 0% to

100% RH. Moreover, comparing the Ni/MO with the α-Al_2O_3, the CH_4 conversions were almost the same, suggesting the absence of a catalytic effect for the CH_4 conversion.

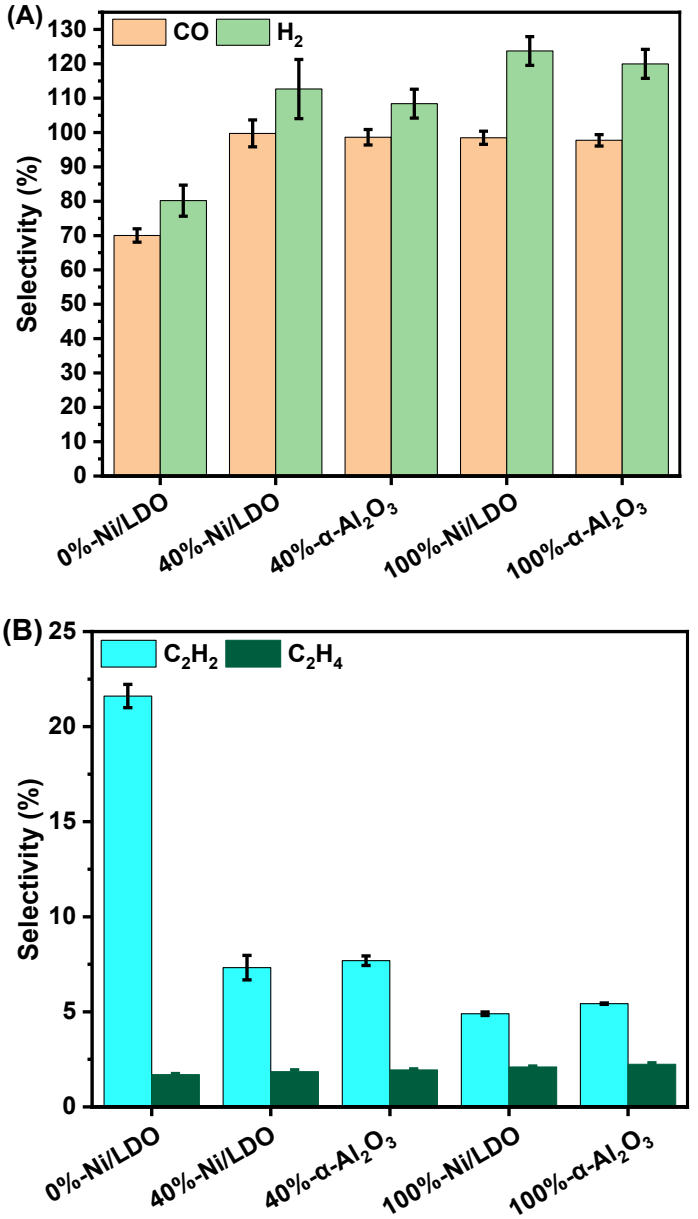

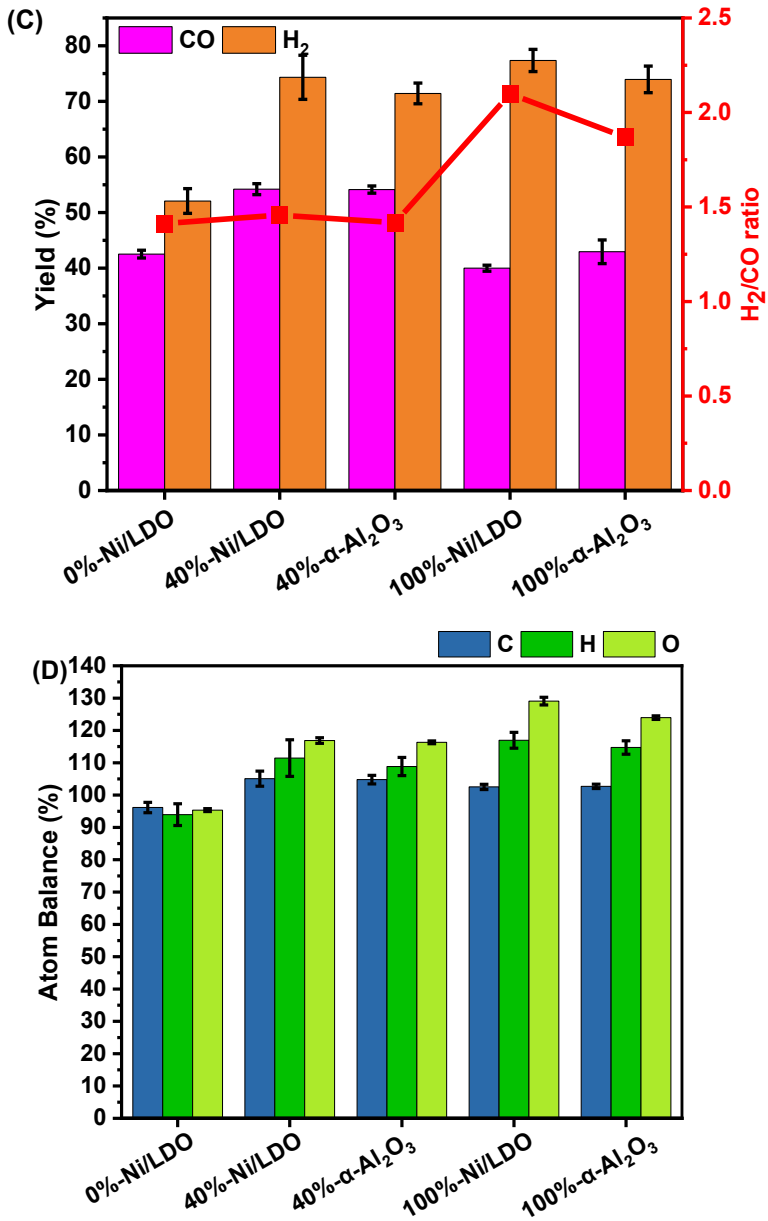

Fig. 4.17. Selectivity, yield, H_2/CO ratio and atom balance for DRM in the GAP catalytic system with the addition of different RH. (A) selectivity of CO and H_2, (B) Selectivity of C_2H_2 and C_2H_4, (C) Yield of CO and H_2, and H_2/CO ratio, and (D) C, H and O atom balance. Gas composition: $N_2/CH_4/CO_2$ = 8/1/1, GHSV: 480 $L \cdot g_{cat}^{-1} h^{-1}$.

As the peak of H_2O was hard to be analysed by the GC and a lot of H_2O was condensed on the inside wall of the reactor, it was hard to know exactly how much

H_2O was truly used in the reaction. Therefore, for the calculation of the H_2 selectivity and yield and H atom balance, CH_4 was used as the only H source to offer a qualitative analysis of how the RH affected the results.

With the addition of H_2O, the selectivity of both CO and H_2 increased (see Fig. 4.17A). The CO selectivity increased from 70% to about 100% and remained stable at around 100% for both 40% RH and 100% RH, suggesting that a lower amount of H_2O (40% RH for example herein) was already enough to achieve 100% CO selectivity. For the H_2 selectivity, its value increased from 80% to around 112% upon 40% RH and further increased to about 124% with the addition of 100% RH. This phenomenon demonstrated that apart from the WGSR reaction, direct dissociation of H_2O by the plasma contributed to the enhancement of H_2 production as well. The main by-product C_2H_2 was also heavily affected by the addition of H_2O, as shown in Fig 4.17B. It dropped from 22% to 7% with 40% RH and using the Ni/MO catalyst and further decreased to 5% when adding 100% RH. These values were slightly lower than those obtained with α-Al_2O_3, implying a small inhibition effect of the Ni/MO catalyst for C_2H_2 production. Compared with the decreasing trend of C_2H_2 selectivity, the C_2H_4 selectivity slightly increased from 1.7% to 1.9% in the 40% RH case and to 2.1% in the 100% RH case.

When looking at the yields, it first increased for CO with the addition of 40% RH due to the dramatic increase in CO selectivity, while it then decreased in the 100%

RH case because the CO selectivity remained at around 100% while the CO_2 conversion dropped significantly. A qualitative trend was shown that the H_2 yield increased clearly from 52% without any H_2O addition to 74% with the addition of 40% RH and further increased to 77% with 100% RH. Thus a higher H_2/CO ratio of 2.1 was achieved with Ni/MO in the 100% RH case. As the added H_2O contains H and O atoms and because for calculating the atom balance, only CO_2 and CH_4 in the feed gas were included, the balance of H and O atoms was much higher than 100%. Due to the existence of H_2O, deposited carbon can be oxidized, resulting in a C balance reaching around 100%, i.e., higher than 96% in the absence of H_2O.

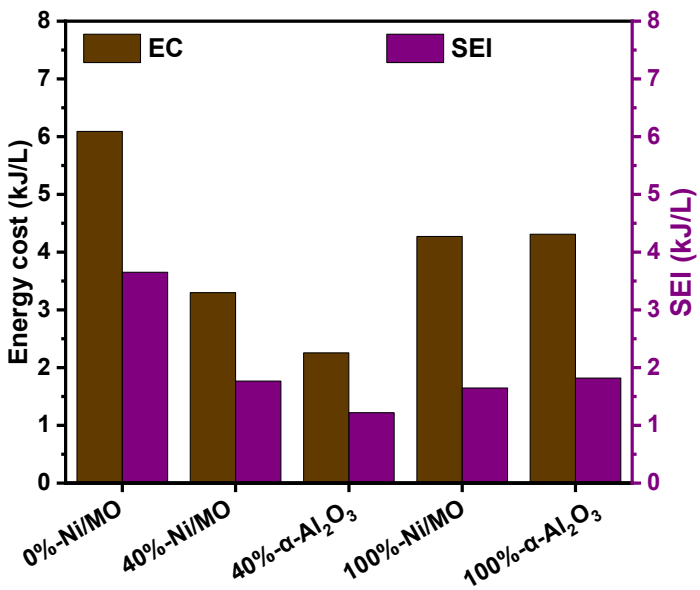

Fig. 4.18. Energy cost (EC) and specific energy input (SEI) for the DRM reaction in the GAP catalytic system with the addition of different RH. Gas composition: $N_2/CH_4/CO_2$ = 8/1/1, GHSV: 480 $L \cdot g_{cat}^{-1} h^{-1}$.

When H_2O was added, the EC and SEI both decreased (see Fig. 4.18). A clear decrease in SEI appeared in the case of 40% RH with α-Al_2O_3 from 3.7 kJ/L

without H_2O to 1.2 kJ/L, i.e., lower than 1.8 kJ/L with Ni/MO catalyst. The reason for this is unknown. Although the addition of 100% RH resulted in a lower SEI than in absence of H_2O, the SEI was still higher than for the 40% RH case. In addition, the trends of EC values were the same as those of SEI with increasing H_2O amount. This was reasonable because a low H_2O amount yielded a higher total conversion of CO_2 and CH_4 and lower SEI values, suggesting less energy was needed to convert the CO_2 and CH_4.

The addition of H_2O into the DRM system was beneficial to decrease carbon deposition and increase H_2 production, which resulted in a higher H_2/CO (i.e., syngas) ratio. Moreover, it resulted in a lower EC compared with the absence of H_2O. However, due to the limitation of reactor design and the GC, it was difficult to accurately quantify the products formed. However, when combined with Ni/MO catalyst, the CO_2 conversion decreased a lot. This indicated that carbon deposition is not the reason why there is no improvement effect on the PPC DRM system or at least, it cannot be counteracted by the use of water, which might create additional issues due to the WGSR.

4.4. Conclusion

Several factors were examined to determine their impact on the Dry Reforming of Methane (DRM) in the Gliding Arc Plasmatron (GAP) post-plasma catalytic

system, including the distance between the catalyst and the plasma exhaust, the amount of catalyst used, the application of extra heating and the addition of H_2O. The distance and quantity of the catalyst showed limited influence on the conversions of CO_2 and CH_4. However, for improving the selectivity of CO and H_2, 1 g of Ni/MO catalyst positioned at a distance of 2 or 3 cm was found to be optimal for achieving higher values. The application of external heating enhanced the CH_4 conversion from 65% to 69% in the H-250 scenario. Notably, there was a significant increase in selectivity, from 70% and 80% without heating to 81% and 96% for CO and H_2, respectively, in the H-250 case. Nevertheless, this improvement came with an increased energy cost from the external applied extra heating. Further analysis indicated that a considerable amount of heat was lost due to the inefficient design of the heating jacket in relation to the reactor. Introducing H_2O into the feed gas effectively improved the selectivity of CO and H_2 and reduced carbon deposition. However, this led to a considerable decrease in CO_2 conversion, dropping from 55% without H_2O to just 15% with 100% relative humidity (RH) when using the Ni/MO catalyst, which was hypothesized to be at least partly due to the WGSR reaction. Moreover, part of the decrease in CO_2 conversion is not associated to the catalyst itself, as also the filling material showed a decrease in CO_2 conversion.

In summary, increasing the temperature of the catalyst bed was beneficial for the improvement of DRM in this GAP plasma system, indicating that the main reason

why the catalyst did not show catalytic performance is because there is not enough heat from the plasma outlet transferred to the catalyst. Therefore, either a better post-plasma reactor design to efficiently utilize the extra heating and/or a well-designed catalyst bed to facilitate the collection of heat from the plasma is necessary for the post-plasma GAP system, which will be the focus of the next chapter.

4.5 References

[1] Snoeckx, R.; Bogaerts, A. Plasma Technology – a Novel Solution for CO_2 Conversion? Chem. Soc. Rev. 2017, 46, 5805.

[2] Feng, J.; Sun, X.; Li, Z.; Hao, X.; Fan, M.; Ning, P.; Li, K. Plasma-Assisted Reforming of Methane. Adv. Sci. 2022, 9 (34), 1–36. https://doi.org/10.1002/advs.202203221.

[3] Puliyalil, H.; Lašič Jurković, D.; Dasireddy, V. D. B. C. .; Likozar, B. A Review of Plasma-Assisted Catalytic Conversion of Gaseous Carbon Dioxide and Methane into Value-Added Platform Chemicals and Fuels. RSC Adv. 2018, 8 (48), 27481–27508. https://doi.org/10.1039/c8ra03146k.

[4] Martin-Del-Campo, J.; Uceda, M.; Coulombe, S.; Kopyscinski, J. Plasma-Catalytic Dry Reforming of Methane over Ni-Supported Catalysts in a Rotating Gliding Arc - Spouted Bed Reactor. Journal of CO_2 Utilization. 2021. https://doi.org/10.1016/j.jcou.2021.101474.

[5] Zhu, F.; Zhang, H.; Yan, X.; Yan, J.; Ni, M.; Li, X.; Tu, X. Plasma-Catalytic Reforming of CO_2-Rich Biogas over Ni/γ-Al_2O_3 Catalysts in a Rotating Gliding Arc Reactor. Fuel 2017, 199, 430–437. https://doi.org/10.1016/j.fuel.2017.02.082.

[6] Liu, J. L.; Li, Z.; Liu, J. H.; Li, K.; Lian, H. Y.; Li, X. S.; Zhu, X.; Zhu, A. M. Warm-Plasma Catalytic Reduction of CO_2 with CH_4. Catal. Today 2019, 330 (December 2017), 54–60. https://doi.org/10.1016/j.cattod.2018.05.046.

[7] Zhan, Y.; Song, K.; Shi, Z.; Wan, C.; Pan, J.; Li, D.; Au, C.; Jiang, L. Influence of Reduction Temperature on Ni Particle Size and Catalytic Performance of Ni/Mg(Al)O Catalyst for CO_2 Reforming of CH_4. Int. J. Hydrogen Energy 2020, 45, 2794–2807.

[8] Ren, Y.; Ma, Y. Y.; Mo, W. L.; Guo, J.; Liu, Q.; Fan, X.; Zhang, S. P. Research Progress of Carbon Deposition on Ni-Based Catalyst for CO_2-CH_4

Reforming. Catalysts 2023, 13 (4), 647. https://doi.org/10.3390/catal13040647.

[9] Lin, X.; Li, R.; Lu, M.; Chen, C.; Li, D.; Zhan, Y.; Jiang, L. Carbon Dioxide Reforming of Methane over Ni Catalysts Prepared from Ni-Mg-Al Layered Double Hydroxides: Influence of Ni Loadings. Fuel 2015, 162, 271–280. https://doi.org/10.1016/j.fuel.2015.09.021.

[10] Theofanidis, S. A.; Galvita, V. V.; Poelman, H.; Marin, G. B. Enhanced Carbon-Resistant Dry Reforming Fe-Ni Catalyst: Role of Fe. ACS Catal. 2015, 5 (5), 3028–3039. https://doi.org/10.1021/acscatal.5b00357.

[11] Zhang, H.; Li, L.; Xu, R.; Huang, J.; Wang, N.; Li, X.; Tu, X. Plasma-Enhanced Catalytic Activation of CO_2 in a Modified Gliding Arc Reactor. Waste Disposal and Sustainable Energy. 2020, pp 139–150. https://doi.org/10.1007/s42768-020-00034-z.

[12] Allah, Z. A.; Whitehead, J. C. Plasma-Catalytic Dry Reforming of Methane in an Atmospheric Pressure AC Gliding Arc Discharge. Catal. Today 2015, 256 (P1), 76–79. https://doi.org/10.1016/j.cattod.2015.03.040.

[13] Chaudhary, P. K.; Koshta, N.; Deo, G. Effect of O_2 and Temperature on the Catalytic Performance of Ni/Al_2O_3 and $Ni/MgAl_2O_4$ for the Dry Reforming of Methane (DRM). Int. J. Hydrogen Energy 2020, 45 (7), 4490–4500. https://doi.org/10.1016/j.ijhydene.2019.12.053.

[14] de Medeiros, F. G. M.; Lopes, F. W. B.; Rego de Vasconcelos, B. Prospects and Technical Challenges in Hydrogen Production through Dry Reforming of Methane. Catalysts 2022, 12 (4), 363. https://doi.org/10.3390/catal12040363.

[15] Ponomarev, A. A.; Aleksandrov, N. L. Kinetics of Energetic O^- Ions in the Discharge Plasmas of Water Vapor and H_2O-Containing Mixtures. Plasma Physics Reports. 2018, pp 986–995. https://doi.org/10.1134/S1063780X18100100.

[16] Hrabovsky, M.; Hlina, M.; Kopecky, V.; Maslani, A.; Krenek, P.; Serov, A.; Hurba, O. Steam Plasma Methane Reforming for Hydrogen Production. Plasma Chemistry and Plasma Processing. 2018, pp 743–758. https://doi.org/10.1007/s11090-018-9891-5.

[17] Xia, Y.; Lu, N.; Jiang, N.; Shang, K.; Wu, Y. Combined Steam and CO_2 Reforming of CH_4 for Syngas Production in a Gliding Arc Discharge Plasma. J. CO_2 Util. 2020, 37, 248–259.

CHAPTER 5

Improving the performance of gliding arc plasma-catalytic dry reforming via a new post-plasma tubular catalyst bed

This chapter is adapted from the paper: “Improving the performance of gliding arc plasma-catalytic dry reforming via a new post-plasma tubular catalyst bed; Wencong Xu, Lukas C. Buelens, Vladimir V. Galvita, Annemie Bogaerts, Vera Meynen”; to be submitted to Journal of Energy Chemistry.

Abstract

A combination of a gliding arc plasmatron (GAP) reactor and a newly designed tubular catalyst bed (N-bed) was applied to investigate the post-plasma catalytic (PPC) effect for dry reforming of methane (DRM). In comparison, a traditional tray-type plasma catalyst bed (T-bed) was also utilized. The post-plasma catalytic effect of a Ni-based mixed oxide (Ni/MO) catalyst with a thermal catalytic performance of 77% CO_2 and 86% CH_4 conversion at 700 °C was studied. Although applying the T-bed had little effect on plasma-based CO_2 and CH_4 conversion, an increase in selectivity to H_2 was obtained with a maximum value of 89% at a distance of 2 cm. However, even when only non-catalytic α-Al_2O_3 packing material was used in the N-bed configuration, compared to the plasma alone and the T-bed, an increase of the CO_2 and CH_4 conversion from 53% and 67% to 69% and 83% was achieved. The addition of the Ni/MO catalyst further enhanced the DRM reaction, resulting in conversions of 79% for CO_2 and 91% for CH_4. Hence, although no insulation nor external heating was applied to the N-bed post plasma, it provides a slightly better conversion than the thermal catalytic performance with the same catalyst, while being fully electrically driven. In addition, an enhanced CO selectivity of 96% was obtained and the energy cost was reduced from ~ 6 kJ/L (plasma alone) to 4.3 kJ/L. To our knowledge, it is the first time that a post-plasma catalytic system achieves this excellent catalytic performance for DRM without extra external heating or insulation.

5.1 Introduction

Simultaneously converting CH_4 and CO_2 through dry reforming of methane (DRM) has been a topic of significant interest for researchers worldwide for decades [1–3]. Due to the high stability of CO_2 molecules, the reaction is endothermic ($CO_2 + CH_4 \rightarrow 2CO + 2H_2, \Delta H^0 = 247\ kJ/mol$) which requires the reaction to usually happen at high temperatures over 700 °C. Furthermore, during the reaction, carbon deposition on the catalyst and catalyst sintering can lead to deactivation, thereby limiting its potential for further industrial application [1].

Among the various types of technologies to improve the state of the art, plasma, the fourth state of matter containing reactive species (electrons, ions, radicals, and excited molecules), provides a particularly unique pathway as it can use flexible and renewable electrical energy sources, and can relatively easily be scaled up [4–7]. In its simplest case, plasma is a (partially) ionized gas, which is produced by gas flowing between two electrodes, between which there is an electric potential difference. This causes gas breakdown and the creation of free electrons and ions. The electrons collide with the gas molecules, producing other reactive species, such as radicals and excited molecules. This chemical species cocktail creates a reactive environment that facilitates the dissociation of stable molecules, such as CO_2 and CH_4 under DRM conditions [8]. The product obtained from the plasma DRM reaction mainly contains syngas (H_2/CO), as well as hydrocarbons and oxygenates

[8–13]. Extensive investigation for plasma-based DRM has been done with various types of plasma technologies, such as dielectric barrier discharge (DBD) [10,14–19], radio-frequency (RF) discharges [20–22], glow discharges [13,23], microwave (MW) discharges [24–27], corona discharges [28,29], and gliding arc (GA) discharges [8,30–35]. It is worth noting that the GA plasma is a promising plasma type for DRM, as it can generate electrons with an energy of around 1 eV, which is ideal for the CO_2 vibrational excitation during the dissociation process [31,36,37].

However, the classical two-dimensional (2D) GA plasma is still facing limitations, such as limited conversion of 10 to 40%, because a considerable fraction of feed gas does not pass through the plasma region [37–41]. Therefore, new designs were developed with improvements of cylindrical electrodes and tangential gas entrances, which allow the formation of a vortex flow, resulting in longer residence times and eventually higher conversions of 14 to 65% [8,30–32,42,43]. Among them, a gliding arc plasmatron (GAP), developed by Nunnally et al. [44], showed high potential for DRM [8,30,31]. Nevertheless, the highest conversion is still in the range of 40 to 60% in the plasma alone case [30], which is lower than the typical value of around 90% achieved in thermal catalytic DRM at high temperatures above 750 °C [45–47]. Therefore, a method to improve its plasma performance is needed. Implementing a catalyst bed after the plasma, forming a post-plasma catalytic (PPC) system, can be a possible way to further improve the gas conversion.

Currently, for the GAP setup, no systematic study on PPC DRM was performed. But lessons can be learnt from other types of GA PPC DRM systems. Zhang et al. [48] showed by means of simulations that after adding a catalyst bed, a strong backflow of gas above the catalyst bed occurred, which partly flowed back to the plasma area, where it was further treated by the plasma. Li et al. [49] investigated the relation between distance and temperature in a GA plasma system and summarized how the distance between a catalyst bed and plasma affected the results of reforming biogas with a feed gas molar ratio of CH_4:CO_2:O_2 = 3:2:1.8. They found that the catalyst mid-bed temperature elevated from 647 °C to 779 °C as the distance between the catalyst bed and the top of the plasma reactor cylinder decreased from 11 to 4 cm, which was attributed to the decrease of heat loss from the GA plasma when approaching the plasma area. Consequently, the conversions of CH_4 and CO_2 increased from 82% and 4% to 92% and 20%, respectively [49].

Martin-Del-Campo et al. [42] recently investigated the performance of DRM in a rotating gliding arc (RGA) plasma coupled with a spouted bed reactor system with and without catalysts. The authors found that the conversions of CO_2 and CH_4 for plasma alone were higher than those with catalysts. A possible reason was that the presence of a catalyst bed filled with materials interfered with the arc formation, which limited the formation of active species produced by the plasma [42]. On the

contrary, in another study reported by Zhu et al. [34], an enhancement in the conversion of CH_4 from 52.6% to 58.5% was observed when the RGA plasma was combined with a Ni/γ-Al_2O_3 catalyst loaded with 10 wt% Ni, compared with plasma alone for DRM. However, the presence of the catalyst had almost no effect on the CO_2 conversion. Liu and colleagues [50] reported that supplying extra heat to the catalyst reactor after plasma could be a possible way to improve the GA plasma-catalytic system. Compared to warm plasma alone (WP) (no catalyst), warm plasma catalysis without heating (WPC-NH) resulted in almost the same conversions of CO_2 and CH_4, suggesting that the Ni-based catalyst did not contribute to the DRM reaction, although it had good performance in the conventional thermal catalytic (CC) case. This was due to the low temperature of the after-plasma gas flow, which was only in the range of 350 °C to 500 °C, at which the Ni-based catalyst is inactive for DRM. Once extra heating was added at a temperature of 850 °C, the warm plasma catalysis with heating (WPC) case exhibited the highest conversions for both CO_2 and CH_4. Moreover, these values increased as the feed gas flow rate decreased, resulting in 94% CH_4 conversion and 91% CO_2 conversion at a gas hourly space velocity (GHSV) of 3200 h^{-1}. In another newly reported paper, Lian et al. [51] compared warm plasma co-reforming of dilute bioethanol and methane to produce hydrogen, with the warm plasma-catalysis case, in which extra heating at 800 °C improved the carbon conversion from 66% to 97%, the hydrogen yield from 55% to 78% and the energy efficiency

from 80% to 85%. Their research suggested the importance of extra heating in the warm plasma-catalytic system, which also proves that temperature is an important parameter for post-plasma catalysis. Thus, the question comes up whether there is a solution able to transfer more heat from the plasma to the catalyst and improve the catalytic conversion, without any extra heating? This would indeed be the ultimate goal to obtain a fully electrically driven process including heat (energy) integration of the plasma to the post-plasma catalyst [52].

Due to its good performance in thermal catalysis (see Chapter 4), a Ni-based mixed oxide (Ni/MO) catalyst derived from LDH (layered double hydroxide) was coupled with a GAP reactor for DRM. Different from the tray-type catalyst bed (T-bed), we propose a newly designed tubular catalyst bed (N-bed) with the purpose to enhance mass and heat transfer to the catalyst bed, as this was hypothesized as the key reason for the absence of catalytic performance in Chapter 4, while heating was also highlighted essential by several references in the state-of-the-art, as stated above. Therefore, the N-bed was directly connected to the plasma chamber and positioned inside the post-plasma quartz tube, forming a double wall effect, which was hypothesized to avoid the need for insulation or external heating. The latter is a key difference and innovation in this chapter with respect to the state-of-the-art. To evaluate the impact of the catalyst bed design, only the type of catalyst bed (N-type or T-type) was changed, while keeping the plasma operating conditions, gas

composition and catalyst identical. When using the N-bed at the same plasma conditions, we achieved excellent conversion results, i.e., 79% for CO_2 and 91% for CH_4, which were higher than the values obtained in the T-bed with catalyst (i.e., 53% for CO_2 conversion and 65% for CH_4 conversion). In addition, the selectivity towards syngas increased to 96% for CO and 92% for H_2. Moreover, compared with the plasma alone or T-bed with catalyst, the energy cost decreased by about 28%.

5.2 Experimental

5.2.1 Catalyst preparation and characterization

The support of MgAl-LDH was synthesized via the co-precipitation method as reported [53]. Then, 10 wt% Ni was loaded on the MgAl-LDH via the wet impregnation method, by contacting the MgAl-LDH with $Ni(NO_3)_2.6H_2O$ solution for 12 h while stirring, after which the Ni/MgAl-LDH was dried at 80 ℃ overnight and calcined at 800 °C for 6 h. The obtained Ni/MgAl mixed metal oxide (denoted as Ni/MO) powder was pressed into tablets at 5 MPa. Then, the tablets were crushed and sieved into a size of 0.4 – 0.6 mm. The obtained materials were reduced at 800 °C for 6 h with a flow rate of around 100 mL/min 2% H_2/Ar gas with a heating rate of 10 °C/min before they were applied for reaction. α-Al_2O_3 spheres (Alfa Aesar, 3/16 inch) were crushed and sieved into the same size fraction to be utilized as filling material. Before being used for reaction, the Ni/MO and α-

Al_2O_3 were uniformly mixed in a bottle. For a fair comparison, both thermal and GAP catalytic DRM were performed at the same weight GHSV of 480 $L \cdot g_{cat}^{-1} h^{-1}$.

Thermogravimetric (TG) analysis was performed on a 100 mg mixture of catalyst and α-Al_2O_3 after plasma or thermal catalytic DRM reaction to analyze the carbon deposition on the catalysts, using a Mettler Toledo TGA/SDTA851e thermal balance coupled with a Hiden HPR-20 R&D Mass Spectrometer (MS). Specifically, the sample was heated to 1000 ℃ under a flow of 80 mL/min O_2 with a heating rate of 10 ℃/min to determine the deposited carbon content. The MS signals for m/z within the range of 2 to 100 were collected. In addition, Raman spectra (Xplora Plus, Horiba Scientific) were recorded to understand the crystal structure of the carbon collected after plasma reaction from the reactor tube or on the catalyst. The Raman spectra were measured at a laser excitation wavenumber of 532 nm (with a filter value of 10%) in a spectral range of 100 – 3500 cm^{-1}.

5.2.2 Plasma-catalytic DRM

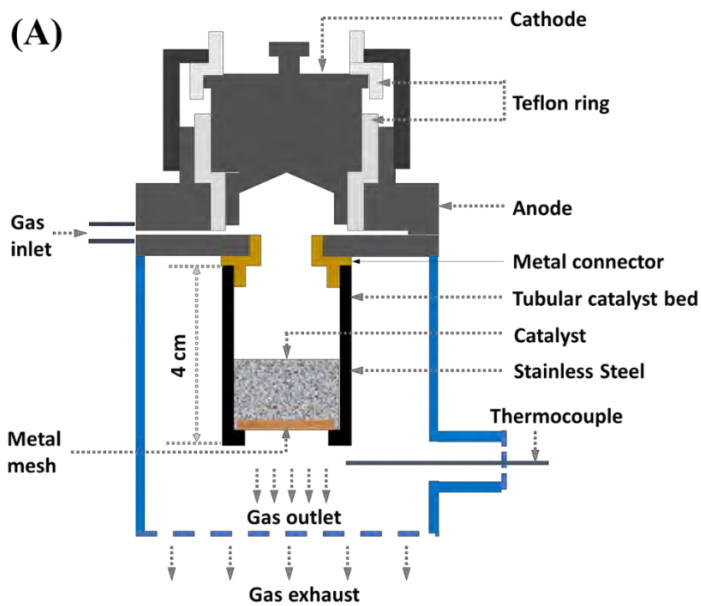

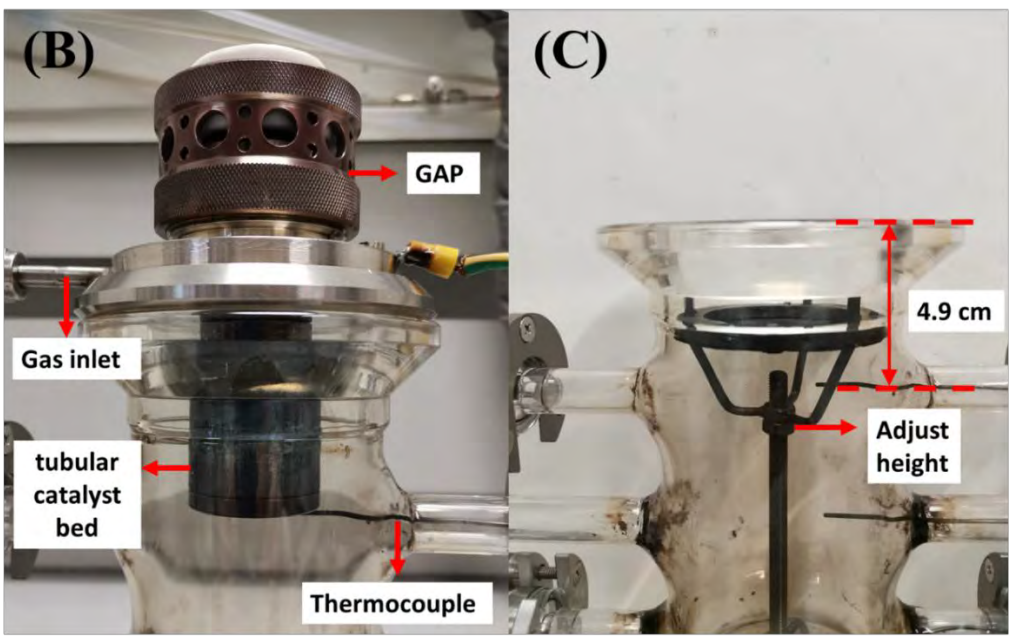

Fig. 5.1. (A) Schematic description of the newly designed tubular catalyst bed (N-bed), (B) photograph of the N-bed connected to the plasma-catalytic system, and (C) photograph of the traditional tray-type catalyst bed (T-bed) used in the plasma-catalytic system.

Experiments were performed with a GAP device, which was described in previous papers [36,54,55]. For the DRM, feed gas was supplied to the plasma with a composition of $N_2/CH_4/CO_2$ = 8/1/1 (or 8/0.6/1) at a total gas flow rate of 8 L/min (Air Liquide, N_2 purity 99.999%, CO_2 purity 99.998%, and CH_4 purity 99.995%). The flow rate of each gas was controlled by Bronkhorst mass flow controllers. The plasma in the GAP was generated by applying a high voltage to the cathode with a DC power supply (APS – Advanced Plasma Solutions). The voltage applied was measured by a high-voltage probe (Pintek HVP-15HF) and the current was obtained via a resistor of 3 Ω. The data of voltage and current were collected by a two-channel digital storage oscilloscope (Tektronix TDS 2012C). The current used for the plasma was around 0.25 A and the voltage was around 0.8 – 1.0 kV. The plasma power was calculated based on the measured voltage and current.

The post-plasma reactor tube was made of quartz with an inside diameter of 6.4 cm. There are six outlets at different positions on the reactor with a diameter of 1 cm to allow extra gas to be added through them or implement thermocouples. Herein, they were all sealed by valves during the reaction process. A thermocouple is placed after the catalyst bed through the first outlet to record the temperature of the gas that passes through the catalyst bed. The distance from the thermocouple to the top of the quartz reactor is 4.9 cm (Fig. 5.1C). To add the catalyst just after the post-plasma exhaust, we developed a newly designed tubular catalyst bed (N-

bed), as shown in Fig. 5.1A-B. Detailed pictures are shown in Fig C.1. The N-bed is directly connected to the anode of the plasma reactor by a stainless steel connector (detailed photographs, see Appendix C, Fig. C.1A-B). A tubular body with a diameter of 3.5 cm and height of 4.5 cm was utilized and at the bottom, a mesh was stacked inside where the catalyst can be placed on. In comparison, the tray-type catalyst bed (T-bed) was also utilized (Fig. 5.1C), which was made of a metal ring combined with a mesh tray and which can be adjusted in distance from the plasma exhaust. The distance between the T-bed and the plasma varied from 2 cm to 4 cm and the reaction conditions were denoted as T-bed-l, where l is the distance in centimetre.

For the plasma-catalytic DRM reaction, 1 g reduced catalyst with 4 g α-Al_2O_3 filling material was mixed uniformly and placed in/on the catalyst bed for both configurations. In comparison, plasma alone or with 5 g α-Al_2O_3 filling material only was also tested at the same reaction conditions. A total gas flow rate of 8 L/min with composition of $N_2/CO_2/CH_4$ = 8/1/1 was applied to generate the plasma. A GHSV of 480 $L \cdot g_{cat}^{-1} h^{-1}$ was obtained. Besides this, with the same gas flow rate, a higher CO_2/CH_4 ratio of 1.0/0.6 was also tested in the N-bed case. Furthermore, a blank experiment with only the N-bed was performed in this ratio. After starting the plasma, gas data was collected by a Thermo Scientific/Interscience Trace 1300

Gas Chromatograph (GC). Error bars were obtained by calculating the standard error on the calculated data from each loop of the GC data.

5.2.3 Thermal catalytic DRM

To compare with the plasma-catalytic DRM, the Ni/MO catalyst was also used in thermal catalytic DRM tests. For these experiments, the catalyst size fraction was 0.25 – 0.4 mm, considering the size of the quartz tube reactor used. 10 mg unreduced Ni/MO catalyst and 100 mg α-Al_2O_3 with the same size fraction were mixed uniformly before they were filled into a quartz tube fixed bed reactor supported on quartz wool. Before starting the DRM reaction, the uniform mixture was reduced by 20% H_2/Ar with a flow rate of 80 mL/min at 800 °C for 0.5 h. Then, the gas was changed to pure Ar with the same gas flow rate for another 0.5 h. To start the reaction, the gas was changed to a ratio of Ar/CO_2/CH_4 = 8/1/1 with a total gas flow rate of 80 mL/min to keep the same GHSV as in the plasma catalysis condition. After the reduction of the catalyst and flushing by Ar, the catalytic activity was measured at discrete temperature steps. The temperature was decreased point by point from 800 to 400 °C and pure Ar was utilized during the temperature-decreasing process. At each temperature point, the reaction was maintained for more than one hour and during this period the outlet gas was collected and analyzed by a Thermo Scientific Trace 1300 GC.

5.2.4 Gas analysis

For the plasma-catalytic DRM system, the products were analyzed by the trace GC. Nitrogen was used as an internal standard gas. The definitions and formulas to calculate the conversions, carbon-based selectivity (for CO, C_2H_2, and C_2H_4) and carbon balance, hydrogen-based selectivity (for H_2), yield, specific energy input (SEI), and energy cost are shown in the Appendix C.

5.3. Results and discussion

5.3.1 Thermal catalytic activity

The thermal catalytic performance of the Ni/MO catalyst at various temperatures is shown in Fig. 5.2. To isolate the impact of the α-Al_2O_3 filling material from the catalytic effect, an experiment was conducted using 110 mg of α-Al_2O_3 following the same procedure. As shown in Fig. 5.2, both CO_2 and CH_4 showed 0% conversion in the temperature range of 400-800 °C. This confirms that α-Al_2O_3 has no catalytic effect on DRM within this temperature range. For the catalyst, its catalytic activity enhanced as the temperature increased. Maximum conversions of CO_2 and CH_4 of 86% and 96% were obtained at 800 ℃, which decreased to 77% and 86% for CO_2 and CH_4 as the temperature decreased to 700 ℃. The selectivity of CO and H_2 (see Table C.1), however, did not change and remained around 88% for CO and 100% for H_2. Moreover, the H_2/CO ratio was 0.9 in both conditions.

Usually, if a side reaction due to the reverse water gas shift reaction (RWGS, $CO_2 + H_2 \rightarrow CO + H_2O, \Delta H^0 = 41\,kJ/mol$) would happen in the DRM process, the conversion of CO_2 would be expected to be higher than that of CH_4. However, the conversion of CH_4 was higher than that of CO_2 at all temperature points measured. This may be explained by the occurrence of other side reactions. The first potential side reaction is the direct decomposition of methane into carbon and H_2 ($CH_4 \rightarrow C + 2H_2, \Delta H^0 = 75\,kJ/mol$), which promotes the consumption of CH_4. Another side reaction can be the Boudouard reaction ($2CO \rightarrow C + CO_2, \Delta H^0 = -172\,kJ/mol$) which leads to carbon deposition and the formation of CO_2 [45,56].

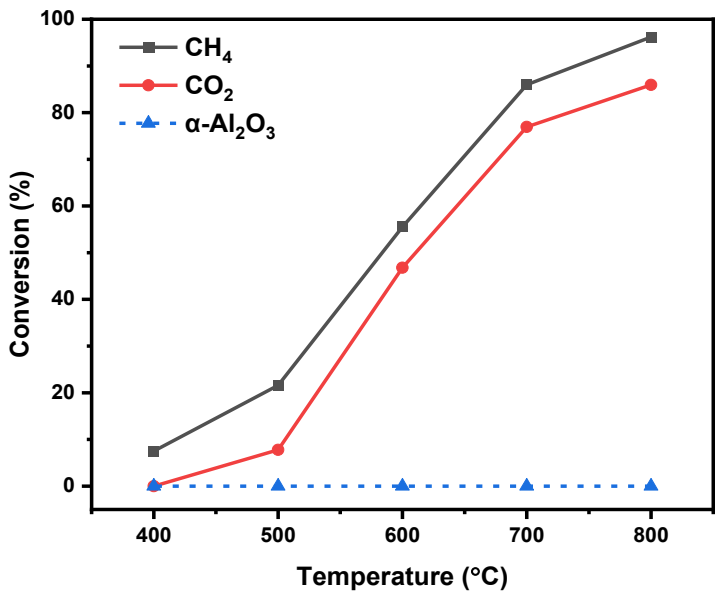

Fig. 5.2. CH_4 and CO_2 conversions by the Ni/MO catalyst and α -Al_2O_3 during the thermal catalytic DRM reaction at different temperatures. In the α-Al_2O_3 case, the 10 mg catalyst was replaced by 10 mg α-Al_2O_3. Experimental conditions: catalyst: 10 mg, gas flow rate: 80 mL/min (GHSV = 480 $L \cdot g_{cat}^{-1} h^{-1}$), gas composition: Ar/$CO_2$/$CH_4$ = 8/1/1.

5.3.2 GAP plasma-catalytic activity

The T-bed with an adjustable distance between the plasma and catalyst was applied, in addition to the N-bed configuration. To study the potential catalytic performance of the catalyst, excluding the filling effect of the post-plasma bed itself, experiments were compared with tests using only α-Al_2O_3 in the same total amount. Besides this, in the T-bed configuration, to keep the heat produced by plasma in the reactor, aluminium silicate insulation cotton was wrapped around the T-bed reactor, as shown in Fig. C.2. The performance of plasma-catalytic DRM in the T-bed configuration is shown in Fig. C.3. Moreover, considering carbon deposition on the catalyst in the early plasma stage, which may lead to the deactivation of the catalyst and a decrease in the plasma-catalytic performance, a lower CH_4/CO_2 ratio of 0.6 was also tested in both T-bed and N-bed cases and compared to a ratio of 1, to study how it affected the results. These results are shown in the Appendix C (Fig. C.4-6).

5.3.2.1 Plasma-catalytic DRM with CH_4/CO_2 ratio of 1

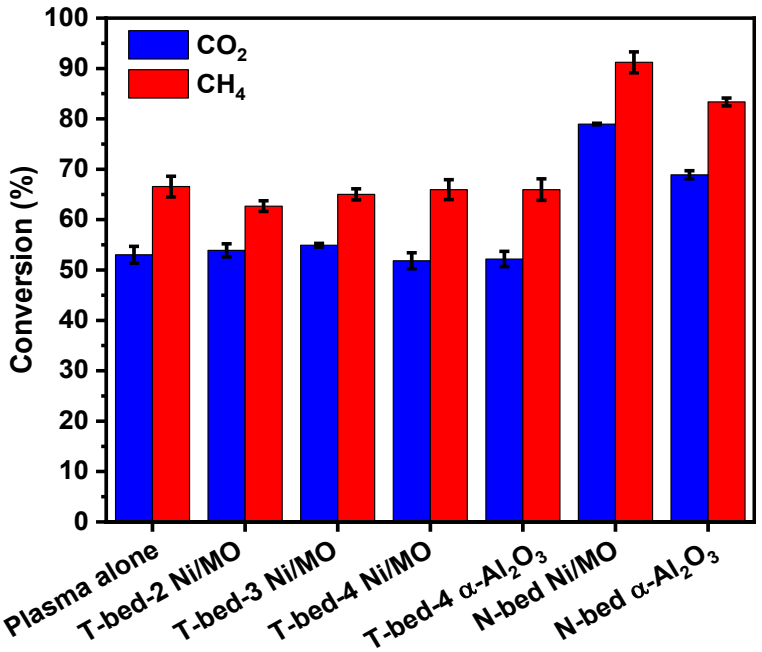

Fig. 5.3. Conversions of CH_4 and CO_2 at different GAP post-plasma catalytic configurations. Gas composition: $N_2/CH_4/CO_2$ = 8/1/1, GHSV: 480 $L \cdot g_{cat}^{-1} h^{-1}$.

The conversions of CO_2 and CH_4 for DRM in the GAP plasma-catalytic system at a CH_4/CO_2 ratio of 1 are shown in Fig. 5.3. These results illustrate that by adding the catalyst at a distance of 2 cm (T-bed-2 Ni/MO), the conversion of CO_2 remained almost unchanged around 53-54%, while the CH_4 conversion decreased from 66% to 63%. Upon increasing the distance between the catalyst bed and the plasma from 2 cm to 3 cm, both the conversion of CO_2 and CH_4 increased a bit to 55% for CO_2 and 65% for CH_4, although the increase of CO_2 was within the error range. Although the increase of the CH_4 conversion was higher than the error (from 63% to 65%), it was still slightly lower (65% vs 66%) compared to the plasma alone

configuration. When moving the distance further away from the plasma exhaust to 4 cm, however, the CO_2 and CH_4 conversion became similar to the pure plasma case. The different tendency changes for CO_2 and CH_4 in the T-bed cases could imply that a possible backflow to some degree was beneficial for CO_2 but inhibited to some extent the CH_4 dissociation, but further research is needed to confirm this. The decreasing effect of Ni-based catalysts (loaded on Al_2O_3 and SiO_2) on the conversions in plasma-catalytic DRM in a GA plasma system was also reported in literature [42] The influence disappeared when the distance of the T-bed to the plasma exhaust was increased to 4 cm, which could be due to a weakened effect of the backflow. Changing the catalyst with the filling material of α-Al_2O_3 and comparing it with Ni/MO at 4 cm distance showed no obvious changes in conversions, which implies that the catalyst had no catalytic activity at this distance.

As suggested by Fig. 5.2 and the literature [50], higher temperatures benefit the catalyst to improve the DRM results. Therefore, a comparison experiment with insulation material wrapping around the reactor to avoid heat losses was conducted in the T-bed configuration (see photographs of the reactor in Fig. C.2). After being wrapped with insulation material, the temperature after the catalyst bed increased, although it remained limited to about 450 °C. However, when looking at the conversion and selectivity, no improvement was achieved (Fig. C3), as the

temperature still remains too low compared to what is needed to thermally activate the catalyst (Fig 5.2).

Therefore, a new catalyst bed (N-bed) was designed to collect more heat from the GAP device, by directly connecting it with a metal connector to the plasma reactor segment and forming a double-walled configuration with the quartz tube around the smaller N-bed connected to the plasma, hypothesized as a means to prevent the need for external heating and insulation material to be added. Once the N-bed configuration was applied, even when only α-Al_2O_3 was used, the conversion of both CO_2 and CH_4 increased to 69% for CO_2 and 83% for CH_4. This cannot be due to catalytic activity, as it was proven that α-Al_2O_3 did not exhibit catalytic effects in previous studies. Therefore, we believe this is attributed to differences in the flow behaviour such as strong backflow, caused by the special design of the N-bed. Due to the sealed tubular body, all the gas is forced to go through the filling material before expanding in the wider quartz tube, and due to blocking effects (i.e., a slight increase in the feed gas pressure from about 0.25 bar to 0.3 bar, which was measured by a pressure gauge described in Chapter 4) by the catalyst bed, more gas is expected to form a stronger backflow, possibly resulting in a longer residence time for the reactants as well as radicals formed in the plasma region, which could explain the higher conversions. Although, as reported by Zhang et al. [48], the addition of a T-bed can cause backflow as well, the unsealed side part of the T-bed

could provide a pathway for the gas to go through, which weakens the backflow. Varying the distance of the catalyst bed post-plasma can to some degree affect the strength of the backflow. However, based on the results, the combined effect of backflow, other flow behaviour differences, and catalytic activity in the T-bed configuration is still negligible compared with the effect in the N-bed configuration with α-Al_2O_3. To exclude the effect of the presence of the N-bed itself from the packing and catalyst effect, it was added to the GAP DRM without any catalysts or filling materials inside (as shown in Fig. C.4). Compared with the plasma alone (no catalyst or α-Al_2O_3 filling material), the conversions of both CO_2 and CH_4 remained almost the same. This proved that the N-bed itself did not cause any backflow of plasma gas without the addition of packing materials (either α-Al_2O_3 or catalysts).

In the presence of the Ni/MO catalyst, the CO_2 conversion was further improved to 79% and that of CH_4 increased to 91%. As the 1g α-Al_2O_3 was replaced by 1g Ni/MO catalyst with the same particle size, the distance between the catalyst or the α-Al_2O_3 and post-plasma are the same, suggesting the same gas backflow behaviour. Therefore, this improvement can be attributed to the thermal catalytic performance of the catalyst. In contrast to the T-bed, the design of the N-bed benefits from the catalyst, due to the direct connection of the catalyst bed to the plasma device, helping the transfer of mass and heat from the plasma to the catalyst

bed, which contributes to the heating of the catalyst. Furthermore, the metal connector helps the heat transfer from the electrode to the catalyst bed as well. Moreover, just like in the N-bed α-Al_2O_3 case, all the feed gas flows through the catalyst, while in the T-bed, some gas tends to go through the path of least resistance or pressure drop, which means part of the gas would pass directly from the side part of the T-bed rather than passing through the catalyst. This decreases the contact between feed gas and catalyst and finally leads to very limited, if any, catalytic activity. An additional positive effect might result from the double-walled configuration formed by the N-bed and the post-plasma cylinder (see Fig. 5.1B), in which the catalyst bed is embedded in a larger outer quartz reactor tube containing exhaust gas of the catalyst bed. This might insulate the heat of the N-bed to some extent, as is also visible by the temperature differences at 4.9 cm for the T-bed and N-bed configuration (Fig 5.4 and Fig. C.6). Although, without the catalyst or α-Al_2O_3 filling material, this insulation (formed by the double-wall of the N-bed and inside the quartz wall) seems insufficient, as deduced from the experiment with the empty N-bed.

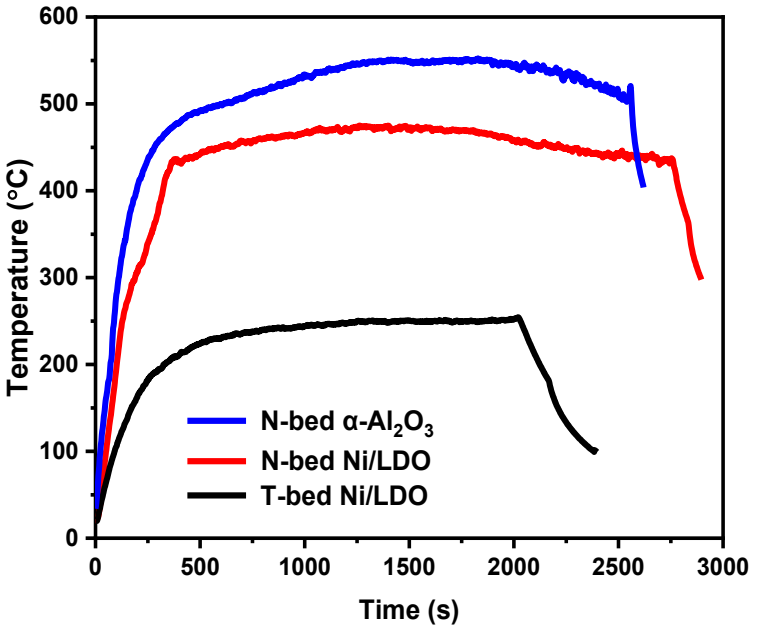

Fig. 5.4. Temperature of the gas after the catalyst bed, measured at 4.9 cm (shown in Fig. 1C). Gas composition: $N_2/CH_4/CO_2$ = 8/1/1, GHSV: 480 $L \cdot g_{cat}^{-1} h^{-1}$.

As shown in Fig. 5.1B-C, the temperature at 4.9 cm post-plasma was measured by a thermocouple, which was placed after the catalyst bed once the catalyst was added. The temperature data shown in Fig. 5.4 illustrates that a higher temperature was achieved in the N-bed configuration, i.e., around 450 °C during the reaction process for the Ni/LDO catalyst, and even around 550 °C for the α-Al_2O_3. In the T-bed-3 Ni/MO catalyst case, the temperature was only around 250 °C. It indicates the temperature in the catalyst layer in the N-bed is higher than in the T-bed and this higher temperature promotes the catalyst, explaining its higher catalytic activity. As shown in Fig. C.2, in the T-bed case with insulation, the temperature after the catalyst bed can reach about 450 °C, similar with that in the N-bed with

Ni/MO, however, the latter had improved performance for GAP DRM. This illustrates that the design of the N-bed, which can cause better mass and heat transfer and might have a different impact on flow behaviour (slight change in feed gas pressure from 0.25 bar to 0.3 bar), plays a crucial role for the enhancements. Moreover, the fact that for α-Al_2O_3 in the N-bed, the temperature was higher than for the Ni/MO catalyst proves the catalytic effect of the catalyst, as DRM is an endothermic reaction, which leads to a decrease in the temperature. This phenomenon also appeared in the configuration with a CH_4/CO_2 ratio of 0.6 (Fig. C.6).

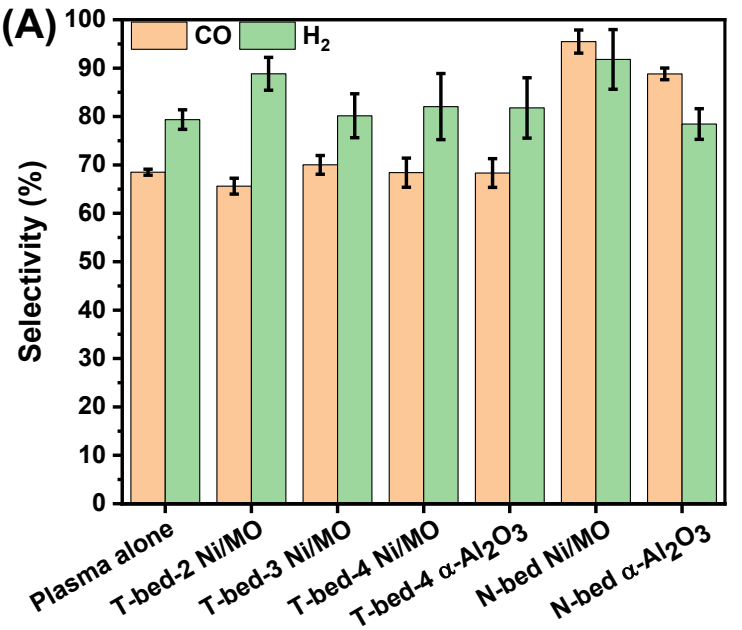

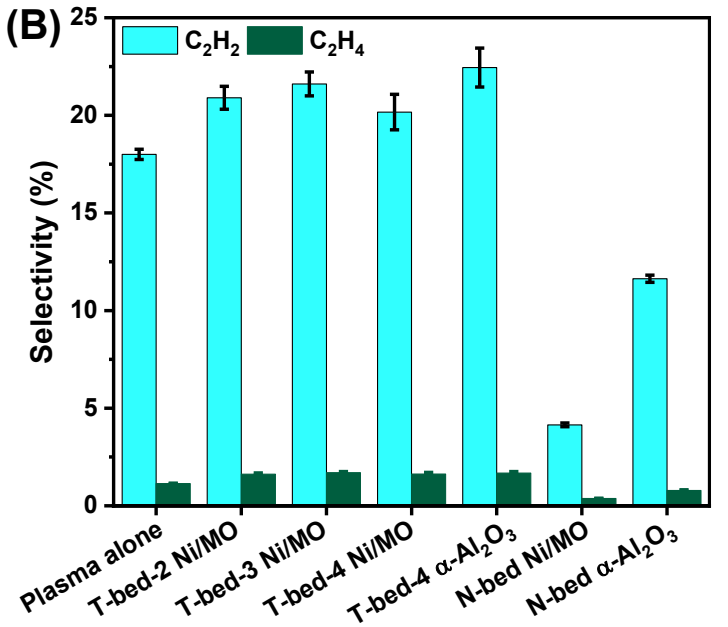
(B)
C_2H_2
C_2H_4
Selectivity (%)
0
5
10
15
20
25
Plasma alone
T-bed-2 Ni/MO
T-bed-3 Ni/MO
T-bed-4 Ni/MO
T-bed-4 α-Al_2O_3
N-bed Ni/MO
N-bed α-Al_2O_3

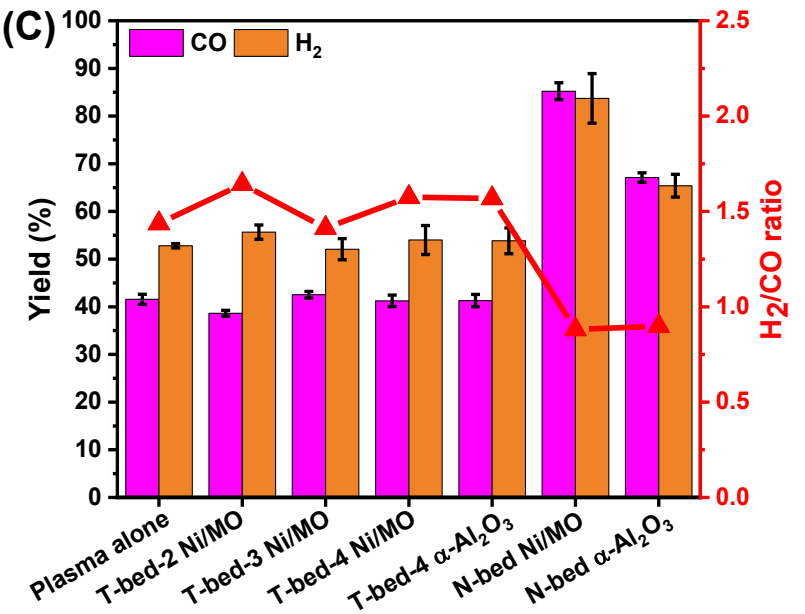
(C)
CO
H_2
Yield (%)
H_2/CO ratio
0
10
20
30
40
50
60
70
80
90
100
0.0
0.5
1.0
1.5
2.0
2.5
Plasma alone
T-bed-2 Ni/MO
T-bed-3 Ni/MO
T-bed-4 Ni/MO
T-bed-4 α-Al_2O_3
N-bed Ni/MO
N-bed α-Al_2O_3

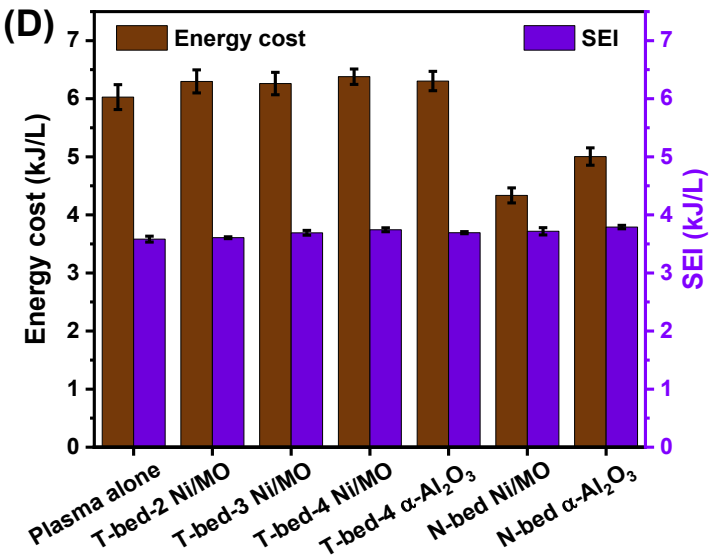

Fig. 5.5. (A) Selectivity of CO and H_2, (B) Selectivity of C_2H_2 and C_2H_4, (C) Yield of CO and H_2 and the H_2/CO ratio, and (D) Energy cost of the conversion (left y-axis) and specific energy input (SEI) into the system (right y-axis) in different cases. Gas composition: $N_2/CH_4/CO_2$ = 8/1/1, GHSV: 480 $L \cdot g_{cat}^{-1} h^{-1}$.

In contrast with the CH_4 and CO_2 conversion, which were little affected by the position of the catalyst in the T-bed, the selectivity of H_2 and by-products (C_2H_2 and C_2H_4) varied significantly, as shown in Fig. 5.5A-B. With the addition of the T-bed, at 2 cm, the selectivity of CO decreased from 69% to 66%, whereas that of H_2 increased from 79% to 89% at this position. By increasing the distance to 3 cm and 4 cm, the selectivity of CO remained almost unchanged, whereas the H_2 selectivity decreased a bit to around 80%, i.e., to almost the same value as without T-bed and catalyst. When using the N-bed without a catalyst, the selectivity to H_2 was 78%, i.e., almost the same as with the plasma-alone configuration. However, the selectivity to CO was enhanced from 69% for plasma alone to 89% for the α-Al_2O_3 filled N-bed. A further increase of the CO and H_2 selectivity was obtained

with the addition of Ni/MO catalyst, resulting in the highest selectivity value of 96% for CO and 92% for H_2, respectively. This can be due to the facilitating effect of the N-bed, which improves the mass and heat transfer to the catalyst and eventually promotes the catalyst, explaining its higher catalytic activity.

An increase in the selectivity to C_2H_2 from 18% to 20-22% was observed when the T-bed was added (cf. Fig. 5.5B). Changing the distance and filling material (catalyst or α-Al_2O_3) caused the C_2H_2 selectivity values to fluctuate around 21%, suggesting that the distance and catalyst had limited effect on the C_2H_2 selectivity in the T-bed. However, the selectivity to C_2H_2 dropped from around 20-22% for plasma alone and the T-bed configurations, to 4% for the N-bed with Ni/MO catalyst and to 12% for the N-bed with α-Al_2O_3. The same decreasing trend happened for the C_2H_4 selectivity, which declined from around 1.6% (T-bed) to 0.4% (N-bed with Ni/MO) and 0.8% (N-bed with α-Al_2O_3). These changes are in accordance with the selectivity-enhancing trend of CO and H_2. On the one hand, this can be attributed to the catalytic effect of the catalyst. On the other hand, the efficient transfer of heat from the plasma to the inside region of the catalyst bed may cause a higher temperature environment, which may not be beneficial for the production of relatively unstable products like C_2H_2 and C_2H_4. Moreover, the backflow of gas into the plasma afterglow, containing reactive species, might provide a positive effect.

The yield of CO and H_2 (Fig. 5.5C) shows that the highest yields were achieved in the N-bed case with catalyst, yielding 85% for CO and 84% for H_2, respectively, while in the T-bed, for all cases, the CO and H_2 yields were very similar as in the plasma alone case. However, the H_2/CO ratio increased to 1.6 (for T-bed with catalyst at a distance of 2 cm), as compared to 1.4 in plasma alone configuration, due to the increase of selectivity towards H_2. However, with the N-bed, the H_2/CO ratio was lower than 1 (0.88 for N-bed with Ni/MO, and 0.89 for N-bed with α-Al_2O_3). This can be attributed to two reasons. Firstly, the catalytic effect promotes the CO_2 conversion and thus produces more CO (see also the thermal DRM result in Fig. 5.2). In addition, some deposited carbon might be converted into CO as the carbon balance increased to around 100% in the N-bed configuration (Fig. C.7A).

The specific energy input (SEI) for the various configurations is plotted in Fig. 5.5D (right y-axis), and illustrates that compared with plasma alone, upon addition of the catalyst bed, no matter whether T-bed or N-bed, the SEI is almost constant around the values of 3.6 – 3.8 kJ/L, as the plasma power and flow were constant. Therefore, since the conversions barely changed in the T-bed at different positions with Ni-LDO catalyst or α-Al_2O_3, the energy cost was stable in the range of 6.3 - 6.4 kJ/L (see Fig. 5.5D: left y-axis). As the N-bed improves the plasma-catalytic conversions of CO_2 and CH_4, the energy cost values for the plasma-catalytic

process are lower, i.e., 5.0 kJ/L in the case of α-Al_2O_3 and 4.3 kJ/L for the Ni/MO catalyst. These results demonstrate that the N-bed can efficiently improve the GAP post-plasma catalytic DRM reaction.

Considering the catalyst can be deactivated due to carbon deposition, which may also happen in this plasma-catalytic DRM system, the hypothesis was verified whether the catalyst can already be deactivated due to carbon deposition at the early plasma start-up before the temperature was reached at which the catalyst was active. For this reason, experiments with a lower CH_4/CO_2 ratio of 0.6 (gas composition: N_2:CH_4:CO_2 = 8:0.6:1) were performed to compare the performance of the catalyst in the different catalyst beds (results see Fig. C.4-6). The results indicate that this is not the reason why the T-bed is not working properly (see conversion, selectivity, yield, SEI and energy cost data in Fig. C.4-5). The temperature after the T-bed and N-bed was collected as well (Fig. C.6), showing that the gas temperature after the N-bed was also higher than after the T-bed. Hence, the combined effects of the higher temperature, strong backflow or change in flow behaviour and double-walled insulation formed by the specially designed structure must be an important reason why the N-bed works well and the T-bed was inactive.

5.3.2.2 Carbon deposition and analysis

Nevertheless, carbon deposition is one of the main drawbacks of catalyst deactivation in DRM. Therefore, it is meaningful to study the carbon deposition in

the plasma-catalytic DRM. The carbon balance of the plasma alone and coupled with catalysts for the different types of catalyst bed configurations for DRM are shown in Table C.2. It can be noticed that reducing the CH_4/CO_2 ratio from 1 to 0.6 can decrease the loss of carbon, which, in the plasma alone case, increases from 93% to 99%. This difference became negligible in the N-bed cases, as the carbon balance was 100% in both cases. Moreover, in the plasma alone or with T-bed configurations at a CH_4/CO_2 ratio of 1, some carbon can be collected by a paper on the inside wall of the post-plasma tube, which became negligible in the N-bed configurations.

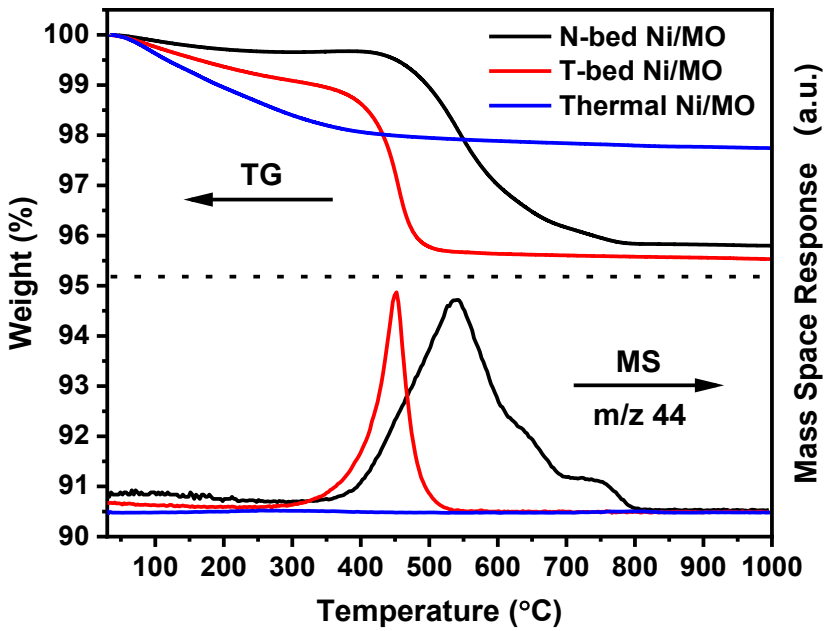

Fig. 5.6. TG, DTG and the MS results of Ni/MO catalyst obtained after DRM reaction in different reactor configurations (In T-bed plasma configuration, the reaction time is around 35 min, in N-bed configuration, the reaction time is around 45 min, and in the thermal catalytic reaction, the reaction time is the entire temperature range procedure). Gas composition: $N_2/CH_4/CO_2 = 8/1/1$, GHSV: 480 $L \cdot g_{cat}^{-1} h^{-1}$.

TG in O_2 gas coupled with MS was used to analyze the amount of carbon deposition on the catalyst after about 35-45 min of DRM reaction in the different reactor configurations at a CH_4/CO_2 ratio of 1 (see Fig. 5.6). Combined with the DTG result in Fig. C.8A, it can be seen that there was only about 2% total weight loss for thermal utilized Ni/MO catalyst at a temperature below about 400 °C. Enlarging the result of the MS at m/z = 44 (Fig. C.8B) indicates two peaks of CO_2 in the temperature range of 100-500 °C and 700-850 °C. The MS results at m/z = 28 and 18 (Fig. C.8C) suggest the presence of H_2O and the absence of CO as part of the weight loss. Much more weight loss was observed in both T-bed and N-bed post-plasma configurations. In the T-bed configuration, carbon was lost in a temperature range of around 300 °C up to about 550 °C, coinciding with about 3.6% weight loss. The MS data at m/z of 28 and 18 show that a small amount of CO was formed, visible from the sharp peak at around 400-500 °C, while no H_2O signal was observed in this temperature range. Similar phenomena were found in the N-bed case although with some difference. The weight loss occurred in a larger temperature range of around 350-800 °C with 3.8% weight loss and the CO peak was wider from about 420 °C to 650 °C. The TG results suggest that the carbon deposited on the catalyst mixture in the N-bed configuration had stronger interaction than those in the thermal catalytic or T-bed configurations or that the type of carbon formed was different. Furthermore, although in the thermal catalytic DRM, the least carbon deposition was found, the carbon balance was only 89%,

which is lower than the values in the T-bed and N-bed configurations (i.e., 96% and 100%, respectively). Several reasons may lead to this. A possible reason is that for the TG process, around 100 mg mixture of Ni/MO catalyst and α-Al_2O_3 sample was utilized, while this implies only 1/11 weight of catalyst in the thermal catalytic case (as 10 mg catalyst was mixed with 100 mg α-Al_2O_3) and in the T-bed and N-bed configurations this value is 1/5 (as 1 g catalyst is mixed with 4 g α-Al_2O_3). Assuming all the carbon would be deposited on the catalyst, after correction, the carbon deposition should be around 4.4%, a bit higher than in the T-bed and N-bed configurations, which might indicate that in the entire temperature range of 800 °C down to 400 °C other volatile side products have been formed that were not calibrated for in the GC and hence do not appear in the carbon balance nor in the TGA if they do not adsorb on the catalyst in significant amounts. Besides this, considering that the carbon deposition in the N-bed configuration was 100%, this conflicted with the carbon loss in TG-MS. This could be caused by the carbon deposition before the plasma reaches its maximum conversion and thus temperature. Furthermore, as the internal standard gas N_2 was present in the feed gas, it may have led to some larger errors in the results. Hence, the underlying reasons are not yet fully clear and require more research, which is outside the scope of this chapter, focusing on the benefits of the N-bed versus the T-bed.

The carbon collected in the plasma cases was further studied via Raman spectra (Fig. C.9). The spectra of the samples all exhibited typical carbon signals at around 1346 cm^{-1} (D band) and 1574 cm^{-1} (G band), whereas the G band peak shifted to a higher wavenumber (1586 cm^{-1}) for the N-bed and an even higher wavenumber (1601 cm^{-1}) for the T-bed. Furthermore, the spectrum for plasma alone showed a 2D band (2678 cm^{-1}), attributed to the overtone of the D band.

The ratio of the relative intensity of the D band to the G band (I_D/I_G) in the Raman spectrum (Fig C.9) is commonly used to quantify the defects and crystallinity of graphene samples. The low value of I_D/I_G indicates a high degree of graphitization of the samples [40,57,58]. For the three cases, the I_D/I_G values were approximately 0.79 for plasma alone, 0.97 for the T-bed, and 1.12 for the N-bed, showing a decreasing trend of graphitization of the carbon formed.

5.3.3 Comparison of our DRM results with various other plasma configurations

Table 5.1. Operating conditions, CH_4/CO_2 conversion, CO/H_2 selectivity and energy cost in various plasma reactors for DRM.

Plasma	Catalyst	CH_4/CO_2	Power (W)	Total flow rate (L/min)	Conversion		Selectivity		Energy cost[a] (kJ/L)	Ref.
					CH_4	CO_2	CO	H_2		
GA	-	3:7	165	7.5	13.1	8.4	31.4	69.5	14.4	[40]
RGA	Ni/γ-Al_2O_3 [b]	3:7	490	6	58.5	39.5	56	35.3	13	[34]
GA + catalyst [d]	Ni-based catalyst [b]	1:1	494	2.67	94	91	95	97	26.7 [e]	[50]
RGA	15 wt% NiO-Al_2O_3 [b]	2:3	136	3.7	11.8	11.2	88.1	75.3	40.2	[42]

RGA	-	1:1	1800	24	50.5	40.3	81.2	83.5	18.5	[43]
Glow discharge	-	1:3	n/a	1	94	64	n/a	n/a	17	[13]
DBD	Ni-based metal oxide [c]	1:1	33-38	0.03	69	54	74.5	62.5	n/a	[59]
Spark plasma	Ferroelectric ($BaZr_{0.05}Ti_{0.95}O_3$) [c]	1:1	39	0.2	86	82.4	67.4	88.7	9.8	[60]
MW	-	1:2	700	2.1	79.4	44.8	58.4	50.1	n/a	[24]
GAP	Ni-based metal oxide [b]	1:1	508	8	91	79	95	92	4.3	This work

[a] Some energy cost data were reported in different units, therefore, they were calculated into the same unit, except Ref. [14] and [44] which were the data as reported.
[b] Post-plasma catalysis (PPC) model; [c] In-plasma catalysis (IPC) model;
[d] additional heating at 850 °C
[e] The energy cost calculated based on CO_2 and including both plasma energy cost and additional heating energy cost.
GA: gliding arc; RGA: rotating gliding arc; DBD: dielectric barrier discharge; MW: microwave; GAP: gliding arc plasmatron.
n/a: Data not reported or could not be determined from the data mentioned in the paper.

The reactant conversion, product selectivity, and energy cost are important parameters to evaluate the performance of plasma-catalytic DRM. Therefore, we list these performance data in Table 5.1, along with the experimental conditions, i.e., catalyst (if used), CH_4/CO_2 ratio, gas flow rate, and plasma power, for various plasma reactors reported in the literature. Our obtained conversion of CH_4 and CO_2 are higher than most of the reported values for GA, RGA, DBD, spark plasma and MW plasma, while at a significantly lower energy cost and using a higher gas flow rate. Although in the GA plasma with extra external heating to 850 °C, the conversion of CH_4 and CO_2 and the selectivity to CO and H_2 were higher [50], the energy cost was also about 6 times higher. Considering the catalytic performance, our GAP post-plasma-catalytic DRM reaction with N-bed and Ni/MO catalyst is competitive to the current state of the art.

5.4 Conclusion

We present a GAP plasma reactor in combination with a newly designed catalyst bed (N-bed), containing a Ni/MO catalyst derived from LDH, for post-plasma-catalytic dry reforming of methane. The catalytic activity of the catalyst was evaluated and compared with a traditional fixed bed for thermal catalytic DRM and a maximum of 96% CH_4 and 86% CO_2 conversion were achieved at 800 °C. For the post-plasma-catalytic DRM reaction, two types of catalyst bed configurations (tray-type T-bed and newly designed N-bed) were applied to study how the catalyst bed design affects the results. We found that using a traditional tray-type catalyst bed (T-bed) had little effect on the conversion of CO_2 and CH_4, while the use of the newly designed catalyst bed (N-bed) can efficiently enhance both CO_2 and CH_4 conversion, and CO and H_2 selectivity, and decrease the energy cost at the same time, without external insulation or heating, providing a true, fully electrically driven process, transferring the heat produced in the plasma to the post-plasma catalysis. When using a CH_4/CO_2 ratio of 1, the highest conversions of CO_2 of 79% and CH_4 of 91%, in combination with a vast increase in selectivity to CO (96%) and H_2 (91%), were obtained in the N-bed with Ni/MO catalyst present, which are comparable to those achieved in the thermal catalytic DRM at 800 °C. This improvement was proven to be caused by the catalytic activity of the catalyst, which was facilitated by the direct connection of the N-bed to the GAP plasma device, transferring more heat from the GAP device, activating the catalyst, while

also providing beneficial mass transfer and flow behaviour. The latter was deduced from the improved performance in the presence of α-Al_2O_3 filling in the absence of catalytic material, in combination with the lack of enhanced performance in case of an empty N-bed connected to the plasma. To our knowledge, this is the first time that excellent catalytic activity in a PPC system was observed without requiring extra external heating or insulation, which indeed illustrates the high potential of PPC systems towards process electrification and plasma energy, i.e. heat recovery.

5.5 References

[1] Le Saché, E.; Reina, T. R. Analysis of Dry Reforming as Direct Route for Gas Phase CO_2 Conversion. The Past, the Present and Future of Catalytic DRM Technologies. Progress in Energy and Combustion Science. 2022. https://doi.org/10.1016/j.pecs.2021.100970.

[2] Mustafa, A.; Lougou, B. G.; Shuai, Y.; Wang, Z.; Tan, H. Current Technology Development for CO_2 Utilization into Solar Fuels and Chemicals: A Review. J. Energy Chem. 2020, 49, 96–123. https://doi.org/10.1016/j.jechem.2020.01.023.

[3] Yentekakis, I. V.; Panagiotopoulou, P.; Artemakis, G. A Review of Recent Efforts to Promote Dry Reforming of Methane (DRM) to Syngas Production via Bimetallic Catalyst Formulations. Appl. Catal. B Environ. 2021, 296, 120210. https://doi.org/10.1016/j.apcatb.2021.120210.

[4] Anoop, N. .; Sundaramurthy, S.; Jha, J. M.; Chandrabalan, S.; Singh, N.; Verma, J.; Parvatalu, D.; Katti, S. Plasma Catalysis: A Feasible Solution for Carbon Dioxide Valorization? Clean Technol. Environ. Policy 2021, 23 (10), 2789–2811. https://doi.org/10.1007/s10098-021-02203-y.

[5] Chen, G.; Snyders, R.; Britun, N. CO_2 Conversion Using Catalyst-Free and Catalyst-Assisted Plasma-Processes: Recent Progress and Understanding. J. CO_2 Util. 2021, 49 (May), 101557. https://doi.org/10.1016/j.jcou.2021.101557.

[6] Vermeiren, V.; Bogaerts, A. Plasma-Based CO2 Conversion: To Quench or Not to Quench?.Pdf. J. Phys. Chem. C 2020, 124 (34), 18401–18415.

[7] George, A.; Shen, B.; Craven, M.; Wang, Y.; Kang, D.; Wu, C.; Tu, X. A Review of Non-Thermal Plasma Technology: A Novel Solution for CO_2

Conversion and Utilization. Renew. Sustain. Energy Rev. 2021, 135, 109702. https://doi.org/10.1016/j.rser.2020.109702.

[8] Van Alphen, S.; Slaets, J.; Ceulemans, S.; Aghaei, M.; Snyders, R.; Bogaerts, A. Effect of N_2 on CO_2-CH_4 Conversion in a Gliding Arc Plasmatron: Can This Major Component in Industrial Emissions Improve the Energy Efficiency? J. CO_2 Util. 2021, 54, 101767. https://doi.org/10.1016/j.jcou.2021.101767.

[9] Mei, D.; Duan, G.; Fu, J.; Liu, S.; Zhou, R.; Zhou, R.; Fang, Z.; Cullen, P. J.; Ostrikov, K. (Ken). CO_2 Reforming of CH_4 in Single and Double Dielectric Barrier Discharge Reactors: Comparison of Discharge Characteristics and Product Distribution. Journal of CO_2 Utilization. 2021. https://doi.org/10.1016/j.jcou.2021.101703.

[10] Wang, Y.; Chen, Y.; Harding, J.; He, H.; Bogaerts, A.; Tu, X. Catalyst-Free Single-Step Plasma Reforming of CH_4 and CO_2 to Higher Value Oxygenates under Ambient Conditions. Chem. Eng. J. 2022, 450 (P1), 137860. https://doi.org/10.1016/j.cej.2022.137860.

[11] Pan, J.; Chen, T.; Gao, Y.; Liu, Y.; Zhang, S.; Liu, Y.; Shao, T. Numerical Modeling and Mechanism Investigation of Nanosecond-Pulsed DBD Plasma-Catalytic CH_4 dry Reforming. J. Phys. D. Appl. Phys. 2022, 55 (3). https://doi.org/10.1088/1361-6463/ac2ad8.

[12] Pornmai, K.; Suvachitanont, S.; Chavadej, S. Reforming of CO_2-Containing Natural Gas with Steam in AC Gliding Arc Discharge for Hydrogen Production. Int. J. Green Energy 2018, 15 (7), 441–453. https://doi.org/10.1080/15435075.2018.1475285.

[13] Wanten, B.; Maerivoet, S.; Vantomme, C.; Slaets, J.; Trenchev, G.; Bogaerts, A. Dry Reforming of Methane in an Atmospheric Pressure Glow Discharge: Confining the Plasma to Expand the Performance. Journal of CO_2 Utilization. 2022. https://doi.org/10.1016/j.jcou.2021.101869.

[14] Sheng, Z.; Watanabe, Y.; Kim, H. H.; Yao, S.; Nozaki, T. Plasma-Enabled Mode-Selective Activation of CH_4 for Dry Reforming: First Touch on the Kinetic Analysis. Chem. Eng. J. 2020, 399 (May), 125751. https://doi.org/10.1016/j.cej.2020.125751.

[15] Mei, D.; Zhang, P.; Duan, G.; Liu, S.; Zhou, Y.; Fang, Z.; Tu, X. CH_4 Reforming with CO_2 Using a Nanosecond Pulsed Dielectric Barrier Discharge Plasma. J. CO_2 Util. 2022, 62 (March), 102073. https://doi.org/10.1016/j.jcou.2022.102073.

[16] Wang, J.; Bogaerts, A.; Meynen, V. 3d Porous Catalysts for Plasma-Catalytic Dry Reforming of Methane: How Does the Pore Size Affect the Plasma-Catalytic Performance? SSRN Electronic Journal. 2022. https://doi.org/10.2139/ssrn.4218796.

[17] Chen, X.; Kim, H. H.; Nozaki, T. Plasma Catalytic Technology for CH4 and CO_2 Conversion: A Review Highlighting Fluidized-Bed Plasma Reactor. Plasma Process. Polym. 2023. https://doi.org/10.1002/ppap.202200207.

[18] Bouchoul, N.; Fourré, E.; Duarte, A.; Tanchoux, N.; Louste, C.; Batiot-Dupeyrat, C. Plasma-Metal Oxides Coupling for CH_4-CO_2 Transformation into Syngas and/or Hydrocarbons, Oxygenates. Catal. Today 2021, 369 (May), 62–68. https://doi.org/10.1016/j.cattod.2020.06.058.

[19] Wang, J.; Zhang, K.; Meynen, V.; Bogaerts, A. Dry Reforming in a Dielectric Barrier Discharge Reactor with Non-Uniform Discharge Gap: Effects of Metal Rings on the Discharge Behavior and Performance. Chem. Eng. J. 2023, 465, 142953. https://doi.org/10.1016/j.cej.2023.142953.

[20] Devid, E.; Zhang, D.; Wang, D.; Ronda-Lloret, M.; Huang, Q.; Rothenberg, G.; Shiju, N. R.; Kleyn, A. W. Dry Reforming of Methane under Mild Conditions Using Radio Frequency Plasma. Energy Technol. 2020, 8 (5), 1–10. https://doi.org/10.1002/ente.201900886.

[21] Liu, Z.; Huang, B.; Zhu, W.; Zhang, C.; Tu, X.; Shao, T. Phase-Resolved Measurement of Atmospheric-Pressure Radio-Frequency Pulsed Discharges in Ar/CH_4/CO_2 Mixture. Plasma Chem. Plasma Process. 2020, 40 (4), 937–953. https://doi.org/10.1007/s11090-020-10071-5.

[22] Xu, J.; Liu, Y.; Tian, H.; Zhang, Q.; Cao, W.; Chen, K.; Guo, F. Ni-Based Catalysts with Coke Resistance Enhance by Radio Frequency Discharge Plasma for CH_4/CO_2 Reforming. Int. J. Hydrogen Energy 2022, 47 (8), 5240–5249. https://doi.org/10.1016/j.ijhydene.2021.11.131.

[23] Li, D.; Li, X.; Bai, M.; Tao, X.; Shang, S.; Dai, X.; Yin, Y. CO_2 Reforming of CH_4 by Atmospheric Pressure Glow Discharge Plasma: A High Conversion Ability. Int. J. Hydrogen Energy 2009, 34 (1), 308–313. https://doi.org/10.1016/j.ijhydene.2008.10.053.

[24] Alawi, N. M.; Sunarso, J.; Pham, G. H.; Barifcani, A.; Nguyen, M. H.; Liu, S. Comparative Study on the Performance of Microwave-Assisted Plasma DRM in Nitrogen and Argon Atmospheres at a Low Microwave Power. J. Ind. Eng. Chem. 2020, 85, 118–129. https://doi.org/10.1016/j.jiec.2020.01.032.

[25] Sun, H.; Lee, J.; Bak, M. S. Experiments and Modeling of Atmospheric Pressure Microwave Plasma Reforming of a Methane-Carbon Dioxide Mixture. J. CO_2 Util. 2021, 46 (January), 101464. https://doi.org/10.1016/j.jcou.2021.101464.

[26] Zhang, F.; Zhang, X.; Song, Z.; Li, X.; Zhao, X.; Sun, J.; Mao, Y.; Wang, X.; Wang, W. Promotion of Microwave Discharge over Carbon Catalysts for CO_2 Reforming of CH_4 to Syngas. Fuel 2023, 331 (P2), 125914. https://doi.org/10.1016/j.fuel.2022.125914.

[27] Bogaerts, A.; De Bie, C.; Snoeckx, R.; Kozák, T. Plasma Based CO_2 and CH_4 Conversion: A Modeling Perspective. Plasma Process. Polym. 2017, 14 (6). https://doi.org/10.1002/ppap.201600070.

[28] Aziznia, A.; Bozorgzadeh, H. R.; Seyed-Matin, N.; Baghalha, M.; Mohamadalizadeh, A. Comparison of Dry Reforming of Methane in Low Temperature Hybrid Plasma-Catalytic Corona with Thermal Catalytic Reactor over Ni/γ-Al_2O_3. J. Nat. Gas Chem. 2012, 21 (4), 466–475. https://doi.org/10.1016/S1003-9953(11)60392-7.

[29] Nguyen, H. H.; Nasonova, A.; Nah, I. W.; Kim, K. S. Analysis on CO_2 Reforming of CH_4 by Corona Discharge Process for Various Process Variables. J. Ind. Eng. Chem. 2015, 32, 58–62. https://doi.org/10.1016/j.jiec.2015.07.018.

[30] Slaets, J.; Aghaei, M.; Ceulemans, S.; Van Alphen, S.; Bogaerts, A. CO_2 and CH_4 Conversion in "Real" Gas Mixtures in a Gliding Arc Plasmatron: How Do N_2 and O_2 Affect the Performance? Green Chem. 2020, 22 (4), 1366–1377. https://doi.org/10.1039/c9gc03743h.

[31] Cleiren, E.; Heijkers, S.; Ramakers, M.; Bogaerts, A. Dry Reforming of Methane in a Gliding Arc Plasmatron: Towards a Better Understanding of the Plasma Chemistry. ChemSusChem 2017, 10, 4025–4036. https://doi.org/doi.org/10.1002/cssc.201701274.

[32] Lu, N.; Sun, D.; Xia, Y.; Shang, K.; Wang, B.; Jiang, N.; Li, J.; Wu, Y. Dry Reforming of CH_4–CO_2 in AC Rotating Gliding Arc Discharge: Effect of Electrode Structure and Gas Parameters. Int. J. Hydrogen Energy 2018, 43 (29), 13098–13109. https://doi.org/10.1016/j.ijhydene.2018.05.053.

[33] Xu, R.; Kong, X.; Zhang, H.; Ruya, P. M.; Li, X. Destruction of Gasification Tar over Ni Catalysts in a Modified Rotating Gliding Arc Plasma Reactor: Effect of Catalyst Position and Nickel Loading. Fuel 2021, 289 (July 2020), 119742. https://doi.org/10.1016/j.fuel.2020.119742.

[34] Zhu, F.; Zhang, H.; Yan, X.; Yan, J.; Ni, M.; Li, X.; Tu, X. Plasma-Catalytic Reforming of CO_2-Rich Biogas over Ni/γ-Al_2O_3 Catalysts in a Rotating Gliding Arc Reactor. Fuel 2017, 199, 430–437. https://doi.org/10.1016/j.fuel.2017.02.082.

[35] Liu, J. L.; Xue, Z. W.; Zhang, Z. Y.; Sun, B.; Zhu, A. M. Mechanism Study on Gliding Arc (GA) Plasma Reforming: Unraveling the Decisive Role of CH_4/CO_2 Ratio in the Dry Reforming Reaction. Plasma Process. Polym. 2022, e2200175. https://doi.org/10.1002/ppap.202200175.

[36] Ramakers, M.; Trenchev, G.; Heijkers, S.; Wang, W.; Bogaerts, A. Gliding Arc Plasmatron: Providing an Alternative Method for Carbon Dioxide Conversion. ChemSusChem 2017, 10, 2642–2652. https://doi.org/doi.org/10.1002/cssc.201700589.

[37] Snoeckx, R.; Bogaerts, A. Plasma Technology-a Novel Solution for CO_2 Conversion? Chem. Soc. Rev. 2017, 46 (19), 5805–5863. https://doi.org/10.1039/c6cs00066e.

[38] Feng, J.; Sun, X.; Li, Z.; Hao, X.; Fan, M.; Ning, P.; Li, K. Plasma-Assisted Reforming of Methane. Adv. Sci. 2022, 9 (34), 1–36. https://doi.org/10.1002/advs.202203221.

[39] Allah, Z. A.; Whitehead, J. C. Plasma-Catalytic Dry Reforming of Methane in an Atmospheric Pressure AC Gliding Arc Discharge. Catal. Today 2015, 256 (P1), 76–79. https://doi.org/10.1016/j.cattod.2015.03.040.

[40] Tu, X.; Whitehead, J. C. Plasma Dry Reforming of Methane in an Atmospheric Pressure AC Gliding Arc Discharge: Co-Generation of Syngas and Carbon Nanomaterials. International Journal of Hydrogen Energy. 2014, pp 9658–9669. https://doi.org/10.1016/j.ijhydene.2014.04.073.

[41] Bo, Z.; Yan, J.; Li, X.; Chi, Y.; Cen, K. Plasma Assisted Dry Methane Reforming Using Gliding Arc Gas Discharge: Effect of Feed Gases Proportion. Int. J. Hydrogen Energy 2008, 33 (20), 5545–5553. https://doi.org/10.1016/j.ijhydene.2008.05.101.

[42] Martin-Del-Campo, J.; Uceda, M.; Coulombe, S.; Kopyscinski, J. Plasma-Catalytic Dry Reforming of Methane over Ni-Supported Catalysts in a Rotating Gliding Arc - Spouted Bed Reactor. J. CO_2 Util. 2021, 46 (January), 101474. https://doi.org/10.1016/j.jcou.2021.101474.

[43] Kwon, H.; Kim, T.; Song, S. Dry Reforming of Methane in a Rotating Gliding Arc Plasma: Improving Efficiency and Syngas Cost by Quenching Product Gas. SSRN Electron. J. 2022, 70 (February), 102448. https://doi.org/10.2139/ssrn.4302968.

[44] Nunnally, T.; Gutsol, K.; Rabinovich, A.; Fridman, A.; Kemoun, A. Dissociation of CO_2 in a Low Current Gliding Arc Plasmatron. J. Phys. D. Appl. Phys. 2011, 44, 274009. https://doi.org/10.1088/0022-3727/44/27/274009.

[45] Lin, X.; Li, R.; Lu, M.; Chen, C.; Li, D.; Zhan, Y.; Jiang, L. Carbon Dioxide Reforming of Methane over Ni Catalysts Prepared from Ni-Mg-Al Layered Double Hydroxides: Influence of Ni Loadings. Fuel 2015, 162, 271–280. https://doi.org/10.1016/j.fuel.2015.09.021.

[46] Jin, L.; Ma, B.; Zhao, S.; He, X.; Li, Y.; Hu, H.; Lei, Z. Ni/MgO–Al_2O_3 Catalyst Derived from Modified [Ni,Mg,Al]-LDH with NaOH for CO_2 Reforming of Methane. Int. J. Hydrogen Energy 2018, 43 (5), 2689–2698. https://doi.org/10.1016/j.ijhydene.2017.12.087.

[47] Abbas, M.; Sikander, U.; Mehran, M. T.; Kim, S. H. Exceptional Stability of Hydrotalcite Derived Spinel Mg(Ni)Al_2O_4 Catalyst for Dry Reforming of Methane. Catal. Today 2022, 403, 74–85. https://doi.org/10.1016/j.cattod.2021.08.029.

[48] Zhang, H.; Li, L.; Xu, R.; Huang, J.; Wang, N.; Li, X.; Tu, X. Plasma-Enhanced Catalytic Activation of CO_2 in a Modified Gliding Arc Reactor. Waste Disposal and Sustainable Energy. 2020, pp 139–150. https://doi.org/10.1007/s42768-020-00034-z.

[49] Li, K.; Liu, J. L.; Li, X. S.; Zhu, X.; Zhu, A. M. Warm Plasma Catalytic Reforming of Biogas in a Heat-Insulated Reactor: Dramatic Energy Efficiency and Catalyst Auto-Reduction. Chem. Eng. J. 2016, 288, 671–679. https://doi.org/10.1016/j.cej.2015.12.036.

[50] Liu, J. L.; Li, Z.; Liu, J. H.; Li, K.; Lian, H. Y.; Li, X. S.; Zhu, X.; Zhu, A. M. Warm-Plasma Catalytic Reduction of CO_2 with CH_4. Catal. Today 2019, 330 (December 2017), 54–60. https://doi.org/10.1016/j.cattod.2018.05.046.

[51] Lian, H. Y.; Wei, Z.; Yun, S.; Jing, R.; Liu, L. Warm Plasma Catalytic Coreforming of Dilute Bioethanol and Methane for Hydrogen Production. Plasma Process. Polym. 2023, 1–9. https://doi.org/10.1002/ppap.202300062.

[52] Klemm, E.; Lobo, C. M. S.; Löwe, A.; Schallhart, V.; Renninger, S.; Waltersmann, L.; Dietrich, A. S. R.; Costa, R.; Möltner, L.; Meynen, V.; Sauer, A.; Friedrich, K. A. CHEMampere : Technologies for Sustainable Chemical Production with Renewable Electricity and CO_2, N_2, O_2, and H_2O. Can. J. Chem. Eng. 2022, 100 (10), 2736–2761. https://doi.org/doi.org/10.1002/cjce.24397.

[53] Xu, W.; Mertens, M.; Kenis, T.; Derveaux, E.; Adriaensens, P.; Meynen, V. Can High Temperature Calcined Mg–Al Layered Double Hydroxides (LDHs) Fully Rehydrate at Room Temperature in Vapor or Liquid Condition? Materials Chemistry and Physics. 2023. https://doi.org/10.1016/j.matchemphys.2022.127113.

[54] Trenchev, G.; Kolev, S.; Wang, W.; Ramakers, M.; Bogaerts, A. CO2 Conversion in a Gliding Arc Plasmatron: Multidimensional Modeling for Improved Efficiency. J. Phys. Chem. C 2017, 121 (39), 24470–24479. https://doi.org/10.1021/acs.jpcc.7b08511.

[55] Ramakers, M.; Heijkers, S.; Tytgat, T.; Lenaerts, S.; Bogaerts, A. Combining CO_2 Conversion and N_2 Fixation in a Gliding Arc Plasmatron. J. CO_2 Util. 2019, 33 (March 2019), 121–130. https://doi.org/10.1016/j.jcou.2019.05.015.

[56] Theofanidis, S. A.; Galvita, V. V.; Poelman, H.; Marin, G. B. Enhanced Carbon-Resistant Dry Reforming Fe-Ni Catalyst: Role of Fe. ACS Catal. 2015, 5 (5), 3028–3039. https://doi.org/10.1021/acscatal.5b00357.

[57] Sun, D. L.; Hong, R. Y.; Liu, J. Y.; Wang, F.; Wang, Y. F. Preparation of Carbon Nanomaterials Using Two-Group Arc Discharge Plasma. Chem. Eng. J. 2016, 303, 217–230. https://doi.org/10.1016/j.cej.2016.05.098.

[58] Heise, H. M.; Kuckuk, R.; Srivastava, A.; Asthana, B. P. Characterization of Carbon Nanotube Filters and Other Carbonaceous Materials by Raman

Spectroscopy-II: Study on Dispersion and Disorder Parameters. J. Raman Spectrosc. 2011, 42 (3), 294–302. https://doi.org/10.1002/jrs.2723.

[59] Wang, H.; Yang, Y.; Li, Z.; Kong, X.; Martin, P.; Cui, G.; Wang, R. Plasma-Assisted Ni Catalysts: Toward Highly-Efficient Dry Reforming of Methane at Low Temperature. Int. J. Hydrogen Energy 2023, 48, 8921–8931. https://doi.org/10.1016/j.ijhydene.2022.11.287.

[60] Chung, W. C.; Chang, M. B. Dry Reforming of Methane by Combined Spark Discharge with a Ferroelectric. Energy Convers. Manag. 2016, 124, 305–314. https://doi.org/10.1016/j.enconman.2016.07.023.

General Summary

LDH-derived catalysts are effective for the DRM reaction at high temperatures, and plasma can make DRM happen at atmospheric pressure and room temperature. Their combination is attractive as it is possible to achieve good DRM results at atmospheric configurations. To place this research into context, a detailed introduction is given in Chapter 1. The recent research in LDH-derived catalysts for DRM is introduced and summarized. Subsequently, two typical plasmas, i.e., dielectric barrier discharge (DBD) and gliding arc (GA) plasma, are described. Finally, several reported papers about these two types of plasma, assisted with LDH or LDH-derived catalysts for DRM, are analysed.

In order to better understand the catalyst activity, we studied some basic properties of LDH and its derived material (LDO). In Chapter 2, the stability of LDO obtained from LDH at high calcination temperature is investigated. Commonly, after calcination at a temperature below 600 °C, the obtained LDO can be rehydrated into LDH. However, at higher calcination temperatures, the rehydration situation is rarely reported. In this chapter, the LDHs were calcined at temperatures between 600 °C and 900 °C. The obtained LDOs were put into liquid water or vapour H_2O condition at room temperature for 6 to 48 h. XRD characterization proved that all

the LDO can be rehydrated into LDH, both in vapour and liquid conditions, although faster in the latter case. At a calcination temperature of 900 °C, apart from the MgO phase, an additional phase of spinel appeared, which remained in the particles in both rehydration conditions. The difference in the as-synthesized LDH and rehydrated LDOs was investigated with FTIR, SEM, N_2 sorption and TGA-MS. The results illustrated that the process of rehydration of the LDO into LDH produced new LDH rather than reconstructing it into the as-synthesized LDH. This part of the study suggested that even after high-temperature calcination, the materials derived from LDH need to be carefully stored to avoid rehydration even at room temperature.

Before using the plasma setup, a basic study was performed with the GAP device to decide the optimal configurations for the stable running of plasma and for the catalyst to realize its catalytic activity (Chapter 3). This chapter studied the configurations for the GAP plasma, such as gas flow rate, gas composition (N_2/CO_2, $N_2/CO_2/CH_4$), CO_2/CH_4 ratio, and addition of H_2O. In the N_2/CO_2 case, adding N_2 can improve the absolute conversion of CO_2 from 4% (100% CO_2) to 13% (80% N_2 and 20% CO_2). Another gas, namely CH_4, can further improve the CO_2 conversion to 44% at a gas flow rate of 10 L/min with $N_2/CO_2/CH_4$ ratio of 8/1/1. When decreasing the gas flow rate to 6 L/min with the same gas composition, the CO_2 conversion increases to 61%. Varying the CO_2/CH_4 ratio between 0.6 and 1.7

at a fixed N_2 amount (80%) and constant gas flow rate of 8 L/min, the CO_2 conversion fluctuated between 51% ($CO_2/CH_4 = 0.78$) and 58% ($CO_2/CH_4 = 0.6$). Adding H_2O is not beneficial for CO_2 conversion, which decreases from 55% to 22% as the relative humidity (RH) increases from 0% to 100%. Moreover, the addition of H_2O decreased the energy cost from 5.8 kJ/L (0% RH) to 3 kJ/L (40% RH).

The temperature at different positions after the plasma is recorded, and can give detailed information for the future application of the catalysts. In an N_2/CO_2 gas composition configuration, the temperature is highly affected by the amount of CO_2, i.e., the higher the CO_2 concentration is in the feed gas, the lower the temperature is in the same position after the plasma. However, no significant effect of the CO_2/CH_4 ratio on the temperature is observed in the DRM ($N_2/CO_2/CH_4$) conditions. Computational fluid dynamics (CFD) simulations were performed by Senne Van Alphen in PLASMANT to describe the distribution of temperature in the reactor. Although some deviation in absolute value exists, a similar general decreasing trend is observed.

Several factors are examined to determine their impact on the GAP post-plasma-catalytic DRM system, i.e. the distance between catalyst and post-plasma, the amount of catalyst used, extra heating ($\leq$ 250 °C) and the amount of H_2O added

(Chapter 4). We found that the distance and amount of catalyst have a limited effect on the CH_4 and CO_2 conversion. Nevertheless, the selectivity of CO and H_2 is higher in the case of using 1 g Ni/MO catalyst with a distance of 2 or 3 cm. Extra heating to a temperature of 250 °C resulted in a rise of the conversion of CH_4 to 69%. Moreover, the selectivity of CO and H_2 was found to be increased from 70% and 80% without heating to 81% and 96% in the H-250 case for CO and H_2, respectively. However, the energy cost increased as well. Measuring the temperature at a certain position revealed that although extra heating was supplied, an inefficient combination of the heating jacket and reactor led to waste of the heat and no improvement in conversions. Furthermore, the addition of H_2O into the feed gas was found efficient to improve the selectivity of CO and H_2 and to decrease the carbon deposition. However, a serious drop in CO_2 conversion was observed from 55% to 15% upon H_2O addition (from 0% to 100% RH), when using the Ni/MO catalyst.

The parameter study in Chapter 4 suggested that in the current GAP system with a traditional catalyst bed, no improvement can be realized. However, thermal catalytic DRM implies that high temperature is beneficial for the catalyst to realize its catalytic activity. Therefore, either a new reactor design or catalyst bed, or higher external heating is needed.

In Chapter 5, we designed a new catalyst bed (N-bed) and applied it to the GAP reactor for post-plasma catalytic (PPC) DRM. Compared with the traditional catalyst bed (T-bed) used in Chapter 4, when the N-bed was used with a CH_4/CO_2 ratio of 1, an increase in CO_2 and CH_4 conversion from 53% and 67% to 69% and 83% was observed, even when only packing material of α-Al_2O_3 was used. After adding the Ni/MO catalyst, a further increase in conversion was found, achieving a CO_2 conversion of 79% and a CH_4 conversion of 91%. Therefore, although no insulation nor external heating was supplied to the N-bed GAP system, the N-bed still can provide slightly higher conversions than those in a thermal catalytic case at 700 °C, while being fully electrically driven. This improvement may be caused by the direct connection of the N-bed to the GAP plasma device, transferring more heat from the plasma device to the catalyst, and the double wall system formed by the embedding of the N-bed and the quartz reactor cylinder, supplying improved mass and heat transfer and insulation, helping to heat the catalyst to its active temperature range. Moreover, the CO selectivity increased to 96% and the energy cost was reduced from around 6 kJ/L in plasma alone configuration to 4.3 kJ/L. This discovery may generate some ideas for other researchers and even further application of post-plasma catalysis in different beneficial reactions.

Algemene samenvatting

LDH-afgeleide katalysatoren zijn effectief voor droge reforming van methaan (DRM) bij hoge temperatuur, en plasma maakt DRM mogelijk bij atmosfeerdruk en kamertemperatuur. De combinatie van beide is aantrekkelijk, om goede DRM resultaten te bekomen bij atmosferische condities. Om dit onderzoek in context te plaatsen, wordt in hoofdstuk 1 een gedetailleerde introductie gegeven. Het recente onderzoek naar van LDH afgeleide katalysatoren voor DRM wordt geïntroduceerd en samengevat. Vervolgens worden twee typische plasma's beschreven, namelijk diëlektrische barrière-ontlading (DBD) en glijdende boogplasma (GA). Ten slotte worden verschillende gerapporteerde artikels over deze twee soorten plasma, ondersteund door LDH of van LDH afgeleide katalysatoren voor DRM, geanalyseerd.

Om een beter inzicht te krijgen in de activiteit van de katalysator, hebben we enkele basiseigenschappen van LDH en zijn afgeleide materiaal (LDO) bestudeerd. In Hoofdstuk 2 wordt de stabiliteit van LDO verkregen uit LDH bij hoge calcineringstemperatuur onderzocht. Gewoonlijk kan het verkregen LDO na calcineren bij een temperatuur onder 600 °C worden gerehydrateerd tot LDH. Bij een hogere calcineertemperatuur wordt de rehydratatiesituatie echter zelden

gemeld. In dit hoofdstuk werden de LDH's gecalcineerd bij een temperatuur tussen 600 °C en 900 °C. De verkregen LDO's werden gedurende 6 tot 48 uur bij kamertemperatuur in vloeibaar water of H_2O damp conditie gebracht. XRD karakterisering bewees dat alle LDO kan worden gerehydrateerd tot LDH, zowel in damp- als vloeibare omstandigheden, hoewel sneller in het laatste geval. Bij een calcineringstemperatuur van 900 °C verscheen naast de MgO-fase een extra fase van spinel, die in beide rehydratatie-omstandigheden in de deeltjes achterbleef. Het verschil in deze gesynthetiseerde LDH en gerehydrateerde LDO's werd onderzocht met FTIR, SEM, N_2 sorptie en TGA-MS. De resultaten illustreerden dat het proces van rehydratatie van de LDO in LDH nieuwe LDH produceerde in plaats van het te reconstrueren in de gesynthetiseerde LDH. Dit deelonderzoek suggereerde dat zelfs na calcineren bij hoge temperatuur de materialen die zijn afgeleid van LDH zorgvuldig moeten worden bewaard om rehydratatie te voorkomen, zelfs bij kamertemperatuur.

Voordat de plasma-opstelling werd gebruikt, werd er basisonderzoek gedaan met de GAP-reactor om de optimale configuraties te bepalen voor een stabiele werking van plasma en voor de katalysator om zijn katalytische activiteit te realiseren. Hoofdstuk 3 bestudeerde de configuraties voor het GAP-plasma, zoals gasstroomsnelheid, gassamenstelling (N_2/CO_2, $N_2/CO_2/CH_4$), CO_2/CH_4 verhouding en toevoeging van H_2O. In het geval van N_2/CO_2 kan toevoeging van

N_2 de absolute conversie van CO_2 verbeteren van 4% (100% CO_2) naar 13% (80% N_2 en 20% CO_2). Een ander gas, namelijk CH_4, kan de CO_2 conversie verder verbeteren tot 44% bij een gasdebiet van 10 l/min met een $N_2/CO_2/CH_4$ verhouding van 8/1/1. Bij het verlagen van het gasdebiet naar 6 L/min bij dezelfde gassamenstelling stijgt de CO_2 conversie naar 61%. Door de CO_2/CH_4 verhouding te variëren tussen 0.6 en 1.7 bij een vast N_2 gehalte (80%) en een constant gasdebiet van 8 L/min schommelde de CO_2 omzetting tussen 51% (CO_2/CH_4 = 0.78) en 58% (CO_2/CH_4 = 0.6). Het toevoegen van H_2O is ongunstig voor de CO_2 omzetting, die daalt van 55% naar 22% naarmate de relatieve vochtigheid (RH) stijgt van 0% naar 100%. Bovendien verlaagde de toevoeging van H_2O de SEI en energiekosten van 3.5 kJ/L (bij 0% RH) naar 1.6 kJ/L (bij 40% RH) en van 5.8 kJ/L (bij 0% RH) naar 3 kJ/L (bij 40% RH).

De temperatuur op verschillende posities na het plasma wordt geregistreerd, wat gedetailleerde informatie kan geven voor de toekomstige toepassing van een katalysator. In een configuratie met een N_2/CO_2 gassamenstelling wordt de temperatuur sterk beïnvloed door de hoeveelheid CO_2: hoe hoger de CO_2 concentratie in het voedingsgas, hoe lager de temperatuur in dezelfde positie na plasma. Er wordt echter geen significant effect van de CO_2/CH_4-verhouding op de temperatuur waargenomen in de DRM-omstandigheden ($N_2/CO_2/CH_4$). “Computational fluid dynamics” (CFD) simulaties worden uitgevoerd door Senne

Van Alphen (PLASMANT) om de temperatuursverdeling in de reactor te beschrijven. Hoewel er enige afwijking in absolute waarde bestaat, wordt een bevredigende overeenkomst in trend waargenomen tussen de simulatie en experimenten.

Om te bestuderen welke parameters het post-plasma-katalytische DRM-systeem van de GAP beïnvloeden, worden de effecten van afstand, hoeveelheid katalysator, temperatuur (≤ 250 °C) en toevoeging van H_2O onderzocht in Hoofdstuk 4. Onderzoek wees uit dat de afstand en hoeveelheid katalysator een beperkt effect hebben op de CH_4 en CO_2 conversie. Desalniettemin is de selectiviteit van CO en H_2 hoger bij gebruik van 1 g Ni/MO-katalysator met een afstand van 2 of 3 cm. Extra verwarming tot een temperatuur van 250 °C voor de reactor wordt geprobeerd en de conversie van CH_4 wordt verhoogd tot 69%. Bovendien blijkt de selectiviteit van CO en H_2 te zijn toegenomen van 70% en 80% zonder verhitting tot 81% en 96% in het geval van H-250 voor respectievelijk CO en H_2. Maar ook de energiekosten stegen. Nader onderzoek door de temperatuur op een bepaald punt te meten, wees uit dat hoewel er extra verwarming werd gegeven, een inefficiënte combinatie van de verwarmingsmantel en de reactor leidde tot verspilling van de warmte, en geen verbetering van de conversies. Bovendien bleek toevoeging van H_2O aan het ontladingsgas efficiënt om de selectiviteit van CO en H_2 te verbeteren en de situatie van koolstofafzetting te verminderen. Er werd echter

een duidelijke daling van de CO_2 omzetting waargenomen van 55% naar 15% wanneer de RH werd verhoogd van 0% naar 100% bij gebruik van de Ni/MO-katalysator.

De parameterstudie in Hoofdstuk 4 suggereerde dat in het huidige GAP-systeem met een traditioneel katalysatorbed geen verbetering kan worden gerealiseerd. Thermisch katalytische DRM impliceerde echter dat hoge temperaturen gunstig zijn voor de katalysator om zijn katalytische activiteit te realiseren. Daarom is ofwel een nieuw ontwerp in de reactor of het katalysatorbed, ofwel een hogere externe verwarming nodig.

In hoofdstuk 5 werd een nieuw katalysatorbed (N-bed) ontworpen en toegepast in de GAP-reactor voor post-plasma katalytische (PPC) DRM. Vergeleken met het traditionele katalysatorbed (T-bed) gebruikt in hoofdstuk 4, levert het N-bed voor een CH_4/CO_2 verhouding van 1, een toename van de CO_2 en CH_4 conversie van 53% en 67% naar 69% en 83%, zelfs wanneer alleen pakkingsmateriaal van α-Al_2O_3 werd gebruikt. Door toevoeging van de Ni/MO katalysator werd een verdere toename van de omzetting gevonden, tot een CO_2 omzetting van 79% en een CH_4 omzetting van 91%. Daarom, hoewel er geen isolatie of externe verwarming werd geleverd aan het N-bed GAP systeem, kan de N-bed toepassing nog steeds iets hogere conversies bieden dan die in een thermisch katalytische behuizing bij

700 °C, terwijl ze volledig elektrisch wordt aangedreven. Deze verbetering kan worden veroorzaakt door de directe verbinding van het N-bed en de GAP plasmareactor, waardoor meer warmte van de plasmareactor naar de katalysator wordt overgedragen, en het dubbele wandsysteem dat wordt gevormd door de inbedding van het N-bed en de kwartsreactorcilinder. Hierdoor vindt verbeterde massa- en warmteoverdracht en isolatie plaats, waardoor de katalysator wordt verwarmd tot zijn actieve temperatuursbereik. Bovendien nam de CO selectiviteit toe tot 96% en werden de energiekosten verlaagd van ongeveer 6 kJ/L in de configuratie alleen met plasma tot 4.3 kJ/L. Deze ontdekking kan leiden tot enkele ideeën voor andere onderzoekers en zelfs tot verdere toepassing van post-plasma-katalyse in verschillende andere chemische reacties.

Future outlook

CO_2 dry reforming of methane (DRM) has been an attractive field for decreasing the greenhouse gases CO_2 and CH_4,. Either the use of LDH-derived catalyst alone for thermal catalysis or to drive the reaction via electricity by plasma, especially gliding arc plasmatron (GAP), is attracting many researchers. The combination of them is also promising, in which thermal catalysts can make use of the heat produced by the GAP plasma, forming post-plasma catalytic DRM. However, many papers found in such post-plasma catalysis system limited enhancement if no external heating or insulation was applied. In this research, the improvement of the DRM performance (higher CO_2 and CH_4 conversion, higher syngas selectivity, and lower energy cost) is realized by the utilization of a newly designed catalyst bed (N-bed). This design enables the catalyst bed to be directly connected to the GAP device, which can facilitate the heat and mass transfer from the plasma to the catalyst bed. The greater transfer of heat from the plasma made the temperature for the catalyst layer high enough, so that the catalyst can perform its catalytic effect. Besides this, the double wall formed by the embedding of the N-bed and the quartz reactor cylinder might help heat insulation.

In general, for the whole post-plasma catalysis area, the discovery in this thesis makes the full use of heat produced by warm plasma (GAP herein) to become a reality. It expands the application of post-plasma catalysis. Therefore, some directions in this area can be studied in the future.

1. As introduced in Chapter 1, promoted Ni-LDH-derived catalysts can have higher stability and coke resistance. Therefore, it is worth trying such promoted Ni/MO catalyst, which - compared to the Ni/MO catalyst - may further improve the results of DRM in this PPC GAP system.

2. Although the performance of the N-bed PPC GAP system is a new discovery, considering no external heating or insulation is needed, the mechanism behind the improvement is not yet clear. It is believed that the direct connection and the double wall effect are beneficial for the improvement. However, more experiments with different lengths of the N-bed catalyst and computer simulations will help to understand clearly how and why this system works better than the traditional (T-bed).

3. The combination of N-bed and GAP plasma system for DRM suggests the possibility of post-plasma catalysis (PPC). Therefore, other thermal catalytic reactions can also be evaluated in this system.

In conclusion, this thesis gives a small discovery about the current state of the art of post-plasma catalysis (PPC) with warm plasma (GAP) for DRM. It also offers a possible direction for the further study of the PPC area to some degree.

Appendix A: Supporting information for Chapter 2

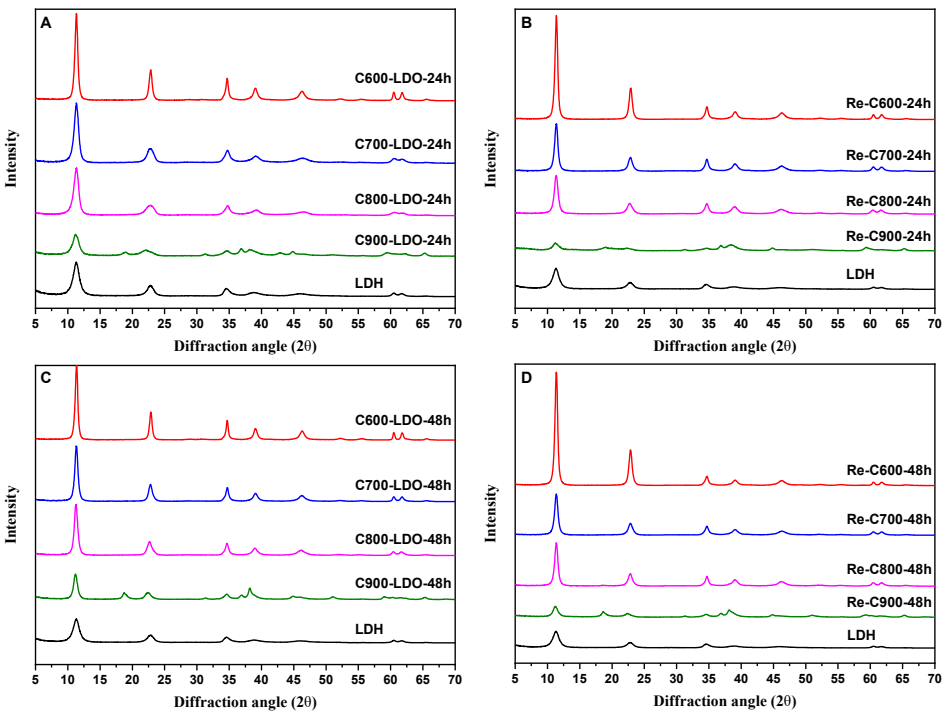

Fig. A.1. XRD patterns of as-synthesized LDH and samples rehydrated 24 h and 48 h from different calcined LDOs in water vapour (A and C) and liquid water (B and D).

Table A.1. Crystal lattice parameters of as-synthesized LDH and rehydrated LDHs are calculated from the peaks of the XRD patterns displayed in Figure 2.1A and Figure 2.2. The basal spacing is calculated by the formula $c' = 1/2 \cdot (d_{003} + 2d_{006})$. The unit cell parameters are calculated as follows: c-axis parameter $c = 3 \cdot c'$, lattice parameter $a = 2 \cdot d_{110}$.

Sample	$d_{(003)}$ (Å)	$d_{(006)}$ (Å)	$d_{(110)}$ (Å)	c‘ (Å)	a (Å)	c (Å)
LDH	7.80	3.90	1.53	7.80	3.06	23.40
C600-6h	7.74	3.84	1.52	7.71	3.05	23.13
C600-12h	7.80	3.90	1.53	7.80	3.05	23.40
C600-24h	7.80	3.89	1.53	7.79	3.06	23.36
C600-48h	7.77	3.89	1.53	7.77	3.06	23.32
Re-C600-6h	7.74	3.89	1.53	7.76	3.06	23.28
Re-C600-12h	7.77	3.88	1.53	7.76	3.06	23.29
Re-C600-24h	7.77	3.87	1.53	7.76	3.06	23.28
Re-C600-48h	7.77	3.89	1.53	7.77	3.06	23.32
C700-6h	7.69	3.84	1.52	7.68	3.04	23.05
C700-12h	7.71	3.83	1.52	7.69	3.04	23.07
C700-24h	7.80	3.90	1.53	7.80	3.05	23.40
C700-48h	7.82	3.89	1.53	7.81	3.06	23.42
Re-C700-6h	7.80	3.89	1.53	7.79	3.06	23.38
Re-C700-12h	7.77	3.90	1.53	7.79	3.06	23.36
Re-C700-24h	7.74	3.89	1.53	7.76	3.06	23.28
Re-C700-48h	7.77	3.89	1.53	7.78	3.06	23.33
C800-6h	7.71	3.78	1.52	7.64	3.04	22.92
C800-12h	7.69	3.83	1.52	7.67	3.05	23.01
C800-24h	7.77	3.88	1.53	7.77	3.05	23.30
C800-48h	7.83	3.92	1.53	7.83	3.06	23.50
Re-C800-6h	7.77	3.92	1.53	7.81	3.07	23.42
Re-C800-12h	7.74	3.90	1.53	7.77	3.06	23.32
Re-C800-24h	7.77	3.91	1.53	7.80	3.07	23.40
Re-C800-48h	7.77	3.89	1.53	7.78	3.06	23.34
C900-6h	7.64	3.83	1.55	7.65	3.11	22.94
C900-12h	7.88	3.84	1.56	7.78	3.11	23.33
C900-24h	7.91	3.86	1.55	7.81	3.10	23.44
C900-48h	7.88	3.96	1.56	7.90	3.13	23.71
Re-C900-6h	7.80	3.85	1.55	7.74	3.11	23.23
Re-C900-12h	7.82	3.87	1.56	7.78	3.11	23.34
Re-C900-24h	7.88	3.83	1.56	7.77	3.11	23.31
Re-C900-48h	7.83	3.97	1.56	7.88	3.12	23.65

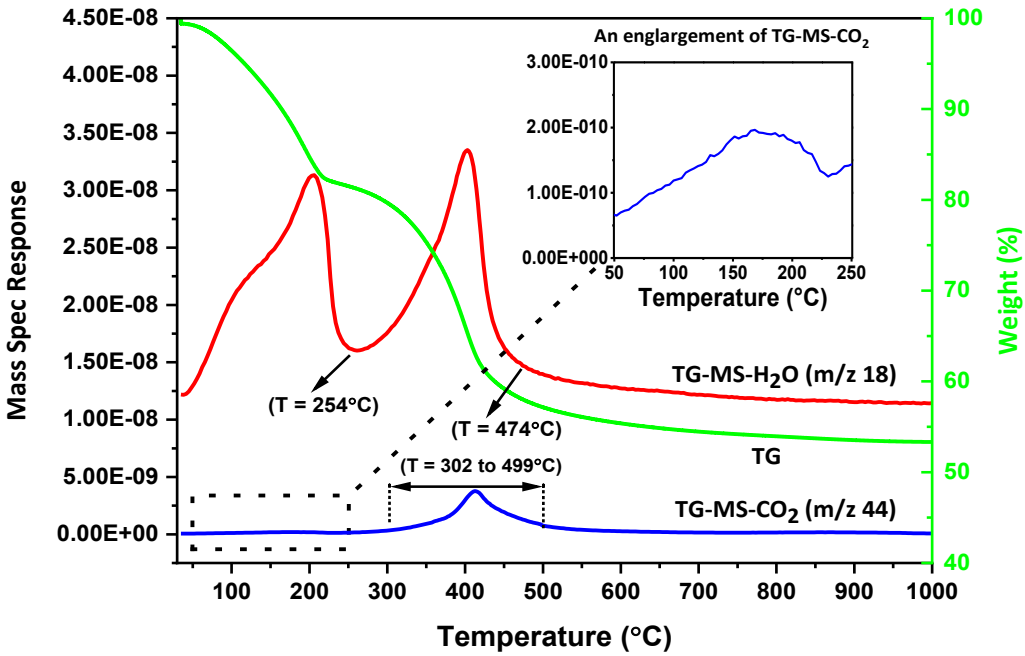

Fig. A.2. TG-MS of as-synthesized LDH

Figure A.3. includes the TG-MS of C600-LDO and the rehydrated samples for 6 h and 24 h in water vapour or liquid water.

A. TG-MS of C600-LDO

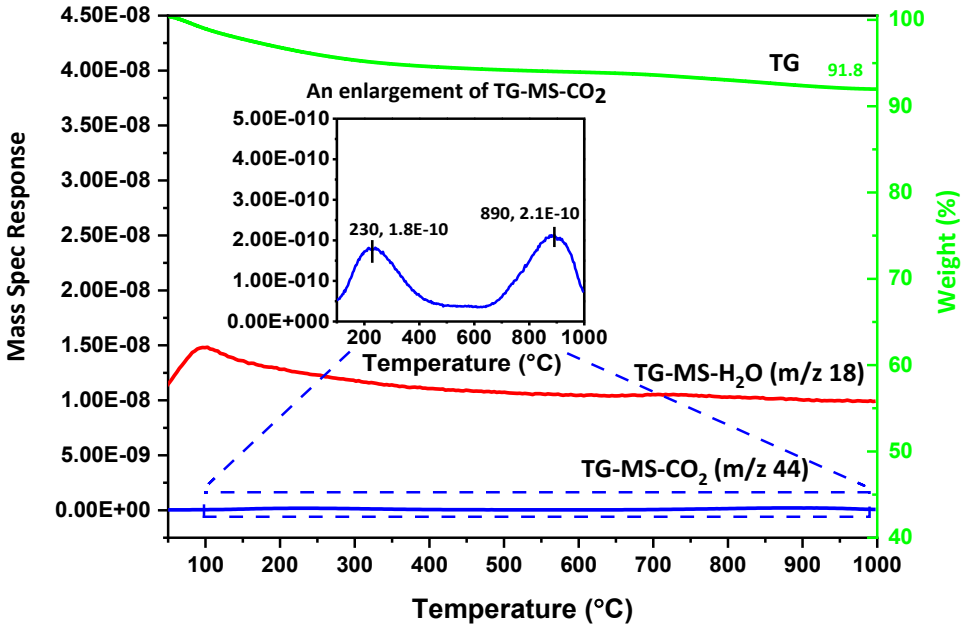

B. TG-MS of C600-LDO-6h

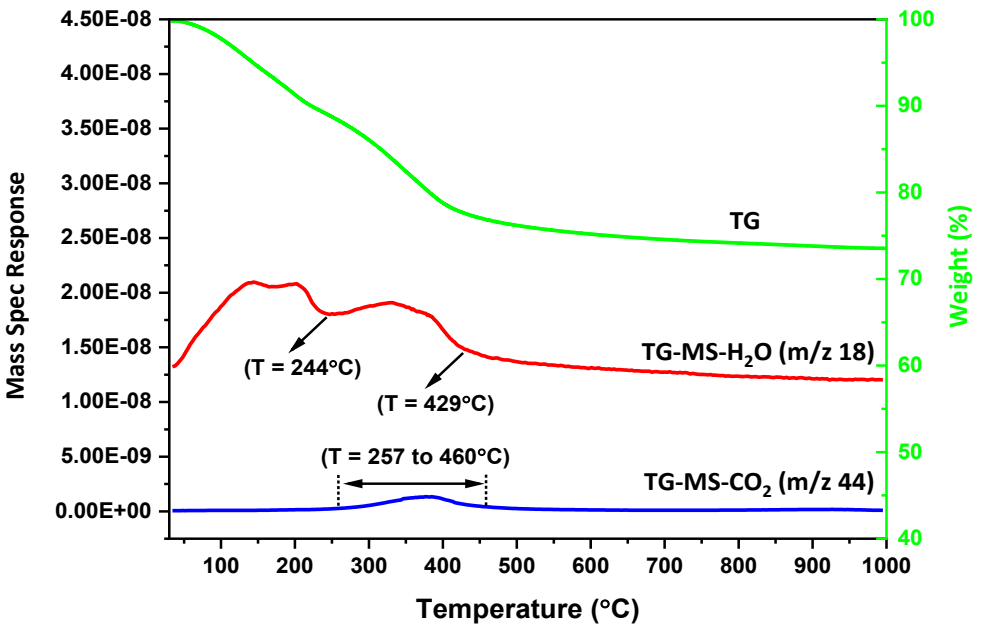

C. TG-MS of C600-LDO-24h

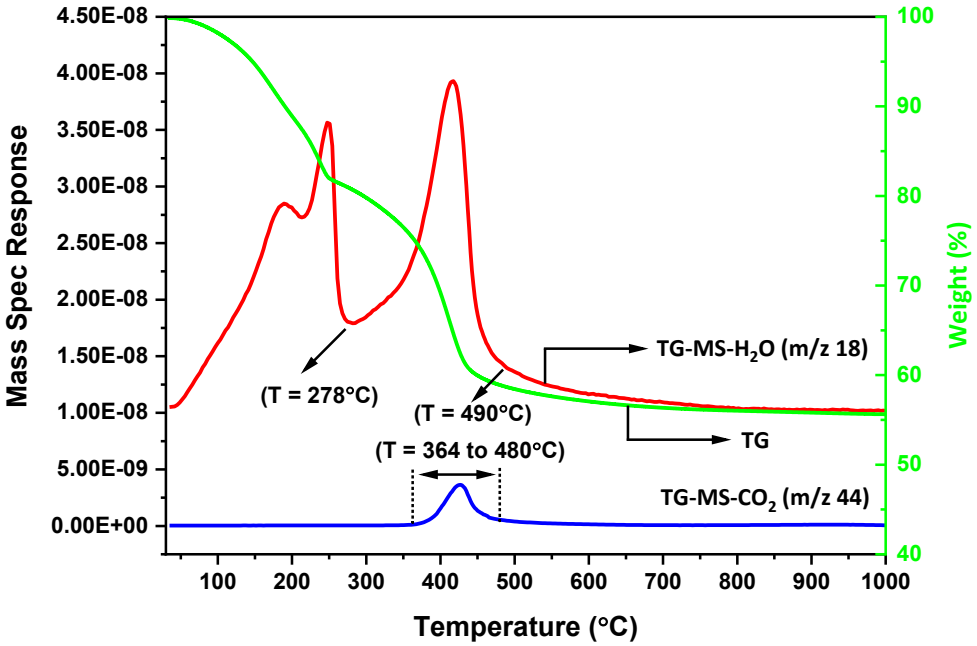

D. TG-MS of Re-C600-6h

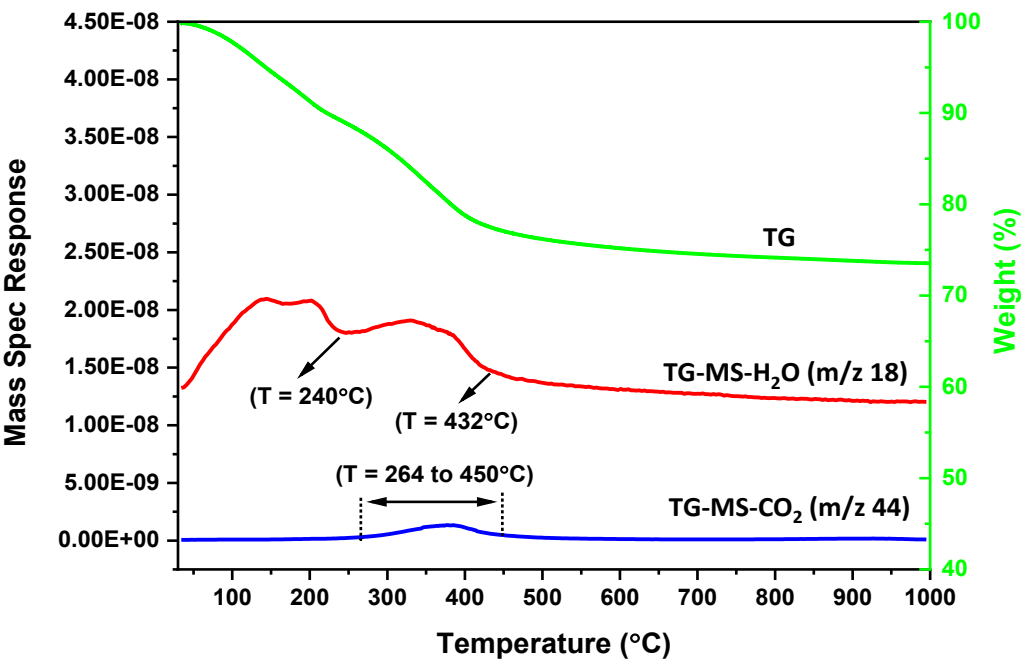

E. TG-MS of Re-C600-24h

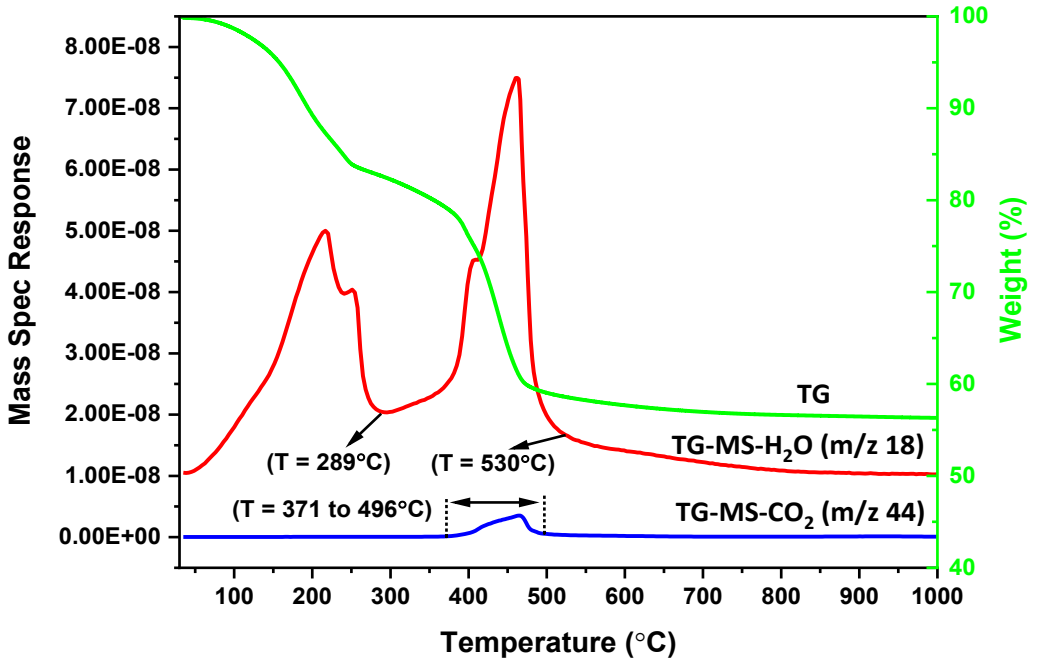

Fig. A.3. TG-MS of C600-LDO and the rehydrated samples for 6 h and 24 h in water vapour or liquid water.

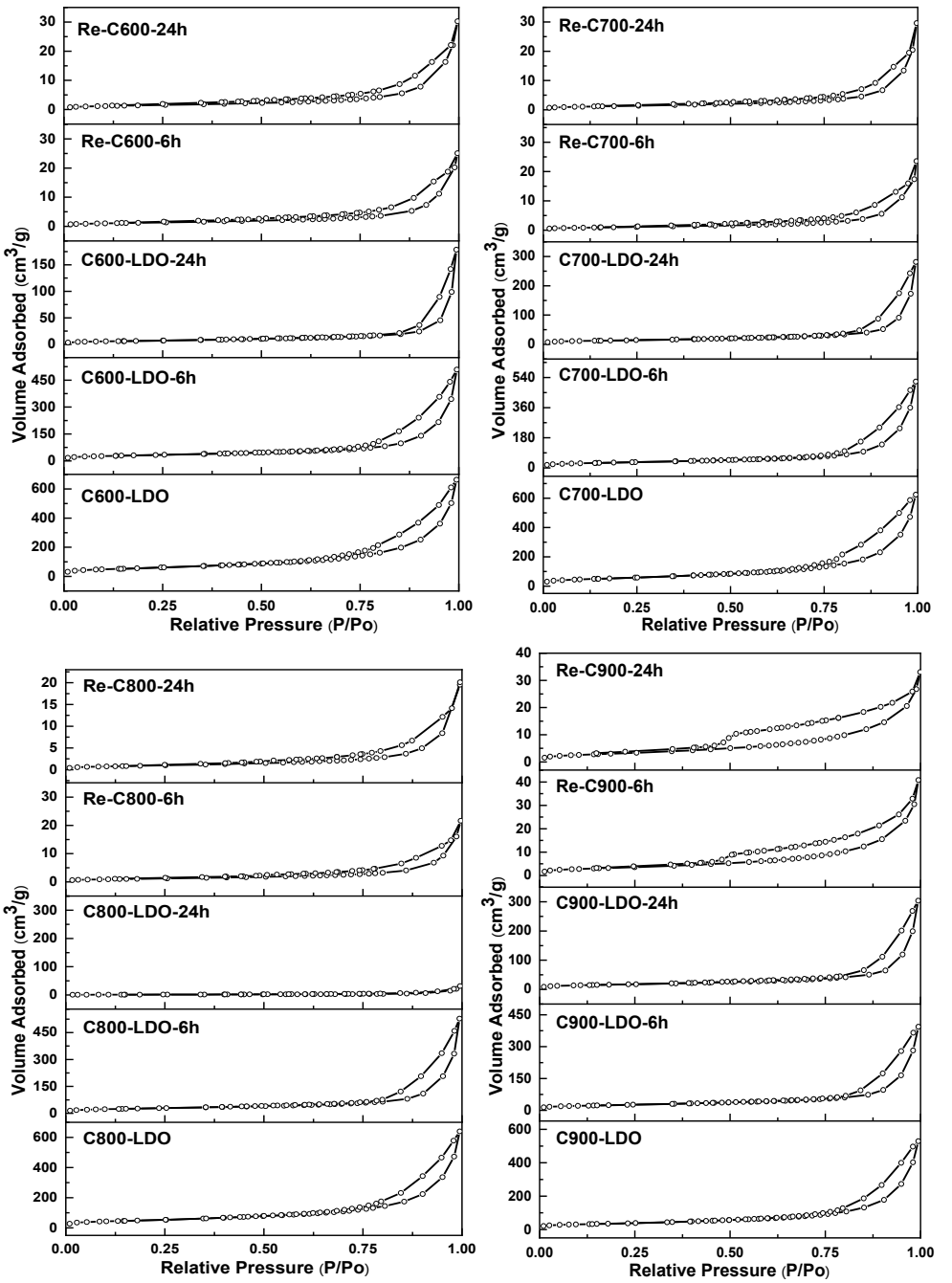

Fig. A.4. Nitrogen adsorption/desorption isotherms at -196 °C of LDO calcined at different temperatures rehydrated of 6h and 24h in vapour or liquid water condition with degassing temperature of 80 °C.

Table A.2. Specific surface area (degassing at 200 °C for 16 h) of samples obtained at different calcination temperatures and rehydration conditions.

Sample	S_{BET} (m^2/g)	Sample	S_{BET} (m^2/g)	Sample	S_{BET} (m^2/g)	Sample	S_{BET} (m^2/g)
LDH	83	-	-	-	-	-	-
C600-LDO	215	C700-LDO	197	C800-LDO	180	C900-LDO	118
C600-LDO-6h	149	C700-LDO-6h	183	C800-LDO-6h	173	C900-LDO-6h	146
C600-LDO-24h	17	C700-LDO-24h	17	C800-LDO-24h	37	C900-LDO-24h	85
Re-C600-6h	9	Re-C700-6h	6	Re-C800-6h	5	Re-C900-6h	36
Re-C600-24h	5	Re-C700-24h	7	Re-C800-24h	5	Re-C900-24h	25

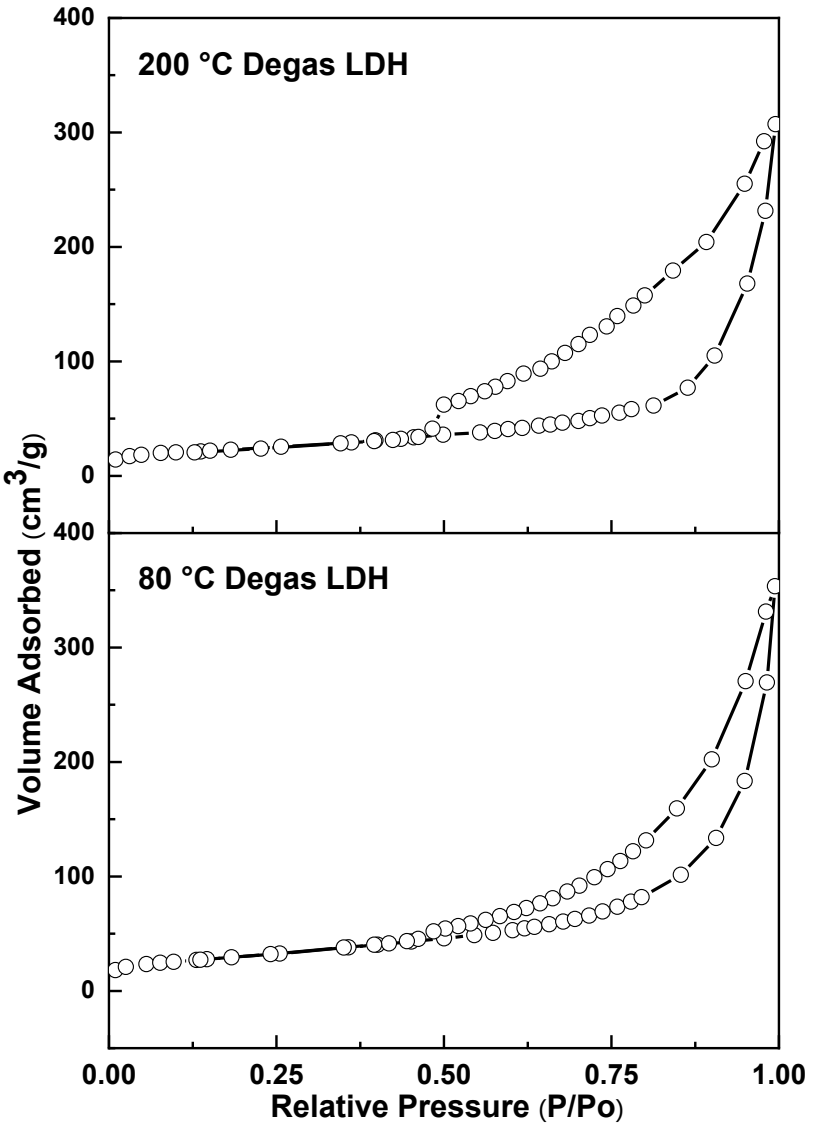

Fig. A.5. Nitrogen adsorption/desorption isotherms at -196 °C of as-synthesized LDH at degassing temperatures of 200 °C and 80 °C.

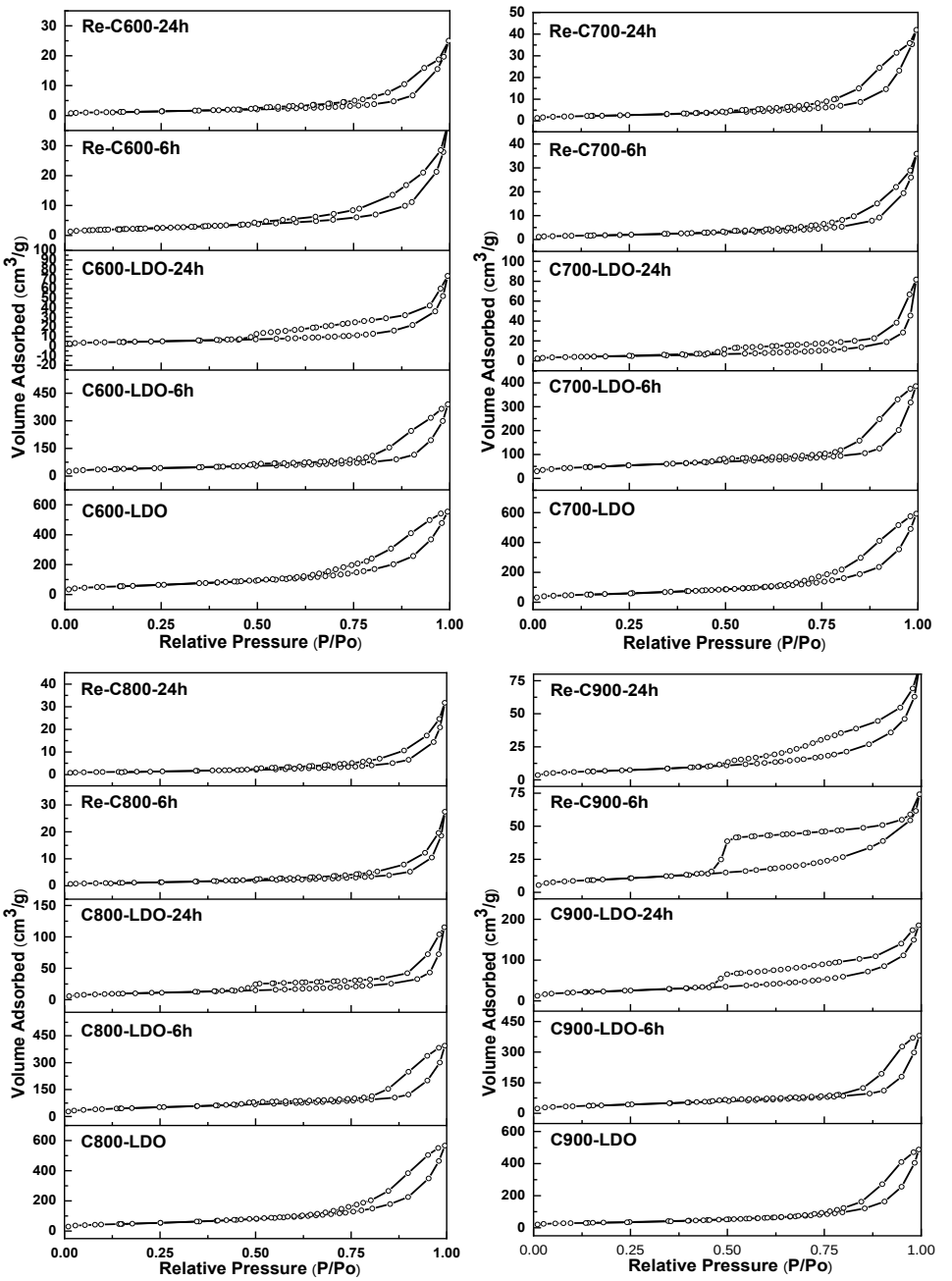

Fig. A.6. Nitrogen adsorption/desorption isotherms at -196 °C of LDO calcined at different temperatures rehydrated of 6h and 24h in vapour or liquid water condition with degassing temperature of 200 °C.

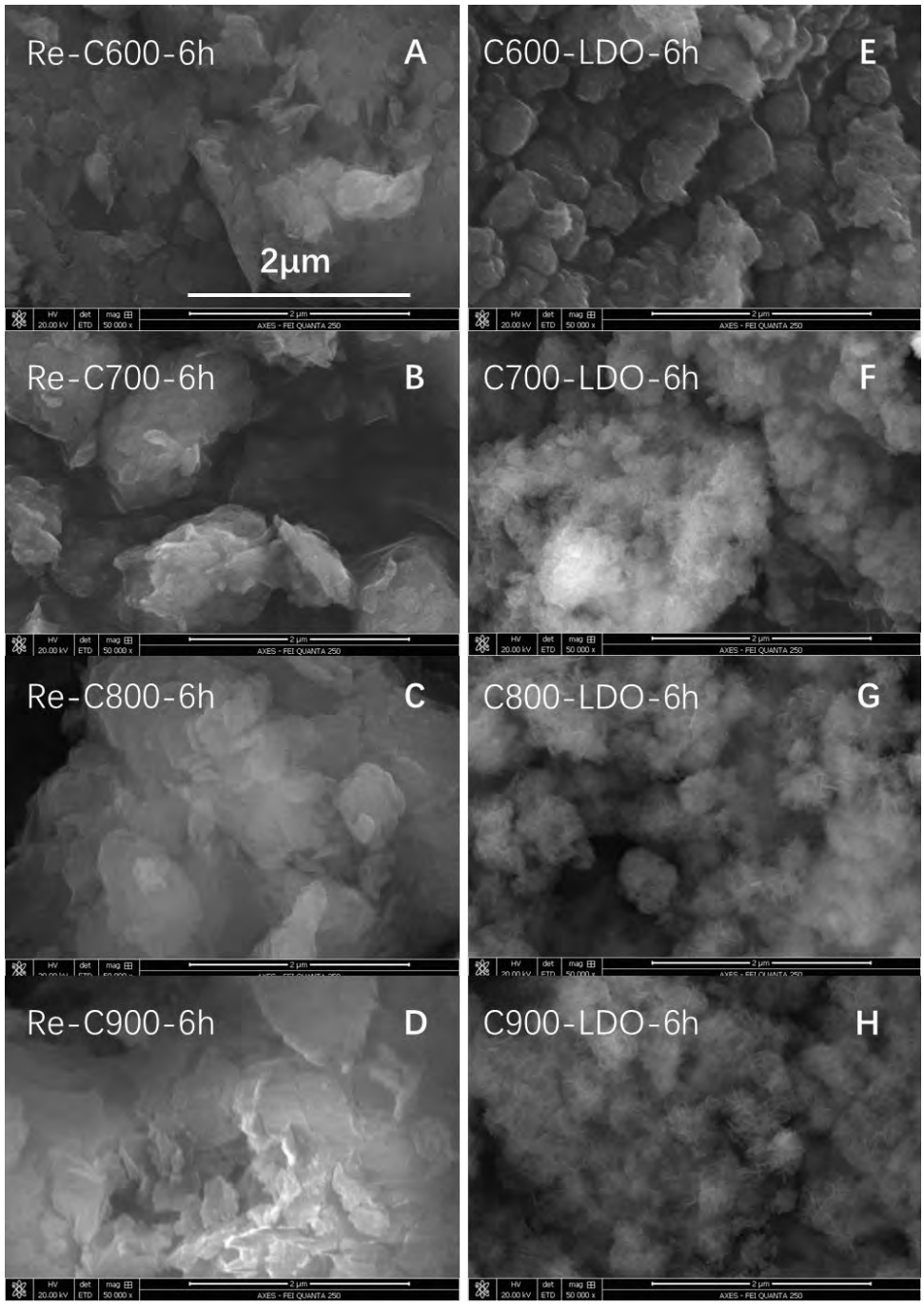

Fig. A.7. SEM images of rehydrated samples from LDO calcined at different temperatures and rehydrated in water vapour and liquid water for 6 h. A-D: rehydrated samples in liquid water; E-H: rehydrated samples in water vapour. All the SEM images are in a reference scale of 2 µm.

Appendix B: Supporting information for Chapter 3

B1. Effective conversions of CO_2 and CH_4 as a function of gas composition, gas flow rate and RH.

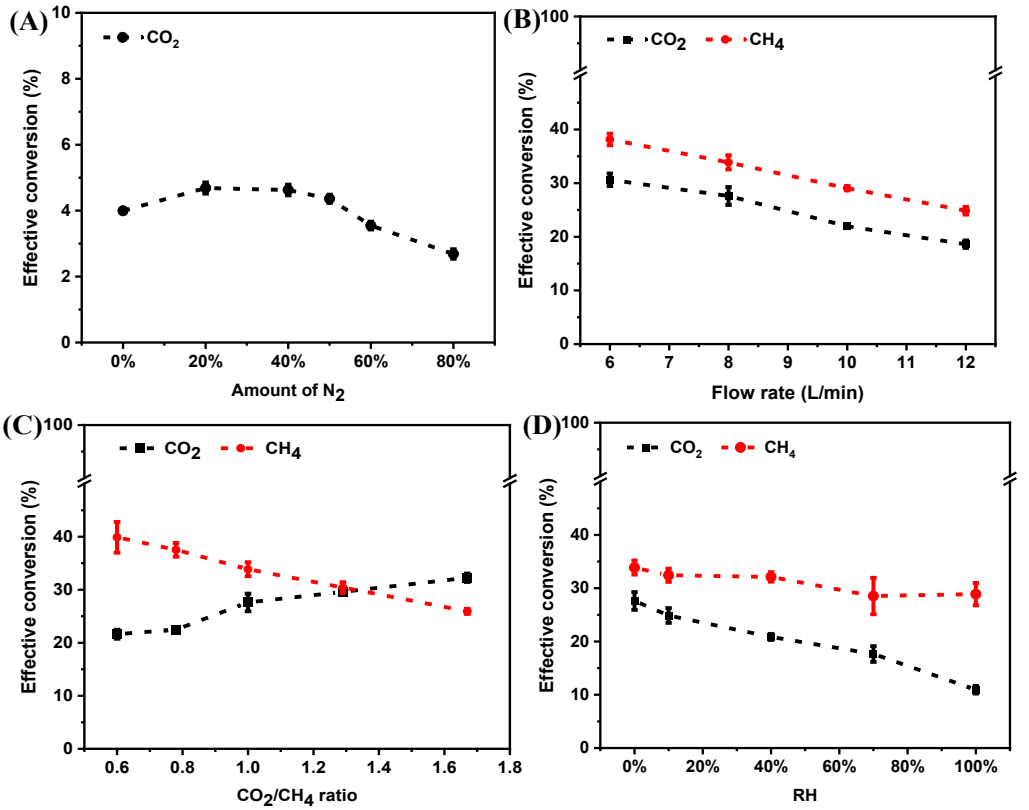

Fig. B1.1. Effective conversions of CO_2 and CH_4 as a function of gas composition, gas flow rate and RH. (A) CO_2 conversion in CO_2/N_2 mixture: Total gas flow rate = 10 L/min, N_2 fraction varying from 0% to 80%. (B) Total gas flow rate varied from 6 to 12 L/min, $CO_2/CH_4/N_2$ = 1/1/8. (C) Total gas flow rate = 8 L/min, N_2 = 6.4 L/min, CO_2/CH_4 ratio: 0.6 - 1.67. (D) Total gas flow rate = 8 L/min, $CO_2/CH_4/N_2$ = 1/1/8, H_2O amount: 0 - 100% RH.

B2. Raman spectrum of solid carbon product collected from the GAP DRM process

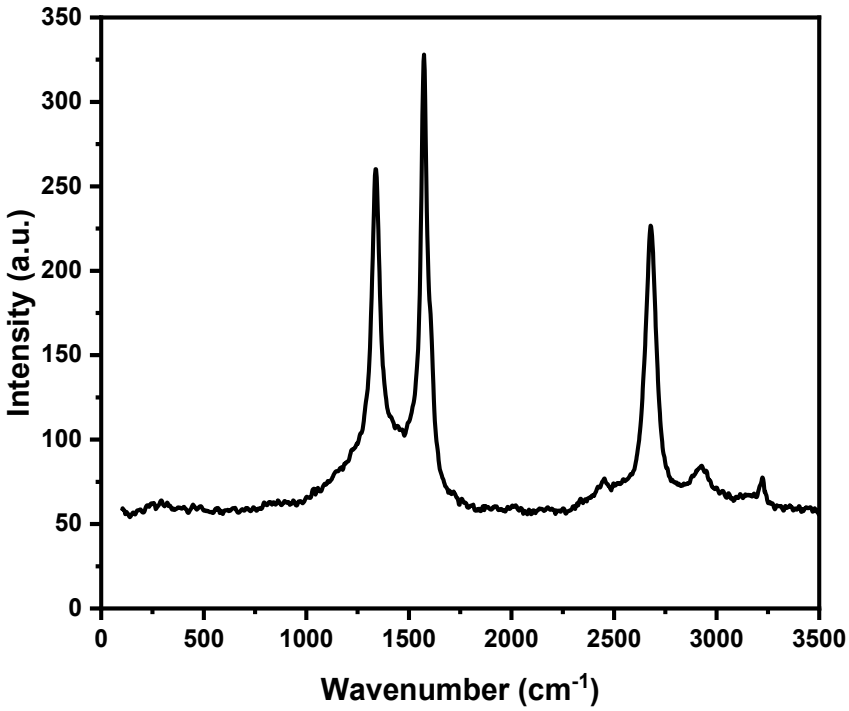

Fig. B2.1. Raman spectrum of the solid carbon product collected from the GAP DRM with a gas flow rate of 8L/min and gas composition of $N_2/CO_2/CH_4$=8/0.6/1.

B3. Figures for temperatures at different conditions

Fig. B3.1. N_2/CO_2 with constant gas flow rate of 10 L/min, but changing the amount of CO_2 from 0 to 100%.

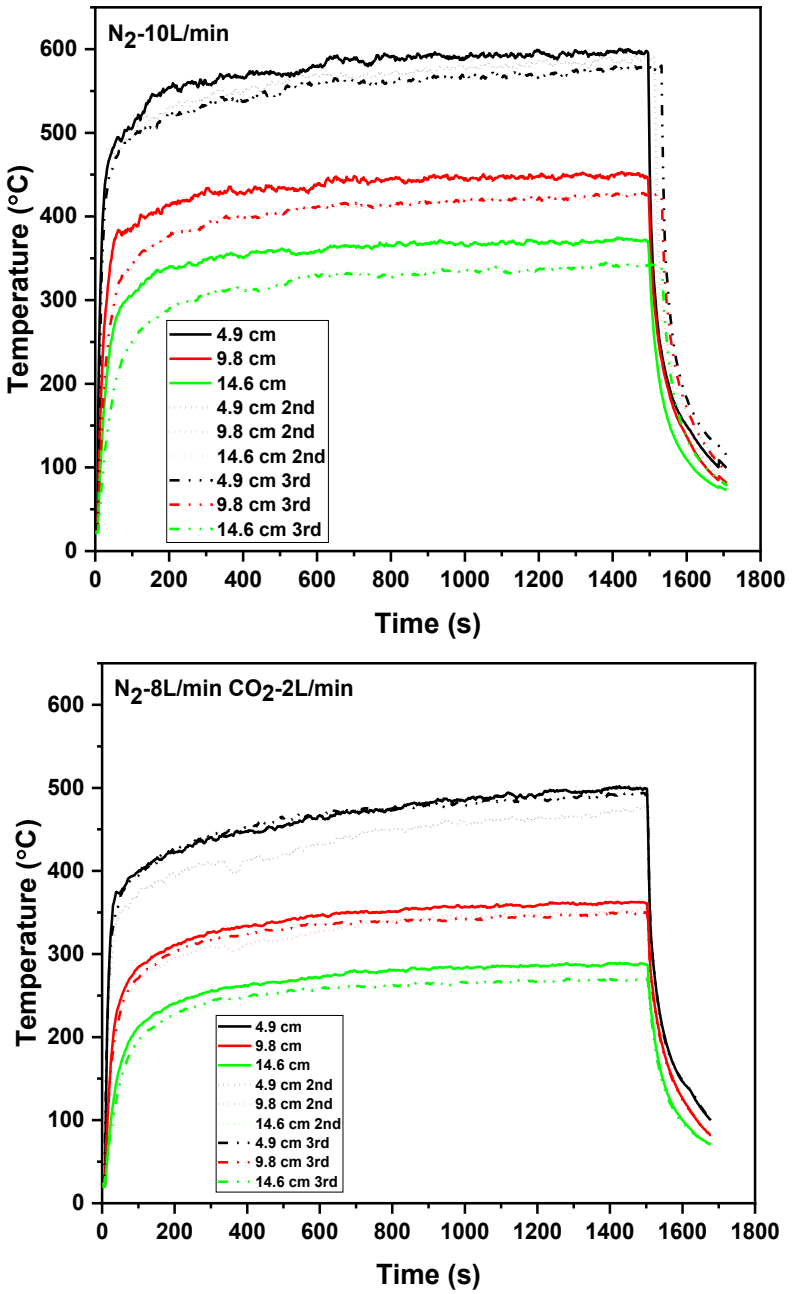

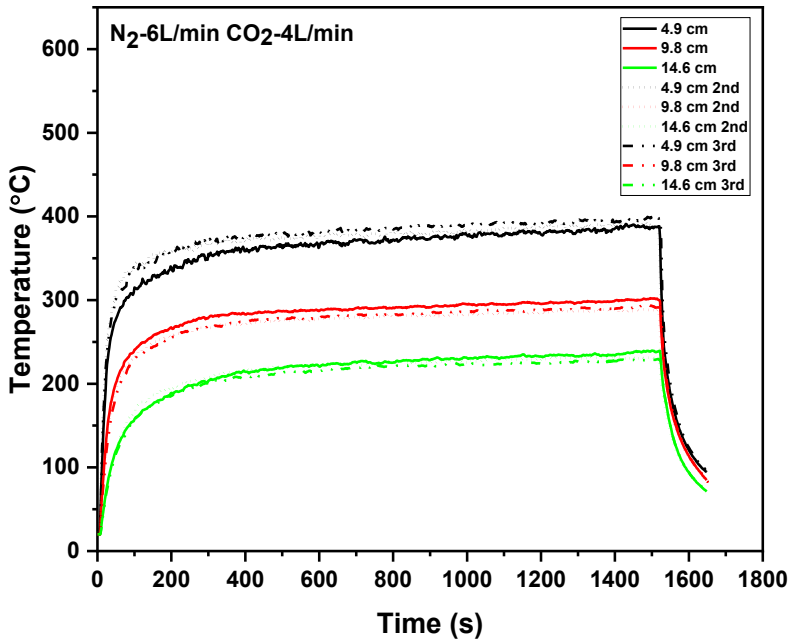
N2-6L/min CO2-4L/min
4.9 cm
9.8 cm
14.6 cm
4.9 cm 2nd
9.8 cm 2nd
14.6 cm 2nd
4.9 cm 3rd
9.8 cm 3rd
14.6 cm 3rd
Temperature (°C)
Time (s)
0
100
200
300
400
500
600
0
200
400
600
800
1000
1200
1400
1600
1800

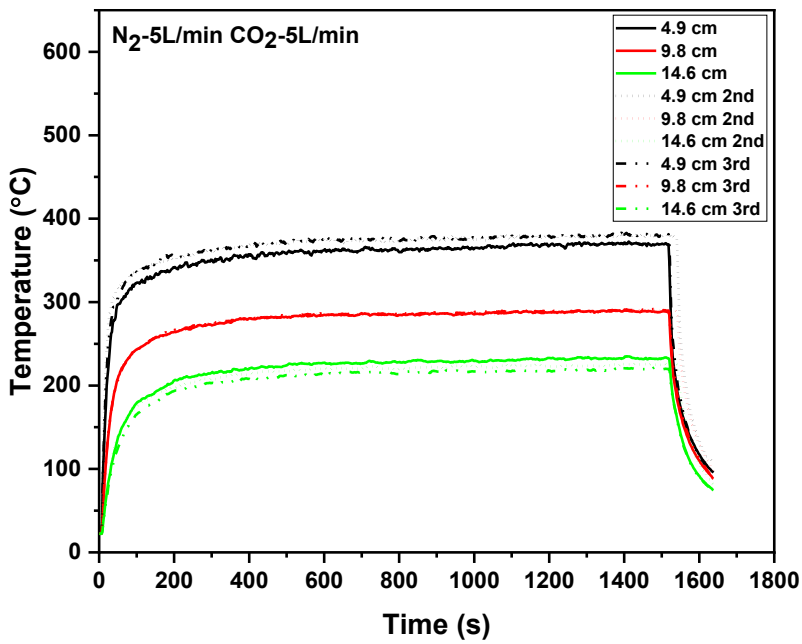
N2-5L/min CO2-5L/min
4.9 cm
9.8 cm
14.6 cm
4.9 cm 2nd
9.8 cm 2nd
14.6 cm 2nd
4.9 cm 3rd
9.8 cm 3rd
14.6 cm 3rd
Temperature (°C)
Time (s)
0
100
200
300
400
500
600
0
200
400
600
800
1000
1200
1400
1600
1800

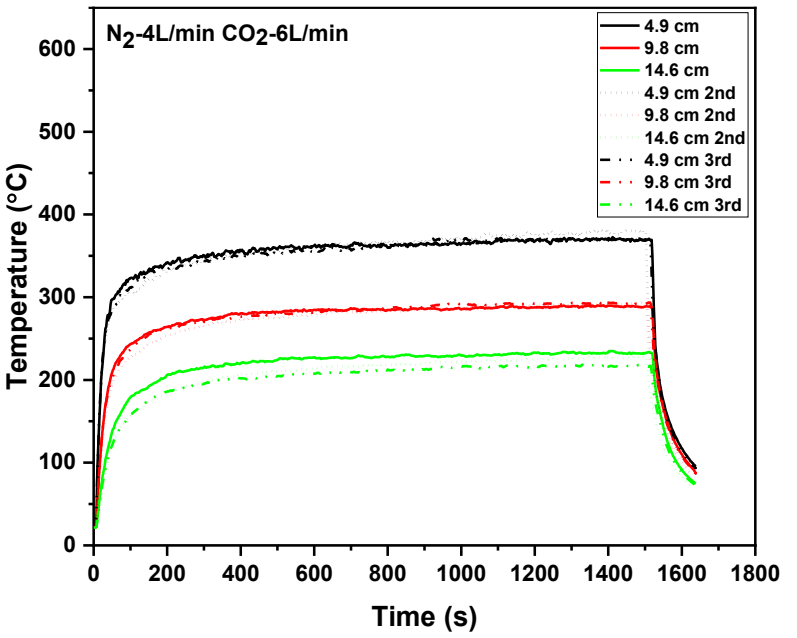
N2-4L/min CO2-6L/min
4.9 cm
9.8 cm
14.6 cm
4.9 cm 2nd
9.8 cm 2nd
14.6 cm 2nd
4.9 cm 3rd
9.8 cm 3rd
14.6 cm 3rd
Temperature (°C)
Time (s)
0
100
200
300
400
500
600
0
200
400
600
800
1000
1200
1400
1600
1800

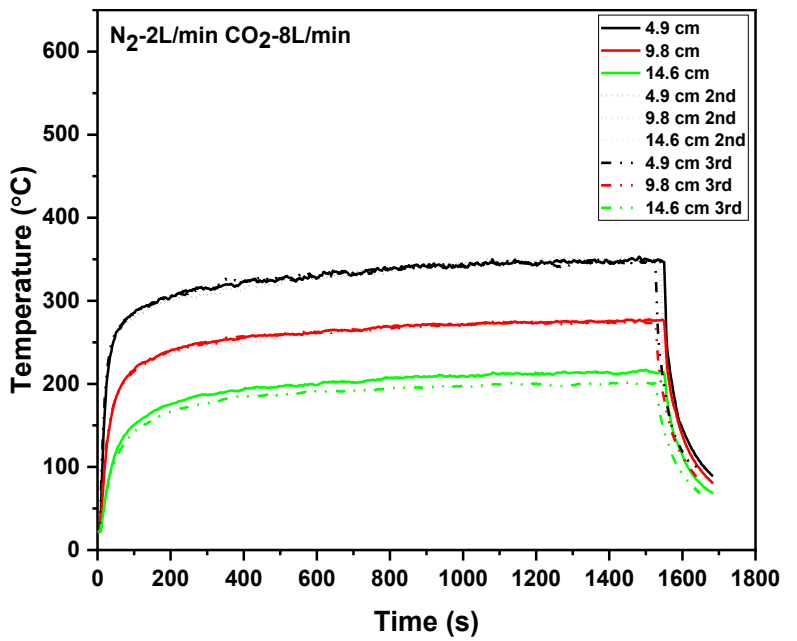
N2-2L/min CO2-8L/min
4.9 cm
9.8 cm
14.6 cm
4.9 cm 2nd
9.8 cm 2nd
14.6 cm 2nd
4.9 cm 3rd
9.8 cm 3rd
14.6 cm 3rd
Temperature (°C)
Time (s)
0
100
200
300
400
500
600
0
200
400
600
800
1000
1200
1400
1600
1800

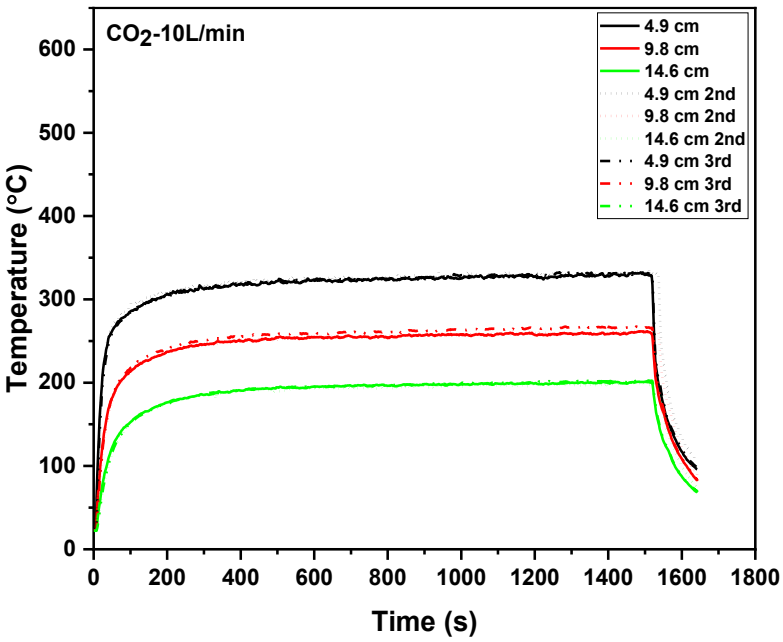
CO2-10L/min
4.9 cm
9.8 cm
14.6 cm
4.9 cm 2nd
9.8 cm 2nd
14.6 cm 2nd
4.9 cm 3rd
9.8 cm 3rd
14.6 cm 3rd
Temperature (°C)
Time (s)
0
100
200
300
400
500
600
0
200
400
600
800
1000
1200
1400
1600
1800

Fig. B3.2. $N_2/CO_2/CH_4$ with different gas flow rates varying from 6 L/min to 12 L/min, but with same gas ratio of $N_2/CO_2/CH_4$=8/1/1.

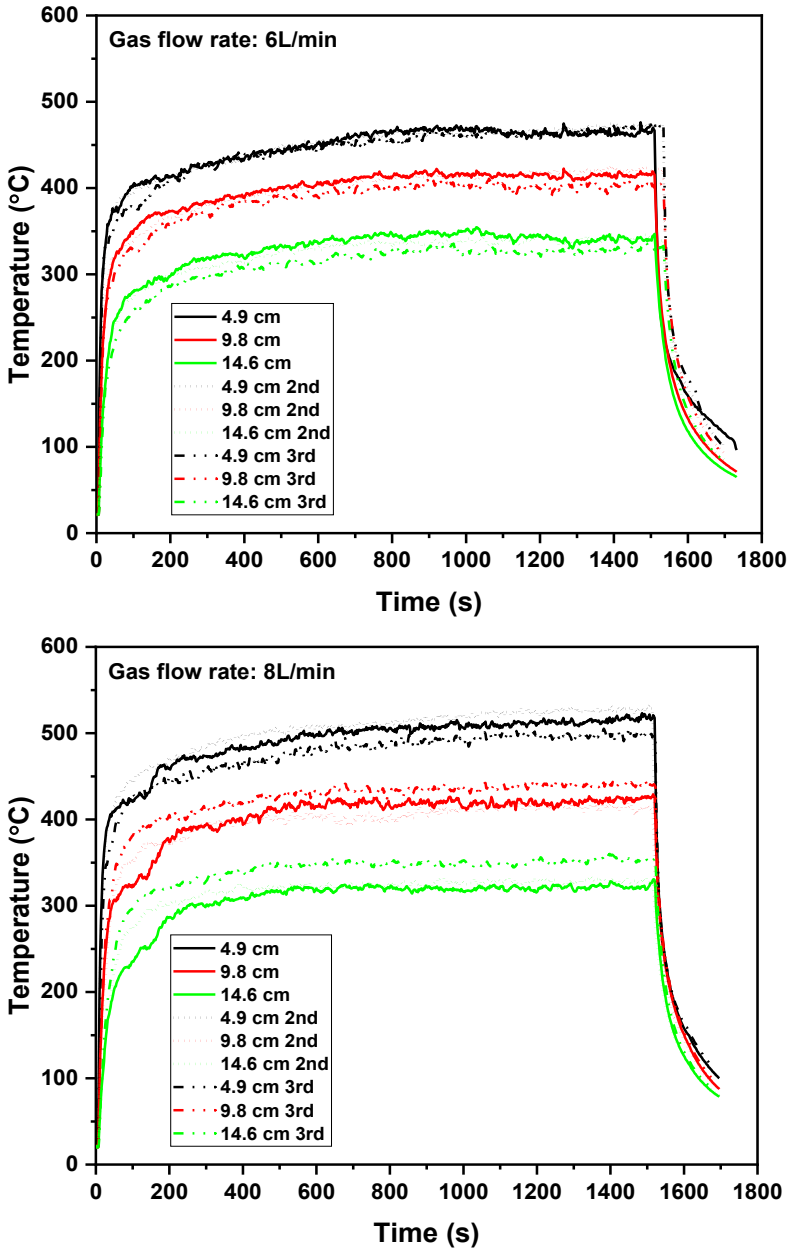

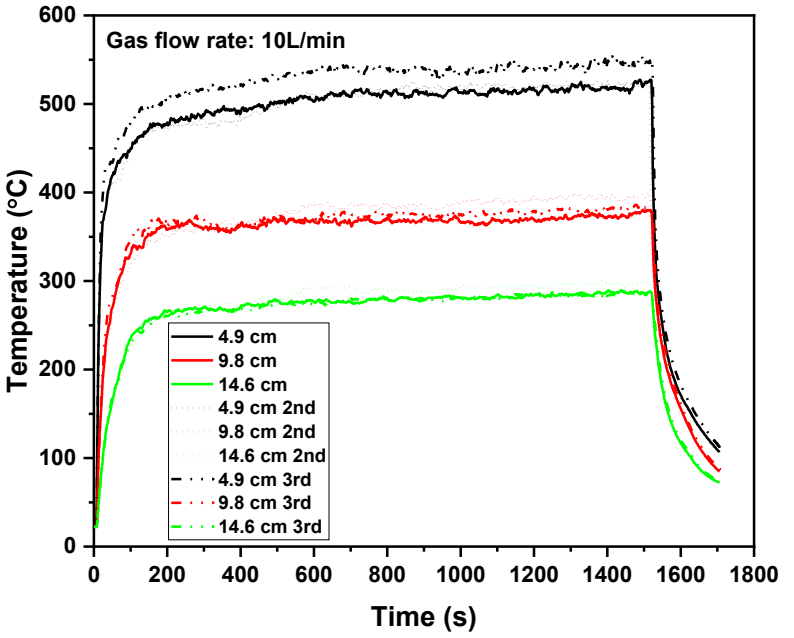
Gas flow rate: 10L/min
Temperature (°C)
Time (s)
0
100
200
300
400
500
600
0
200
400
600
800
1000
1200
1400
1600
1800
4.9 cm
9.8 cm
14.6 cm
4.9 cm 2nd
9.8 cm 2nd
14.6 cm 2nd
4.9 cm 3rd
9.8 cm 3rd
14.6 cm 3rd

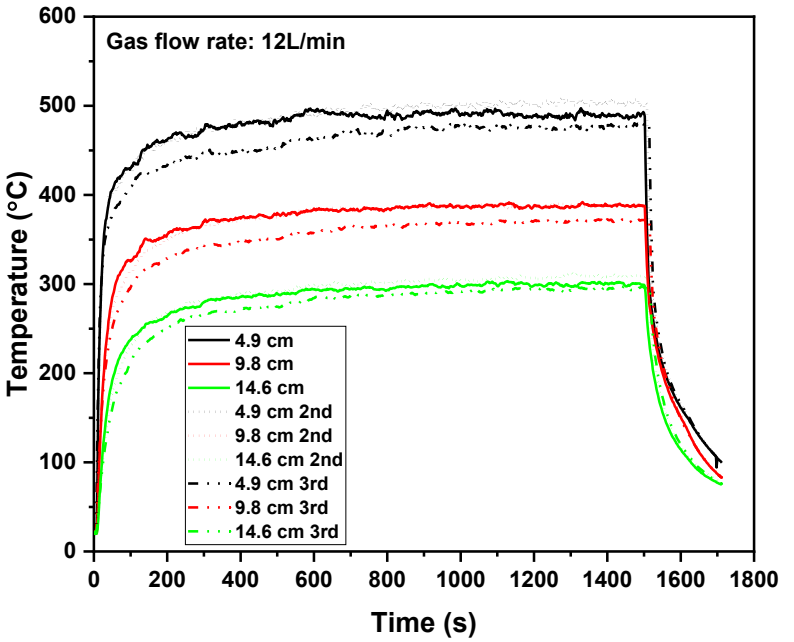
Gas flow rate: 12L/min
Temperature (°C)
Time (s)
0
100
200
300
400
500
600
0
200
400
600
800
1000
1200
1400
1600
1800
4.9 cm
9.8 cm
14.6 cm
4.9 cm 2nd
9.8 cm 2nd
14.6 cm 2nd
4.9 cm 3rd
9.8 cm 3rd
14.6 cm 3rd

Fig. B3.3. $N_2/CO_2/CH_4$ with the same gas flow rate of 8 L/min, and N_2 flow rate kept at 6.4 L/min, but the ratio of CO_2/CH_4 changed from 0.6/1 to 1/0.6.

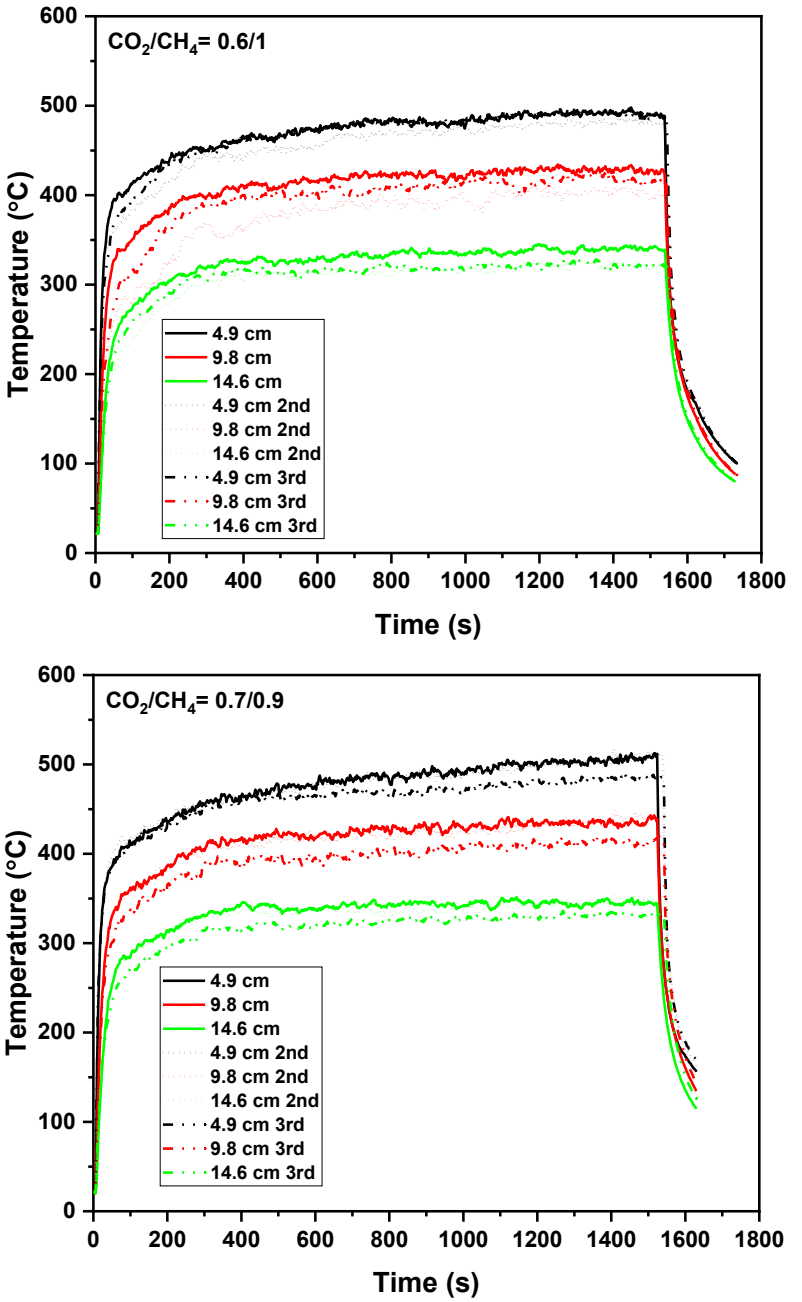

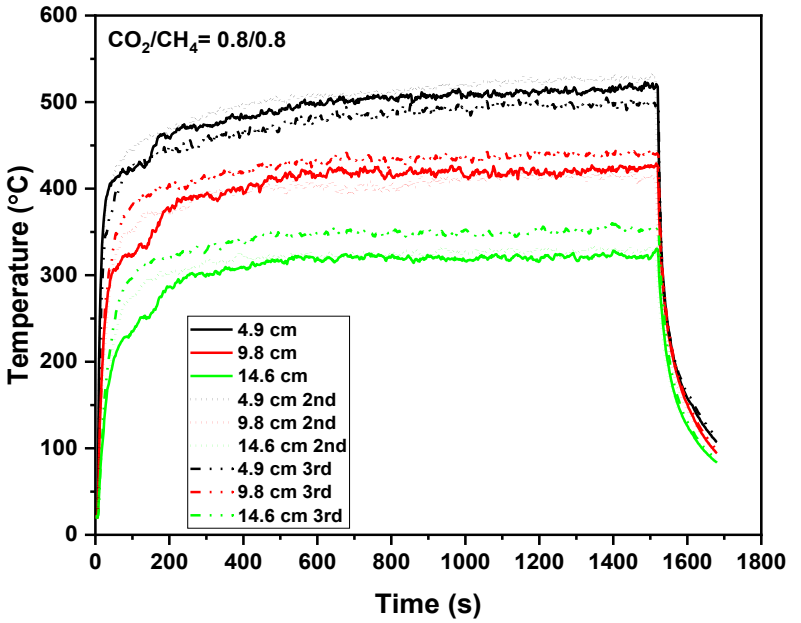
CO2/CH4= 0.8/0.8
Temperature (°C)
Time (s)
4.9 cm
9.8 cm
14.6 cm
4.9 cm 2nd
9.8 cm 2nd
14.6 cm 2nd
4.9 cm 3rd
9.8 cm 3rd
14.6 cm 3rd

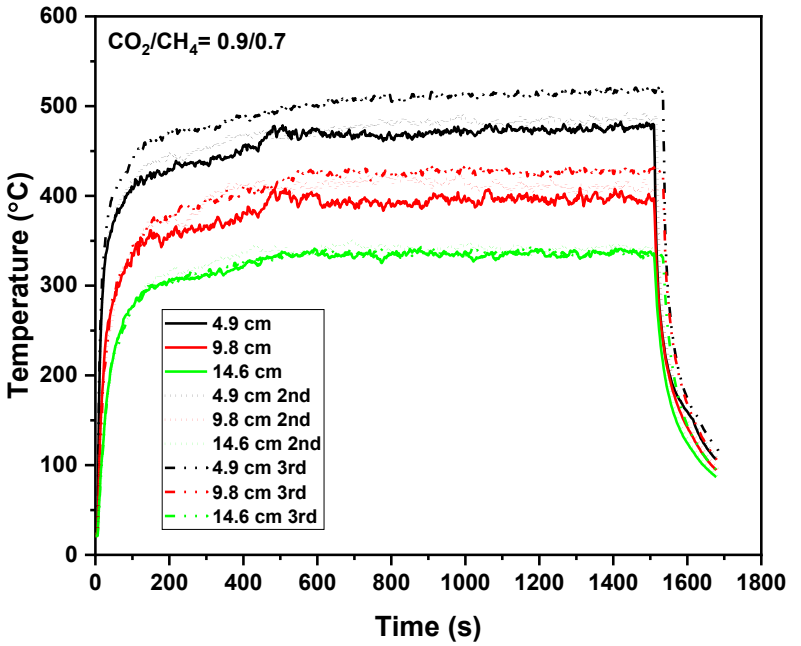
CO2/CH4= 0.9/0.7
Temperature (°C)
Time (s)
4.9 cm
9.8 cm
14.6 cm
4.9 cm 2nd
9.8 cm 2nd
14.6 cm 2nd
4.9 cm 3rd
9.8 cm 3rd
14.6 cm 3rd

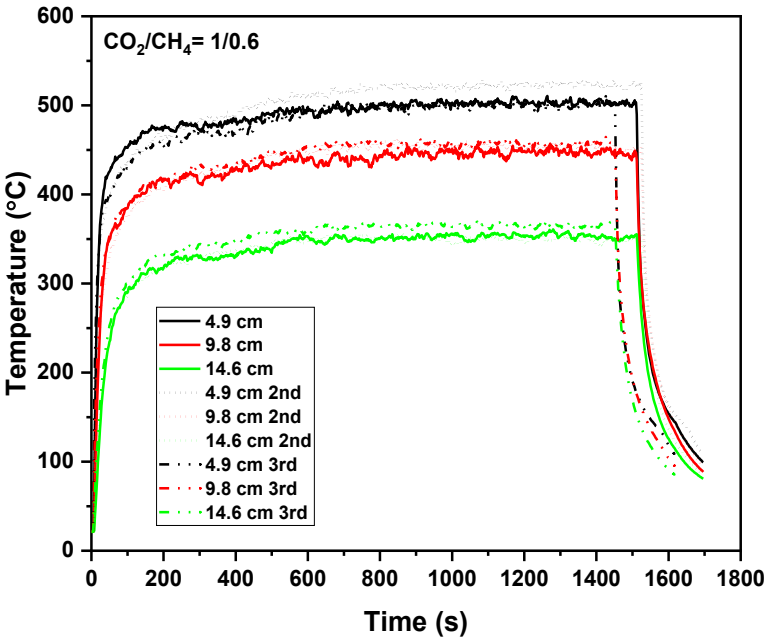
CO2/CH4= 1/0.6
Temperature (°C)
Time (s)
0
100
200
300
400
500
600
0
200
400
600
800
1000
1200
1400
1600
1800
4.9 cm
9.8 cm
14.6 cm
4.9 cm 2nd
9.8 cm 2nd
14.6 cm 2nd
4.9 cm 3rd
9.8 cm 3rd
14.6 cm 3rd

Fig. B3.4. $N_2/CO_2/CH_4/H_2O$ with the same gas flow rate of 8 L/min and the same gas ratio of $N_2/CO_2/CH_4$=8/1/1, changing the amount of H_2O from 0 to 100% RH. The amount of H_2O was calculated by a controlled evaporator mixer.

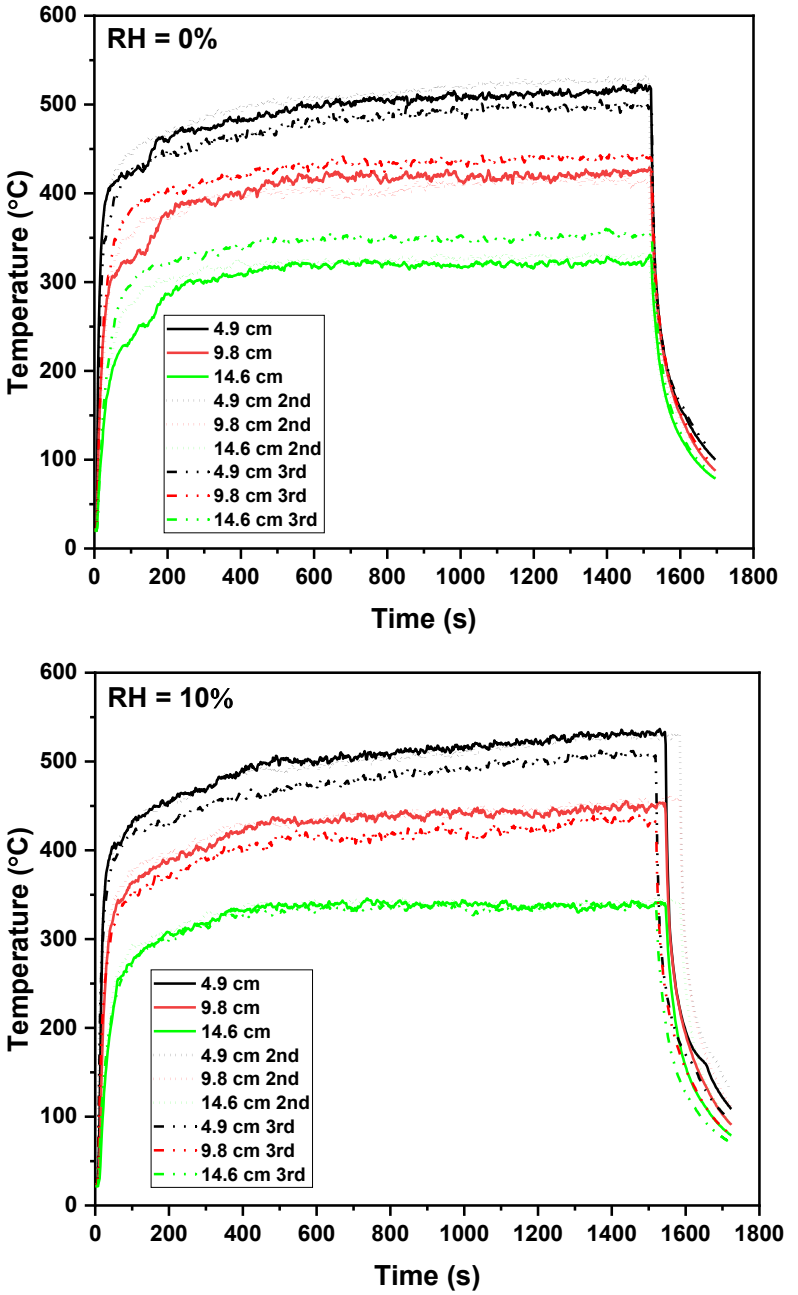

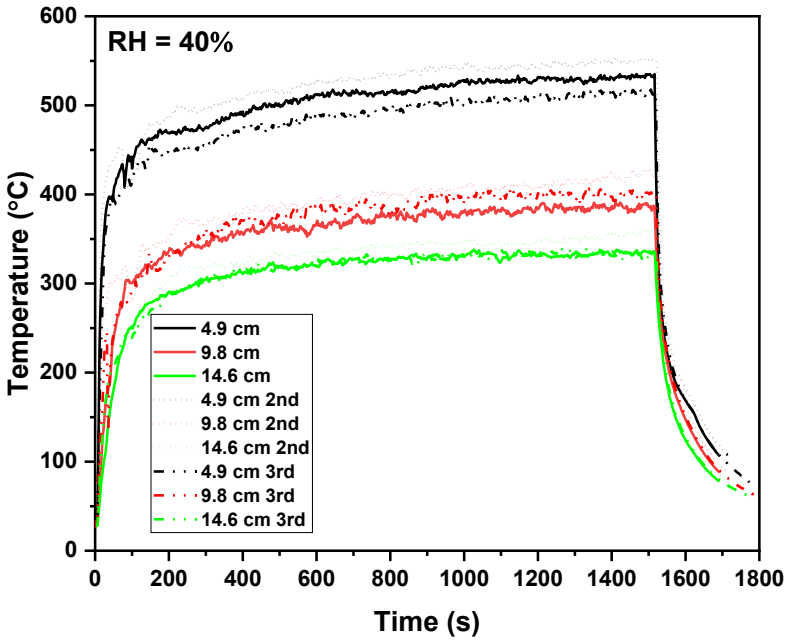
RH = 40%
Temperature (°C)
Time (s)
4.9 cm
9.8 cm
14.6 cm
4.9 cm 2nd
9.8 cm 2nd
14.6 cm 2nd
4.9 cm 3rd
9.8 cm 3rd
14.6 cm 3rd

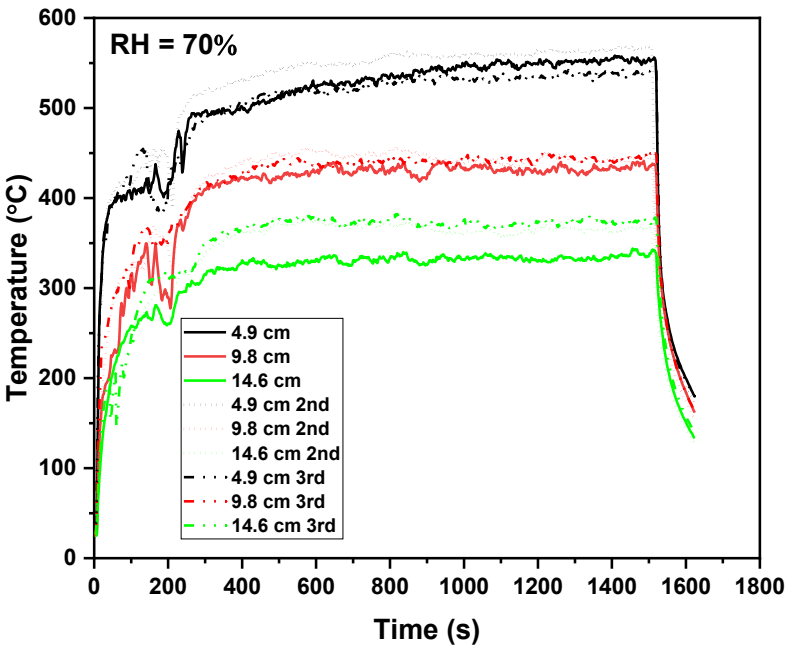
RH = 70%
Temperature (°C)
Time (s)
4.9 cm
9.8 cm
14.6 cm
4.9 cm 2nd
9.8 cm 2nd
14.6 cm 2nd
4.9 cm 3rd
9.8 cm 3rd
14.6 cm 3rd

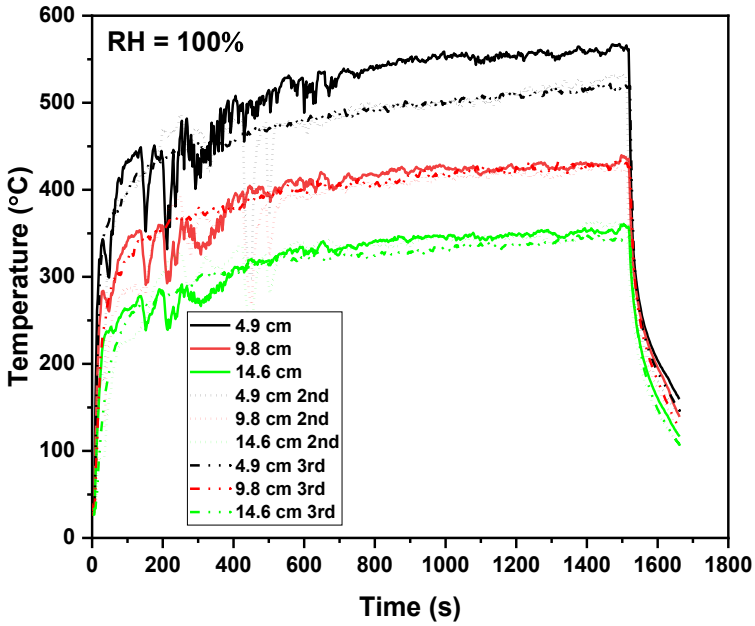

B4. Computational details

To gain a deeper insight into the temperature profile inside the reactor, the GAP reactor and post-plasma reactor tube were simulated using computational fluid dynamics (CFD) for a 1/1/8 $CO_2/CH_4/N_2$ gas mixture at a flow rate of 8 L/min. The geometry of the GAP reactor was simulated in 3D, which was required due to its complex geometry and tangential reactor inlets, as shown in Fig. B4.1A, while the geometry of the post-plasma reactor tube was simulated in a 2D axisymmetric model, due to its symmetrical shape, as shown in Fig. B4.1B.

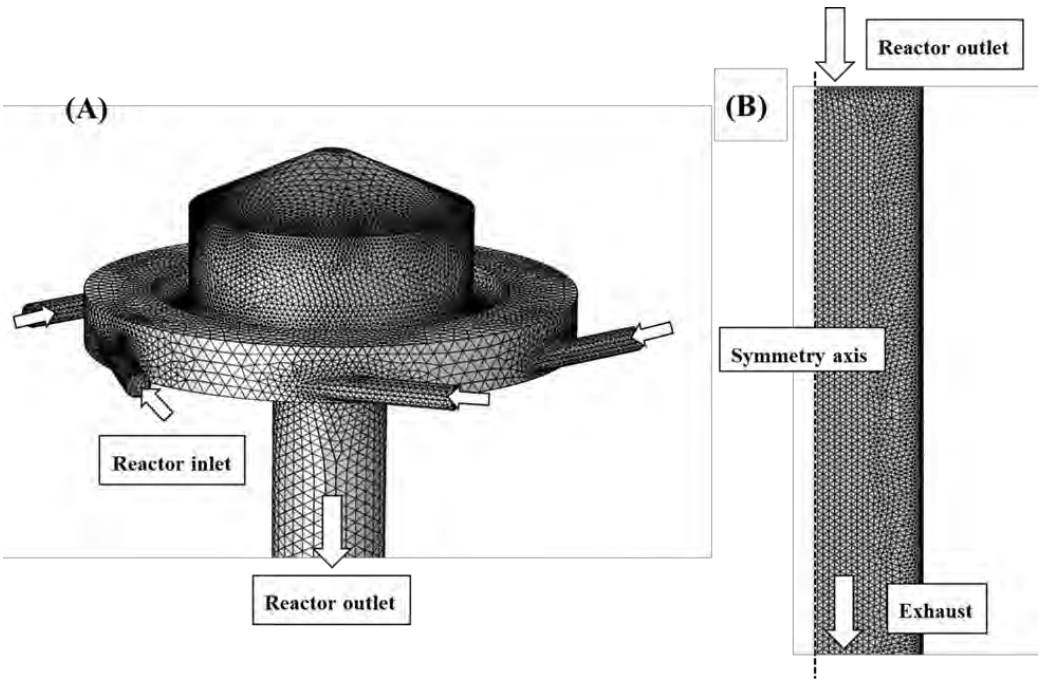

Fig. B4.1. (A) Model geometry and finite element mesh of the GAP reactor in the 3D CFD model and (B) model geometry and finite element mesh of the post-plasma reactor tube in the 2D axisymmetric CFD model.

B4.1. Describing the gas flow

The gas flow behaviour was described using the Navier Stokes equations for laminar flow, solving the following mass continuity and momentum continuity equations for a Newtonian fluid.

$$\rho_g \frac{\partial \vec{u}}{\partial t} + \rho_g(\vec{u} \cdot \nabla)\vec{u} = \nabla \cdot \left[-p\vec{I} + \mu(\nabla\vec{u} + \nabla(\vec{u})^T) - \frac{2}{3}\mu(\nabla \cdot \vec{u})\vec{I}\right] + \vec{F} \quad \text{(B1)}$$

$$\rho_g \frac{\partial \vec{u}}{\partial t} + \nabla \cdot (\rho_g \vec{u}) = 0 \quad \text{(B2)}$$

Where ρ_g stands for the gas density, $\vec{u}$ is the gas flow velocity vector, superscript T stands for transposition, p is the gas pressure, μ is the dynamic

viscosity, $\vec{I}$ the unity tensor and $\vec{F}$ the body force vector (which includes forces like gravity, but was considered zero as they were not the driving force of the fluid flow in this model).

B4.2. Calculating the heat balance

The gas temperature was calculated by representing the plasma as a heat source Q, using the following thermal balance equation:

$$\rho_g C_p \frac{\partial T_g}{\partial t} + \rho_g C_p \vec{u} \cdot \nabla T_g + \nabla \cdot \vec{q} = Q_{heat} \quad \text{(B3)}$$

Where ρ_g stands for the gas density, C_p for the isobaric heat capacity, T_g is the gas temperature, $\vec{u}$ the gas velocity, Q_{heat} the heat source term representing the heating from the plasma, and $\vec{q}$ the conductive heat flux vector, which was calculated by:

$$\vec{q} = -k_g \nabla T_g \quad \text{(B4)}$$

Where k_g is the thermal conductivity of the gas.

Within the chemically active zone of the plasma, gas heating occurs as a result of exothermic chemical reactions and the relaxation reactions of excited species, which was represented in equation (B5) by the heat source term Q_{heat}. This term was calculated using two different parameters, i.e. (i) the amount of power transferred to gas heating (P_{heat}, in W) and (ii) the plasma volume (V_{plasma}, in m³), such that the ratio of the two yields the power density (Q_{heat}, in W/m³):

$$Q_{heat} = \frac{P_{heat}}{V_{plasma}} \tag{B5}$$

For P_{heat} (see equation (B6)) in quasi-thermal plasmas at atmospheric pressure, it is reasonable to assume that all the power absorbed by the electrons that did not go into chemical reactions is nearly fully transferred to gas heating [1,2], which allows the plasma power transferred to heating to be calculated using the experimental plasma power P_{plasma}, and the energy efficiency (EE; see below). The plasma power P_{plasma} was calculated using the voltage-current characteristics of the plasma setup measured by the oscilloscope.

$$\mathrm{P}_{heat} = P_{plasma}(100\% - EE) \tag{B6}$$

For V_{plasma}, both experimental measurements [3] and computational models [4–6] have been used in previous work to determine the arc shape in the GAP reactor. Using this data as input, V_{plasma} was calculated, assuming an arc diameter of 2 mm.

The experimental energy efficiency EE was calculated from the concentrations of the plasma products at the outlet:

$$EE = \frac{\alpha \cdot \mathrm{c}_{CO}^{\mathrm{in}} \cdot H_{f,CO} - \left(X_{CH_4} \cdot c_{CH_4}^{in} \cdot H_{f,CH_4} + X_{CO_2} \cdot c_{CO_2}^{in} \cdot H_{f,CO_2}\right)}{SEI\,(kJ\ L^{-1}) \cdot V_{mol}(L\ mol^{-1})} \tag{B7}$$

H_f is the enthalpy of formation ($H_{f,CO}$= -110,5 kJ mol^{-1}; H_{f,CH_4}= -74,8 kJ mol^{-1}; H_{f,CO_2}= -393,5 kJ mol^{-1}).) [7]. This formula only considers the main DRM products CO and H_2 ($H_{f,H}$ = 0 thus not included in the formula).

B4.3. Properties of the gas mixture

As the gas undergoes chemical transformations in the plasma, the gas composition and thus the physical properties of the gas, change significantly. These effects were accounted for in the simulation by calculating the influence of the chemistry on the thermodynamic and transport properties of the gas that were of importance to the CFD calculation, i.e. the gas density (ρ_g), the heat capacity (C_p), heat conductivity (k_g) and viscosity (μ). These properties were calculated for an N_2/CO_2/CH_4 (8/1/1) mixture over a wide range of gas temperatures, using the Gri-mech 3.0 database [8], assuming thermal equilibrium. This approach avoids coupling a complicated chemistry set to the 3D flow simulations, which would take months to solve and lies out of the scope of this research.

For these look-up tables, C_p was calculated using [9]:

$$C_p = \sum_i \omega_i \times \frac{C_{p,i}}{M_i} \quad \text{(B8)}$$

In which ω_i is the weight fraction of each component i in the mixture at its equilibrium concentration at a given temperature, and $C_{p,i}$ is the heat capacity at constant pressure of each of those species. M_i was the weight of species i.

k_g can be expressed as [9]:

$$k_g = 0.5\left(\sum_i x_i k_i + \frac{1}{\sum_i {x_i}/{k_i}}\right) \quad \text{(B9)}$$

Here, x_i is the molar fraction of species i in the gas mixture and k_i is the thermal conductivity of species i, which was calculated using [9–12]:

$$k_i = 2.669 \times 10^{-6} \frac{\sqrt{TM_i \times 10^3}}{\sigma_i^2 \Omega_k} \times \frac{1.15C_{p,i} + 0.88R_g}{M_i} \quad \text{(B10)}$$

σ_i is the characteristic length of the Lennard-Jones potential of species i, and Ω_k is the dimensionless collision integral given by [9,11,12]:

$$\Omega_k = \frac{b_1}{(T^*)^{b_2}} + \frac{b_3}{exp(b_4 T^*)} + \frac{b_5}{exp(b_6 T^*)} + \frac{4.998 \cdot 10^{-40} \mu_{D,i}^4}{k_b^2 T^* \sigma_i^6}, T^* = T\frac{\varepsilon_i}{k_b} \quad \text{(B11)}$$

Here, b_x are empirical constants, $\mu_{D,i}$ is the dipole constant of species i, ε_i is the potential energy minimum value, and k_b is the Boltzmann constant. These values are tabulated data taken from reported literature [9]. μ was calculated using [9,13]:

$$\mu = \sum_{i=1}^{n} \frac{\mu_i}{1 + \frac{1}{x_i}\sum_{j=1, j\neq i}^{n} x_j \phi_{ij}}, \quad \phi_{ij} = \frac{(1 + (\mu_i/\mu_j)^{0.5}\left(M_j/M_i\right)^{0.25})^2}{\left(4/\sqrt{2}\right)\left(1 + M_i/M_j\right)^{0.5}} \quad \text{(B12)}$$

In this equation μ_i is the dynamic viscosity of each species i:[9,11,12]

$$\mu_i = 2.669 \times 10^{-6} \frac{\sqrt{TM_i \times 10^3}}{\sigma_i^2 \Omega_D} \quad \text{(B13)}$$

Here, Ω_D is expressed similar to Ω_k in equation (14), via:[9,11,12]

$$\Omega_D = \frac{b_1}{(T^*)^{b_2}} + \frac{b_3}{exp(b_4 T^*)} + \frac{b_5}{exp(b_6 T^*)} + \frac{4.998 \times 10^{-40} \mu_{D,i}^4}{k_b^2 T^* \sigma_i^6}, T^* = T \frac{k_b}{\varepsilon_i} \quad \text{(B14)}$$

The gas density of the mixture was calculated using the ideal gas law:[9]

$$\rho_g = \frac{pM_N}{R_g T} \quad \text{(B15)}$$

This formula uses the pressure p, the gas constant R_g, the temperature T and the mean molar mass of the mixture M_N.

B5. Computational results and considerations for the post-plasma catalyst bed

Fig. B5.1 shows the temperature profile in the GAP reactor as calculated by the 3D CFD model. The figure shows that the gas temperature reaches values close to 3500 K in the centre of the plasma, which is in line with the calculated gas temperatures for CO_2 and CH_4 plasmas in the GAP from previous work [4,5]. Once the gas reaches the outlet of the reactor, it has cooled down to a gas temperature of around 1100 K. Fig. B5.2A shows the gas temperature profile beyond the GAP reactor in the post-plasma reactor tube, as calculated by the 2D axisymmetric CFD model. This profile shows how the gas cools down further as it leaves the reactor body and flows through the post-plasma reactor tube. From this profile, it is clear that the

heat of the exhaust gas is not transported evenly over the whole volume of the tube, but is concentrated in the centre of the reactor. This is attributed to the high gas flow velocity that is present as the gas flows out through the small reactor outlet, as demonstrated by the calculated gas flow velocity profile in Fig. B5.2B. The high gas flow drags the heat along through convective heat transport, leaving no time for the gas to diffuse in the radial direction through conductive heat transport.

This has important implications for considering a post-plasma catalyst bed inside the tube, as catalysts located in the centre of the tube will experience a significantly higher temperature compared to catalysts near the edge of the tube. As the activity and stability of a catalyst are strongly dependent on the temperature, this is an important factor for the post-plasma catalyst process in combination with GAP reactors. For the implementation of a post-plasma catalyst bed, it could thus prove beneficial to disturb the centralized flow stream, by e.g. modifying the reactor outlet with a nozzle, introducing more gas mixing and/or more radial heat transport in the post-plasma tube. Introducing the catalyst bed in the tube will also, to some degree, already introduce some disturbance to the central flow stream. In addition, the experimental results of section 3.4.4 show a different temperature depending on the distance of the catalyst bed from the plasma exhaust. Finally, also the feed composition will influence temperature and exhaust gas composition, as

demonstrated by the above results and discussion in section 3.4.4, which can also affect the catalytic performance.

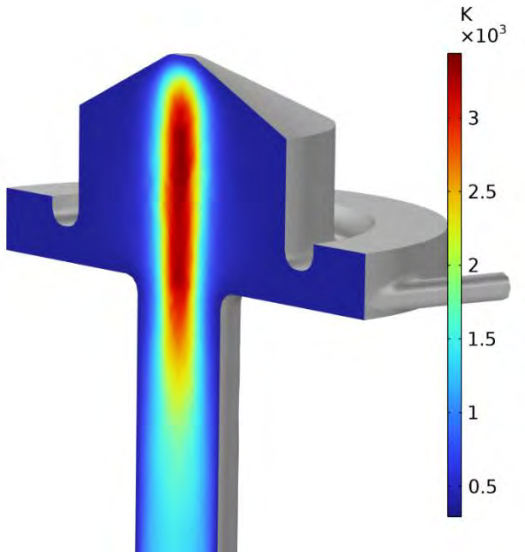

Fig. B5.1. Calculated gas temperature profile in the GAP reactor for a 1/1/8 $CO_2/CH_4/N_2$ gas mixture and a flow rate of 8 L/min.

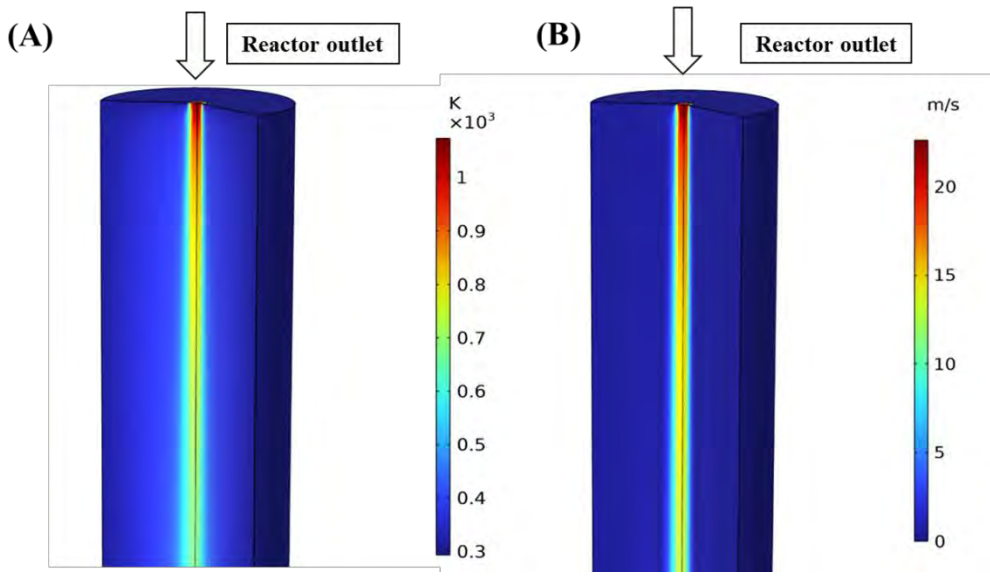

Fig. B5.2. (A) Calculated gas temperature profile and (B) calculated flow velocity profile in the post-plasma reactor tube for a 1/1/8 $CO_2/CH_4/N_2$ mixture gas mixture and a flow rate of 8 L/min.

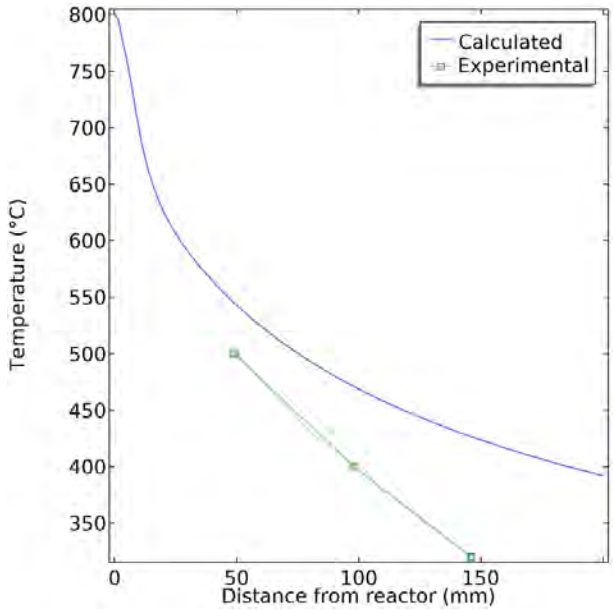

Fig. B5.3. Comparison of temperature measured and modelled for the GAP reactor, as a function of distance from the reactor outlet, at a gas flow rate of 8 L/min and gas composition $CO_2/CH_4/N_2$ = 1/1/8.

Fig. B5.3 displays the axial temperature profile in the centre of the post-plasma reactor tube, as calculated by the 2D axisymmetric CFD model, and compared to the thermocouple measurements shown in paper Fig. 3.7, serving as a validation for the modelling results. While some deviation in absolute values is present and the trend is not the same, a decreasing temperature is observed in both the model and experiments. In general, these results can give us a better idea of where to place a post-plasma catalyst bed. Combined with the experimental results of thermal catalytic DRM [14–16], which indicated that a temperature above 500 °C is necessary for the catalysts to show catalytic activity, we recommend that the distance of a post-plasma catalyst bed should be below 5 cm. Considering the

closer the distance from the plasma exhaust, the higher the temperature will be, as well as the backflow effect caused by the addition of a catalyst bed [17], the distance of a post-plasma catalysis bed should be carefully investigated.

B6. References

[1] Wolf, A. J.; Righart, T. W. H.; Peeters, F. J. J.; Bongers, W. A.; Van De Sanden, M. C. M. Implications of Thermo-Chemical Instability on the Contracted Modes in CO_2 Microwave Plasmas. Plasma Sources Sci. Technol. 2020, 29 (2), 025005. https://doi.org/10.1088/1361-6595/ab5eca.

[2] Van Den Bekerom, D. C. M.; Linares, J. M. P.; Verreycken, T.; Van Veldhuizen, E. M.; Nijdam, S.; Berden, G.; Bongers, W. A.; Van De Sanden, M. C. M.; Van Rooij, G. J. The Importance of Thermal Dissociation in CO_2 Microwave Discharges Investigated by Power Pulsing and Rotational Raman Scattering. Plasma Sources Sci. Technol. 2019, 28 (5), 055015. https://doi.org/10.1088/1361-6595/aaf519.

[3] Gröger, S.; Ramakers, M.; Hamme, M.; Medrano, J. A.; Bibinov, N.; Gallucci, F.; Bogaerts, A.; Awakowicz, P. Characterization of a Nitrogen Gliding Arc Plasmatron Using Optical Emission Spectroscopy and High-Speed Camera. J. Phys. D. Appl. Phys. 2019, 52 (6), 065201. https://doi.org/10.1088/1361-6463/aaefe4.

[4] Van Alphen, S.; Slaets, J.; Ceulemans, S.; Aghaei, M.; Snyders, R.; Bogaerts, A. Effect of N_2 on CO_2-CH_4 Conversion in a Gliding Arc Plasmatron: Can This Major Component in Industrial Emissions Improve the Energy Efficiency? J. CO_2 Util. 2021, 54, 101767. https://doi.org/10.1016/j.jcou.2021.101767.

[5] Trenchev, G.; Kolev, S.; Wang, W.; Ramakers, M.; Bogaerts, A. CO_2 Conversion in a Gliding Arc Plasmatron: Multidimensional Modeling for Improved Efficiency. J. Phys. Chem. C 2017, 121 (39), 24470–24479. https://doi.org/10.1021/acs.jpcc.7b08511.

[6] Trenchev, G.; Kolev, S.; Bogaerts, A. A 3D Model of a Reverse Vortex Flow Gliding Arc Reactor. Plasma Sources Sci. Technol. 2016, 25 (3). https://doi.org/10.1088/0963-0252/25/3/035014.

[7] Cleiren, E.; Heijkers, S.; Ramakers, M.; Bogaerts, A. Dry Reforming of Methane in a Gliding Arc Plasmatron: Towards a Better Understanding of the Plasma Chemistry. ChemSusChem 2017, 10, 4025–4036. https://doi.org/doi.org/10.1002/cssc.201701274.

[8] Smith, G. P.; Golden, D. M.; Frenklach, M.; Moriarty, N. W.; Eiteneer, B.; Goldenberg, M.; Bowman, T. C.; Hanson, R. K.; Song, S.; Gardiner, W. C. J.; Lissianski, V. V.; Qin, Z. GRI-MECH 3.0.

[9] Chemical Reaction Engineering Module, COMSOL Multiphysics. COMSOL AB: Stockholm, Sweden pp 34–56.

[10] Stiel, L. I.; Thodos, G. The Viscosity of Polar Substances in the Dense Gaseous and Liquid Regions. AIChE J. 1964, 10 (2), 275–277. https://doi.org/10.1002/aic.690100229.

[11] Brokaw Richard S. Predicting Transport Properties of Dilute Gases. Ind. Eng. Chem. Process Des. Dev. 1969, 8, 240–253.

[12] Neufeld, P. D.; Janzen, A. R.; Aziz, R. A. Empirical Equations to Calculate 16 of the Transport Collision Integrals Ω(l,8)* for the Lennard-Jones (12-6) Potential. J. Chem. Phys. 1972, 57 (3), 1100–1102. https://doi.org/10.1063/1.1678363.

[13] Wilke, C. R. A Viscosity Equation for Gas Mixtures. J. Chem. Phys. 1950, 18 (4), 517–519. https://doi.org/10.1063/1.1747673.

[14] Lin, X.; Li, R.; Lu, M.; Chen, C.; Li, D.; Zhan, Y.; Jiang, L. Carbon Dioxide Reforming of Methane over Ni Catalysts Prepared from Ni-Mg-Al Layered Double Hydroxides: Influence of Ni Loadings. Fuel 2015, 162, 271–280. https://doi.org/10.1016/j.fuel.2015.09.021.

[15] Kalai, D. Y.; Stangeland, K.; Jin, Y.; Yu, Z. Active and Stable Hydrotalcite Derived Ni Catalysts for CO_2 Reforming of Methane: Comparison with Catalysts by Incipient Wetness. J. CO_2 Util. 2018, 25, 346–355. https://doi.org/10.1016/j.jcou.2017.12.018.

[16] Taherian, Z.; Shahed Gharahshiran, V.; Khataee, A.; Orooji, Y. Synergistic Effect of Freeze-Drying and Promoters on the Catalytic Performance of Ni/MgAl Layered Double Hydroxide. Fuel. 2022. https://doi.org/10.1016/j.fuel.2021.122620.

[17] Zhang, H.; Li, L.; Xu, R.; Huang, J.; Wang, N.; Li, X.; Tu, X. Plasma-Enhanced Catalytic Activation of CO_2 in a Modified Gliding Arc Reactor. Waste Disposal and Sustainable Energy. 2020, pp 139–150. https://doi.org/10.1007/s42768-020-00034-z.

Appendix C: Supporting information for Chapter 5

Table C.1. Selectivity, yield, H_2/CO ratio and carbon balance results of DRM in the thermal catalytic reaction.

Temperature (°C)	Selectivity (%)		Yield (%)		H_2/CO ratio	C balance
	CO	H_2	CO	H_2		
800	88	100	81	80	0.9	89
700	89	100	73	70	0.9	91
600	92	100	48	41	0.8	96
500	100	100	18	11	0.6	101
400	100	100	3	1	0.3	103

Table C.2. Carbon balance for different plasma and plasma-catalytic DRM configurations. Gas composition: $N_2/CH_4/CO_2$ = 8/1/1 or 8/0.6/1, GHSV: 480 $L \cdot g_{cat}^{-1} h^{-1}$.

Configurations	Carbon balance (%)	
	CH_4/CO_2 = 1	CH_4/CO_2 = 0.6
Plasma alone	92.9±0.7	98.7±0.8
T-bed-3 Ni/MO	96.2±1.6	99.7±1.6
N-bed Ni/MO	100.8±0.8	100.5±0.7
N-bed α-Al_2O_3	100.2±1.0	100.2±0.6

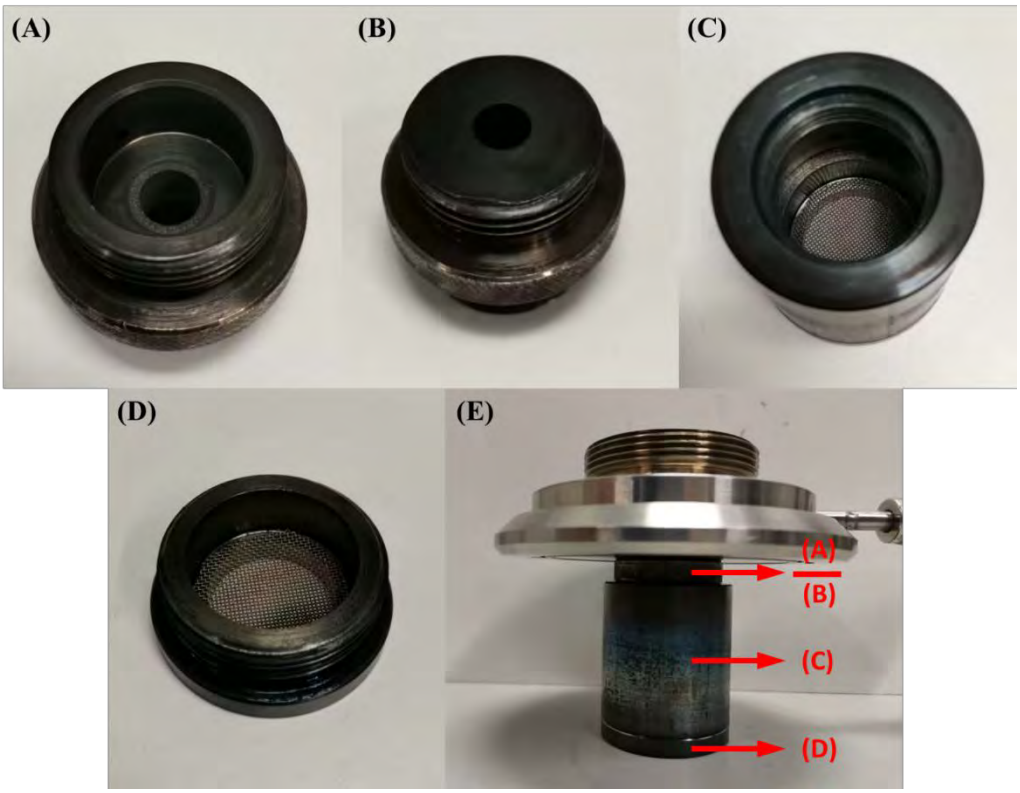

Fig. C.1. Photographs of the N-bed. (A)&(B) the top and bottom sides of the connector. (C) tubular body of the N-bed. (D) bottom with metal mesh of the N-bed. (E) N-bed connection to the plasma device part.

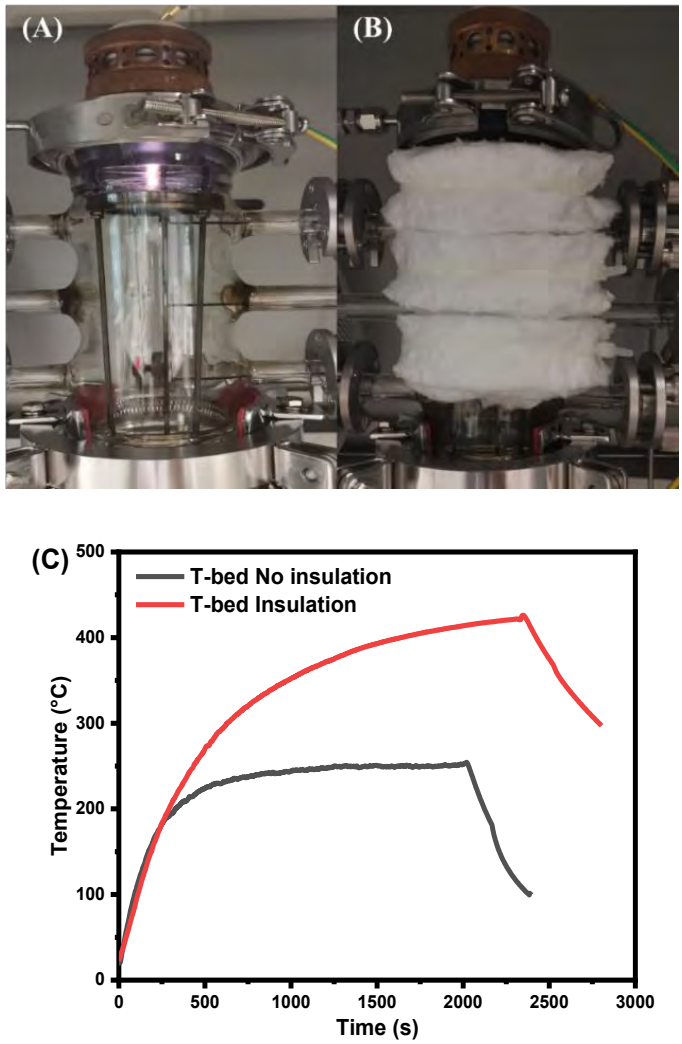

Fig. C.2. Photographs of the GAP setup without (A) and with (B) insulation, and (C) temperature measured after the catalyst bed during the reaction. Gas composition: $N_2/CH_4/CO_2$ = 8/1/1, GHSV: 480 $L \cdot g_{cat}^{-1} h^{-1}$.

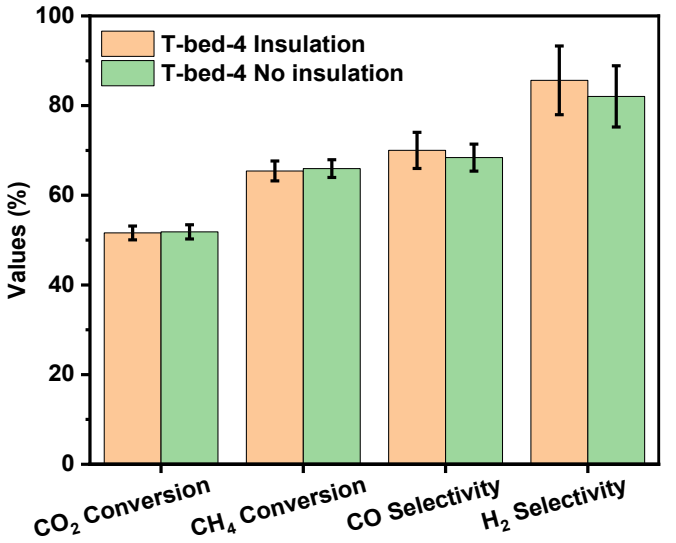

Fig. C.3. Results of conversion and selectivity obtained in the T-bed configuration at a distance of 4 cm, with or without insulation in the system. Gas composition: $N_2/CH_4/CO_2$ = 8/1/1, GHSV: 480 $L \cdot g_{cat}^{-1} h^{-1}$.

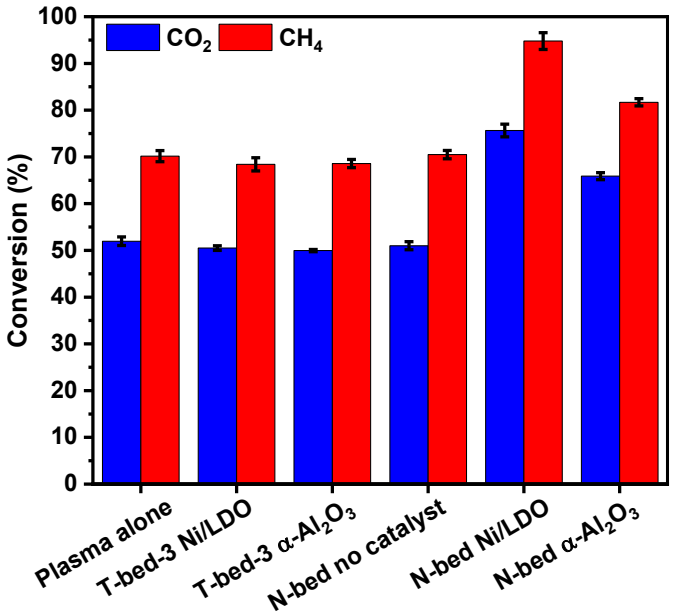

Fig. C.4. Conversion of CO_2 and CH_4 in the GAP post-plasma-catalytic DRM at different conditions with a CH_4:CO_2 ratio of 0.6. Gas composition: N_2: 6.4 L/min, CH_4: 0.6 L/min, CO_2:1 L/min (CH_4/CO_2=0.6), GHSV: 480 $L \cdot g_{cat}^{-1} h^{-1}$.

Figure C.5. includes the Selectivity, yield, H_2/CO ratio, SEI and EC results for a CH_4/CO_2 ratio of 0.6.

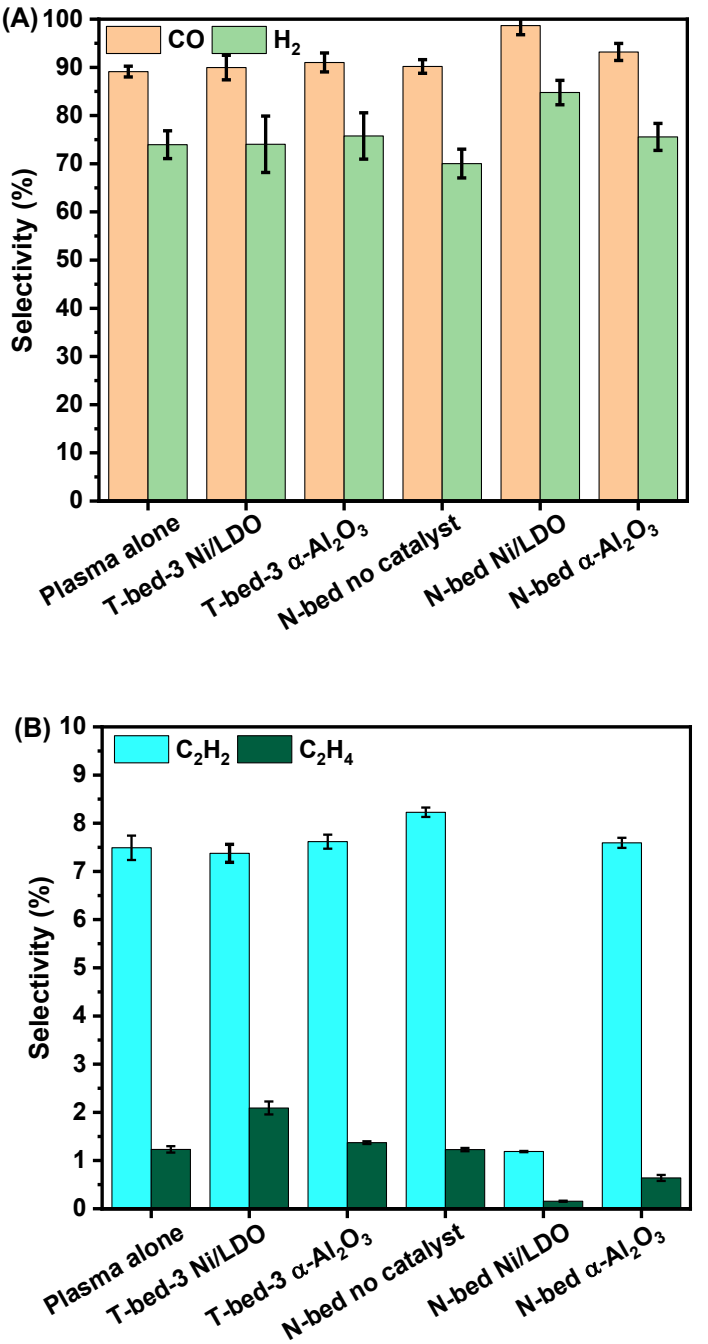

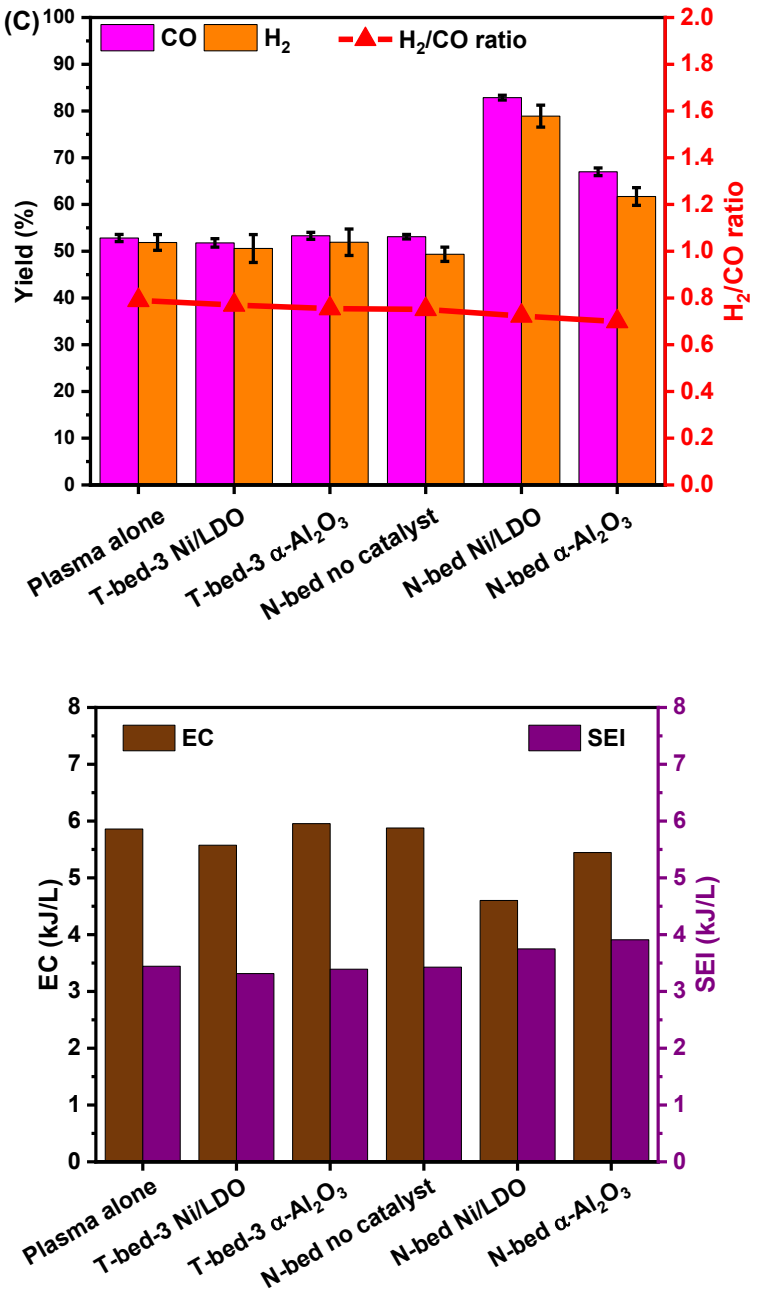

Fig. C.5. Selectivity, yield, H_2/CO ratio, EC and SEI result for a CH_4/CO_2 ratio of 0.6 in the GAP PPC DRM reaction. (A) Selectivity of CO and H_2, (B) Selectivity of C_2H_2 and C_2H_4, (C) Yield of CO and H_2 and H_2/CO ratio, and (D) Energy cost (EC) of the conversion and specific energy input (SEI) into the system in different configurations. Gas composition: N_2: 6.4 L/min, CH_4: 0.6 L/min, CO_2:1 L/min (CH_4/CO_2=0.6), GHSV: 480 $L \cdot g_{cat}^{-1} h^{-1}$.

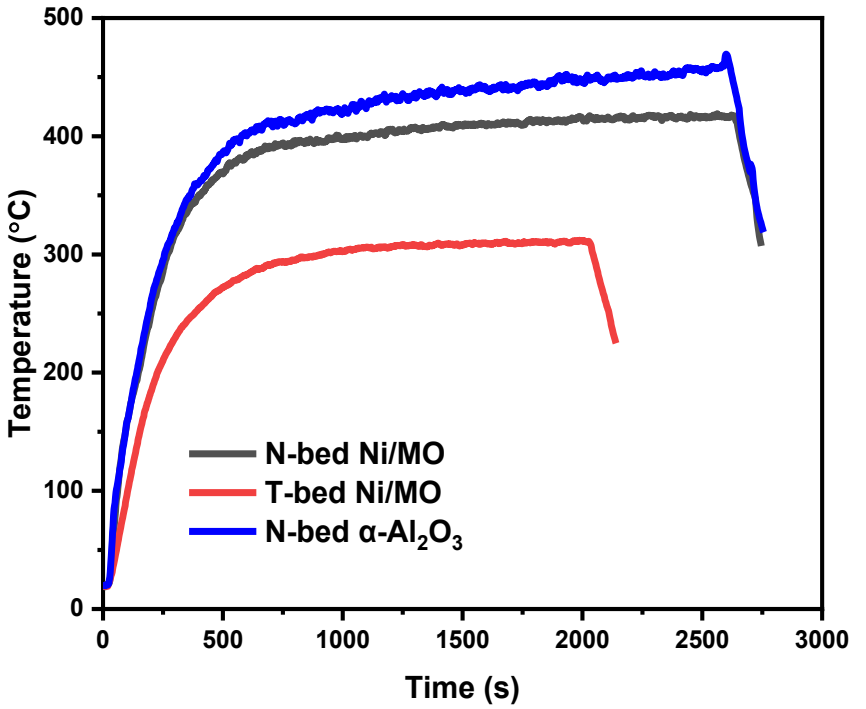

Fig. C.6. Temperature of the gas after the catalyst bed, measured at 4.9 cm. Gas composition: N_2: 6.4 L/min, CH_4: 0.6 L/min, CO_2:1 L/min (CH_4/CO_2=0.6), GHSV: 480 $L \cdot g_{cat}^{-1} h^{-1}$.

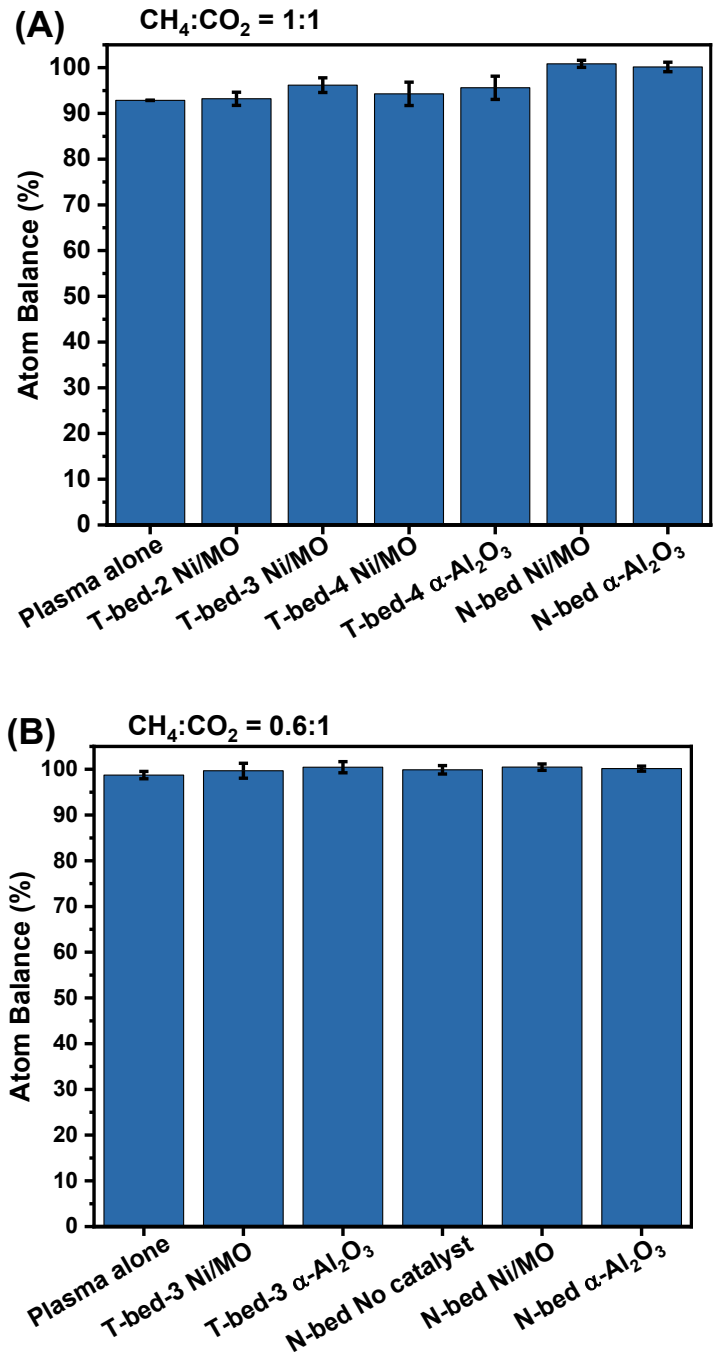

Fig. C.7. Carbon balance in different cases. Gas composition: (A) $N_2/CH_4/CO_2$ = 8/1/1, (B) $N_2/CH_4/CO_2$ = 8/0.6/1, GHSV: 480 $L \cdot g_{cat}^{-1} h^{-1}$.

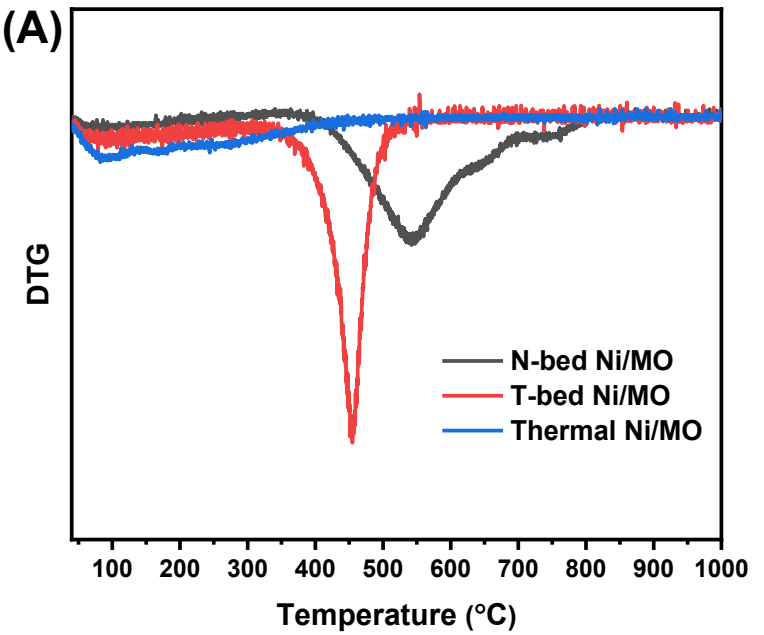
(A)
DTG
N-bed Ni/MO
T-bed Ni/MO
Thermal Ni/MO
100
200
300
400
500
600
700
800
900
1000
Temperature (°C)

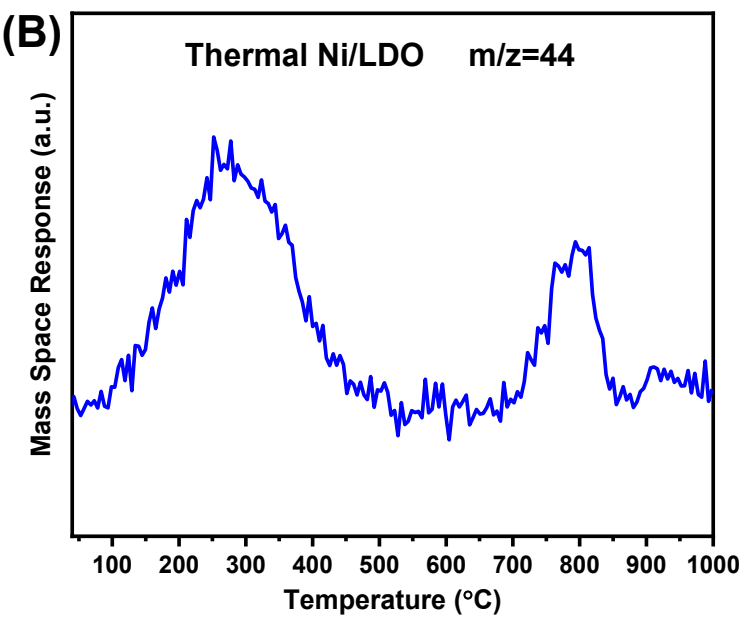
(B)
Thermal Ni/LDO m/z=44
Mass Space Response (a.u.)
100
200
300
400
500
600
700
800
900
1000
Temperature (°C)

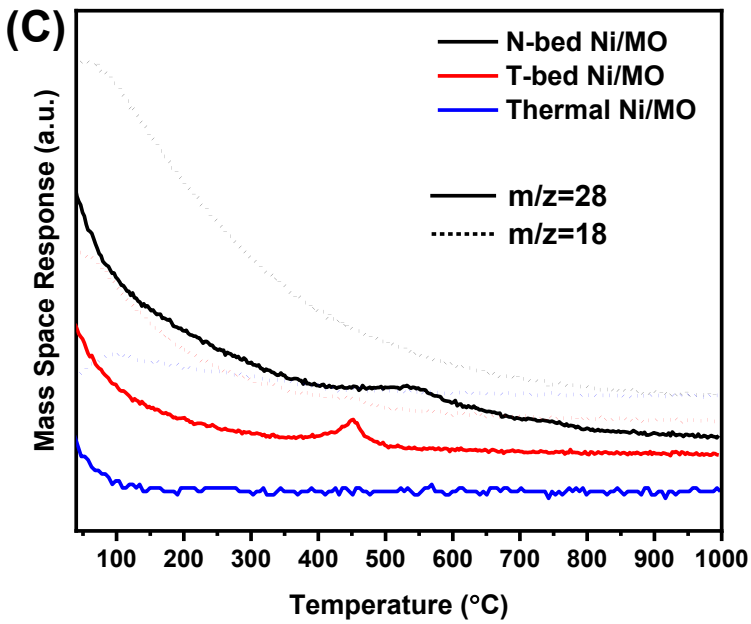

Fig. C.8. (A) DTG of Ni/MO catalyst in different cases after reaction, (B) Enlarged figure of the MS result with m/z=44 for thermal Ni/MO catalysis, and (C) MS result (at m/z=28 and 18) of Ni/MO catalyst in different cases after reaction. Gas composition: $N_2/CH_4/CO_2$ = 8/1/1, GHSV: 480 $L \cdot g_{cat}^{-1} h^{-1}$.

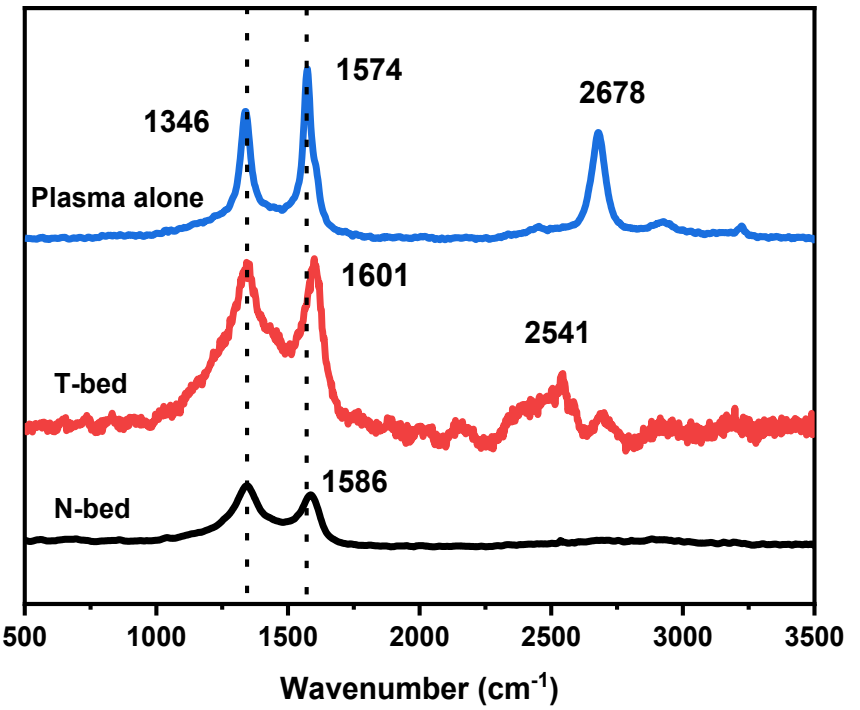

Fig. C.9. Raman spectra of carbon produced under plasma or plasma-catalytic conditions.

Equations for calculation of the performance metrics in plasma-based DRM:

To calculate the performance metrics in case of $CO_2/CH_4/N_2$ DRM, the formulas were used as reported in the literature [1]–[3] (references listed at the end Appendix C). Considering the gas expansion, the expansion factor can be determined by adding an internal standard gas to the outlet gas flow stream after the reactant gas has passed through the plasma. Internal standard gasses can in principle be N_2, He, or Ar. However, in our case, He is impossible as it is the carrier gas of the GC. Neither can Ar be used, as its peak overlaps with the one of O_2. For N_2, in principle, it is also not a suitable gas, because it is used in the mixture which passes through the GAP reactor. However, considering the conversion of N_2 in the GAP plasma DRM is barely converted (< 0.05%) [4], [5], it is used in our case as the internal standard gas. Two correction factors α and β were defined via the following equations:

$$\beta = \frac{\mathrm{N}_{2,in}}{CO_{2,in} + CH_{4,in}} \quad (C1)$$

where $\mathrm{N}_{2,in}$, $CO_{2,in}$, and $CH_{4,in}$ were the gas flow rate of N_2, CO_2, and CH_4 in the feed gas, respectively.

The value of α is corrected by β with equation (C2):

$$\alpha = \frac{\mathrm{N}_{2,\mathrm{blank}}}{\mathrm{N}_{2,\mathrm{plasma}}}(1 + \beta) - \beta \quad (C2)$$

Where $N_{2,blank}$ and $N_{2,plasma}$ represent the amount of N_2 measured before and after starting the plasma.

The concentrations were corrected with equation (C3):

$$C_{i,out} = C_{i,out,m}(1 + \beta/\alpha) \quad (C3)$$

Where $C_{i,out,m}$ means the concentration of sample i, i.e., CH_4, CO_2, CO, and H_2, measured by the GC.

The absolute conversion of CO_2, X_{abs,CO_2} and effective conversion of CO_2, X_{eff,CO_2} were calculated with equation (C4) and equation (C5), respectively. $C_{CO_{2,in}}$ was the concentration of CO_2 measured going through the GAP before the plasma was turned on. $C_{CO_{2,out}}$ was the concentration of outlet gas.

$$X_{abs,CO_2}(\%) = \frac{C_{CO_{2,in}} - C_{CO_{2,out}}}{C_{CO_{2,in}}} \times 100\% \quad (C4)$$

$$X_{eff,CO_2}(\%) = X_{abs,CO_2}(\%) \cdot Fraction_{CO_2} \quad (C5)$$

where $Fraction_{CO_2}$ means the concentration of CO_2 in the inlet gas.

The absolute and effective conversions of CH_4 were defined as equation (C6) and equation (C7):

$$X_{abs,CH_4}(\%) = \frac{C_{CH_{4,in}} - C_{CH_{4,out}}}{C_{CH_{4,in}}} \times 100\% \quad (C6)$$

$$X_{eff,CH_4}(\%) = X_{abs,CH_4} \cdot Fraction_{CH_4} \quad (C7)$$

The C-based selectivity of CO and other chemicals including carbon atoms, the H-based selectivity of H_2, and the yield of CO, and H_2 were defined as equations from (C8) to (C12):

$$S_{H_2} = \frac{C_{H_{2,out}}}{2 \times (C_{CH_{4,in}} - C_{CH_{4,out}})} \times 100\% \quad (C8)$$

$$S_{CO} = \frac{C_{CO_{out}}}{(C_{CH_{4,in}} - C_{CH_{4,out}}) + (C_{CO_{2,in}} - C_{CH_{2,out}})} \times 100\% \quad (C9)$$

$$S_{C_xH_yO_z} = \frac{x \times C_{C_xH_yO_{z,out}}}{(C_{CH_{4,in}} - C_{CH_{4,out}}) + (C_{CO_{2,in}} - C_{CH_{2,out}})} \times 100\% \quad (C10)$$

$$Y_{CO} = \frac{Fraction_{CH_4} \times X_{abs,CH_4} + Fraction_{CO_2} \times X_{abs,CO_2}}{(C_{CH_{4,in}} - C_{CH_{4,out}}) + (C_{CO_{2,in}} - C_{CH_{2,out}})} \times S_{CO} \quad (C11)$$

$$Y_{H_2} = X_{abs,CH_4} \times S_{H_2} \quad (C12)$$

The specific energy input (SEI) and energy cost (EC) were defined as equation (C13) and equation (C14).

$$SEI(kJ/L) = \frac{\text{Plasma Power (kW)} \cdot 60\ (s/min)}{\text{Total gas flow rate (L/min)}} \quad (C13)$$

$$EC(kJ/L) = \frac{SEI\ (kJ/L)}{X_{eff,CO_2}} \quad (C14)$$

For the balance of C atoms in the products versus in the reactants, the equation was as followed:

$$Balance_C = \frac{\alpha \cdot (C_{CO_2(out)} + C_{CH_4(out)} + C_{CO(out)} + 2 \cdot C_{C_2(out)} + 3 \cdot C_{C_3(out)})}{C_{CO_2(in)} + C_{CH_4(in)}} \quad (C15)$$

References

[1] N. Pinhão, A. Moura, J. B. . Branco, and J. Neves, Influence of gas expansion on process parameters in non-thermal plasma plug-flow reactors: A study applied to dry reforming of methane, Int. J. Hydrogen Energy, vol. 41, no. 22, pp. 9245–9255, 2016.

[2] S. Van Alphen, J. Slaets, S. Ceulemans, M. Aghaei, R. Snyders, and A. Bogaerts, Effect of N_2 on CO_2-CH_4 conversion in a gliding arc plasmatron: Can this major component in industrial emissions improve the energy efficiency?, Journal of CO_2 Utilization, vol. 54. 2021. doi: 10.1016/j.jcou.2021.101767.

[3] B. Wanten, S. Maerivoet, C. Vantomme, J. Slaets, G. Trenchev, and A. Bogaerts, Dry reforming of methane in an atmospheric pressure glow discharge: Confining the plasma to expand the performance, Journal of CO_2 Utilization, vol. 56. 2022. doi: 10.1016/j.jcou.2021.101869.

[4] E. Cleiren, S. Heijkers, M. Ramakers, and A. Bogaerts, Dry Reforming of Methane in a Gliding Arc Plasmatron: Towards a Better Understanding of the Plasma Chemistry, ChemSusChem, vol. 10, no. 20, pp. 4025–4036, 2017, doi: 10.1002/cssc.201701274.

[5] J. Slaets, M. Aghaei, S. Ceulemans, S. Van Alphen, and A. Bogaerts, CO_2 and CH_4 conversion in “real” gas mixtures in a gliding arc plasmatron: How do N_2 and O_2 affect the performance?, Green Chem., vol. 22, no. 4, pp. 1366–1377, 2020, doi: 10.1039/c9gc03743h.

Appendix D: List of Publications and Conferences

Publications

Can high temperature calcined Mg–Al layered double hydroxides (LDHs) fully rehydrate at room temperature in vapor or liquid condition?
Wencong Xu, Myrjam Mertens, Thomas Kenis, Elien Derveaux, Peter Adriaensens, Vera Meynen
Materials Chemistry and Physics, 2023, 295, 127113.
doi.org/10.1016/j.matchemphys.2022.127113

Improving the performance of gliding arc plasma-catalytic dry reforming via a new post-plasma tubular catalyst bed
Wencong Xu, Lukas C. Buelens, Vladimir V. Galvita, Annemie Bogaerts, Vera Meynen
To be submitted to Journal of Energy Chemistry.

Effect of Gas Composition on Temperature and CO_2 Conversion in a Gliding Arc Plasmatron reactor: Insights for Post-plasma Catalysis from Experiments and Computation
Wencong Xu, Senne Van Alphen, Vladimir V. Galvita, Vera Meynen, Annemie Bogaerts
To be submitted to Fuel

A review on LDH-derived catalysts for DRM: Can their excellent performance in thermal catalysis also be exploited in plasma catalysis?

Wencong Xu, Vladimir V. Galvita, Annemie Bogaerts, Vera Meynen

To be submitted to Catalysts

Conferences

Poster presentation at the Chemistry Conference for Young Scientists (ChemCYS 2020), in Blankenberge, Belgium, on February 19-21, 2020, presenting "Conversion of CO_2 to Formic Acid with Gliding Arc Plasma and Catalyst"
Wencong Xu, Vladimir V. Galvita, Vera Meynen, Annemie Bogaerts

Attending the 7th ENMIX (European Nanoporous Materials Institute of Excellence) Young Researchers Meeting, online meeting, 2020

Poster presentation at the conference European Congress on Advance Materials and Processes (EUROMAT 2021), online meeting, on September 13-17, 2021, presenting "Room temperature rehydration of high temperature calcined Mg-Al layered double hydroxides (LDHs) in gas and liquid condition"
Wencong Xu, Myrjam Mertens,Vera Meynen

Oral presentation at the 5th International Symposium on Plasmas for Catalysis and Energy Materials 2022 (ISPCEM-2022), Liverpool, July 3-7, 2022, presenting: "Effect of gas composition on CO_2 conversion in a gliding arc Plasmatron"
Wencong Xu, Annemie Bogaerts, Vera Meynen